LARGE EDDY SIMULATION OF EARLY STAGE AIRCRAFT CONTRAILS

by

A. A. Shirgaonkar & S. K. Lele

Prepared with support from the
Stanford Graduate Fellowship and
the Federal Aviation Administration

Report No. TF-100

Flow Physics and Computational Engineering Group
Department of Mechanical Engineering
Stanford University
Stanford, CA 94305-3035

April 2007

Abstract

Aircraft contrails at cruise altitudes present a unique problem in atmospheric sciences due to their location where other anthropogenic sources of particulate emissions are absent, and due to their potential impact on the Earth's radiative balance. The scale separation between contrails and atmospheric motions contributes to the large uncertainties in contrail models used in global atmospheric calculations. We study the early-stage contrail growth using high-fidelity Large Eddy Simulations (LES) to better characterize the early contrail-scale processes.

We develop an extended Boussinesq approximation to improve the traditional Boussinesq approximation for inertia-dominated flows with buoyancy. We develop an Eulerian-Lagrangian ice microphysics model and couple it to the flow solver. Verification and validation of the model and the numerical method are discussed. The choice of the number of Lagrangian computational particles required to adequately represent particle statistics is studied.

We investigate the behavior of two dimensional aircraft wakes containing exhaust jets. A mechanism is identified by which the jet-induced baroclinic vorticity influences the wake dynamics. The jets strengthen the primary vorticity and reduce the primary vortex pair spacing, causing accelerated wake descent.

Three-dimensional LES of contrails are carried out for the first 20 second duration of contrail life, starting at 1 second behind the aircraft. The initial conditions at 1 s correspond to a typical large subsonic aircraft. Three different regimes of early contrail growth are found, which are controlled by jet humidity, jet turbulence and ice particle-induced perturbations, and ambient relative humidity with respect to ice (RHi) respectively. Sensitivity of ice properties to atmospheric temperature and relative humidity, initial ice nuclei size and number density is characterized. Ambient temperature and RHi are found to be critical in determining the rate of ice growth. Particle size distribution is skewed to

higher radii for higher RHi. The total ice area, ice particle size, and number density are found to be sensitive to the initial ice nuclei number density, but the total ice mass remains insensitive to it at least in the regime considered. Ice growth is found to be relatively insensitive to the initial particle size for the size range considered.

Acknowledgements

This work was supported by the Federal Aviation Administration's PARTNER Center of Excellence under grant number USDot, FAA, 03-C-NE-SU with Dr. Mohan Gupta as the program manager. Additional support from the Eric and Illeana Benhamou Stanford Graduate Fellowship is acknowledged. Computational resources were provided by the San Diego Supercomputer Center and the National Center for Supercomputing Applications. We have benefitted from discussions with Dr. Steven L. Baughcum and Dr. Richard C. Miake-Lye. We thank Dr. Baughcum and Boeing for providing their RANS data for use in the initial conditions for our simulations. Comments from Dr. Michael Danilin and Dr. Jeffrey Crouch are acknowledged. We thank Boeing and Aerodyne Research, Inc. for providing their box model microphysics results for comparison. Comments from Professors Parviz Moin and Mark Z. Jacobson on a draft of the report are gratefully acknowledged.

Contents

Abstract **iii**

Acknowledgements **v**

1 Introduction **1**

1.1 Global impact of contrails: Research needs 2

1.1.1 Particulate emissions in the context of contrails 3

1.1.2 Contrail modeling at global and regional scales 5

1.2 Contrails: Theoretical background 6

1.2.1 Contrails as a multiscale problem 7

1.2.2 Modeling contrails for different time-scale regimes 7

1.3 Contrail simulations: Previous work 9

1.4 Overview and accomplishments 11

2 The Extended Boussinesq Approximation **14**

2.1 Asymptotic analysis 17

2.1.1 Equation of state 24

2.1.2 Energy equation 24

2.2 Low Mach number flows 25

2.2.1 Buoyancy-driven low Mach number shallow flows 27

2.3 "Nearly incompressible" hydrostatic state 27

2.4 Vorticity dynamics 30

2.5 Algorithmic simplification for slowly varying flows 31

2.6 Numerical tests with the extended model 32

2.6.1 Isolated Taylor vortex 32

2.6.2 2D Taylor vortex array 34
2.7 Conclusions 37

3 Formulation of the Contrail Problem **40**
3.1 Initial conditions 44
3.2 Flow Physics: Large Eddy Simulation 45
3.2.1 Filtered equations and subgrid scale modeling 46
3.3 Microphysics model 48
3.4 Numerical Method 52
3.4.1 Spatial discretization 52
3.4.2 Temporal discretization 55
3.4.3 Convective terms and control of aliasing errors 55
3.4.4 Poisson equation for pressure solution 57
3.4.5 Microphysics Solution 57
3.4.6 Code performance 58

4 Verification and Validation **60**
4.1 Laminar wake descent in a stratified atmosphere 61
4.2 Subgrid scale model 62
4.3 Microphysics model 62
4.4 Passive scalar transport 64
4.5 Convective terms: Equipartition of energy 67
4.6 Buoyancy terms: Rayleigh-Benard Instability 69
4.7 Effect of boundary conditions 72
4.8 Jet stage 73
4.8.1 Turbulence development 74
4.8.2 Evaluation of ice particle statistics 74
4.9 Grid sensitivity of contrail simulations 80
4.9.1 Sensitivity to Eulerian grid size 80
4.9.2 Temporal convergence 81
4.9.3 Convergence with number of Lagrangian particles 81

5 Two-dimensional Behavior of Buoyant Wake-Jets **94**
5.1 Introduction 94

5.2 Model problem 96
5.3 Role of jet buoyancy 99
5.3.1 Effect of jet temperature 102
5.4 Isolated effect of jet buoyancy 102
5.5 Traditional vs. extended Boussinesq model 103
5.6 Conclusion 104

6 Sensitivity Study of Early Stage Contrails **117**
6.1 Generation of initial conditions 120
6.1.1 Flow data 120
6.1.2 Particle data 121
6.2 Baseline case 121
6.3 Effect of relative humidity 123
6.4 Effect of ambient temperature 143
6.5 Sensitivity to the number of ice nuclei 146
6.6 Sensitivity to initial ice particle size 148
6.7 Role of initial fluid turbulence seed 154
6.8 Sensitivity to initial conditions 154
6.9 Conclusion 159

7 Convergence of Lagrangian Statistics **162**
7.1 Background 162
7.2 Convergence with respect to Eulerian grid 164
7.3 Criteria for number of Lagrangian particles 166
7.4 Conclusion 170

8 Conclusions **176**
8.1 Recommendations for future work 179

Bibliography **180**

List of Tables

2.1 Nondimensional parameters 20

3.1 Aircraft parameters at the jet exit plane. Superscript '*' on dimensional variables is omitted for brevity. 42
3.2 Atmospheric parameters. Superscript '*' on dimensional variables is omitted for brevity. 43
3.3 Physical scales and nondimensional parameters 47
3.4 Coefficients for the LDDRK4 scheme 56

6.1 Simulation cases 119

List of Figures

1.1 Contrails at various stages of their life. Photo by Anup Shirgaonkar 2

1.2 Aircraft radiative forcing (RF) from various factors for 1992. Adopted from the IPCC report (1999). Error bars denote 67% confidence interval. The remarks at the bottom end of the figure indicate our level of understanding of the factors. 3

1.3 Aircraft radiative forcing from various factors for 1992 and 2000. Adopted from Sausen *et al.* (2005). The lines with circles display different estimates for the possible range of RF from aviation-induced cirrus clouds. Dashed lines with cross indicate an estimate of the range for RF from aviation-induced cirrus. The total does not include the contribution from cirrus clouds. Error bars denote 67% confidence interval. 4

1.4 Scales involved in the contrail problem. The rightmost column indicates models used. The sub-grid evaporation model is not used in this study but is listed as a future modeling possibility. 8

2.1 Initial condition for the Taylor vortex case. Lines: Vorticity; Filled: Nonhydrostatic density, ρ'. 33

2.2 Vorticity contours at $t = 2$ for the Taylor vortex with (a) Traditional Boussinesq and (b) Extended Boussinesq approximation. 34

2.3 A-posteriori comparison of terms in the momentum equation at $t = 2$, computed using the extended Boussinesq approximation. (a) Perturbation density, ρ' (b) Gravity term, $-\eta_1\rho'/Fr$ (c) Magnitude of the extended Boussinesq term, $|Ext_n|$ (d) Magnitude of the error, $|Err_n|$. 35

2.4 Contours of ρ' for the Taylor vortex array at $t = 120$ with (a) Traditional Boussinesq and (b) Extended Boussinesq approximation. 36

2.5 Effect of the extended terms on flow quantities for the Taylor vortex array. 37

3.1 Schematic of the flow development behind a typical subsonic aircraft. 40
3.2 Evolution of R, the ratio of the jet momentum relative to the vortex momentum, along the jet axis, indicating the beginning of the interaction regime approximately three wing spans (300 jet diameters) downstream. 41
3.3 Variation of (a) Mach number and (b) Jet temperature downstream of the aircraft. Dashed line indicates ambient temperature. All values are in a stationary domain through which the jet passes at cruise speed. The x-axis corresponds to the distance of the stationary observation point from the moving jet nozzle. 45
3.4 Saturation pressure of water vapor over ice, taken from Murphy and Koop (2005). 51
3.5 Modified wavenumber for the first derivative scheme OPT6 of Lui & Lele (2001) 53
3.6 Modified wavenumber for the second derivative scheme OPT6 of Lui & Lele (2001) 54

4.1 Stratified vortex pair descent rate comparison with experiments by Sarpkaya (1983) and simulations by Spalart (1996). 62
4.2 Comparison of LES results with experiments of Comte-Bellot and Corrsin (1971) (CBC). Lines: LES, Symbols: CBC 63
4.3 Comparison among the microphysical models from —, this study; – –, Aerodyne; and –·–, Boeing for the box model baseline test case. Irregularities in the curves at $t < 10\ s$ are due to digitization errors. 64
4.4 Initial flowfield at 5 wingspans for tracer validation runs. It is obtained by interpolation of and turbulence addition to the data provided by Boeing which was obtained by RANS simulations performed by Boeing. All variables are normalized. 66
4.5 Plume-integrated passive scalar normalized by the initial value. 67
4.6 Evolution of passive scalar for the validation case. 68
4.7 Normalized tracer computed in Eulerian and Lagrangian manners at 75 wing spans. 69
4.8 Line plots of tracer along the horizontal line passing through the vortex cores ($y = 2.518$) and away from the cores ($y = 2.294$). 69

4.9 Passive scalar at 100 wing spans from this study and from LES by West Virginia University group (Huebsch & Lewellen, 2006). 70
4.10 Spectra at approximately 8.27 eddy turnover times: -, initial condition: –. . 70
4.11 Growth rate for the Rayleigh-Benard instability. 72
4.12 Evaluation of domain length on wake descent. The step-structure is an artifact of the vortex detection algorithm. 73
4.13 Spectra at $t = 0.9$ for the temporal jet LES. 74
4.14 Turbulent jet at $t = 0.9$ from the temporal LES. 75
4.15 Jet spreading characteristics from the temporal LES. 76
4.16 Radial profiles at various times. Velocity and scalar are scaled by their centerline values, and radial distance by the jet half-width. 76
4.17 Axially averaged view of the jet at $t = 0.9$. Only a homogeneously chosen subset of the total 0.5 million particles is shown to maintain clarity. 77
4.18 Error in the conservation of total (vapor plus ice) water in the jet LES. . . 77
4.19 Radial profiles of jet axial velocity and particle number density at $t = 0.9$. Symbols: Probe locations. 78
4.20 Plot showing the number of particles N_{p1}, N_{p2}, N_{p3} in the three different particle samples used at each probe for the convergence study. The x-locations of symbols indicate probe locations. The three samples correspond to taking every 4th, every 2nd, and every particle in the tube. 78
4.21 Histogram of ice particles at various probe locations as defined in Figure 4.19. 79
4.22 Variation of moments of particle distribution with sampling rate. 82
4.23 Error in moments with sampling rate. 82
4.24 Convergence of histograms with sample size. ΔN_p has been normalized by the total sample size. 83
4.25 Passive scalar contours with nominal and finer grids at 100 wing spans. . . 84
4.26 Z-averaged nondimensional flow quantities from tracer LES at 100 wing spans along the horizontal line passing through the vortex centers. Solid line: nominal grid, dashed line: finer grid. 85
4.27 Z-averaged water vapor density contours (in kg/m^3) with nominal and finer grids at 100 wing spans. 86
4.28 Z-averaged ice density contours (in mg/m^3) with nominal and finer grids at 100 wing spans. 86

4.29 Z-averaged nondimensional flow quantities from case A1 at 100 wing spans along the horizontal line $y = 2.71$. Solid line: nominal grid, dashed line: finer grid. 87

4.30 Contours of particle number density in $\#/cc$ showing probe locations at $(x, y) = (2.25, 2.40)$, $(2.70, 2.40)$, $(2.40, 2.10)$, and $(2.10, 2.00)$. 88

4.31 Ice particle size distribution integrated in a rectangular tube of area $4\Delta x \times 4\Delta y$ with center at the respective probe location, with nominal, —; and finer, – – grid. 89

4.32 Domain integrated ice properties from case A1. Solid line: nominal grid, dashed line: finer grid. 90

4.33 Temporal convergence of initial evolution of ice properties from case A1. Time step $dt = 0.06s$, —; $dt/2$, – –; $dt/10$, –·–. 91

4.34 Domain integrated ice properties from case A1. Solid line: $N_{comp} = 1000,000$, dashed line: $N_{comp} = 250,000$. 92

4.35 Ice particle size distribution integrated in a rectangular tube of area $4\Delta x \times 4\Delta y$ with center at the respective probe location, with $N_{comp} = 1000,000$, —; and $N_{comp} = 250,000$, – –. 93

5.1 Initial configuration of vortices and jets. Filled contours: axial vorticity; lined contours (centered at $(x, y) = (1.75, 6.9)$ and $(2.25, 6.9)$): temperature with contour levels from 0.1 to 0.9 with increments of 0.1. 98

5.2 Movement of vortex centers for the baseline case. The vertical arrest of the descent due to stable stratification is visible around $t = 2$. The initial fluctuations in vortex spacing are due to the wobbling motion of vortex cores caused by the elliptic shape of the finite vortex cores. 100

5.3 Positive, negative components and total circulation in the left half ($x < 2$) for the baseline case. 101

5.4 Vorticity evolution in the jet-wake flow, baseline case. Note that in (a) to (d) only the left vortex is shown for clarity. The right side is symmetric about $x = 2$. 106

5.5 Movement of vortex centers for the baseline case with three grid sizes – coarse, $(N_x, N_y) = (256, 640)$; nominal, $(384, 960)$; fine, $(512, 1280)$. 107

5.6 Vorticity contours with three grid sizes – coarse, $(N_x, N_y) = (256, 640)$; nominal, $(384, 960)$; fine, $(512, 1280)$. 107

5.7 Jet fluid transport represented by passive scalar in the jet-wake flow, baseline case. Note that in (a) to (d) only the left half of the domain is shown for clarity. The right side is symmetric about $x = 2$. 108

5.8 Jet perturbation temperature evolution in the jet-wake flow, baseline case. Note that in (a) to (d) only the left half of the domain is shown for clarity. The right side is symmetric about $x = 2$. 109

5.9 Schematic showing the motion induced by the baroclinic vorticity on the primary vorticity. 110

5.10 Vortex descent and separation for no jet, $\beta = 0$; weak jet, $\beta = 0.02$; strong jet, $\beta = 0.05$. 110

5.11 Vorticity evolution for no jet, $\beta = 0$ (top); weak jet, $\beta = 0.02$ (middle); strong jet, $\beta = 0.05$ (bottom). For $t < 4$ only the left half of the domain is shown for clarity. 111

5.12 Passive scalar transport at $t = 4$ for no jet, $\beta = 0$; weak jet, $\beta = 0.02$; strong jet, $\beta = 0.05$. 112

5.13 Vortex descent and separation in an unstratified atmosphere without the jet, $\beta = 0$; and with jet, $\beta = 0.05$. 112

5.14 Vorticity (top) and passive scalar (bottom) transport at $t = 3.5$ in an unstratified atmosphere without the jet, $\beta = 0$; and with jet, $\beta = 0.05$. 113

5.15 Positive, negative components and total circulation in the left half ($x < 2$) in an unstratified atmosphere without the jet, $\beta = 0$; and with jet, $\beta = 0.05$. 114

5.16 Vorticity evolution for the baseline case using traditional (upper) and extended (lower) Boussinesq approximations. Note that up to $t = 2$ only the left vortex is shown for clarity. The right side is symmetric about $x = 2$. . . 115

5.17 Movement of vortex centers for the baseline case with traditional and extended Boussinesq approximation. 116

5.18 Passive scalar distribution at $t = 4$ with traditional and extended Boussinesq approximation. 116

6.1 Initial flowfield at 5 wingspans. It is obtained by interpolation of and turbulence addition to the data provided by Boeing which was obtained by RANS simulations performed by Boeing. All variables are normalized. 124
6.2 Initial ice properties at 5 wingspans. Number density of particles is made proportional to the water vapor density at each grid point. Particle size distribution is unimodal with $r_p = 0.1\mu m$. 125
6.3 Isosurface of vorticity magnitude 1.5 at $t = 20\ s$ for the baseline case. Elongated vorticity structures are visible. 126
6.4 Evolution of water vapor density for case A1. 127
6.5 Evolution of perturbation temperature for case A1. 128
6.6 Evolution of ice particle number density (in $\#/cc$) for case A1. 129
6.7 Evolution of ice water content (in mg/m^3) for case A1. 130
6.8 Total water budget 131
6.9 Domain-integrated ice particle properties for case A1. 132
6.10 Ice particle size distribution at various times for Case $A1$. At $t = 1s$ the distribution is unimodal with radius $0.1\mu m$. Broadening of the PDF is visible in the intermerdiate stage. 133
6.11 Evolution of water vapor density for case A2. 134
6.12 Evolution of perturbation temperature for case A2. 135
6.13 Evolution of ice particle number density (in $\#/cc$) for case A2. 136
6.14 Evolution of ice water content (in mg/m^3) for case A2. 137
6.15 Evolution of water vapor density for case A3. 138
6.16 Evolution of perturbation temperature for case A3. 139
6.17 Evolution of ice particle number density (in $\#/cc$) for case A3. 140
6.18 Evolution of ice water content (in mg/m^3) for case A3. 141
6.19 RHi field in the initial conditions with constant ambient water vapor. 142
6.20 Domain-integrated ice particle properties for —, $RHi = 110\%$; – –, 130%; –·–, 90%. 144
6.21 Dependence of particle size distribution on RHi at $t = 1.2\ s$, —; $5\ s$, – –; $10\ s$, – · –; $15\ s$, –○–; $20\ s$, –□– 145
6.22 Domain-integrated ice particle properties for —, $T_{amb} = 218.8\ K$; – –, $200\ K$; –·–, $240\ K$. RHi is kept constant at 110% for all three cases. 147

6.23 Saturation pressure of water vapor over ice, taken from Murphy and Koop (2005). 148

6.24 Dependence of particle size distribution on ambient temperature at $t = 1.2\ s$, —; 5 s, – –; 10 s, – · –; 15 s, –○–; 20 s, –□– 149

6.25 Domain-integrated ice particle properties for —, $Np = 5.787 \times 10^{12}\#/m$; – –, $2.894 \times 10^{12}\#/m$; –·–, $1.447 \times 10^{12}\#/m$. 150

6.26 Sensitivity of particle size distribution to initial ice nuclei number at $t = 1.2\ s$, —; 5 s, – –; 10 s, – · –; 15 s, –○–; 20 s, –□– 151

6.27 Domain-integrated ice particle properties for —, $r_{po} = 0.1\mu m$; – –, $0.05\mu m$; –·–, $0.2\mu m$. 152

6.28 Sensitivity of particle size distribution to initial ice particle size at $t = 1.2\ s$, —; 5 s, – –; 10 s, – · –; 15 s, –○–; 20 s, –□– 153

6.29 Domain-integrated ice particle properties for —, with initial turbulent seed and – – without the seed. 155

6.30 Dependence of particle size distribution on the presence of the initial turbulence seeding. Quantitative change is observed but qualitative trend is similar. 156

6.31 Initial vortex-jet configuration. Jet and vortex radii not drawn to scale. . . 157

6.32 Idealized initial flowfield at 5 wingspans with realistic turbulent jets. All variables are normalized. The distortions visible in all fields correspond to the jet turbulence. 158

6.33 Domain-integrated ice particle properties for —, case $A1$; – –, case $A1S$ . . 160

6.34 Sensitivity of particle size distribution to initial conditions at $t = 1.2\ s$, —; 5 s, – –; 10 s, – ·–; 15 s, –○–; 20 s, –□– . Note that the vertical scales are different. 161

7.1 Domain-integrated ice particle properties for the baseline case with different grid sizes in the flight direction. 166

7.2 Domain-integrated ice particle size distribution for the baseline case with different grid sizes in the flight direction. 167

7.3 Contours of particle number density in $\#/cc$ showing probe locations at $(x, y) = (2.25, 2.40)$, $(2.70, 2.40)$, $(2.40, 2.10)$, and $(2.10, 2.00)$. 167

7.4 Ice particle size distribution integrated in a rectangular tube of area $4\Delta x \times 4\Delta y$ with center at the respective probe location, with different grid sizes in the flight direction. 168
7.5 Volume-averaged particle statistics for the box model test with $RHi = 100.5\%$ for $N_{comp} = 8$, –□–; 32, –○–; 128, –∗–; 512, —; 2048, – – ; 4096, – · – 171
7.6 Relative error $\epsilon(r_p)$ in mean particle radius at $t = 300s$ with the box model calculations with $RHi = 100.5\%$. The solution with $N_{comp} = 4096$ has been regarded as the exact solution in defining ϵ. 172
7.7 Particle size distribution in the full domain for various N_{comp} for the box model calculations. 172
7.8 Standard deviation of particle radius distribution at $t = 300s$ vs number of Lagrangian particles. 173
7.9 Standard deviation of the particle size distribution for the box model calculations for $N_{comp} = 8$, –□–; 32, –○–; 128, –∗–; 512, —; 2048, – – ; 4096, – · –. Note that the mean particle radius at $300s$ is $1.6\mu m$. 173
7.10 Volume-averaged particle statistics for the box model test with $RHi = 110\%$ for $N_{comp} = 8$, –□–; 32, –○–; 128, –∗–; 512, —; 2048, – – ; 4096, – · – 174
7.11 Relative error $\epsilon(r_p)$ in mean particle radius at $t = 300$ s with the box model calculations with $RHi = 110\%$. The solution with $N_{comp} = 4096$ has been regarded as the exact solution in defining ϵ. 175

Chapter 1

Introduction

Aircraft condensation trails (contrails) consist of ice particles formed in the wake of an aircraft when conducive atmospheric conditions are present. The particulate emissions from the jet exhaust act as nuclei for ice growth on which the moisture from the jet exhaust and from the atmosphere deposits to form contrails. Contrails are distinctive features in the sky due to their visible prominence and peculiar structures as seen in Figure 1.1. They can spread and evolve into cirrus clouds in the long term. Contrail-induced cirrus clouds are indistinguishable from naturally occurring cirrus clouds (Minnis *et al.*, 2004) and can cause changes in the atmosphere. For instance, observations during the three-day air traffic shutdown immediately after September 11, 2001 indicate that the diurnal temperature range (DTR) over three-day periods showed an increase of about 1.1^oC over the normal 1971-2000 values, the only increase more than two standard deviations away from the mean DTR (Travis *et al.*, 2002).

Contrails are a part of the larger research area of environmental impact of aviation. The aviation-induced impact can be broadly classified into many components including noise, emissions, and vortex wake hazard. The latter is important only in the vicinity of airports for air traffic control (ATC) and has received much attention due to its direct economical impact (Spalart, 1998). Particulate and gaseous emissions in and around the airport also have important health and socio-economical consequences for the local communities. However, aviation's global impact on the environment is mainly related to the direct and indirect effects of aircraft emissions in the atmosphere. Contrails are one of the prime indirect effects of aircraft emissions. They occupy a unique position in this area because of their location which is in the upper troposphere/lower stratosphere region where other anthropogenic

Figure 1.1: Contrails at various stages of their life. Photo by Anup Shirgaonkar

sources of emissions are absent.

1.1 Global impact of contrails: Research needs

The Intergovernmental Panel on Climate Change (IPCC) published a comprehensive status report on the global environmental impacts of aviation in 1999 (Penner *et al.*, 1999). This report constitutes a landmark effort which summarizes the status of understanding at that time, and makes many recommendations to scientists and policymakers about the needs for further research. The report (hereafter referred to as IPCC-99) estimates CO_2 emissions from aircraft to be 0.14 $Gt/year$ in 1992 which is about 2% of the total anthropogenic CO_2 emissions, and 13% of those from all transportation sources. Aircraft-related CO_2 emissions are estimated to increase by a factor of 1.6 to 10 by 2050, for the scenarios considered in IPCC-99. The report also gives estimates of the total radiative forcing (RF) caused by aviation-related factors for the year 1992 (Figure 1.2). The figure also shows our degree of understanding of how various factors contribute to the RF. In 1992 the aviation-induced RF contributed 3.5% to the total anthropogenic RF (IPCC-99). The figure indicates the direct radiative forcing by various emissions as well as indirect effect through contrails and aviation-induced cirrus clouds. Although this measure (RF) is an important measure, it does not take into account the social and economical impact in the broader sense which is desirable to know for policy decisions. IPCC-99 discusses, beyond the direct RF impact,

policy issues as well as technological issues such as engine technology and air traffic control. Nevertheless, for the aim of advancing our scientific understanding, Figure 1.2 has been a key figure in the past half decade emphasizing the need for further research. Subsequently updated estimates are available due to Sausen *et al.* (2005) and are depicted in Figure 1.3. They show the relative increase of RF due to various factors since the IPCC report.

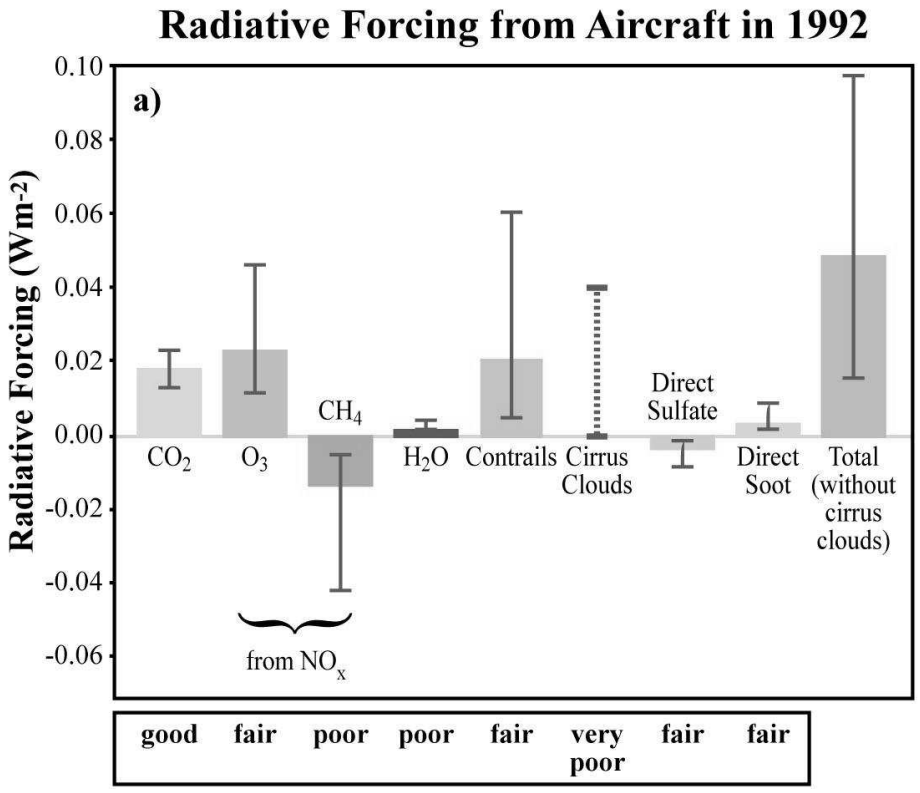

Figure 1.2: Aircraft radiative forcing (RF) from various factors for 1992. Adopted from the IPCC report (1999). Error bars denote 67% confidence interval. The remarks at the bottom end of the figure indicate our level of understanding of the factors.

1.1.1 Particulate emissions in the context of contrails

It is seen from Figure 1.2 that the contrail-induced RF is a significant fraction of the total aviation-induced RF, and the uncertainties in its estimation are high. These uncertainties can arise in part due to the lack of understanding of the behavior of particulate emissions in the atmosphere, and the lack of data to reliably predict their ability to act as ice nuclei.

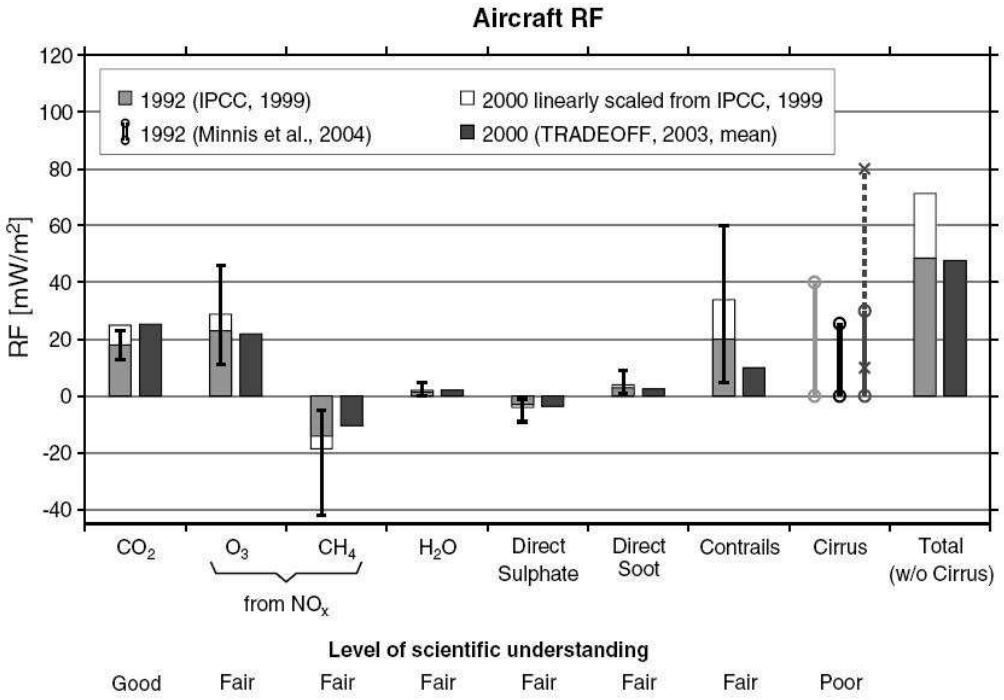

Figure 1.3: Aircraft radiative forcing from various factors for 1992 and 2000. Adopted from Sausen *et al.* (2005). The lines with circles display different estimates for the possible range of RF from aviation-induced cirrus clouds. Dashed lines with cross indicate an estimate of the range for RF from aviation-induced cirrus. The total does not include the contribution from cirrus clouds. Error bars denote 67% confidence interval.

The uncertainties in the amount and properties of particle emissions from an aircraft engine directly contribute to the inaccuracies of contrail models.

Several activities have added to the knowledge and data regarding aircraft emissions, such as the NASA Experiment to Characterize Aircraft Volatile Aerosol and Trace Species Emissions (EXCAVATE) (Anderson *et al.*, 2003) and the NASA Stratospheric Photochemistry, Aerosol and Dynamics Expedition (SPADE) program (Fahey, 1995). These and other programs have included the studies of the dependence of emission properties (both gaseous and particulate) on aircraft parameters such as engine power, aircraft type, fuel composition and plume age. Several studies also exist that develop and use models and numerical methods to determine the impact of near-field plume processes (Brown *et al.*, 1996; Kärcher *et al.*, 1996*a*) and design/operational conditions (Lukachko & Waitz, 2005) on aircraft emissions.

Another area of extensive research is the basic microphysical processes such as nucleation, coagulation, condensation, hydration, dilution, and chemistry (Jacobson & Seinfeld, 2004). This research sheds light on the detailed microphysics at nanometer scales. All of the above aspects of research on particulate emissions provide useful input to contrail models, but themselves involve various sources of uncertainties especially when applying the results to different sets of operating conditions. Two important implications can be drawn here from the contrail perspective – firstly, the particle emissions and microphysics research needs to be advanced in parallel with contrail modeling to get better input data, and secondly, the sensitivity of contrails to possible uncertainties in particulate properties needs to be studied. This is one of the main goals of the current study.

1.1.2 Contrail modeling at global and regional scales

Estimates of RF resulting from contrails and aviation-induced cirrus involve uncertainties to such extents that improvements are necessary to reduce them (e.g. Lee *et al.*, 2000). A detailed review of the status of knowledge about contrail formation, their properties and climatic effects is given by Schumann (2005). The incorporation of the available knowledge about contrails into global calculations is restricted to some extent by the difficulties in reliably capturing the contrail physics using simple lower-order models. In a global climate model (GCM), contrails are typically represented using simplified models because the contrail-scale processes are sub-grid and can not be resolved. The contrail occurrence frequency and coverage is computed using criteria due to Appleman (1953) and Schumann (1996). For instance, the Federal Aviation Administration's System for assessing Aviation's Global Emissions (SAGE) provides the emission index of water and engine efficiency for a particular engine type along radar-detected aircraft trajectories (Klima & Waitz, 2006). The criteria are then used to predict the formation as well as persistence of contrails in a given region (Schrader, 1997). The criteria are applied in a GCM using available atmospheric data and all aircraft trajectories in a grid cell are modeled as linear contrails.

Ponater *et al.* (2002) first provided a parameterization scheme for contrails in GCM. The advantage of parameterization is that the contrail RF is then sensitive to the local atmospheric conditions. Although improved models exist which use tailored versions of the criteria for specific aircraft (Schrader, 1997) and couple the contrail parameterization scheme with the cloud parameterization scheme (Ponater *et al.*, 2002), recent studies indicate that the uncertainties in contrail RF from various models can differ by an order of magnitude

(Marquart & Mayer, 2002). This can be partially attributed to uncertainties in atmospheric data and insufficient resolution of available data in a given region. Other factors are the inability of the contrail parameterizations to include effects of spreading (Minnis *et al.*, 2004) and the difficulties in incorporating the effect of many physical parameters such as the engine type and ice nuclei size in complete detail. Due to the large grid sizes of GCM calculations, many physical details are empirically modeled or simply assumed. For example, non-spherical geometry of ice particles is accounted for by an empirical asymmetry parameter, and overlap between cloud layers is sometimes assumed to be maximum or random (Marquart & Mayer, 2002).

Studying contrails at higher resolutions than those allowed by GCM has the potential of taking into account many of these factors thereby improving the accuracy of predictions. Such simulations provide much more detailed physical effects, e.g. plume dynamics, buoyancy effects, turbulence and fluid dynamical instabilities. The insights and numerical databases generated by the simulations would be useful in developing improved models for use in GCM. The reminder of this introduction provides an overview of contrail simulations at various scales and levels of accuracy, and identifies questions where high-fidelity simulations can be a valuable tool for finding answers.

1.2 Contrails: Theoretical background

The formation and evolution of contrails consist of many different stages. The jet exhaust products that are released into the atmosphere are subject to the very low temperatures ($\sim$ 220 K) typical of the cruise altitudes ($\sim$ 10.5 km). The initial processes governing the aerosol particle size and number density in the jet exhaust are complex and we have to rely on experimental data to obtain the ice nuclei properties. Typically not all of the aerosol particles act as effective ice nuclei (IN). The IN consist of sulfate and hydrocarbon particles formed by nucleation process in the very early plume (IPCC-99). The atmospheric and jet exhaust moisture condenses on the nuclei and subsequently freezes. The famous Appleman criterion (Appleman, 1953; Schumann, 1996; Schrader, 1997) states that for contrails to form, the warm, unsaturated jet exhaust gas, when it mixes with the ambient air, should reach saturation with respect to liquid water.

The initially formed ice particles are then subject to the motions imposed by the aircraft

trailing vortices. The ice along with the exhaust gases gets entrained into the trailing vortices, and is transported by the three-dimensional fluid dynamics of the vortex wake which include wake descent, buoyant motions, turbulence, and long-wave instabilities finally leading to dispersion of the wake. Depending on the fluid dynamics and atmospheric conditions, the ice grows or decays.

1.2.1 Contrails as a multiscale problem

The ice nuclei – volatile (liquid) and nonvolatile (soot and metallic particles) – typically have a lognormal size distribution with mean radius in the range of $10 - 20\ nm$ (Kärcher *et al.*, 1998; Penner *et al.*, 1999). The shape of IN is not spherical because it is an agglomerate of smaller particles. But this core size is much smaller compared to the ice particle sizes encountered in the first 20 seconds of contrail life ($0.1\ \mu m - 1.5\ \mu m$) (Kärcher *et al.*, 1998; Lewellen & Lewellen, 2001; Shirgaonkar & Lele, 2006*a*), and hence the modeled shape is not expected to affect the contrail results significantly, and here the IN are modeled as spherical particles. These particles are subject to turbulent motions, the most energetic scales of which are proportional to the exhaust jet diameter, which is roughly 15 m after the spreading of the jet from the exit plane to 5 wing spans downstream of the aircraft where we start our simulations. Next in the scale hierarchy is the vortical motion of the aircraft wake which scales with the wing span ($\sim 50\ m$). The atmospheric density and temperature vary on the scale of a few kilometers, and in this study, only the effect of the small locally linear variation in density and temperature is taken into account on the scale of the wingspan. The three-dimensional vortex instabilities in the case of contrail evolution for 2 minutes and longer have wavelengths around 10 wingspans or less. The multiscale nature of the problem is illustrated in Figure 1.4.

1.2.2 Modeling contrails for different time-scale regimes

Traditionally, three different regimes exist in the evolution of a contrail. The jet regime spans approximately the first 1 second (or a few wing spans downstream of the aircraft) where chemical changes in exhaust gases and particulates and microphysical processes such as coagulation are abundant. This stage is relatively expensive to tackle with high-resolution fluid dynamical simulations because of the very small scales involved. Fluid dynamical models are mature enough to accurately predict the vorticity dynamics and plume behavior

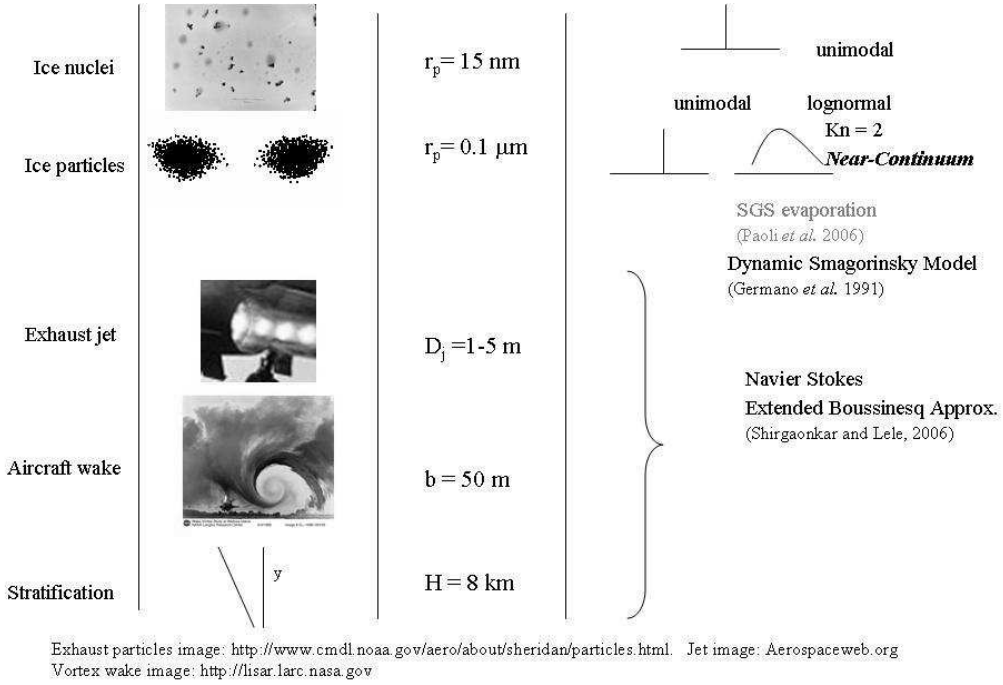

Figure 1.4: Scales involved in the contrail problem. The rightmost column indicates models used. The sub-grid evaporation model is not used in this study but is listed as a future modeling possibility.

in this regime, but the microphysics needs lower-order models as described in the previous section.

The next, vortex regime, extends up to roughly $2-4$ minutes. It is defined by the strong interaction between the rolled-up trailing vortices and the jet plume. The jet exhaust species get entrained into the vortex wake, and large changes in ice properties are known to take place in this regime. Stratification effects are found to be important at these times (Lewellen & Lewellen, 2001). The early portion of the vortex regime (up to 20 seconds) is especially important from a scientific understanding point of view because in this duration the long-wave instabilities of the trailing vortices are still in the incipient stage (Rennich, 1997) and radiation effects are not yet important (Jensen *et al.*, 1998). This is the regime of interest in this study.

In the dispersion regime (2-20 minutes), the contrail is dominated by atmospheric perturbations (turbulence and wind shear) when they can spread and change drastically in shape and area. All the above durations marking the different regimes are only estimates,

and can vary significantly depending on the specific aircraft considered, operating conditions, and atmospheric conditions. The photograph in Figure 1.1 illustrates these regimes. Many airplanes have passed through the region in the image at various times prior to taking the picture. Three contrails are prominently visible: the lowermost one is a young contrail in the jet or the early vortex regime where it retains its linear shape. The middle contrail is in the late vortex regime where effect of descent is seen through its increased vertical extent, and the vortex breakdown following long-wave instabilities is evident from its puffy structure. The uppermost contrail has spread considerably due to atmospheric motions.

1.3 Contrail simulations: Previous work

Perhaps the most important factor that generates the need for improved accuracy of contrail models is the scale disparity between the smallest resolved scales in a GCM and the contrails scales. The former can be as low as a 700 meters in vertical direction and as high as a few hundred kilometers in the horizontal (Ponater *et al.*, 2002). The contrail plume processes take place on scales of the order of meters (Paoli *et al.*, 2004; Lewellen & Lewellen, 2001; Shirgaonkar & Lele, 2006*a*). Therefore box models are used to treat plume mixing, early particle size changes, and chemistry (e.g. Kraabøl *et al.*, 2000). Since such models do not account for the detailed microphysics and heterogeneous chemistry, coupled trajectory box models are required which treat both plume and background atmospheric conditions in separate but coupled boxes (Meilinger *et al.*, 2005). But box models do not take into account the fluid dynamical details which we show in this study to be important for ice growth characteristics. For example, the mixing of the plume with the ambient air is modeled in a simplistic way according to

$$\frac{d\chi}{dt} = -\omega(\chi - \chi_{amb}) \tag{1.1}$$

where χ is the gas phase mixing ratio of species in the plume and $\omega = \alpha/t$ is the average entrainment rate, taken as a constant (Meilinger *et al.*, 2005). This clearly misses some important physics of turbulent mixing.

Two- or three- dimensional simulations of contrails can provide a much more detailed prediction of contrail properties because the simulations involve fewer modeling assumptions and more physical effects are directly simulated. For instance, the entrainment, detrainment, and mixing of the jet plume into the ambient air have been studied using parabolized

Navier-Stokes simulations (Quackenbush *et al.*, 1996). This study investigates the dilution of the plume passive scalar and temperature, and qualitative dependence of plume dispersion on buoyancy of the jet. Such details are thought to be important inputs for regional/global contrail calculations, and need to be studied in more depth. The current study attempts to do a parametric study of two dimensional plumes in aircraft wakes to find out the fundamental mechanism behind plume entrainment.

Lower-order models that track the evolution of thermodynamic properties (supersaturation, temperature) in air parcels following a set of given trajectories can have detailed chemistry and microphysics (e.g. Kärcher, 1994; Brown *et al.*, 1996) and are computationally inexpensive. However, they involve many simplifying assumptions regarding the three-dimensional flow phenomena occurring in an actual contrail. For example, the effect of turbulent transport is incorporated by using an exchange coefficient, ϵ, which is only a function of the downstream distance (Kärcher, 1994), and the loss of ice crystals due to sublimation is sometimes tackled using a tunable parameter (Sussman & Gierens, 2001). It is not known which of the early-stage physical effects would impact the global effect of contrails to a degree that they must be modeled directly into contrail calculations, as opposed to indirectly modeling them in a tailored way for a particular set of conditions. High-resolution three-dimensional simulations would help us get closer to knowing this, although it will take sustained research programs to generate sufficient knowledge base for a variety of atmospheric and aircraft conditions.

Because of the different characteristics of various regimes of contrail life, the numerical simulations are carried out at different levels of modeling. Several studies have been devoted to the exhaust species and particulate evolution including observations (Schumann *et al.*, 1995), and simulations (DÜrbeck & Gerz, 1995) but there are relatively few high-resolution contrails simulation studies. Two-dimensional studies of contrails including both the jet and vortex regimes have been done by Sussman & Gierens (1999) where their interest was to investigate the role of the secondary wake on contrail growth. Two-dimensional large eddy simulations of Gierens (1996) study contrails of age 100 s and later, and do not treat the initial duration of the vortex stage which is important for contrail predictions. More advanced three-dimensional simulations by Chlond (1998) investigate contrails in the late dispersion phase ($>$ 1000 s). Obtaining initial conditions for such longer time simulations is a necessary task and LES has recently emerged as a potential promising approach for it. The detailed simulations of Lewellen & Lewellen (2001) consist of a limited parametric study

of contrails at a few sets of atmospheric and aircraft conditions. The range of parameters covered is still not sufficient to infer which physical parameters are important to the long-term contrail growth. Ambient relative humidity, as expected, emerges as one of the most crucial parameters affecting contrail growth (Lewellen & Lewellen, 2001) as we later confirm in this study. More physical processes should be investigated in such simulations.

The very early jet and vortex stages have been simulated using LES by Paoli *et al.* (2004) to study the flow physics and thermodynamics in the first 3 s of contrail evolution. It is highly desirable to extend the time duration of contrail LES to include the jet, vortex, and dispersion regimes. Furthermore, a parametric study at different aircraft and ambient conditions is necessary to obtain useful information about contrail sensitivity to various parameters. The main objective of the current study is to provide such a parametric study for the jet and vortex regimes.

1.4 Overview and accomplishments

The principal objective of this study is to develop and demonstrate capability to perform high-fidelity LES of early stage contrails of a typical subsonic transport aircraft, and to apply it to study the physics of early contrail growth and its sensitivity to atmospheric and aircraft conditions. This study attempts to address many related theoretical and numerical questions during the course. The main contributions are summarized below.

The extended Boussinesq approximation

An improved version of the Boussinesq approximation was derived using perturbation analysis of the Navier-Stokes equations in the regime where inertial effects are significant. The primary advancements achieved are:

- A unified theory for flows of compressible and incompressible fluids at low Mach numbers was provided to elucidate the physical effects of inertia, stratification, buoyancy and small external entropy perturbations.
- A nondimensional number was derived which allows us to distinguish between compressible and incompressible hydrostatic states.
- A correction was provided to the traditional Boussinesq approximation that improves its accuracy for inertia-dominated flows by accounting for the interaction between flow

inertia and buoyancy. A simple numerical treatment was proposed to obtain efficient numerical solution to the extended approximation for flows developing slowly in time.

Microphysics model

A microphysics model was developed for contrail LES which uses the mixed Eulerian-Lagrangian approach. It was built on the basic model of Paoli *et al.* (2002) with improvements to attain more realistic microphysical behavior. The model was validated against other models using very different methodologies (Eulerian binned microphysics (Jensen *et al.*, 1994), and trajectory tracking model (Brown *et al.*, 1996)) and good level of agreement was found.

Large eddy simulations of early contrails

Our goal was to develop and use computational tools with high performance computing to study contrails. The main contributions were:

- An LES code with mixed Eulerian-Lagrangian computational approach for ice microphysics was developed. The code was validated for various test cases and for the accuracy of the Lagrangian approach. Specifically, sensitivity to some key numerical parameters was examined to ensure sufficient accuracy of ice particle statistics.
- We investigated the influence of buoyant exhaust jets in aircraft wakes in an idealized two-dimensional setting. A mechanism was identified by which the baroclinic vorticity generated by the jets changes the wake descent and vortex separation.
- An array of contrail LES simulations were conducted to study the sensitivity of early contrails to atmospheric temperature and relative humidity, initial ice particle size and number density. Three different regimes of early contrail growth – the early jet-controlled regime showing rapid ice growth, an intermediate regime where jet turbulence effects are felt, and the subsequent regime mainly controlled by atmospheric relative humidity – were found.
- The role of fluid turbulence in comparison with that of ice particle statistical fluctuations was studied. It was found that the latter has a much larger influence on the overall ice properties than the former.

The remaining chapters are organized as follows. Chapter 2 derives the Extended Boussinesq approximation. Chapter 3 formulates the contrail problem and describes the modeling

and numerical method. In Chapter 4 we present some aspects of verification and validation of the model and the numerical method. Chapter 5 studies the behavior of laminar wakes with buoyant exhaust jets. Chapter 6 presents the sensitivity study for early contrails. Chapter 7 presents some numerical considerations for the Eulerian-Lagrangian numerical approach. Chapter 8 concludes the study and remarks on future work.

Chapter 2

The Extended Boussinesq Approximation*

Aircraft contrails present a multiphase fluid dynamical problem involving stratification and buoyancy induced by the jets. For this type of problems the Boussinesq approximation is often used. In this chapter we discuss the applicability of Boussinesq approximation and find that the traditional Boussinesq approximation is not sufficient to capture the complete physics. We extend the approximation for a class of problems of which the contrail problem is a special case. The equations solved are the Navier-Stokes equations with the thermal energy equation, all cast in the primitive variables (velocities, temperature and pressure).

Depending on the Mach number, different asymptotic regimes exist in a fluid flow where different physical balances are prevalent (Lele, 1998). In many low Mach number flows of interest, acoustic waves are not important if the initial conditions are "balanced" and one is to study the dynamical behavior of the flow on slow non-acoustic time scales. It is desirable to filter the acoustic waves from the equations so that the resultant approximation allows for larger time steps during numerical integration. Extensive research can be found that formulates the flow equations in a way that avoids the acoustic time step restriction in numerical solution procedures for various regimes such as non-Boussinesq and Boussinesq flows, shallow and deep convection (see Thunis & Bornstein, 1996 and references therein).

The Boussinesq approximation (also known as the Boussinesq-Oberbeck approximation)

*This chapter is reproduced under copyright agreement from the article "On the extension of the Boussinesq approximation for inertia dominated flows," A. A. Shirgaonkar and S. K. Lele, Physics of Fluids, 18, pp. 066601, June 2006. Copyrighted by the American Institute of Physics, 2006.

is a special case of the low Mach number equations for small density and temperature variations with gravity included. Traditionally, the Boussinesq approximation has two main components (Spiegel & Veronis, 1960): (1) density fluctuations resulting from motion result principally from thermal (as opposed to pressure) effects, and (2) perturbation density is important only in the gravity term. In this paper we show that (2) can be extended to include the perturbation density effect in the inertial terms if the Froude number is large.

Under the Boussinesq approximation the energy equation is coupled with the momentum equation only through the buoyancy term (if fluid properties are assumed constant, which is a reasonable assumption for small temperature variations). Extensions to the Boussinesq approximation have been proposed to account for adiabatic heating and viscous dissipation (Steinbach *et al.*, 1989; Christensen & Yuen, 1985), and to improve scalar transport prediction (McDougall *et al.*, 2002). The effect of flow inertia has, however, been traditionally neglected, with a few exceptions such as Aigner & Grimshaw (2001); Shimomura (1999); Soong & Chyuan (1998); Lewellen & Lewellen (1996). Shimomura (1999) and Lewellen and Lewellen (1996) included the product of temperature fluctuations and pressure gradient to include the effects of inertia on buoyancy. The pressure solution in this case is more complicated due to the additional term. Aigner and Grimshaw (2001) have proposed the extension to study predominantly horizontal flows over topography. The rotational buoyancy has been included by Soong and Chyuan (1998) in studying flow over a rotating disk to make the equations analytically tractable. The inertia-buoyancy coupling can be important in many geophysical flows where the base state is a time-evolving flow over which buoyant fluctuations evolve. It is common in analyzing such problems to reduce the complexity of the base state and emphasize the behavior of perturbations (Dutton & Fichtl, 1969; Gough, 1969). This is justified in studies of wave phenomena in the atmosphere in which the principal dynamics are buoyancy induced, and the base flow is either absent or simple. If the base flow is strong then buoyancy forces can be small, large, or comparable to inertial forces, depending on the Froude number.

It is desirable to systematically derive an extension to the traditional Boussinesq equations that accounts for effects of variable inertia. This is one of the main goals of this paper. Another aim of this work is to clarify the role of "flow compressibility" and "fluid compressibility" in the equations governing stratified flows. The former has been treated extensively in the literature using low Mach number asymptotics (Müller, 1999). The latter,

often not treated explicitly, is independent of motion and depends on a particular hydrostatic state. Effect of compressibility on linear gravity wave propagation and in particular, their phase speed, have been discussed by Eckart (1960) and Yih (1980). Expressions for buoyancy frequency have been also given by Gill (1982) for atmosphere and ocean. But it is observed that the term "Boussinesq approximation" is commonly used in the context of incompressible fluids. "Atmospheric" stratification may be incompressible (e.g. ocean density variation due to temperature or salinity) or compressible (atmospheric flows), even though the fluctuations can be treated in an incompressible manner owing to the low Mach numbers. Many authors discuss the deep and shallow flow equations (e.g. Dutton & Fichtl, 1969; Ogura & Phillips, 1962; Spiegel & Veronis, 1960), but the difference between compressible and incompressible fluids in the context of shallow flows and Boussinesq approximation has not been directly addressed. To our knowledge, a nondimensional parameter which makes this distinction and guides the simplification of the equations is not available. We propose a nondimensional number to help the choice of equations between the incompressible kind (e.g. Chandrasekhar, 1981) and the compressible kind (e.g. Emanuel, 1994; Pedlosky, 1998). It is observed that the incompressible-atmosphere approximation is applied to some atmospheric flows in which the hydrostatic state is compressibly balanced (Spalart, 1996; Hill, 1975; Robins & Delisi, 1990). We show (Section 2.3) that this leads to an inconsistent representation of buoyancy forces and results in an inaccurate buoyancy frequency.

In Section 2.1 we present an asymptotic analysis of the governing equations to formally deduce a set of equations which include the base flow inertial effects on fluctuations. In Section 2.2 we derive the extended Boussinesq approximation for low Mach number, shallow flows. Section 2.3 deduces a criterion to characterize the compressibility of the fluid with respect to stratification effects. Section 2.4 presents the implication of the extended equations in terms of vorticity dynamics. For flows in which unsteadiness of the base state is small, we propose a simple numerical procedure in Section 2.5 to obtain accurate solutions without an iterative procedure. In Section 2.6 we present the example of a Taylor vortex with an initially imposed density perturbation, and of a two dimensional Taylor vortex array with an initial density perturbation. Section 2.7 gives summary and conclusions.

2.1 Asymptotic analysis

In this section we start with the governing equations for compressible, stratified flows for a general Newtonian fluid, and expand them in fluctuations and restrict them to low Mach numbers. Small temperature fluctuations are allowed in the initial conditions. In the subsequent sections, various nondimensional parameters will allow us to specialize the equations for inertia-dominated or buoyancy-dominated flows, and for low or high compressibility environments such as oceans or atmosphere.

Choosing a coordinate system where the y-axis points opposite to gravity, we split any general variable as (superscript '*' denotes dimensional variable)

$$\phi^*(x,y,z,t) = \phi^*_{ref} + \phi^*_h(y) + \phi^*_{nh}(x,y,z,t) \tag{2.1}$$

where ϕ^*_{ref} is a constant reference value, ϕ^*_h is the hydrostatic variation due to stratification, and ϕ^*_{nh} is the nonhydrostatic, i.e. space-time dependent fluctuating part resulting from motion. We choose a frame of reference such that $\mathbf{u}^*_{ref} = \mathbf{0}$, hence $\mathbf{u}^* = \mathbf{u}^*_{nh}$. The compressible flow equations with Stokes' constitutive relation and the assumption of constant viscosity, thermal conductivity, and heat capacity for small temperature fluctuations are

$$\frac{D^*\rho^*}{Dt^*} + \rho^*\nabla^*\cdot\mathbf{u}^* = 0 \tag{2.2}$$

$$\rho^*\frac{D^*\mathbf{u}^*}{Dt^*} = -\nabla^* p^*_{nh} - \rho^*_{nh} g^* \hat{\mathbf{e}}_\mathbf{y} + \mu^*\nabla^{*2}\mathbf{u}^* + \frac{\mu^*}{3}\nabla^*(\nabla^*\cdot\mathbf{u}^*) \tag{2.3}$$

$$\rho^* C^*_p \frac{D^*T^*}{Dt^*} = k^*_p T^* \frac{D^*p^*}{Dt^*} + k^*\nabla^{*2}T^* + \Phi^* \tag{2.4}$$

where μ^* and k^* are the dynamic viscosity and thermal conductivity, and C^*_p and C^*_v are the specific heat capacities, evaluated at the reference state. $\Phi^* = \tau^*_{ij}S^*_{ij}$ is the viscous dissipation, $\tau^*_{ij} = 2\mu^*(S^*_{ij} - \frac{1}{3}\delta_{ij}S^*_{kk})$ is the viscous stress tensor, $S^*_{ij} = \frac{1}{2}(\frac{\partial u^*_i}{\partial x^*_j} + \frac{\partial u^*_j}{\partial x^*_i})$ is the strain rate tensor, and $\frac{D^*}{Dt^*} \equiv \frac{\partial}{\partial t^*} + \mathbf{u}^*\cdot\nabla^*$. The hydrostatic part has been subtracted from the momentum equation. Coriolis forces have been neglected. The form of the energy equation containing C^*_p instead of C^*_v on the left hand side is chosen (see discussion about the energy equation paradox in Panton (1996), although both forms yield mathematically equivalent sets of equations. $\hat{\mathbf{e}}_\mathbf{y}$ is the unit vector in the direction opposite to gravity. The isobaric compressibility $k^*_p = -(1/\rho^*_{ref})(\partial\rho^*/\partial T^*)_{p^*_{ref}}$ is evaluated at the reference state.

Similarly we define the isothermal compressibility, $k_T^* = (1/\rho_{ref}^*)(\partial\rho^*/\partial p^*)_{T_{ref}^*}$. The energy equation (2.4) with the in-situ temperature as the dependent variable is given in Panton (e.g. Panton, 1996, p. 32, Eq. 5.11.1). The equation governing entropy is

$$\rho^* T^* \frac{D^* s^*}{Dt^*} = k^* \nabla^{*2} T^* + \Phi^* \tag{2.5}$$

Two different but equivalent forms of the equation of state will be used:

$$\rho^* = \rho^*(p^*, T^*) \tag{2.6}$$

$$\rho^* = \rho^*(p^*, s^*) \tag{2.7}$$

We non-dimensionalize the equations by density ρ_{ref}^*, pressure p_{ref}^*, velocity U^*, characteristic length L^*, the convective time $\tau^* = L^*/U^*$, and temperature T_{ref}^*. Let the Eulerian time scale be τ_E^*. In the case of wave motions, τ_E^* can be taken as $\frac{1}{\omega^*}$ where ω^* is the characteristic frequency of waves. Entropy change is nondimensionalized by C_p^*.

The analysis will use the following non-dimensional parameters: Reynolds number $Re = \rho_{ref}^* U^* L^*/\mu^*$, Prandtl number $Pr = \nu^*/\alpha^*$ where $\alpha^* = k^*/\rho_{ref}^* C_p^*$ is the thermal diffusivity (assumed constant), Mach number $M = U^*/c_{ref}^*$ where c_{ref}^* is the speed of sound at the reference state, and the Froude number $Fr = U^{*2}/g^* L^*$. Denoting nondimensional variables by symbols without the superscript '*', the variable splitting (Eq. (3.2)) is

$$\phi(x, y, z, t) = \phi_{ref} + \phi_h(y) + \phi_{nh}(x, y, z, t) \tag{2.8}$$

where ϕ can be $\mathbf{u}$, ρ, p, T, or s. Note that $\rho_{ref} = 1$, $p_{ref} = 1$, $T_{ref} = 1$, $\mathbf{u}_{ref} = \mathbf{0}$, and $\mathbf{u}_h = \mathbf{0}$. The governing equations become

$$\frac{D\rho}{Dt} + \rho \nabla \cdot \mathbf{u} = 0 \tag{2.9}$$

$$\rho \frac{D\mathbf{u}}{Dt} = -\frac{\theta_1}{M^2} \nabla p_{nh} - \frac{1}{Fr} \rho_{nh} \hat{\mathbf{e}}_\mathbf{y} + \frac{1}{Re} \left[\nabla^2 \mathbf{u} + \frac{1}{3} \nabla (\nabla \cdot \mathbf{u}) \right] \tag{2.10}$$

where $\theta_1 = \frac{p_{ref}^*}{\rho_{ref}^* c_{ref}^{*2}}$.

$$\rho \frac{DT}{Dt} = \theta_2 T \frac{Dp}{Dt} + \frac{1}{RePr} \nabla^2 T + \frac{M^2 \theta_2}{Re \theta_1 \lambda_p} \Phi \tag{2.11}$$

where $\theta_2 = \frac{p^*_{ref} k^*_p}{\rho^*_{ref} C^*_p}$ and $\lambda_p = T^*_{ref} k^*_p$ is the nondimensional isobaric compressibility. The equation of state becomes

$$\rho = \rho(p, T) \tag{2.12}$$

$$\rho = \rho(p, s) \tag{2.13}$$

To analyze the above equations we use the following nondimensional parameters: The depth parameter $\delta = L^*/H^*$ where $H^* = \frac{p^*_{ref}}{-dp^*_h/dy^*}$ is the *local* scale height for pressure, Strouhal number $St = \tau^*/\tau^*_E$, the hydrostatic entropy variation parameter, $\epsilon = \frac{L^*}{C^*_p}\frac{ds^*_h}{dy^*}$, and the buoyancy parameter $\beta = \Delta\rho^*/\rho^*_{ref}$ where $\Delta\rho^*$ is the scale of the imposed density fluctuation. This work considers shallow flows ($\delta \ll 1$) with low Mach numbers ($M^2 \ll 1$). We assume $Re \gg 1$ and low temperature fluctuations ($\beta \ll 1$). The analysis below assumes $St = 1$, but it is applicable for $St \leq 1$, allowing both convectively dominated flows and buoyancy-dominated flows such as internal gravity waves.

We expand all nonhydrostatic variables in powers of M^2, ϵ, and β,

$$\begin{aligned}
p_{nh} &= M^2 p_{00} + \epsilon p_{01} + \beta p_s + ... \\
\rho_{nh} &= M^2 \rho_{10} + \epsilon \rho_{01} + \beta \rho_s + ... \\
T_{nh} &= M^2 T_{10} + \epsilon T_{01} + \beta T_s + ... \\
\mathbf{u}_{nh} &= \mathbf{u}_{00} + M^2 \mathbf{u}_{10} + \epsilon \mathbf{u}_{01} + \beta \mathbf{u}_s + ...
\end{aligned} \tag{2.14}$$

Note that $M^2 p_{00}$ is the "incompressible" pressure, and

$$M^2 p_{00} \sim \mathcal{O}(\rho^*_{ref} U^{*2}/p^*_{ref}) \sim \mathcal{O}(M^2/\theta_1) \tag{2.15}$$

The nondimensional parameters used in the analysis are summarized in Table 2.1. The choice of M^2, ϵ, and β is motivated by perturbations due to compressibility, stratification, and initial conditions respectively. The small parameter ϵ appears naturally in the equations when they are expanded about the hydrostatic state. Such an expansion is developed later in this section. Here we anticipate the definition of ϵ which emerges in Eq. (2.37) through the transport of the hydrostatic pressure and temperature gradients by perturbation velocity. Strict expansion would require the inclusion of higher order terms in δ, and cross terms

Table 2.1: Nondimensional parameters

Parameter	**Definition**
Reynolds number, Re	$\rho^*_{ref}U^*L^*/\mu^*$
Prandtl number, Pr	ν^*/α^*
Mach number, M	U^*/c^*_{ref}
Froude number, Fr	U^{*2}/g^*L^*
Strouhal number, St	τ^*/τ^*_E
θ_1	$p^*_{ref}/\rho^*_{ref}c^{*2}_{ref}$
θ_2	$p^*_{ref}k^*_p/\rho^*_{ref}C^*_p$
Isobaric compressibility, λ_p	$-(T^*_{ref}/\rho^*_{ref})(\partial\rho^*/\partial T^*)_{p^*_{ref}}$
Isothermal compressibility, λ_T	$(p^*_{ref}/\rho^*_{ref})(\partial\rho^*/\partial p^*)_{T^*_{ref}}$
Depth parameter, δ	L^*/H^*
Hydrostatic entropy variation parameter, ϵ	$(L^*/C^*_p)(ds^*_h/dy^*)$
Buoyancy parameter, β	$\Delta\rho^*/\rho^*_{ref}$
η_1	$max\{M^2,\epsilon,\beta\}$
η_2	$max\{M^4,\epsilon^2,\beta^2,M^2\epsilon,M^2\beta,\epsilon\beta\}$

involving δ and (M^2,ϵ,β). Here we restrict ourselves to sufficiently small δ. Defining

$$\begin{aligned}
\tilde{p} &= M^2 p_{00} + \epsilon p_{01} + \beta p_s \\
\tilde{\rho} &= M^2 \rho_{10} + \epsilon \rho_{01} + \beta \rho_s \\
\tilde{T} &= M^2 T_{10} + \epsilon T_{01} + \beta T_s \\
\tilde{\mathbf{u}} &= \mathbf{u}_{00} + M^2 \mathbf{u}_{10} + \epsilon \mathbf{u}_{01} + \beta \mathbf{u}_s
\end{aligned} \tag{2.16}$$

we note that for all variables, $\phi_{nh} = \tilde{\phi} + \mathcal{O}(\eta_2)$, where $\eta_2 = max\{M^4,\epsilon^2,\beta^2,M^2\epsilon,M^2\beta,\epsilon\beta\}$, the subscript '2' signifying the second (quadratic or bilinear) order. Similarly we define $\eta_1 = max\{M^2,\epsilon,\beta\}$. The subscripts '00', '10', '01', and 's' denote, respectively, the incompressible motion, compressibility due to motion, perturbations resulting from the hydrostatic entropy gradient (stratification), and the variations due to an initially imposed entropy perturbation. Since entropy modes are isobaric (Chu & Kovásznay, 1958), $p_s = 0$. Fluid particles are assumed to adjust to the local pressure instantly, so $p_{01} = 0$. The latter assumption is consistent with the goal of filtering the acoustic modes, i.e., adjustments to pressure changes take place rapidly compared to the convective flow time scales. Thus,

$$\tilde{p} = M^2 p_{00} \tag{2.17}$$

The above expansion is a multiple parameter expansion where the relative magnitude of ϵ and β is not known until a specific flow is considered. For low Mach numbers the resultant solution is interpreted as follows. In flow regions where the imposed temperature perturbations are larger than those due to stratification ($\beta \gg \epsilon$), the $\mathcal{O}(\epsilon)$ solution is a correction small compared to the retained terms. In the regions with small external temperature fluctuations, i.e., where the dominant temperature change is due to stratification ($\beta \ll \epsilon$), the $\mathcal{O}(\beta)$ solution is again a small correction. A hierarchy of equations can be derived by retaining the $\mathcal{O}(M^2)$, $\mathcal{O}(\epsilon)$, and $\mathcal{O}(\beta)$ components of the governing equations separately. The equation of state (2.12) gives

$$\frac{D\rho}{Dt} = \lambda_T \frac{Dp}{Dt} - \lambda_p \frac{DT}{Dt} \tag{2.18}$$

where $\lambda_T = p^*_{ref} k^*_T$ and $\lambda_p = T^*_{ref} k^*_p$ are the nondimensional compressibility coefficients. Using Eq. (2.18) and Eq. (2.9) in Eq. (2.11) we get

$$\frac{\rho^2}{\lambda_p} \nabla \cdot \mathbf{u} = \left(\theta_2 T - \rho \frac{\lambda_T}{\lambda_p} \right) \frac{Dp}{Dt} + \frac{1}{RePr} \nabla^2 T + \frac{M^2 \theta_2}{Re \theta_1 \lambda_p} \Phi \tag{2.19}$$

which gives

$$\begin{aligned} \nabla \cdot \mathbf{u} &= \left(\frac{\theta_2 T \lambda_p}{\rho^2} - \frac{\lambda_T}{\rho} \right) \left(v \frac{dp_h}{dy} + M^2 \frac{Dp_{00}}{Dt} \right) \\ &\quad + \frac{\lambda_p}{\rho^2} \frac{1}{RePr} \nabla^2 \left(T_h + M^2 T_{10} + \epsilon T_{01} + \beta T_s \right) \\ &\quad + \frac{M^2 \theta_2}{Re \theta_1} \frac{\Phi}{\rho^2} + \mathcal{O}(\eta_2) \end{aligned} \tag{2.20}$$

The hydrostatic variation can be considered to be locally linear (since $\delta \ll 1$), making $\frac{d^2 T_h}{dy^2}$ of the order δ^2. Using binomial expansion for $1/\rho$ and recalling that $\frac{dp_h}{dy} \sim \mathcal{O}(\delta)$, we get

$$\begin{aligned} \nabla \cdot \mathbf{u} &= \mathcal{O}\left(max\left\{ \frac{\theta_2}{\theta_1} \lambda_p M^2, \frac{\lambda_T}{\theta_1} M^2, \theta_2 \lambda_p \delta, \lambda_T \delta \right\} \right) \\ &\quad + \mathcal{O}(\lambda_p / RePr) \mathcal{O}(\eta_1) + \mathcal{O}\left(\frac{M^2 \theta_2}{Re \theta_1} \right) + \mathcal{O}(\eta_2) \end{aligned} \tag{2.21}$$

where we have used Eq. (2.15). For typical fluids such as air and water the constants λ_T, λ_p, θ_2, θ_2/θ_1, and λ_T/θ_1 are at the most $\mathcal{O}(1)$. Hence for high Re, the last two terms are

negligible. Up to $\mathcal{O}(\eta_2)$, we can write

$$\nabla \cdot \mathbf{u} \quad \sim \quad \mathcal{O}(max\{M^2, \delta\}) \tag{2.22}$$

or equivalently,

$$\nabla \cdot \tilde{\mathbf{u}} \quad \sim \quad \mathcal{O}(max\{M^2, \delta\}) \tag{2.23}$$

Using Eq. (2.23) into Eq. (2.10) yields

$$\begin{aligned}
& (1 + \rho_h + M^2\rho_{10} + \epsilon\rho_{01} + \beta\rho_s + \mathcal{O}(\eta_2)) \\
& \left[\frac{\partial}{\partial t}(\mathbf{u}_{00} + M^2\mathbf{u}_{10} + \epsilon\mathbf{u}_{01} + \beta\mathbf{u}_s + \mathcal{O}(\eta_2))\right. \\
& +(\mathbf{u}_{00} + M^2\mathbf{u}_{10} + \epsilon\mathbf{u}_{01} + \beta\mathbf{u}_s + \mathcal{O}(\eta_2)) \\
& \left.\cdot\nabla(\mathbf{u}_{00} + M^2\mathbf{u}_{10} + \epsilon\mathbf{u}_{01} + \beta\mathbf{u}_s + \mathcal{O}(\eta_2))\right] \\
= \quad & -\frac{\theta_1}{M^2}\nabla(M^2 p_{00} + \mathcal{O}(\eta_2)) \\
& -\frac{1}{Fr}(M^2\rho_{10} + \epsilon\rho_{01} + \beta\rho_s + \mathcal{O}(\eta_2))\hat{\mathbf{e}}_\mathbf{y} \\
& +\frac{1}{Re}\nabla^2(\mathbf{u}_{00} + M^2\mathbf{u}_{10} + \epsilon\mathbf{u}_{01} + \beta\mathbf{u}_s + \mathcal{O}(\eta_2)) \\
& +\mathcal{O}(max\{M^2/Re, \delta/Re\})
\end{aligned} \tag{2.24}$$

To leading order,

$$\frac{D_0\mathbf{u}_{00}}{Dt} = -\theta_1\nabla p_{00} + \frac{1}{Re}\nabla^2\mathbf{u}_{00} \tag{2.25}$$

where $\frac{D_0}{Dt} \equiv \frac{\partial}{\partial t} + \mathbf{u}_{00}\cdot\nabla$. Here we have assumed $Fr \gg M^2$. In flows where the leading order dynamics are buoyancy driven, this criterion may not be satisfied. This case is discussed in Section 2.2.1. At $\mathcal{O}(\eta_1)$,

$$\begin{aligned}
& \frac{\partial}{\partial t}(M^2\mathbf{u}_{10} + \epsilon\mathbf{u}_{01} + \beta\mathbf{u}_s) + \mathbf{u}_{00}\cdot\nabla(M^2\mathbf{u}_{10} + \epsilon\mathbf{u}_{01} + \beta\mathbf{u}_s) \\
& +(M^2\mathbf{u}_{10} + \epsilon\mathbf{u}_{01} + \beta\mathbf{u}_s)\cdot\nabla\mathbf{u}_{00} \\
& +(\rho_h + M^2\rho_{10} + \epsilon\rho_{01} + \beta\rho_s)\left[\frac{\partial\mathbf{u}_{00}}{\partial t} + \mathbf{u}_{00}\cdot\nabla\mathbf{u}_{00}\right] \\
= \quad & -\theta_1\nabla(M^2 p_{10}) - \frac{1}{Fr}(M^2\rho_{10} + \epsilon\rho_{01} + \beta\rho_s)\hat{\mathbf{e}}_\mathbf{y} \\
& +\frac{1}{Re}\nabla^2(M^2\mathbf{u}_{10} + \epsilon\mathbf{u}_{01} + \beta\mathbf{u}_s)
\end{aligned} \tag{2.26}$$

where we have assumed that δ is the same order as η_1. Adding Eq. (2.25) and Eq. (2.26) we get

$$\frac{\tilde{D}\tilde{\mathbf{u}}}{Dt} = -\frac{\theta_1}{M^2}\nabla\tilde{p} - \frac{1}{Fr}\tilde{\rho}\hat{\mathbf{e}}_{\mathbf{y}} - (\rho_h(y)+\tilde{\rho})\frac{\tilde{D}\tilde{\mathbf{u}}}{Dt} + \frac{1}{Re}\nabla^2\tilde{\mathbf{u}} + \mathcal{O}(\eta_2) \tag{2.27}$$

where $\frac{\tilde{D}}{Dt} = \frac{\partial}{\partial t} + \tilde{\mathbf{u}}\cdot\nabla$. Note that the $\mathcal{O}(\eta_2)$ error has contribution from the replacement of $\frac{D_0}{Dt}$ by $\frac{\tilde{D}}{Dt}$. This equation is in contrast with the Boussinesq approximation which is widely applied to flows driven by buoyancy and with a trivial base state, $\mathbf{u}_{00} = \mathbf{0}$. For strongly vortical base flows $\frac{D\tilde{\mathbf{u}}}{Dt}$ is $\mathcal{O}(1)$ and the term $(\rho_h(y)+\tilde{\rho})\frac{D\tilde{\mathbf{u}}}{Dt}$ in Eq. (2.27) should be retained; it is of the same order as the buoyancy force, depending on the Froude number. The buoyancy force depends on the parameter η_1/Fr. If Fr is small, the flow tends to natural convection and a different scaling of the variables can be employed to arrive at the traditional Boussinesq approximation (see Section 2.2.1). When $Fr \sim \mathcal{O}(1)$, often the traditional Boussinesq equations are applied. The above extended Boussinesq approximation is expected to be a better approximation. Eq. (2.27) is also

$$(1+\rho_h(y)+\tilde{\rho})\frac{\tilde{D}\tilde{\mathbf{u}}}{Dt} = -\frac{\theta_1}{M^2}\nabla\tilde{p} - \frac{1}{Fr}\tilde{\rho}\hat{\mathbf{e}}_{\mathbf{y}} + \frac{1}{Re}\nabla^2\tilde{\mathbf{u}} + \mathcal{O}(\eta_2) \tag{2.28}$$

which, after using the binomial expansion,

$$\frac{1}{(1+\rho_h(y)+\tilde{\rho})} \approx (1-\rho_h(y)-\tilde{\rho})$$

becomes

$$\begin{aligned}\frac{\tilde{D}\tilde{\mathbf{u}}}{Dt} &= -\frac{\theta_1}{M^2}(1-\rho_h(y)-\tilde{\rho})\nabla\tilde{p} - \frac{1}{Fr}(1-\rho_h(y)-\tilde{\rho})\tilde{\rho}\hat{\mathbf{e}}_{\mathbf{y}} \\ &+\frac{1}{Re}(1-\rho_h(y)-\tilde{\rho})\nabla^2\tilde{\mathbf{u}} + \mathcal{O}(\eta_2)\end{aligned} \tag{2.29}$$

Lewellen and Lewellen (2001; 1996) use an equivalent equation by including the product of the perturbation potential temperature and pressure gradient. It produces an elliptic diagnostic equation for pressure with variable coefficients and is difficult to solve numerically especially in conjunction with higher order schemes. In Section 2.5 we propose an alternative numerical formulation to remedy this.

2.1.1 Equation of state

The nondimensional form of the entropy equation (2.5) is

$$\rho T\frac{Ds}{Dt} = \frac{1}{RePr}\nabla^2 T + \frac{M^2}{Re}\frac{\theta_2}{\lambda_p\theta_1}\Phi \tag{2.30}$$

For shallow flows, $\nabla^2 T \approx \nabla^2 T_{nh}$. Hence

$$\frac{Ds}{Dt} = \mathcal{O}(max\{\eta_1/RePr, M^2/Re\}) \tag{2.31}$$

That is, to leading order the flow evolution is isentropic. We split all variations $\tilde{\phi}$ into a sum of an isentropic part, $\tilde{\phi}_{isentr}$, and an isobaric part, $\tilde{\phi}_{isob}$. Note that $\tilde{p}_{isentr} = M^2 p_{00} = \tilde{p}$, $\tilde{T}_{isentr} = M^2 T_{10}$, $\tilde{\rho}_{isentr} = M^2\rho_{10}$, $\tilde{T}_{isob} = \epsilon T_{01} + \beta T_s$, and $\tilde{\rho}_{isob} = \epsilon\rho_{01} + \beta\rho_s$. The density changes can be expressed using Taylor series expansion of the equation of state up to first order. In this way $\tilde{\rho}_{isentr}$ is obtained using Eq. (2.13),

$$\tilde{\rho}_{isentr} = \left(\frac{\partial\rho}{\partial p}\right)_s \tilde{p}_{isentr} = \theta_1 M^2 p_{00} \tag{2.32}$$

and $\tilde{\rho}_{isob}$ from Eq. (2.12)[1],

$$\tilde{\rho}_{isob} = \left(\frac{\partial\rho}{\partial T}\right)_p \tilde{T}_{isob} = -\lambda_p\tilde{T}_{isob} \tag{2.33}$$

2.1.2 Energy equation

The energy equation (Eq. (2.11)) to leading order becomes

$$\begin{aligned}
&\frac{\partial}{\partial t}(M^2 T_{10} + \epsilon T_{01} + \beta T_s)\\
&+\mathbf{u}_{00}\cdot\nabla(M^2 T_{10} + \epsilon T_{01} + \beta T_s) + \mathbf{u}_{00}\cdot\nabla T_h\\
&= \theta_2\left\{\frac{\partial}{\partial t}(M^2 p_{00}) + \mathbf{u}_{00}\cdot\nabla(p_h + M^2 p_{00})\right\}\\
&+\frac{1}{RePr}\nabla^2(T_h + M^2 T_{10} + \epsilon T_{01} + \beta T_s)
\end{aligned} \tag{2.34}$$

[1]It is straightforward to extend Eq. (2.33) to moist air when the water vapor mass fraction Y is small, as $\tilde{\rho}_{isob} = -(-Y + Y/\xi) - \lambda_p\tilde{T}_{isob}$ where $\xi = m_w^*/m_a^*$, and m_w^* and m_a^* are the molecular weights of water and air.

where viscous dissipation has been neglected. Within an $\mathcal{O}(\eta_2)$ error, the $\mathcal{O}(M^2)$ component is

$$\frac{\tilde{D}(M^2 T_{10})}{Dt} = \theta_2 \frac{\tilde{D} M^2 p_{00}}{Dt} + \frac{1}{RePr}\nabla^2(M^2 T_{10}) + \mathcal{O}(\eta_2) \tag{2.35}$$

The $\mathcal{O}(\epsilon)$ component is

$$\frac{\tilde{D}(\epsilon T_{01})}{Dt} = -\epsilon v_{00} + \frac{1}{RePr}\nabla^2(\epsilon T_{01}) + \mathcal{O}(\eta_2) \tag{2.36}$$

where

$$\epsilon = \frac{ds_h}{dy} = \frac{L^*}{C_p^*}\frac{ds_h^*}{dy^*} = \frac{dT_h}{dy} - \theta_2 \frac{dp_h}{dy} \tag{2.37}$$

The $\mathcal{O}(\beta)$ component is

$$\frac{\tilde{D}(\beta T_s)}{Dt} = \frac{1}{RePr}\nabla^2(\beta T_s) + \mathcal{O}(\eta_2) \tag{2.38}$$

Adding the above three components we obtain

$$\frac{\tilde{D}\tilde{T}}{Dt} = \theta_2 \frac{\tilde{D}\tilde{p}}{Dt} - \epsilon\tilde{v} + \frac{1}{RePr}\nabla^2\tilde{T} + \mathcal{O}(\eta_2) \tag{2.39}$$

Note that strict expansion would require the material derivative operator to be $\frac{D_0}{Dt}$, but for later convenience we use $\frac{\tilde{D}}{Dt}$ which includes an $\mathcal{O}(\eta_1)$ correction to $\frac{D_0}{Dt}$. Also v_{00} has been replaced by $\tilde{v}$ which introduces an $\mathcal{O}(\eta_2)$ error in Eq. (2.36). The component equations (2.35), (2.36), and (2.38) represent the transport associated with the base flow motion, stratification, and a pure advective-diffusive evolution of the initially imposed entropy perturbation. This is similar to the modal decomposition for compressible flows (Kovásznay, 1953) with the difference that we have split the entropic mode into two parts - those due to stratification and due to initial temperature fluctuations.

2.2 Low Mach number, moderate Froude number shallow flows

Consider a general three dimensional base flow with moderate Froude number. Under the assumption of low Mach number and small vertical extent of the flow, all terms with subscript '10' drop out. $\tilde{\rho}_{isentr}$ and $\tilde{T}_{isentr}$ become negligible compared to $\tilde{\rho}_{isob}$ and $\tilde{T}_{isob}$

respectively. We define $p' = \theta_1 p_{00}$, $\rho' = \tilde{\rho}/\eta_1$, and $T' = \tilde{T}/\eta_1$ so that p', ρ' and T' are order unity. The governing equations for $\tilde{\mathbf{u}}$, p', ρ' and T' are, up to $\mathcal{O}(\eta_1)$,

$$\nabla \cdot \tilde{\mathbf{u}} = 0 \tag{2.40}$$

$$\frac{\tilde{D}\tilde{\mathbf{u}}}{Dt} = -\nabla p' - \frac{\eta_1}{Fr}\rho' \hat{\mathbf{e}}_{\mathbf{y}} - (\rho_h(y) + \eta_1 \rho')\frac{\tilde{D}\tilde{\mathbf{u}}}{Dt} + \frac{1}{Re}\nabla^2 \tilde{\mathbf{u}} \tag{2.41}$$

$$\frac{\tilde{D}T'}{Dt} = -\frac{\epsilon}{\eta_1}\tilde{v} + \frac{1}{RePr}\nabla^2 T' \tag{2.42}$$

$$\rho' = -\lambda_p T' \tag{2.43}$$

No particular equation of state has been assumed. For an ideal gas $\lambda_p = 1$, and $\theta_2 = (\gamma - 1)/\gamma$ which for air is 0.286. For water at $1atm$ pressure and $293K$, $\theta_2 \approx 2.8 \times 10^{-4}$, and $\lambda_p \approx 6 \times 10^{-2}$.

The effect of perturbation pressure on buoyancy term can be neglected solely based on the low Mach numbers, through Eq. (2.32). The restrictive assumptions that this effect is negligible compared to the hydrostatic pressure gradient (Spiegel & Veronis, 1960; Dutton & Fichtl, 1969), or that the Froude number is low (Mahrt, 1986) are not required, as Eq. (2.32) is valid for both incompressible and compressible fluids, with or without stratification.

The above equations assume that no heat sources are present. The initially imposed temperature fluctuation is assumed to be isobaric. When significant (nonisentropic) heat addition is present, the low Mach number equations (e.g. Lele, 1998) should be used. For deep convection, the anelastic approximation should be used. The linearized form of the equations derived here produce the correct Brunt-Väisälä frequency N^*, given by

$$N^{*2} = g^* k_p^* \left(\frac{dT_h^*}{dy^*} - \frac{k_p^* T_{ref}^*}{\rho_{ref}^* C_p^*} \frac{dp_h^*}{dy^*} \right) \tag{2.44}$$

These equations can in general be solved using an iterative scheme at every time step to deal with the extended Boussinesq term (e.g. Aigner & Grimshaw, 2001). For slowly varying flows, iterations can be avoided with some approximation (see Section 2.5). The equations are expected to apply to flows dominated by stratification, flows involving externally imposed, but small, temperature fluctuations, and turbulent flows. Coriolis effects can be included with additional terms. The formulation is more general than those used for strongly rotating nonisothermal flows (Serre *et al.*, 2004; Soong & Chyuan, 1998). For

completeness, the *dimensional* equations for the extended Boussinesq approximation are

$$\nabla^* \cdot \tilde{\mathbf{u}}^* = 0 \tag{2.45}$$

$$\rho^*_{ref} \frac{\tilde{D}^* \tilde{\mathbf{u}}^*}{Dt^*} = -\nabla^* \tilde{p}^* - \tilde{\rho}^* g^* \hat{\mathbf{e}}_{\mathbf{y}} - (\rho^*_h + \tilde{\rho}^*) \frac{\tilde{D}^* \tilde{\mathbf{u}}^*}{Dt^*} + \mu^* \nabla^{*2} \tilde{\mathbf{u}}^* \tag{2.46}$$

$$\rho^*_{ref} C^*_p \frac{\tilde{D}^* \tilde{T}^*}{Dt^*} = \tilde{v}^* \left(k^*_p T^*_{ref} \frac{dp^*_h}{dy^*} - \rho^*_{ref} C^*_p \frac{dT^*_h}{dy^*} \right) + k^*_{ref} \nabla^{*2} \tilde{T}^* \tag{2.47}$$

$$\tilde{\rho}^* = -\rho^*_{ref} k^*_p \tilde{T}^* \tag{2.48}$$

where we recall that for all variables, $\tilde{\phi}^*$ is an approximation to ϕ^*_{nh} up to $\mathcal{O}(\eta_1)$.

2.2.1 Buoyancy-driven low Mach number shallow flows

Consider the situation where there is no significant base flow (at least in the direction of gravity), and the motion is driven by buoyancy. The buoyancy scales can be chosen as $U^*_b = \sqrt{k^*_p \Delta T^* g^* L^*}$ and $\tau^*_b = L^*/U^*_b$. The Reynolds number can be expressed in terms of the Grashof number, $Gr = g^* k^*_p \Delta T^* L^{*3}/\nu^{*2}$. In Eq. (5.5), the buoyancy term when rescaled in this manner becomes $\mathcal{O}(1)$ with respect to the convective and unsteady terms, but the extended Boussinesq term is $\mathcal{O}(\eta_1)$, and can be neglected. Thus the extended Boussinesq approximation recovers the traditional Boussinesq approximation in regions where the base flow inertia is not important. Hence the same equations are valid for buoyancy induced wave phenomena.

2.3 Applicability to "nearly incompressible" hydrostatic state

From the analysis of Section 2.1.2, the shallow flow approximation alone is not sufficient to justify neglecting the effect of hydrostatic pressure variation in the energy equation. Motivated by Eq. (2.44) and its nondimensional analog, Eq. (2.37), we define a nearly incompressible fluid as one for which

$$\theta_2 \ll 1 \tag{2.49}$$

Since θ_2 involves both fluid properties and local thermodynamic state, this criterion is for a particular fluid at a particular altitude. Hence the notion of "near incompressibility" must be interpreted as incompressibility of a given hydrostatic state. This is different from the incompressibility with respect to motion, which is characterized by Mach number and

Strouhal number (the latter is relevant in acoustics). It is straightforward to show that (Pierce, 1989, p. 16)

$$-\frac{(\partial s^*/\partial p^*)_{T^*}}{(\partial s^*/\partial T^*)_{p^*}}\bigg|_{ref} = \frac{k_p^* T_{ref}^*}{\rho_{ref}^* C_p^*} \tag{2.50}$$

Nondimensionalization of this equation produces

$$-\frac{(\partial s/\partial p)_T}{(\partial s/\partial T)_p}\bigg|_{ref} = \left(\frac{k_p^* T_{ref}^*}{\rho_{ref}^* C_p^*}\right)\frac{p_{ref}^*}{T_{ref}^*} = \theta_2 \tag{2.51}$$

So physically the inequality (2.49) means that the dependence of entropy on pressure is weak compared to that on temperature. θ_2 is the nondimensional form of the proportionality constant between pressure and temperature gradients under adiabatic conditions (Jarvis & McKenzie, 1980). Assuming that scale heights for temperature and pressure are comparable, Eq. (2.37) gives, when $\theta_2 \ll 1$,

$$\frac{ds_h}{dy} \approx \frac{dT_h}{dy} \tag{2.52}$$

i.e., the background stratification is dominated by temperature stratification.

The compressibility criterion is traditionally based on the dissipation number, $Di = L^*/H_T^*$ where H_T^* is the scale height for background temperature (Christensen & Yuen, 1985; Batchelor, 2000). This does not take into account the separate scalings for the non-hydrostatic temperature fluctuations and the hydrostatic temperature gradient, making the criterion dependent on the vertical length scale L^* of the problem. The criterion (2.49) does not involve L^*, making it applicable to perturbations in a local sense.

The Brunt-Väisälä frequency is now approximated as

$$N^{*2} \approx g^* k_p^* \frac{dT_h^*}{dy^*} \approx -\frac{g^*}{\rho_{ref}^*}\frac{d\rho_h^*}{dy^*} \tag{2.53}$$

where we have used the fact that the hydrostatic variations also obey the nearly incompressible equation of state, i.e., $\rho_h^* = -\rho_{ref}^* k_p^* T_h^*$, giving us

$$\frac{dT_h^*}{dy^*} = -\frac{1}{\rho_{ref}^* k_p^*}\frac{d\rho_h^*}{dy^*} \tag{2.54}$$

The energy equation (2.47) simplifies to

$$\rho_{ref}^* C_p^* \frac{\tilde{D}^*\tilde{T}^*}{Dt^*} = -\rho_{ref}^* C_p^* \frac{dT_h^*}{dy^*}\tilde{v}^* + k_{ref}^* \nabla^{*2}\tilde{T}^* \tag{2.55}$$

This is equivalent to the transport equation for the total (*in situ*) temperature,

$$\rho^*_{ref} C^*_p \frac{\tilde{D}^* T^*}{Dt^*} = k^*_{ref} \nabla^{*2} T^* \tag{2.56}$$

and also for the *in situ* density (by virtue of the nearly incompressible equation of state, Eq. (2.48), and by Eq. (2.54)),

$$\rho^*_{ref} C^*_p \frac{\tilde{D}^* \rho^*}{Dt^*} = k^*_{ref} \nabla^{*2} \rho^* \tag{2.57}$$

These equations are applicable only when $\theta_2 \ll 1$. It is found that this model is sometimes also applied to atmospheric flows which do not satisfy this constraint. For example, in studies of aircraft wakes, frequently the Brunt-Väisälä frequency is defined by Eq. (2.53) (Spalart, 1996; Hill, 1975; Robins & Delisi, 1990). But if the results therein are to be applied to the atmosphere, this definition should be interpreted differently. The density gradient in Eq. (2.53) should be regarded as the potential density gradient (Kundu & Cohen, 2004).

The incompressible Boussinesq equations have been extensively used to explore the physics of stratified flows including the effects of shear and mixing (e.g. Jacobitz *et al.*, 1997; Riley & Lelong, 2000; Peltier & Caulfield, 2003; Holt *et al.*, 1992). The compressible Boussinesq approximation for shallow flows in compressible media is used extensively in meteorology. The difference between the two approximations is rarely acknowledged and the density gradient in Eq. (2.53) is seldom interpreted correctly when applied to a compressible atmosphere. The criterion (2.49) is intended to provide a widely applicable nondimensional parameter to distinguish between the two approximations for a given fluid at a given altitude/depth.

Subtle differences are observed even among different compressible Boussinesq approximations related to the correct representation of the buoyancy force. For example, potential temperature (and not perturbation potential temperature) is sometimes used in the buoyancy term (Sykes *et al.*, 1988; Dubrulle *et al.*, 2002). On the other hand, a study of differences in the inclusion of perturbation pressure is given by Doswell and Markowski (2004). To describe the bouyancy force in the Boussinesq approximation, the use of different quantities such as potential temperature, entropy, and Brunt-Väisälä frequency is common in meteorology, physics, and atmospheric sciences depending on the context. The different treatments are equivalent if the resultant equations are mathematically equivalent to the

equations derived above, and the criterion (2.49) is respected.

2.4 Vorticity dynamics

The traditional Boussinesq approximation, when applied to flows with strong motion, can only account for the hydrostatically generated baroclinic vorticity. The extended approximation accounts for this as well as the base flow induced baroclinic vorticity generation. Consider the vorticity equation obtained by taking the curl of Eq. (5.5),

$$\begin{aligned}\frac{\tilde{D}\tilde{\omega}}{Dt} &= \tilde{\omega}\cdot\nabla\tilde{\mathbf{u}} - \frac{\eta_1}{Fr}\nabla\times(\rho'\hat{\mathbf{e}}_{\mathbf{y}}) - \nabla(\rho_h+\eta_1\rho')\times\frac{\tilde{D}\tilde{\mathbf{u}}}{Dt} \\ &\quad -(\rho_h+\eta_1\rho')\nabla\times\frac{\tilde{D}\tilde{\mathbf{u}}}{Dt} + \frac{1}{Re}\nabla^2\tilde{\omega} \end{aligned} \tag{2.58}$$

The second term on the r.h.s. is the baroclinic vorticity generated by the interaction of density variation with the hydrostatic pressure gradient. The fourth term can be rewritten using Eq (5.5) as

$$\begin{aligned}-(\rho_h+\eta_1\rho')\nabla\times\Big\{&-\nabla p' - \tfrac{\eta_1}{Fr}\rho'\hat{\mathbf{e}}_{\mathbf{y}} - (\rho_h+\eta_1\rho')\tfrac{\tilde{D}\tilde{\mathbf{u}}}{Dt} \\ &+\tfrac{1}{Re}\nabla^2\tilde{\mathbf{u}}\Big\}\end{aligned} \tag{2.59}$$

Neglecting the viscous term inside the curly brackets, we see that this entire term is $\mathcal{O}(max\{\eta_2,\delta\eta_1,\delta^2\})$ and hence can be neglected. The third term on the right hand side of Eq. (2.58), $-\nabla(\rho_h+\eta_1\rho')\times\frac{\tilde{D}\tilde{\mathbf{u}}}{Dt}$, signifies the baroclinic vorticity generated due to the interaction of density variations with the flow acceleration. A similar term was derived by Aigner and Grimshaw (2001) using the vorticity-streamfunction formulation for two dimensional flows with predominantly uniform parallel base flow. For this specific case the base flow inertia terms are small. The current formulation takes into account general base flows and the hydrostatic density in evaluating the extended term, thus retaining density perturbations to a consistent order.

2.5 Algorithmic simplification for slowly varying flows

In order to use the extended Boussinesq approximation in numerical simulations it is desirable to incorporate the additional term without a significant change in the solution algorithm. For many flows such as rotational flows, the Strouhal number is small, and the flow varies slowly so that for the purpose of evaluating the additional non-Boussinesq term, the Eulerian derivative $\frac{\partial \tilde{\mathbf{u}}}{\partial t}$ at the nth time step can be approximated by that at the $(n-1)^{th}$ time step. Then Eq. (5.5) at the nth time step becomes

$$\begin{aligned}\left.\frac{D\tilde{\mathbf{u}}}{Dt}\right|^n &= -\nabla p'\Big|^n - \frac{\eta_1}{Fr}\rho'\Big|^n \hat{\mathbf{e}}_{\mathbf{y}} \\ &-(\eta_1\rho' + \rho_h)\left(\left.\frac{\partial \tilde{\mathbf{u}}}{\partial t}\right|^{n-1} + \tilde{\mathbf{u}}\cdot\nabla\tilde{\mathbf{u}}\Big|^n\right) + \frac{1}{Re}\nabla^2\tilde{\mathbf{u}}\Big|^n\end{aligned} \tag{2.60}$$

Using Taylor series expansion up to first order,

$$\left.\frac{\partial \tilde{\mathbf{u}}}{\partial t}\right|^{n-1} \approx \left.\frac{\partial \tilde{\mathbf{u}}}{\partial t}\right|^n - \Delta t \left.\frac{\partial^2 \tilde{\mathbf{u}}}{\partial t^2}\right|^n \tag{2.61}$$

hence the modified equation has an error term

$$(\eta_1\rho' + \rho_h)\left.\frac{\partial^2 \tilde{\mathbf{u}}}{\partial t^2}\right|^n \Delta t \tag{2.62}$$

which is small for slowly varying flows and small time steps. This simplification allows us to incorporate the extended terms without a major modification to the solution procedure. If the flow is moderately fast, one can employ an iterative procedure as done in Aigner & Grimshaw (2001). The resulting Poisson equation for pressure is

$$\begin{aligned}\nabla^2 p' = \quad \nabla\cdot\Bigg(&-(1+\eta_1\rho'+\rho_h)\tilde{\mathbf{u}}\cdot\nabla\tilde{\mathbf{u}}\Big|^n - \tfrac{\eta_1}{Fr}\rho'\Big|^n \hat{\mathbf{e}}_{\mathbf{y}} \\ &-(\eta_1\rho'+\rho_h)\tfrac{\partial\tilde{\mathbf{u}}}{\partial t}\Big|^{n-1} + \tfrac{1}{Re}\nabla^2\tilde{\mathbf{u}}\Big|^n\Bigg)\end{aligned} \tag{2.63}$$

which has constant coefficients enabling the use of fast elliptic solvers. The price we pay to gain this efficiency is the small error introduced when treating the extended Boussinesq term explicitly in time. Equation (5.5) is valid for turbulent flows. The application of Eq. (2.60) to turbulent flows is largely justified by the Courant-Friedrichs-Levy (CFL) condition. For

the simplification to be valid, the rate of change of $\frac{\partial \tilde{\mathbf{u}}}{\partial t}$ with time should be small compared to the buoyancy terms (from the error term expression (2.62)). So long as the time step is small, the numerical error (2.62) would be small. This is supported by the CFL restriction.

2.6 Numerical tests with the extended model

The equations derived above are solved using a sixth order compact finite difference scheme (Lele, 1992; Lui & Lele, 2001). Time advancement is done with a low storage, low dissipation and dispersion Runge-Kutta (RK) scheme of fourth order (LDDRK4) (Stanescu & Habashi, 1998). The skew-symmetric form of the convective terms is used to ensure discrete conservation of kinetic energy and scalar variance in the inviscid non-buoyant limit. The Poisson equation for pressure is solved using a fast Fourier spectral solver. The domain size was chosen to be sufficiently large to keep the spurious effects of periodic boundary conditions small.

2.6.1 Isolated Taylor vortex

We consider the base flow consisting of an isolated Taylor vortex with counterclockwise rotation, given at initial time t_o by (dropping the superscript '*' for dimensional variables for brevity)

$$v_\theta(r) = \frac{Cr}{\nu t_o^2} exp\left(\frac{-r^2}{4\nu t_o}\right) \tag{2.64}$$

The initial core radius which we define as $r_c = \sqrt{\nu t_o}$ is the length scale L, and is chosen as $2\pi/10$, where 2π is the domain length in either (x or y) direction. The vortex is located initially at the center of the domain, (π, π). t_o was chosen arbitrarily, and C was chosen such that the Reynolds number based on the velocity scale $U = v_\theta(r_c)$ and length scale L was 10^3. Time was nondimensionalized by L/U. The peak azimuthal velocity was $1.266U$. A Gaussian-shape density fluctuation given by

$$\rho_{nh}(r) = -0.05\rho_{ref} \quad exp\left[-\left(\frac{2r}{r_c}\right)^2\right] \tag{2.65}$$

was imposed on the vortex flow with the center of the Gaussian located at $(\pi + 2r_c, \pi)$. Thus, $\eta_1 = \beta = 0.05$ characterizes the density perturbation scale. The Froude number was chosen as 4.5 to match the conditions for the vortex wake of a typical subsonic transport

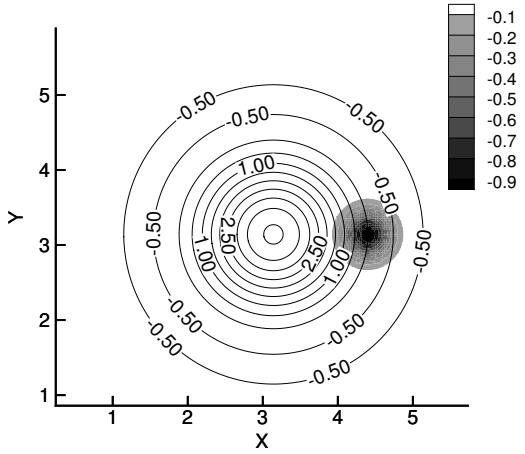

Figure 2.1: Initial condition for the Taylor vortex case. Lines: Vorticity; Filled: Nonhydrostatic density, ρ'.

aircraft, and stratification was set to zero. The domain length $10r_c$ is large compared to the vortex core radius to keep the effect of periodic boundary conditions negligible. The initial configuration is depicted in Fig. 2.1.

Figure 2.2 shows both qualitative and quantitative differences arising from the inclusion of the extra term. The Boussinesq approximation captures only the baroclinic vorticity generated by the hydrostatic pressure gradient. The extended Boussinesq approximation on the other hand captures the additional baroclinic vorticity generated due to the mean flow pressure gradient, which is centripetal. The baroclinic vorticity is stronger in the extended case and as it wraps around, it is pulled toward the vortex core due to buoyancy forces. With the traditional approximation, the fluctuations tend to move predominantly in the tangential direction because the only buoyancy force acting on the fluid particles is that due to gravity, which is smaller than the extended force terms (Fig. 2.3(b) and 2.3(c)).

Figure 2.3 shows the spatial distribution of perturbation density, gravity force term $-\eta_1\rho'/Fr$, magnitude of the extended Boussinesq term

$$Ext_n = -(\eta_1\rho' + \rho_h)\left(\left.\frac{\partial\tilde{\mathbf{u}}}{\partial t}\right|^{n-1} + \tilde{\mathbf{u}}\cdot\nabla\tilde{\mathbf{u}}\right|^{n}\Big),$$

and magnitude of the error in the approximation of the momentum equation by Eq. (2.60),

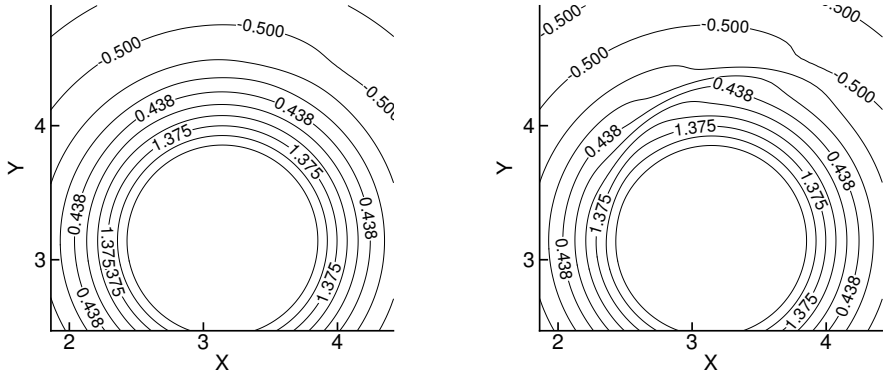

(a) Traditional Boussinesq (b) Extended Boussinesq

Figure 2.2: Vorticity contours at $t = 2$ for the Taylor vortex with (a) Traditional Boussinesq and (b) Extended Boussinesq approximation.

$$Err_n = -(\eta_1 \rho' + \rho_h)\left(\left| \frac{\partial \tilde{\mathbf{u}}}{\partial t} \right|^n - \left| \frac{\partial \tilde{\mathbf{u}}}{\partial t} \right|^{n-1} \right).$$

These terms are spatially correlated with the density fluctuations. The extended term is of significant magnitude and can not be neglected in comparison with the gravity term. In fact, here it is more dominant than the gravity term. The magnitude of the error is indeed very small compared to the retained terms.

2.6.2 2D Taylor vortex array

Next, the problem of a 2D periodic decaying Taylor vortex array is considered. The velocity field is given by

$$\begin{aligned} u &= -cos\left(\frac{2\pi x}{L_p}\right) sin\left(\frac{2\pi y}{L_p}\right) \\ v &= sin\left(\frac{2\pi x}{L_p}\right) cos\left(\frac{2\pi y}{L_p}\right) \end{aligned} \tag{2.66}$$

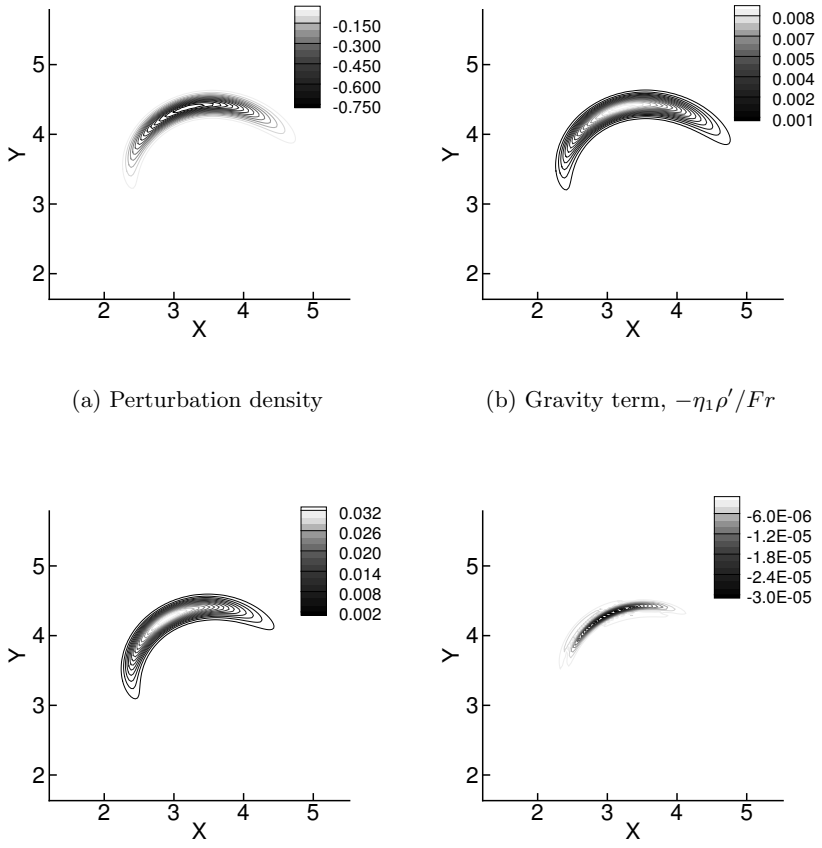

(a) Perturbation density

(b) Gravity term, $-\eta_1\rho'/Fr$

(c) Magnitude of the extended Boussinesq term, $|Ext_n|$

(d) Magnitude of error, $|Err_n|$

Figure 2.3: A-posteriori comparison of terms in the momentum equation at $t = 2$, computed using the extended Boussinesq approximation. (a) Perturbation density, ρ' (b) Gravity term, $-\eta_1\rho'/Fr$ (c) Magnitude of the extended Boussinesq term, $|Ext_n|$ (d) Magnitude of the error, $|Err_n|$.

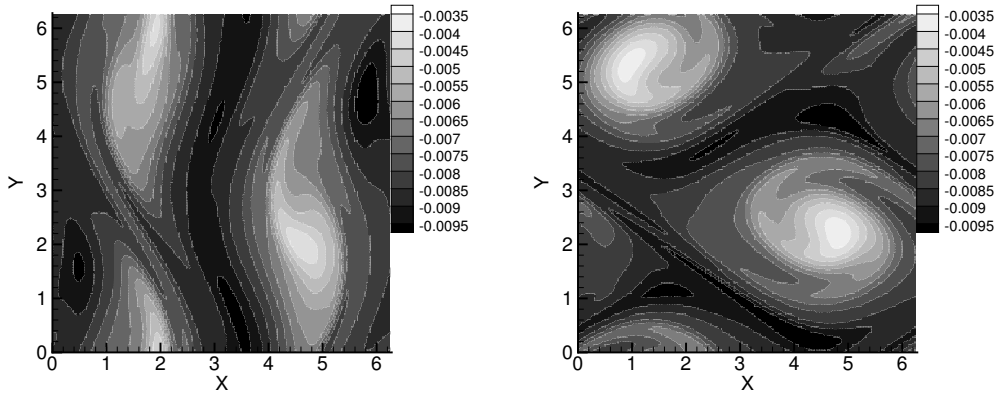

(a) Traditional Boussinesq

(b) Extended Boussinesq

Figure 2.4: Contours of ρ' for the Taylor vortex array at $t = 120$ with (a) Traditional Boussinesq and (b) Extended Boussinesq approximation.

where L_p is the periodicity length in either direction, taken as 2π. An initial Gaussian density fluctuation given by

$$\rho_{nh}(r) = -0.05\rho_{ref} \quad exp\left[-\left(\frac{2r}{(L_p/10)}\right)^2\right] \tag{2.67}$$

was imposed with the center of the Gaussian at $(L_p/2, 3L_p/4)$. The Froude number was 4.5 and the Reynolds number based on velocity scale $U = 1$ was 10^3. The length scale L was taken as $L_p/2\pi$, and time was nondimensionalized by L/U. No stratification was present. Simulations with two different time step sizes were carried out, and the results were almost identical indicating that time stepping errors are small. The perturbation density contours in Figure 2.4 show the differences caused by the extended Boussinesq terms. The traditional approximation results in highly anisotropic streaks aligned with gravity, but the extended approximation shows a relatively more circular, isotropic density distribution, because the centripetal force modeled through the extended term tends to retain the hot fluid near the vortex core.

We quantify the anisotropy of the flow using an anisotropy ratio, defined as $\Gamma =$

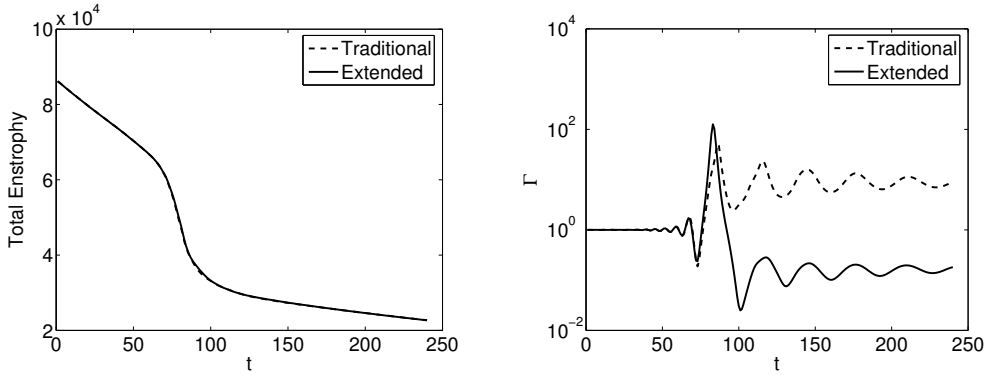

(a) Total enstrophy

(b) Anisotropy ratio

Figure 2.5: Effect of the extended terms on flow quantities for the Taylor vortex array.

$\sum v^2 / \sum u^2$, where u and v are the horizontal and vertical velocity components, and the summation is performed over all grid points in the domain. Similarly we define the total enstrophy in the domain as $\sum \omega^2$ (which differs from the standard definition by a factor $1/2$, with no impact on the conclusions drawn in this chapter). The current code does not use potential enstrophy conserving schemes (Sadourny, 1975; Arakawa & Lamb, 1981) because high spectral accuracy and energy conservation in the inviscid limit are considered more important than the conservation of potential enstrophy. This is just a matter of choice of numerical schemes. The physical problem does not conserve potential enstrophy due to the presence of viscosity. The fine grid and a high-wavenumber spectral filter are used to keep aliasing errors low and spurious enstrophy generation benign.

Figure 2.5 shows the time evolution of these two quantities. It can be seen that although the total enstrophy is not affected by the level of approximation, the anisotropy of the flow is affected. In this particular example, large differences are triggered around $t = 80$ and the asymptotic behavior under the two approximations is quite different.

2.7 Conclusions

The interaction of density perturbations with fluid inertia is neglected when the Boussinesq approximation is applied to shallow flows with strong base flow motions. We have shown that this interaction can be comparable to the gravity forces, depending on the

Froude number. A simple modification to the traditional Boussinesq approximation is proposed to model these interactions. These interactions are relatively unimportant if stratification is small and there is no imposed temperature inhomogeneity, but when the latter is dominant, these effects should be taken into account. The equations derived here can be considered as a generalized form of the existing approximations (Aigner & Grimshaw, 2001; Shimomura, 1999; Soong & Chyuan, 1998) for moderate Froude number, low Mach number, stratified shallow flows possibly containing small initial entropy inhomogeneities. A distinction between temperature changes due to stratification and those due to initial conditions is maintained in the derivation, whereby different physical cases can be clearly distinguished.

Using the nondimensional parameter θ_2, we developed a criterion for an incompressible fluid in the context of stratified flows. Stratification in compressible and incompressible media should be distinguished to obtain a consistent representation of buoyancy forces. The density variable used in the thermal buoyancy term and that used in the energy transport equation must be consistent with the fundamental governing equations.

From the asymptotic analysis it was also transparent that the effect of perturbation pressure on density changes in the buoyancy term can be neglected if the Mach number is low. This is a less restrictive criterion than Spiegel & Veronis (1960); Dutton & Fichtl (1969); Mahrt (1986) for the neglect of the effect of pressure perturbations on buoyancy forces, and this criterion is applicable to both compressible and incompressible fluids.

The effect of the hydrostatic pressure gradient is neglected in the Poisson equation. Hence the corresponding contribution to pressure is neglected in the momentum equation. Although this effect is small when initial entropy perturbations are larger than the entropy gradient due to stratification, the anelastic approximation is admittedly more accurate than the current approximation in this regard. For strong stratification, large externally imposed temperature differences, or deep flows, the anelastic approximation should be used, although it is more difficult to solve than the Boussinesq equations.

The base flow need not be analytically solvable but rather, forms a part of the solution. For slowly varying flows, i.e., low Strouhal number flows, the additional term can be approximated to make the equations amenable to solutions without additional iterations. The traditional Boussinesq algorithm is easily modified to include the above physics in numerical simulations. The equations revert to the traditional Boussinesq approximation in regions where the base flow is not strong. The scale analysis showed that the approximation

is applicable to a variety of flows involving stratification, internal waves, and turbulence. The equations are easily extendible to moist air with small water vapor fraction. For the given range of nondimensional parameters considered, the appropriate asymptotic regime in which the extended Boussinesq approximation is valid has been established, thereby placing it in the general hierarchy of approximations to the Navier-Stokes equations.

Chapter 3

Formulation of the Contrail Problem

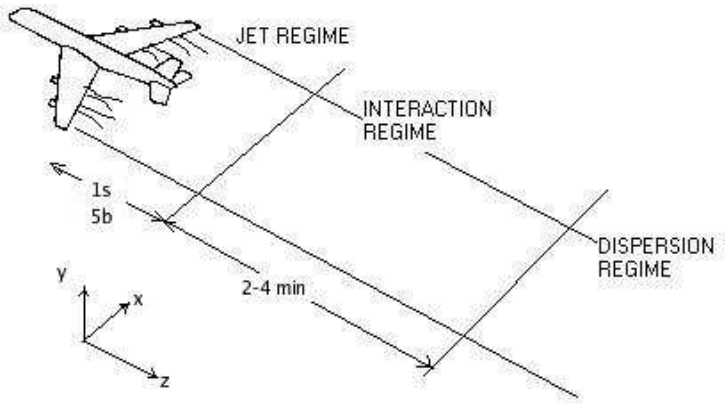

Figure 3.1: Schematic of the flow development behind a typical subsonic aircraft.

Traditionally, aircraft wake evolution is divided into three different regimes – jet regime, interaction regime (also called vortex regime), and dispersion regime (Figure 3.1). The cruise velocity is along the negative z-axis, the x-axis joins the two wing tips and the gravity points in the negative y-direction. Immediately downstream of the wing, the jet evolves independently of the vortex wake because of its strong axial momentum. This regime extends several jet diameters. Also in this stage the trailing vorticity sheet shed by the aircraft is getting rolled-up into a vortex pair. The next regime which spans 2-4 minutes

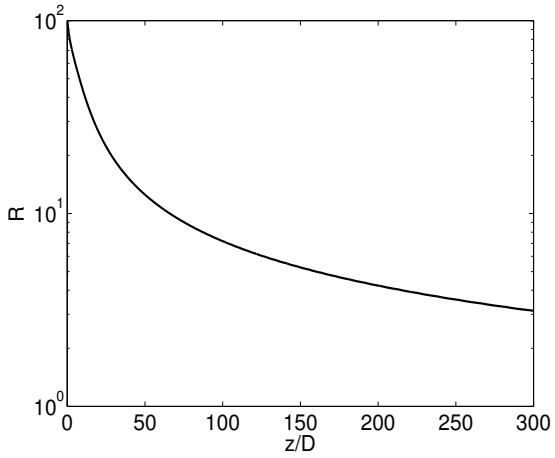

Figure 3.2: Evolution of R, the ratio of the jet momentum relative to the vortex momentum, along the jet axis, indicating the beginning of the interaction regime approximately three wing spans (300 jet diameters) downstream.

is the vortex regime. Here, the jet and the wake affect each other. Finally, after several wing spans, the exhaust gases get dispersed by the turbulence in the wake in the so-called dispersion regime. The wake vortices themselves undergo three-dimensional instabilities, which results in vortex linking and break-up. We are mainly interested in studying the fluid dynamical aspects of contrail growth which occur in the vortex regime.

To assess the overall interaction of the jet and the wake vortices, we define a parameter R as the ratio of the jet axial momentum flux to the vertical impulse of the vortex wake similar to Jacquin & Garnier (1996).

$$R = \frac{\rho_j (V_j - V_o) V_j A(z)}{\rho_o \Gamma_o V_o b} \tag{3.1}$$

where V_j is the jet mean velocity, V_o is the aircraft speed, ρ_o is the ambient density, Γ_o is the total circulation of one of the vortices (Lift $L = \rho_o \Gamma_o V_o b$), b is the vortex spacing, and $A(z)$ is the jet cross section area. Figure 3.2 shows the evolution of R with the downstream distance for a Boeing 767 type passenger aircraft. These data are obtained using a parabolized Reynolds Averaged Navier-Stokes (RANS) code (Choi & Lele, 2001). The co-flow corresponding to the cruise speed is accounted for. The wake starts strongly affecting the jet when R becomes of order unity. In this region the jet regime ends and the interaction regime begins. It is seen that R becomes of order unity roughly after three wing-spans

Table 3.1: Aircraft parameters at the jet exit plane. Superscript '*' on dimensional variables is omitted for brevity.

Altitude, h	$10.5km$
Acceleration due to gravity, g	$9.81m/s^2$
Geometric wing span, b	$47.24m$
Initial vortex separation, b_v	$42.5m$
Cruise speed, U_{cruise}	$236.9m/s$
Vortex circulation, Γ	$390.7m^2/s$
Reynolds number, $Re = \Gamma/\nu$	1.03×10^7
Initial vortex descent speed, $U = \Gamma/2\pi b$	$1.4469m/s$
Reynolds number, $Re = Ub/\nu$	1.804×10^6
Initial descent time scale, $T = b/U$	$32.65sec$
Froude number, $Fr = U^2/bg$	4.517×10^{-3}
Initial vortex core radius, r_c	$5.3m$
Initial peak swirl velocity, U_{peak}	$11.73m/s$
Peak Froude number, $Fr = U_{peak}^2/r_c g$	2.65
Jet exit diameter, D_j	$0.5m$
Jet peak velocity, U_j	$480m/s$
Jet peak temperature, T_j	$580K$

downstream. Consequently we select the location at 3-5 wingspans downstream of the airplane as the initial point for our Large Eddy Simulations (LES). Since our computational domain will be stationary in the Earth's frame of reference, this location corresponds to $3b/U_{cruise} \approx 1s$ after the aircraft passage, where b and U_{cruise} are defined in Table 3.1 along with other aircraft parameters. In other words, we will carry out temporal LES of contrails in a fixed domain of length L_z in the flight direction through which the aircraft passes, starting at $1s$ after the aircraft passage. Typical atmospheric conditions considered at the cruise altitude are listed in Table 3.2. Some of these parameters will be varied later during the parametric study. The following empirical relations have been used to obtain some of the atmospheric properties. Ambient temperature, $T_{ref} = 288.15K - Lh$ where $L = 6.5K/km$ and h is in km. Diffusivity of water vapor in air, $D_v = 2.11 \times 10^{-5}\left(\frac{p_{o1}}{p_{ref}}\right)\left(\frac{T_{ref}}{T_{o1}}\right)^{1.94} m^2/s$ where $p_{o1} = 101,325Pa$, $T_{o1} = 273.15K$ (Pruppacher & Klett, 1978). Mean free path of water molecules, $\lambda = 6.6 \times 10^{-8}\left(\frac{p_{o2}}{p_{ref}}\right)\left(\frac{T_{ref}}{T_{o2}}\right)m$, where $p_{o2} = 101,325Pa$, $T_{o2} = 293.15K$ (Pruppacher & Klett, 1978).

Table 3.2: Atmospheric parameters. Superscript '*' on dimensional variables is omitted for brevity.

Pressure, p_{ref}	238.5 hPa
Temperature, T_{ref}	218.8 K
Universal gas constant, R	$8.314kJ/kmol - K$
Density of air, $\rho_{ref} = p_{ref}/RT_{ref}$	$0.3798kg/m^3$
Diffusivity of water vapor in air, D_v	$5.8542 \times 10^{-5}m^2/s$
Kinematic viscosity, ν	$3.789 \times 10^{-5}m^2/s$
Schmidt number for water vapor, $Sc = \nu/D_v$	0.6472
Prandtl number for air, Pr	0.7
Mean free path of water molecules in air, λ	$2.09 \times 10^{-7}m$

In simulations of atmospheric flows and weather predictions, the use of Eulerian grids is ubiquitous. For tackling the large-scale vortex motion induced by the aircraft, this approach is suitable and hence employed to simulate the fluid dynamics in the present work. For ice particles there are two different approaches available – Eulerian and Lagrangian. In atmospheric transport and pollutant dispersion, the dispersed phase (such as ice particles or water droplets in clouds) is often represented as an Eulerian field variable and its concentration and statistical properties are tracked. These properties may be the first few moments of the size distribution. However, dilute two-phase particulate flows are naturally tackled by the Lagrangian approach due to the inherent particle-based transport. The Lagrangian approach tracks an ensemble of individual particles (or an ensemble of collections of particles) as the particles move in the flow. In studies of clouds, for instance, this approach has been extensively used (Shaw, 2003).

For the current study of contrails, the selection of a suitable approach is done on the basis of the physics to be studied and the computational cost. The Eulerian approach has been used by many authors with binned microphysics (e.g. Chlond, 1998; Huebsch & Lewellen, 2006) and bulk microphysics (e.g. Lewellen & Lewellen, 2001). In the bulk microphysics approach, all particles in a grid cell are assumed monodispersed, losing the information about higher moments of the particle size distribution within the cell. In the binned approach, particles are put into various bin sizes and the concentration in each bin is

evolved on the Eulerian grid. Binned microphysics captures more physical details, e.g. late-time crystal loss due to buoyant sloshing, than the bulk microphysics (Huebsch & Lewellen, 2006). But this approach suffers from numerical diffusion across the bins unless the bin structure is sufficiently fine. These errors can accumulate resulting in numerical broadening of the droplet spectra (Brenguier & Chaumat, 2001). Each bin corresponds to an additional field variable to be solved, hence the cost of the simulation can be high compared to the flow solver. An alternative approach of moment-tracking (Paoli & Shariff, 2003) evolves a fixed number of moments of the particle size distribution. This relies on models for interaction between different moments for closure. The Lagrangian particle tracking approach, on the other hand, is less affected by numerical diffusion because the particles are tracked along the flow trajectories. The only numerical diffusion arises from the coupling to the Eulerian solution containing flow variables including the humidity field. The physics of ice particles in the wake is naturally represented by this Lagrangian approach and the cost was found to be low as discussed later in Chapter 4.

The Lagrangian approach was first used for contrail simulations by Paoli *et al.* (2002). Here we refine their methodology to take into consideration more realistic thermodynamical behavior of ice particles. Thus, in effect, we use a mixed Eulerian-Lagrangian computational approach for contrail simulations where the fluid dynamics is handled using an Eulerian field approach and the ice microphysics is solved using the Lagrangian particle tracking approach. Some of our simulations provide trends similar to Huebsch & Lewellen (2006) underlining some of the basic similarities between the physics simulated. In Chapter 4, we will provide results from numerical tests which indicate that this mixed Eulerian-Lagrangian formulation is an attractive approach to compute dilute multiphase flows at reasonable costs.

3.1 Initial conditions

The initial conditions are obtained by using field variables at 5 wing spans downstream of the engine exit plane of a Boeing 767 aircraft. These fields were provided by Boeing and obtained by RANS computations performed by Boeing. We construct the flow initial conditions by interpolation of and turbulence addition to the data provided by Boeing. Ice particle data was generated in such a way that the particle number density is proportional to the local water vapor content. These procedures for generating initial conditions are explained in detail in Chapter 6.

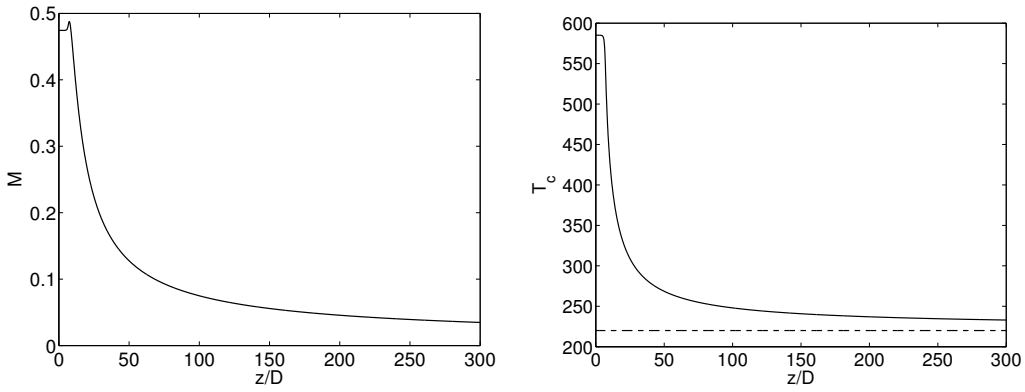

(a) (b)

Figure 3.3: Variation of (a) Mach number and (b) Jet temperature downstream of the aircraft. Dashed line indicates ambient temperature. All values are in a stationary domain through which the jet passes at cruise speed. The x-axis corresponds to the distance of the stationary observation point from the moving jet nozzle.

3.2 Flow Physics: Large Eddy Simulation

Figure 3.3 shows the evolution of the jet centerline Mach number and temperature downstream of the aircraft obtained from the RANS computations mentioned before. The computations were carried out in the reference frame attached to the jet nozzle. Since the nozzle is moving with the cruise velocity (in the Earth's frame of reference), this means the jet, as seen from the frame attached to the jet nozzle, will experience a co-flow with velocity equal to negative of the cruise velocity. This co-flow is taken into account during the RANS simulations. The Mach number reported below has been converted (using the cruise speed) to the stationary frame used for the subsequent temporal LES. It can be seen that the jet excess temperature and Mach number in the regime of interest (more than three wing spans downstream, or $z/D > 300$) are small, allowing us to use the incompressible Boussinesq approximation for the fluid flow. At this stage, i.e. the end of the RANS computations the Mach number is approximately 0.045, the jet peak velocity is roughly $13.7m/s$, and the jet peak temperature excess over the ambient temperature is approximately $10K$.

The splitting introduced in Chapter 2 is used:

$$\phi^*(x, y, z, t) = \phi^*_{ref} + \phi^*_h(y) + \phi^*_{nh}(x, y, z, t) \tag{3.2}$$

The dimensional flow equations 2.45, 2.46, 2.47, 2.48 and an additional active scalar (nondimensional humidity, defined as $(\rho_{tot}q)/\rho_{ref}$ where q is the water vapor mass fraction in $kg_{H_2O}/kg_{dry\,air}$) equation are

$$\nabla \cdot \mathbf{u} = 0 \tag{3.3}$$

$$\rho_{ref}\frac{D\mathbf{u}}{Dt} = -\nabla p - \rho_{nh}g\hat{\mathbf{e}}_{\mathbf{y}} - (\rho_h + \rho_{nh})\frac{D\mathbf{u}}{Dt} + \mu\nabla^2\mathbf{u} \tag{3.4}$$

$$\rho_{ref}C_p\frac{DT_{nh}}{Dt} = v\left(k_pT_{ref}\frac{dp_h}{dy} - \rho_{ref}C_p\frac{dT_h}{dy}\right) + k_{ref}\nabla^2T_{nh} + \omega_T \tag{3.5}$$

$$\rho_{ref}\frac{DY}{Dt} = \rho_{ref}D_v\nabla^2Y + \omega_Y \tag{3.6}$$

$$\rho_{nh} = -\rho_{ref}k_pT_{nh} \tag{3.7}$$

Although we have dropped the superscripts "*" for dimensional variables for convenience, all variables are dimensional. The additional terms ω_T $[kJ/m^3s]$ and ω_Y $[kg/m^3s]$ are the sources (or sinks) of energy and water vapor respectively. They arise due to the ice particle microphysics and are related by the latent heat of sublimation of ice, L, as

$$\omega_T = -\omega_Y L \tag{3.8}$$

Their evaluation is done using the Lagrangian microphysics model and will be described in Section 3.3. For air, the isobaric compressibility k_p is $1/T_{ref}$. The Brunt-Väisälä frequency N is given by

$$N^2 = gk_p\left(\frac{dT_h}{dy} - \frac{k_pT_{ref}}{\rho_{ref}C_p}\frac{dp_h}{dy}\right) \tag{3.9}$$

3.2.1 Filtered equations and subgrid scale modeling

In large eddy simulation we explicitly solve for the resolved flow scales and model the "subgrid" scales (SGS). "Sub-grid" here implies the scales that can not be resolved on a given grid. We model the effect of SGS terms on the resolved scales, but never have access to the SGS themselves. This is done using a conceptual, implicit, spatial grid-filter the cut-off width of which is roughly equivalent to the grid spacing. The grid-filtered variables are

Table 3.3: Physical scales and nondimensional parameters

Length	Initial vortex separation, $b^* = 42.5m$
Perturbation temperature, T^*_{nh}	Jet peak excess temperature, $\Delta T^* = 10K$
Buoyancy parameter, β	$\Delta\rho^*/\rho^*_{ref} = \Delta T^*/T^*_{ref} = 0.045$
Perturbation density, ρ^*_{nh}	$\Delta\rho^* = \beta\rho^*_{ref}$
Velocity	Initial vortex descent speed, $U^* = 2.02m/s$
Pressure	$\rho^*_{ref}U^{*2}$
Energy source, ω^*_T	$\rho^*_{ref}C^*_pU^*T^*_{ref}/b^*$
Water vapor source, ω^*_Y	$\rho^*_{ref}U^*/b^*$

defined as

$$\overline{\phi}(\mathbf{r}) = \int_\Omega G(\mathbf{r},\mathbf{r}')\phi(\mathbf{r}')d\mathbf{r}' \tag{3.10}$$

where G is a conceptual filter with width approximately equal to $\Delta = (\Delta x\Delta y\Delta z)^{1/3}$. The filtered equations become

$$\nabla\cdot\overline{\mathbf{u}} = 0 \tag{3.11}$$

$$\rho_{ref}\frac{\overline{D}\overline{\mathbf{u}}}{Dt} = -\nabla\overline{p} + \mu\nabla^2\overline{\mathbf{u}} - \overline{\rho}g\hat{\mathbf{e}_\mathbf{y}} - (\rho_h+\overline{\rho})\frac{\overline{D}\overline{\mathbf{u}}}{Dt} + \rho_{ref}\nabla\cdot\mathbf{I} \tag{3.12}$$

$$\rho_{ref}C_p\frac{\overline{DT}}{Dt} = k\nabla^2\overline{T} - \overline{v}\left(\rho_{ref}C_p\frac{dT_h}{dy} + k_pT_{ref}\frac{dp_h}{dy}\right) + \rho_{ref}\nabla\cdot\mathbf{H} + \overline{\omega}_T \tag{3.13}$$

$$\rho_{ref}\frac{\overline{DY}}{Dt} = \rho_{ref}D\nabla^2\overline{Y} + \rho_{ref}\nabla\cdot\mathbf{P} + \overline{\omega}_Y \tag{3.14}$$

where we have dropped the subscript "nh" for convenience. These equations are used as a consistent approximation of buoyancy forces in a compressible stratified medium, and to improve the incompressible-medium approximation of the energy transport equation used frequently (e.g. Shirgaonkar & Lele, 2005[1]; Spalart, 1996; Hill, 1975; Robins & Delisi, 1990). The effect of the extended Boussinesq approximation was discussed earlier in Chapter 2. The material derivative $\frac{\overline{D}}{\overline{D}t}$ is defined as $\frac{\partial}{\partial t} + \overline{\mathbf{u}}\cdot\nabla$. The subgrid scale (SGS) tensor $I_{ij} = \overline{u_i}\overline{u_j} - \overline{u_iu_j}$, and the (SGS) vectors $H_j = \overline{u}_i\overline{T} - \overline{u_iT}$ and $P_i = \overline{u}_i\overline{Y} - \overline{u_iY}$, are modeled as

$$\mathbf{I} = 2C\Delta^2|\overline{\mathbf{S}}|\overline{\mathbf{S}} \tag{3.15}$$

[1]Updated version of results presented in Shirgaonkar & Lele (2005) and Shirgaonkar & Lele (2006*a*) are contained in this thesis. The updates include correct implementation of Kelvin effect and more realistic values of microphysical parameters involved.

$$\mathbf{H} = \frac{2C\Delta^2}{Pr_t}|\overline{\mathbf{S}}|\nabla\overline{T} \tag{3.16}$$

$$\mathbf{P} = \frac{2C\Delta^2}{Sc_t}|\overline{\mathbf{S}}|\nabla\overline{Y} \tag{3.17}$$

where $\Delta = (\Delta x \Delta y \Delta z)^{1/3}$ is the grid filter width. $\overline{S}_{ij} = \frac{1}{2}(\frac{\partial \overline{u}_i}{\partial x_j} + \frac{\partial \overline{u}_j}{\partial x_i})$ is the SGS rate of strain tensor. The Smagorinsky constant C, and the turbulent Prandtl and Schmidt numbers, Pr_t and Sc_t are evaluated using the dynamic Smagorinsky model of Moin *et al.* (1991) with Lilly's contraction (Lilly, 1992). The subgrid scale fluxes corresponding to the extended Boussinesq term, and corresponding to the heat and humidity sources are neglected. Filtering and differentiation operators commute for the uniform grid used.

From now onwards we drop the overbar ($\overline{\cdot}$) on filtered variables for simplicity. All variables are henceforth intended to be the filtered variables.

The equation of state is

$$p_{tot} = \rho_{tot} R_{tot} T_{v,tot} \tag{3.18}$$

where $R_{tot} = R_{air}(1 - Y + Y/\epsilon)$ is the effective gas constant of the moist air and $\epsilon = m_w/m_a = 0.62197$, where m_w and m_a are the molecular weights of water and air. After linearizing about the reference state, and noting that the Mach number is low, the equation of state becomes (Shirgaonkar & Lele, 2006*b*)

$$\frac{\rho}{\rho_{ref}} = -\left(-Y + \frac{Y}{\epsilon}\right) - \frac{T}{T_{ref}} \tag{3.19}$$

We have shown that the current set of equations incorporate the physics of buoyancy-inertia interaction that is not included in the traditional Boussinesq approximation (Shirgaonkar & Lele, 2006*b*). In Eq. 3.12, the term $\frac{\overline{D}\overline{\mathbf{u}}}{\overline{D}t}$ appears on the right hand side. To treat this term explicitly at each time step, the time-derivative part of it, $\frac{\partial \overline{\mathbf{u}}}{\partial t}$, is evaluated at the previous time step (Shirgaonkar & Lele, 2006*b*) as described in Section 2.5.

3.3 Microphysics model

The basic microphysics model is similar to that of Paoli *et al.* (2002) with some modifications [2]. For completeness we summarize the microphysics model here. To model the source terms

[2]Discussions with Dr. R. Miake-Lye from Aerodyne Inc. and Dr. S. Baughcum from Boeing contributed to these modifications.

ω_T and ω_Y, we use ice-vapor phase change thermodynamics. The process of early deposition on ice nuclei (IN) is not dealt with in the model, as it is complex and is the subject of other studies (Kärcher, 1994; Miake-Lye *et al.*, 1993; Brown *et al.*, 1996). Here we assume that in the interaction regime, the initial deposition has already taken place and all ice particles have a radius of $0.1\mu m$ which is comparable to that used by Paoli *et al.* (2002) and Kärcher (1994). Each ice particle is modeled as an ice nucleus of spherical shape and radius $15nm$ over which ice has grown. Re-nucleation is allowed, meaning that if a particle completely sublimates so that the IN is exposed, it still is capable of accumulating ice if it encounters favorable thermodynamic conditions. Our a posteriori estimate of the ice particle response time, $\tau_p = \rho_p d_p^2/18\mu$, is around $10^{-5}s$, which is small compared to the vortical flow time scales which are of the order of seconds. This allows us to model the ice particles as a dilute suspended phase which follows the local fluid velocity:

$$\frac{d\mathbf{x_p}}{dt} = \mathbf{u}(\mathbf{x_p}, t) \tag{3.20}$$

where $\mathbf{u}(\mathbf{x_p})$ is the fluid velocity evaluated at the particle location by interpolation. For small Biot numbers, conjugate heat transfer between the solid and vapor phase through conduction is neglected. However, the heat coupling due to phase change is taken into account, as it can be comparable to the temperature change caused by stratification. Mass transfer between the gas and ice phases, and the associated energy transfer through latent heat are modeled. Coagulation and sedimentation are neglected. Particle coagulation and coalescence are important in the very early regime via complex microphysical and chemical processes and have been the subject of extensive research (e.g. Brown *et al.*, 1996; Jacobson & Seinfeld, 2004; Jacobson *et al.*, 2005). Sedimentation is expected to be important in the late stage (beyond two minutes) when the particle size becomes comparable to those found in clouds (in the range $5-25\mu m$ depending upon the number densities involved and relative humidity) (Vaillancourt & Yau, 2000; Shaw, 2003).

We use a total of N_{comp} computational ice particles, each of which represents a collection of n_p physical ice particles, which is equivalent to tracking the zeroth and first moments of a group of n_p physical particles for each computational particle as shown by Paoli *et al.* (2002). The choice of these parameters was based on the following. For the initial nuclei emission index (EI) of $10^{15} particles/kg - fuel$, and fuel flow rate of $0.6855 kg/s/engine$ at the cruise conditions for a two-engine airplane, the estimated number of physical soot

particles per wing-span in the flight direction is $N_{comp} \times n_p = 2.7339 \times 10^{14}$. We choose N_{comp} as 10^6, giving us $n_p = 0.276 \times 10^9$, to within 1% error depending on the integer round-off involved in generating the ensemble of the particles. This choice of N_{comp} will be validated later in Section 4.9.3.

The particle radius r_p changes due to sublimation or freezing of ice/water vapor on the particle surface. The amount of water vapor freezing onto a single physical particle surface is given by

$$J = 4\pi r_p D G(r_p)(X - X_{sat})\rho_{tot} \tag{3.21}$$

where D is the diffusivity of water vapor in air, $G(r_p)$ is the collisional factor, and X is the mole fraction of water vapor in air. The subscript "sat" indicates saturation conditions. This expression is the effective mass flux (mass of water per unit time), calculated using Fick's diffusion law (Young, 1993). The diffusivity is obtained from the empirical relation (Pruppacher & Klett, 1978; Young, 1993)

$$D = 0.211 \times 10^{-4} \left(\frac{T_{tot}}{T_0}\right)^{1.94} \left(\frac{p_0}{p_{tot}}\right) \tag{3.22}$$

where $T_0 = 273.15K, p_0 = 101.325kPa$,and D is in m^2/s. The collisional factor is given by Kärcher (1994)

$$G(r_p) = \left(\frac{1}{1+Kn} + \frac{4Kn}{3\alpha}\right)^{-1} \tag{3.23}$$

Here $Kn = \lambda/r_p$ is the Knudsen number and the constant α is taken as 1 (Pruppacher & Klett, 1978)[3]. The mean free path of vapor molecules λ depends on the cruise temperature and pressure as

$$\lambda = \lambda_{std} \left(\frac{p_{std}}{p_{ref}}\right) \left(\frac{T_{ref}}{T_{std}}\right) \tag{3.24}$$

with $\lambda_{std} = 0.066\mu m$. For the cruise atmospheric conditions, λ is $0.2\mu m$, and the Knudsen number is in the range $0.1 - 2$, indicating near-continuum regime. The saturation conditions over ice are obtained from Murphy & Koop (2005):

$$p_{sat} = K\ exp(9.550426 - 5723.265/T_{tot} + 3.53068 log T_{tot} - 0.00728332 T_{tot}) \tag{3.25}$$

[3]Shirgaonkar & Lele (2006*a*) used $\alpha = 0.1$ following Kärcher (1994), hence the results therein differ from the results in this thesis.

where T_{tot} in (K) and p_{sat} in (Pa). K is a factor that accounts for Kelvin effect, and is given by

$$K = exp\left(\frac{2\sigma\mu}{r_p R T_{tot} \rho_p}\right) \tag{3.26}$$

The surface tension of ice-vapor interface σ is obtained by interpolating/extrapolating its values at 0^oC and -40^oC, which are 104 erg/cm^2 and 106 erg/cm^2 respectively. The saturation pressure curve is shown in Figure 3.4. The saturation vapor mole fraction is

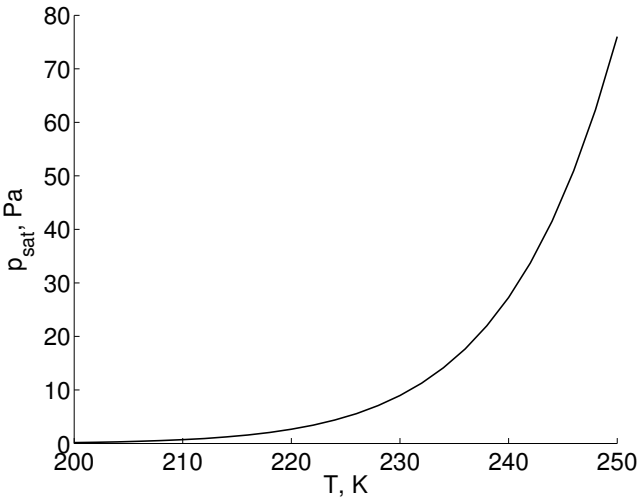

Figure 3.4: Saturation pressure of water vapor over ice, taken from Murphy and Koop (2005).

then obtained as

$$X_{sat} = \frac{p_{sat}}{p_{tot}} \tag{3.27}$$

and the actual mole fraction of water vapor as

$$X = \frac{Y/\epsilon}{1 - Y + Y/\epsilon} \tag{3.28}$$

Eq. (3.22)-(3.28) are used in Eq. (3.21) to find J. The radius of a particle changes according to

$$\frac{dr_p}{dt} = \frac{J}{\rho_p 4\pi r_p^2} \tag{3.29}$$

and the source of water vapor in a given grid cell is obtained by summing over all particles in that cell,

$$\omega_Y^{\Delta V} = \sum -\frac{n}{\Delta V}\frac{dr_p}{dt}\rho_p 4\pi r_p^2 \tag{3.30}$$

where $\Delta V = \Delta x \Delta y \Delta z$ is the volume of the grid cell. This source is then redistributed to the eight neighboring grid points (described soon in Section 3.4.5), which forms the Eulerian source term, ω_Y.

3.4 Numerical Method

Having formulated the equations that govern the contrail dynamics, we now discuss the numerical method to solve them. The flow equations form a coupled set of nonlinear partial differential equations of mixed parabolic-elliptic type. The microphysics equations form a set of nonlinear ordinary differential equations coupled to the flow equations. The coupling is two-way as there is mass and energy exchange between the two phases. The equations are discretized on a uniform grid with equal size in all three directions. The nominal domain size $(L_x, L_y, L_z) = (4b, 5b, 1b)$ and the nominal grid size $(N_x, N_y, N_z) = (256, 320, 64)$ is used for typical simulations. It should be noted that in z direction (which is the flight direction) the domain is one wing span long, and the simulations are temporal simulations beginning at 1 second after the aircraft passes through the domain. The domain is stationary with respect to the Earth's frame of reference. The temporal simulation is justified because the cruise speed (236.9 m/s) is much greater than the typical vortical flow speeds (approximately under 10 m/s).

3.4.1 Spatial discretization

The jet turbulence has a wide range of length scales. The near-spectral resolution of the sixth-order compact finite difference schemes (Lele, 1992) is desirable in this respect. The optimized version of Lui & Lele (2001) is used in all three spatial directions. Periodic boundary conditions are used in all directions. One could use spectral or pseudospectral method for spatial derivatives instead of finite difference schemes, but finite difference schemes were used here for their ability to handle nonperiodic boundary conditions, which is desirable for possible future applications of the LES code. The validity of the periodic boundary conditions will be examined later in Chapter 4. The derivative schemes for the first and second derivatives are described below for completeness.

First derivative

The general form of the compact scheme for the first derivative is

$$\beta_1 f'_{i-2}+\alpha_1 f'_{i-1}+f'_i+\alpha_1 f'_{i+1}+\beta_1 f'_{i+2} = c_1\frac{f_{i+3}-f_{i-3}}{6\Delta x}+b_1\frac{f_{i+2}-f_{i-2}}{4\Delta x}+a_1\frac{f_{i+1}-f_{i-1}}{2\Delta x} \quad (3.31)$$

The coefficients a_1, b_1, c_1, α_1, β_1 were optimized by Lui & Lele (2001) to obtain a formally sixth-order scheme with good spectral properties. The coefficients are listed below and the modified wavenumber is shown in Figure 3.5.

$$\begin{aligned} a_1 &= 1.367577724399269 \\ b_1 &= 0.8234281701082790 \\ c_1 &= 0.01852078348668660 \\ \alpha_1 &= 0.5381301488732363 \\ \beta_1 &= 0.06663319012388112 \end{aligned}$$

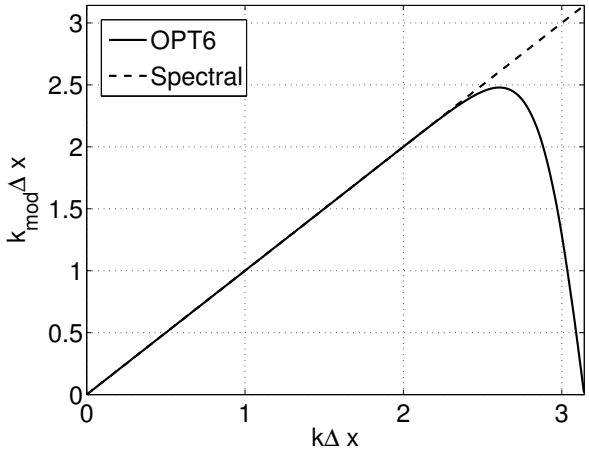

Figure 3.5: Modified wavenumber for the first derivative scheme OPT6 of Lui & Lele (2001)

Second derivative

The general form of the compact scheme for the second derivative is

$$\begin{aligned}\beta_2 f''_{i-2} + \alpha_2 f''_{i-1} + f''_i + \alpha_2 f''_{i+1} + \beta_2 f''_{i+2} &= c_2 \frac{f_{i+3} - 2f_i + f_{i-3}}{9\Delta x^2} + b_2 \frac{f_{i+2} - 2f_i + f_{i-2}}{4\Delta x^2} \\ &\quad + a_2 \frac{f_{i+1} - 2f_i + f_{i-1}}{\Delta x^2} \end{aligned} \tag{3.32}$$

Again, optimization of coefficients for sixth order formal accuracy and good spectral properties produced (Lui & Lele, 2001)

$$\begin{aligned} a_2 &= 0.3855624784762861 \\ b_2 &= 1.486194872274852 \\ c_2 &= 0.09330361806154306 \\ \alpha_2 &= 0.4442052422604100 \\ \beta_2 &= 0.03832524214593041 \end{aligned}$$

The modified wavenumber is shown in Figure 3.6.

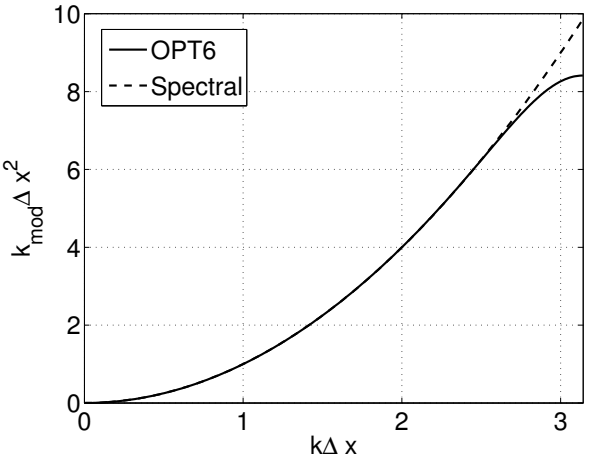

Figure 3.6: Modified wavenumber for the second derivative scheme OPT6 of Lui & Lele (2001)

3.4.2 Temporal discretization

For problems involving fine-scale features such as turbulence or acoustic waves the use of higher-order schemes provides definitive advantages by providing better numerical dissipation and dispersion properties. We use the 4th order Low Dissipation and Dispersion Runge-Kutta scheme (LDDRK4) of Stanescu & Habashi (1998). This is a two-step scheme designed for nonlinear problems and it contains five stages in the first step and six stages in the second step. The scheme requires low storage ($2N$ storage, where N is the number of degrees of freedom, i.e. number of variables $\times$ number of gridpoints) (Stanescu & Habashi, 1998). This scheme solves the ODE

$$\frac{du}{dt} = F(t, u) \tag{3.33}$$

by solving the discrete system

$$t_{i-1} = t^{n-1} + c_i \Delta t \tag{3.34}$$

$$\Delta u_i = \alpha_i \Delta u_{i-1} + \Delta t F(t_{i-1} u_{i-1}) \tag{3.35}$$

$$u_i = u_{i-1} + \beta_i \Delta u_i \tag{3.36}$$

Here, i is the number of stages in the step. The coefficients for the two stages are given in Table 3.4.

3.4.3 Convective terms and control of aliasing errors

The skew-symmetric form of the convective terms is used in the momentum equation,

$$\frac{1}{2}\frac{\partial}{\partial x_j}(u_i u_j) + \frac{1}{2} u_j \frac{\partial u_i}{\partial x_j} \tag{3.37}$$

This form is shown to achieve global energy conservation in the inviscid limit (Horiuti, 1987; Zang, 1991). Blaisdell *et al.* (1996) presented a theoretical analysis showing that aliasing errors are reduced by the skew-symmetric formulation. However, it should be noted that such an analysis is applicable only to one-dimensional problems because the derivative operators operate only in the direction of differentiation.

To keep aliasing errors low, a sharp Fourier spectral filter with the cut-off wavenumber $k\Delta x = 2.6$ corresponding to the peak of the modified wavenumber curve for the first

Table 3.4: Coefficients for the LDDRK4 scheme

Step 1

i	α	β	c
1	0.0	0.2687454388713438496	0.0
2	-0.60512264332862261228	0.8014706973220802933	0.2687454388713438496
3	-2.04375640234761394333	0.50515704269422722538	0.58522806929524303469
4	-0.74069990637544192841	0.56235680379000296407	0.68270664478424678821
5	-4.42317651302968168941	0.05900655127758823335	1.1646854837729261436

Step 2

i	α	β	c
1	0.0	0.11584888181285561688	0.0
2	-0.44127377153877382565	0.37287699051652864918	0.11584888181285561688
3	-1.073982008079781868	0.73795368921435295698	0.32418503640412806853
4	-1.7063570791256758809	0.57981109366311039538	0.61932082035177792368
5	-2.7979293162682443056	1.031284991300145194	0.80344726663359079059
6	-4.0913537120919160454	0.15	0.91841664452065965078

derivative scheme (Figure 3.5) is used for all dependent variables at every time step.

Scalar treatment

For the scalar advective term the same skew-symmetric form is used:

$$\frac{1}{2}\frac{\partial}{\partial x_j}(cu_j) + \frac{1}{2}u_j\frac{\partial c}{\partial x_j} \tag{3.38}$$

where c represents the scalar variable (in our case, water vapor fraction). This formulation of the nonlinear term conserves the total scalar variance. Also the filtering described above reduces Gibbs oscillations in the scalar field.

3.4.4 Poisson equation for pressure solution

The Poisson equation resulting from the momentum equation is of the form

$$\nabla^2 p = \nabla \cdot \mathbf{F} \tag{3.39}$$

where F is the sum of the advective, gravitational buoyancy, and inertial buoyancy (extended Boussinesq term) forces. This equation is solved using an FFT-based approach as

$$\widehat{p}(k) = -\frac{\widehat{\nabla \cdot \mathbf{F}}(k)}{k_x^2 + k_y^2 + k_z^2} \tag{3.40}$$

where k_x, k_y, k_z are the modified wavenumbers corresponding to the first derivative scheme. Since the modified wavenumber approaches zero near the high-wavenumber end (Figure 3.5), the pressure solution would be dominated by noise in this wavenumber range. The sharp spectral filter mentioned in Section 3.4.3 prevents this.

3.4.5 Microphysics Solution

The ODE governing the position of each computational particle is

$$\frac{d\mathbf{x_p}}{dt} = \mathbf{u}(\mathbf{x_p}, t) \tag{3.41}$$

where $\mathbf{u}(\mathbf{x_p}, t)$ is the fluid velocity evaluated at the particle location by interpolation. Trilinear interpolation is used for its conservative and monotonic properties. Equation (3.41)

is integrated using the LDDRK scheme. The equation for particle growth is

$$\frac{dr_p^2}{dt} = \frac{2D}{\rho_p} G(r_p)(X - X_{sat})\rho_{tot} \tag{3.42}$$

This equation is analytically integrated for each computational particle over the time step Δt assuming the molar fractions X and Knudsen number effect $G(r_p)$ remain constant over the time step. This is equivalent to the Euler explicit scheme for r_p^2. To avoid non-physical values of r_p^2, the maximum change in r_p^2 over one time step is restricted such that r_p^2 does not fall below $r_{p,c}^2$, where $r_{p,c} = 15nm$ is the ice nucleus core radius. This time advancement procedure is validated later in Chapter 4 through time-step convergence study for the contrail simulation.

The evaporation/freezing of the particles gives rise to water vapor source/sink in the humidity transport equation. This Eulerian source term is evaluated by summing the particle mass changes over all particles in a grid cell, and then distributing this total mass of water vapor to the vertices of the grid cell in proportion to the proximity of a particle to any particular vertex. For instance, if a particle located at (x_p, y_p, z_p) experiences a mass change of Δm_p, then will contribute a water mass of $\Delta m_{p,i}$ $(i = 1, ..., 8)$ to the 8 nearest vertices (x_i, y_i, z_i) according to

$$\Delta m_{p,i} = \Delta m_p \frac{(\Delta x - |x_p - x_i|)(\Delta y - |y_p - y_i|)(\Delta z - |z_p - z_i|)}{\Delta V} \tag{3.43}$$

where ΔV is the volume of that grid cell. This volume-weighted Lagrangian-to-Eulerian redistribution scheme guarantees conservation of the total amount of water between the two phases.

3.4.6 Code performance

The contrail LES code we have developed is parallel and uses the Message Passing Interface (MPI) library. The domain decomposition is primarily in the x direction, except when evaluating x-derivatives, in which case we transpose the data to decompose the domain in the y direction. For the Poisson solver, the FFTW (Fastest Fourier Transform of the West, www.fftw.org) library was used.

The total time matching code (does not include the pre- and post-processing) line count

was approximately 9546 lines. The Lagrangian particle tracking and microphysics module was approximately 1124 lines, i.e. 11.8% of the total code. The code was run on a cluster of 1.5 GHz Intel® Itanium® 2 processors running SuSE Linux and using Myricom's Myrinet cluster interconnect network. The code was timed for wall-clock time, and for a typical contrail computation with 5.24 million mesh points and 1 million Lagrangian particles, it required 31.67 sec/timestep on 64 processors. The transposition operations involved while computing derivatives, and the three-dimensional FFT operation are the most CPU-intensive tasks. Without the Lagrangian microphysics module, the code took 29.81 sec/timestep. This indicates that only 5.87% of the computation time was taken up by the Lagrangian module. This is a highly desirable performance measure because one of the main advantages of the mixed Lagrangian-Eulerian approach is to be able to compute ice particle statistics accurately but efficiently. The above performance suggests that we can afford to increase the total number of Lagrangian particles if we either need more higher order moments, or need longer domain in the flight direction.

A very limited numerical experimentation was done to get an idea of the parallel scaling of the code. There are two types of parallel scalings – strong scaling and weak scaling. Strong scaling means we keep the problem size fixed and vary the number of processors (also called speed-up). Weak scaling means we vary the number of processors and problem in such a way that the problem size per processor is constant (also called scale-up). Weak scaling is most interesting for problems with linear computational complexity and very large codes. For the present simulations we only did a limited evaluation of the strong scaling by performing two simulations with 32 and 64 processors keeping the problem size constant. The wall-clock time required were 75.49 sec/timestep and 43.49 sec/timestep respectively. This gives roughly 15% loss of speedup during this increase of processors by a factor of two. We attribute it mainly to the fact that the load is not balanced in the Lagrangian solver, an issue that can be improved in future. But since we typically use 64 processors for most of our simulations, this scaling is considered satisfactory for the current purposes.

Chapter 4

Verification and Validation

This chapter presents verification and validation of the model and the numerical method. Model validation means ensuring that the model replicates the actual physics to a desirable level of accuracy. From another viewpoint, it means evaluating the level of accuracy to which the simulation replicates a given base result. Usually the base result is a physical experiment, or it can also be previously validated and verified simulations. Verification means a given model and numerical method produces what we *intend* it to produce, i.e. numerical errors behave "well" and do not contaminate the solution to unacceptable levels. Thus, validation refers to solving the right equations and verification refers to solving the equations correctly. In practice, verification and validation go hand in hand and in this chapter, the categorization into either one of them is fuzzy for some of the tests. More precise classification and definitions of these concepts can be found in Roache (1998) and Oberkampf & Trucano (2002).

First we present model validation where simulation results will be compared to experiments of stratified wake descent, homogeneous isotropic turbulence, and then to simulations of ice microphysics by two other more sophisticated models used by Boeing and Aerodyne Research Inc. We will also present comparison with a passive scalar simulation from a different code used by Boeing. A-*posteriori* validation of the extended Boussinesq model was presented in Chapter 2.

Then we present verification of the model and the numerical method. Convective and buoyancy terms are tested. We choose an optimal domain size for the vortex wake simulations to keep the spurious effects of periodic boundary conditions small. Convergence with respect to the number of Lagrangian computational particles will be verified so as to

sufficiently capture the statistical distribution of ice particle size. Grid sensitivity of the simulation results will be discussed.

4.1 Laminar wake descent in a stratified atmosphere

The test case of a counter-rotating vortex pair descent in a stably stratified atmosphere is simulated to test the model. The vortices were modeled as Lamb-Oseen vortices with core diameter $r_c^* = 0.25\ b_o^*$ where b_o^* is the initial vortex separation. (This matches with Spalart's (1996) value of the parameter $\sigma = r_c^*/b_o^* = 0.25$.) This and other physical parameters were matched with those used for simulations by Spalart (1996) and towing tank experiments by Sarpkaya (1983). The circulation-based Reynolds number was taken as $Re_\Gamma = 6.366 \times 10^3$, the initial vortex separation b_o^* was taken as 47.24 m, the vortex pair descent speed $U^* = 1.32\ m/s$, and the Brunt-Väisälä frequency $N^* = 0.0279\ rad/s$. This resulted in the nondimensional parameters $N = N^* b_o^*/U^* = 1$ and Froude number $Fr = U^{*2}/b_o^* g^* = 3.74 \times 10^{-3}$, as in the case of Sarpkaya (1983). Time is nondimensionalized by b_o^*/U^* and the vertical position of vortices by b_o^*.

The descent of the vortex pair location (defined as the location of peak vorticity) is tracked and is shown in Figure 4.1. For most of the initial descent all three results match very well. In particular, the location of the descent arrest is captured well by the simulations. In the later stage (near $t = 3$) the results do not match so well. We attribute this mismatch to the turbulence that may exist in the experiments and to the different wing types between the simulations and the experiments (delta wing vs. rectangular wing). The qualitative behavior between our simulations and those of Spalart is in agreement, but quantitative differences exist in the late stage probably due to the fact that we use the extended Boussinesq approximation with compressible formulation for stratification as explained in Chapter 2 whereas Spalart uses the traditional Boussinesq approximation and incompressible formulation for stratification. Also, Spalart does not provide a definition of the vortex locations hence it is assumed here that he means the vortex centers of the primary vorticity. Other possible choices may exist such as the centroid of the total vorticity including the primary and the secondary (baroclinic) vorticity. The detection of vortices is susceptible to errors especially due to the emergence of fine baroclinic vorticity structures. Sarpkaya's experimental values for vortex pair location are visually detected in his experiments.

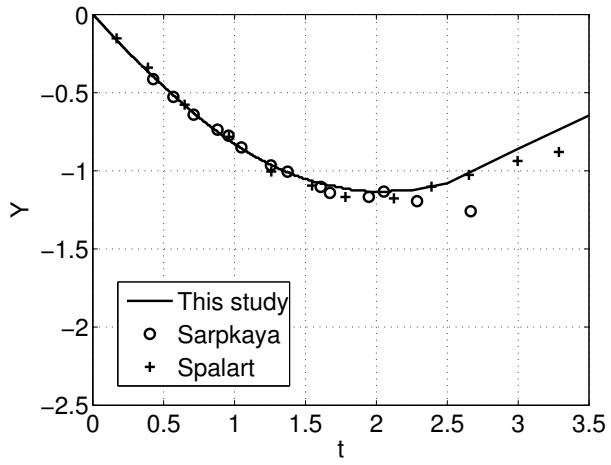

Figure 4.1: Stratified vortex pair descent rate comparison with experiments by Sarpkaya (1983) and simulations by Spalart (1996).

4.2 Subgrid scale model

To test the implementation of the subgrid scale model, the experiment of Comte-Bellot & Corrsin (1971) is chosen for comparison. LES of homogeneous isotropic turbulence was performed on a 32^3 grid with $Re_\lambda = 71.6$. The initial energy spectrum was matched with that of Comte-Bellot & Corrsin (1971) at station $x/M = 42$, where M is the grid spacing in their experiment. The comparison of turbulent kinetic energy (TKE) decay and the energy spectrum is shown in Figure 4.2 and good agreement with experiments is observed.

4.3 Microphysics model

A comparison study was conducted in collaboration with Boeing and Aerodyne Research Inc. to compare three different microphysics models from Boeing, Aerodyne and Stanford (the current work). The goal was to compare the microphysical properties resulting from using these three models in a box model calculation. Box model calculation here means the microphysical properties are computed in a box in which there is no flow or humidity fluctuations to start with. It is used as a means to isolate the microphysics from the fluid dynamics in a test setting and study the microphysics. The parameters were selected to match the typical thermodynamic and atmospheric conditions encountered in an aircraft

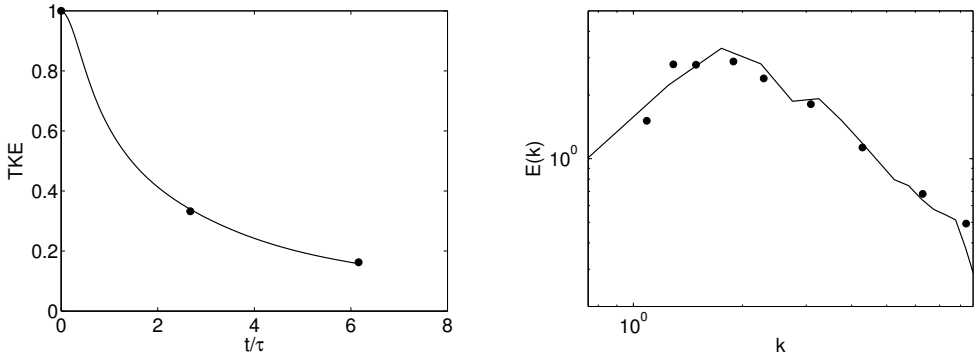

(a) Turbulent kinetic energy

(b) 3D Energy Spectrum at the x/M=98 station in CBC

Figure 4.2: Comparison of LES results with experiments of Comte-Bellot and Corrsin (1971) (CBC). Lines: LES, Symbols: CBC

contrail at cruise. The comparison was conceived and carried out by Boeing with the results from the respective models provided by us and Aerodyne Research Inc. Here we reproduce the digitized version of their plots by permission from Boeing and Aerodyne.

The Boeing model uses the binned microphysics approach (Jensen *et al.*, 1994; Toon *et al.*, 1989), the Aerodyne model computes the ice particle properties in trajectories of fluid parcels, and the current Lagrangian model as described before computes growth of individual ice particles. Figure 4.3 compares key microphysical properties from the three models for the case with parameters matching with our contrail baseline simulation. The ambient temperature, pressure and relative humidity were 220 K, 240 hPa and 110% respectively. The initial ice particle concentration was taken as 400 $/cc$ and the particles are initially monodispersed with radius 0.5 μm. It can be seen that the overall agreement is good, especially between the Stanford and Aerodyne models. Other cases were also compared by Boeing to see other effects such as temperature and humidity variation, initial ice particle size and number density, Kelvin effect for saturation pressure, and time-varying ambient temperature.

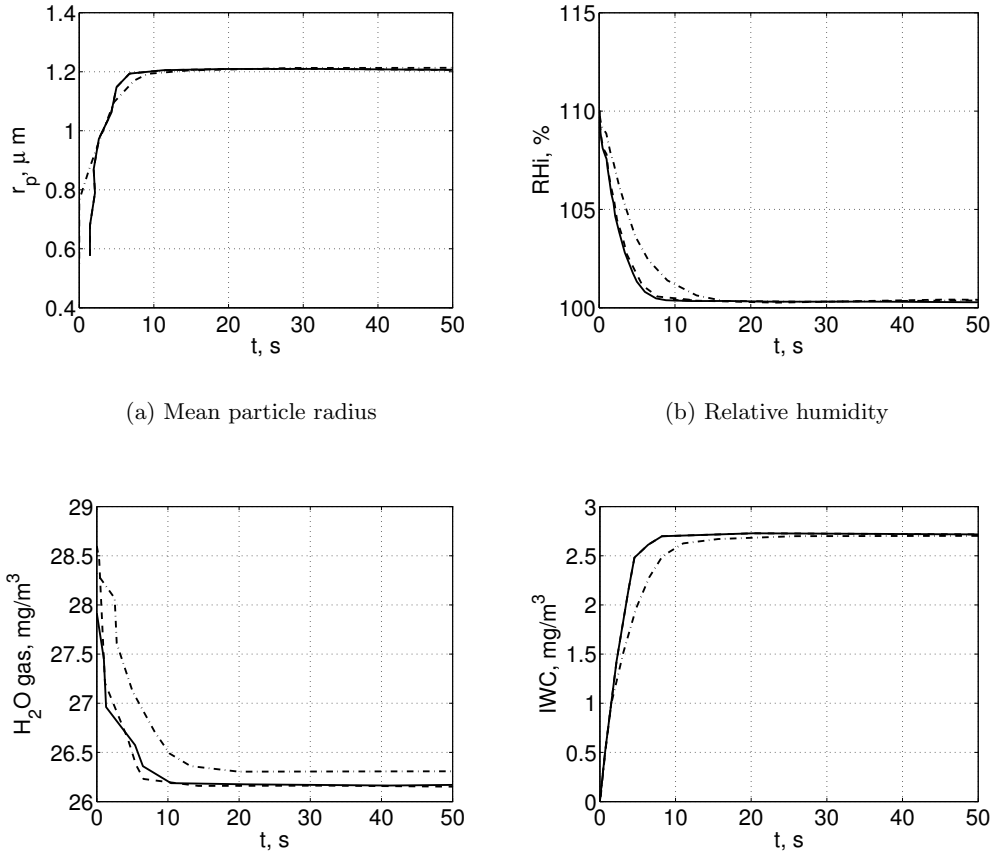

(a) Mean particle radius

(b) Relative humidity

(c) Water vapor content

(d) Ice water content

Figure 4.3: Comparison among the microphysical models from —, this study; – –, Aerodyne; and –·–, Boeing for the box model baseline test case. Irregularities in the curves at $t < 10$ s are due to digitization errors.

4.4 Passive scalar transport

We carried out LES of passive scalar (tracer) in the wake of a Boeing 767 (henceforth referred to as B767) aircraft, starting at 5 wing spans behind the aircraft. The scalar in this case is representative of a passive tracer in the engine exhaust. The initial conditions at 5 wing spans were provided by Boeing (used here by permission). They are shown in Figure 4.4. The physical conditions were matched with the baseline case to be described later in Chapter 6, since this case is later used for the parametric variation in the $3D$ LES. The

domain size $(L_x, L_y, L_z) = (4b, 5b, 1b)$ and grid size $(N_x, N_y, N_z) = (384, 480, 96)$ is used. Conservation of total scalar is satisfied to within 0.15% of the initial total scalar amount (Figure 4.5)[1]. The small non-conservation is attributed to discretization errors since the scheme is not designed to enforce strict scalar conservation. Instead, strict scalar variance conservation has been enforced through the skew-symmetric form of the convective terms to maintain stability. We have tested the scalar variance conservation in the inviscid limit by performing simulations at infinite Reynolds number of homogeneous isotropic turbulence. The temporal evolution of the scalar is depicted in Figure 4.6.

Eulerian vs. Lagrangian transport of passive scalar

In this study we use the Eulerian approach for scalar transport and Lagrangian approach for ice particles. Hence it is necessary to verify that these two approaches provide consistent results. For this two separate simulations of the B767 case – one using Eulerian scalar transport and another using Lagrangian transport – were carried out. The scalar field 75 wingspans behind the aircraft are compared in Figure 4.7. The quantitative comparison of scalar values along two different horizontal lines – one passing through the vortex cores and another below the vortex cores – is done in Figure 4.8. It is seen that the overall agreement between the two approaches is good. Strictly speaking, the two approaches can not be directly compared because the Eulerian approach models the sub-grid scalar fluxes explicitly which the Lagrangian approach does not. Instead, the Lagrangian approach indirectly incorporates partial effects of subgrid fluxes partly because it is coupled to the filtered velocity, and partly due to the interpolation operations between the Eulerian grid and the Lagrangian particle locations. The goal here is to ensure that these difference do not alter the results by large amounts. This is an important step because the small scale scalar fluctuations can affect the ice particle growth. Qualitative results from Figure 4.8 indicate that the two approaches behave similarly as far as scalar transport is concerned. The Lagrangian approach was chosen to gain accuracy in terms of particle statistics.

[1]Similar tests for the contrail calculations gave conservation of total water (vapor and ice) and total thermal energy to within 1% and 2.2% respectively. A.A.S. thanks Ankit Bhagatwala for his help in verifying these tests on conservation.

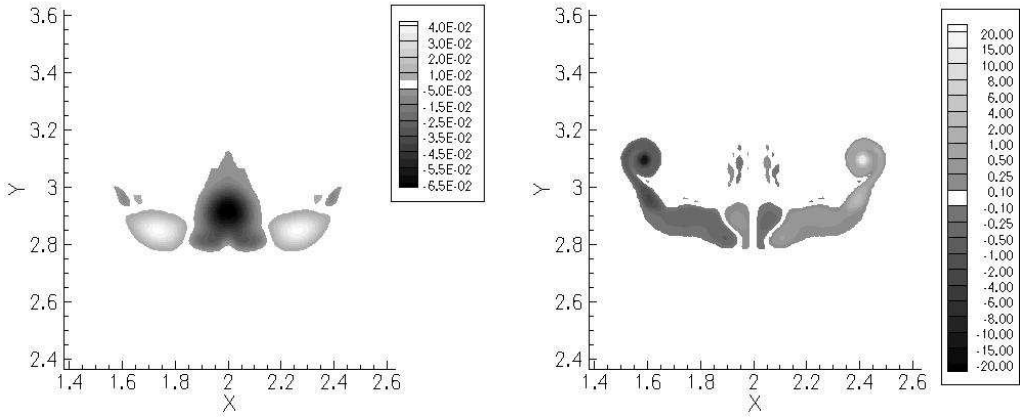

(a) Axial velocity

(b) Axial vorticity

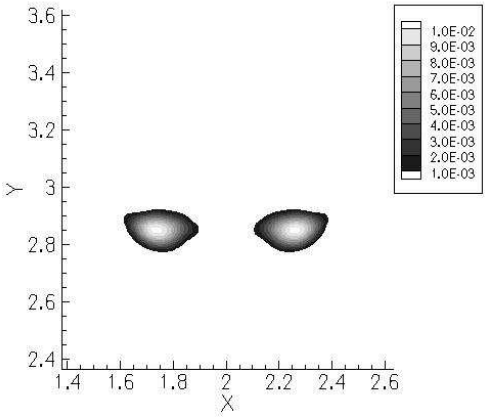

(c) Passive scalar

Figure 4.4: Initial flowfield at 5 wingspans for tracer validation runs. It is obtained by interpolation of and turbulence addition to the data provided by Boeing which was obtained by RANS simulations performed by Boeing. All variables are normalized.

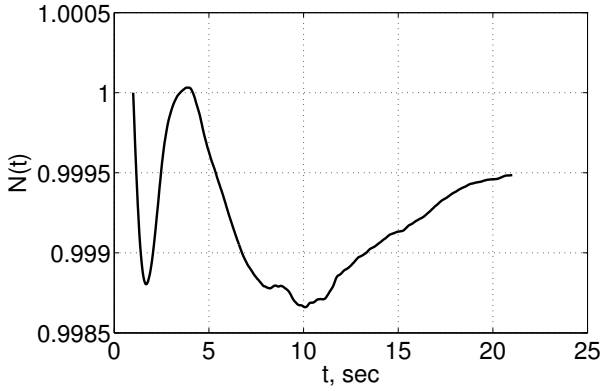

Figure 4.5: Plume-integrated passive scalar normalized by the initial value.

Comparison with Boeing simulations

We compared the passive scalar LES with LES performed by the West Virginia University group and provided to us by Boeing. Only a limited comparison is shown here (Figure 4.9), namely the scalar contours at 100 wing spans.

4.5 Convective terms: Equipartition of energy

In a non-physical numerical experiment with an incompressible fluid where certain amount of kinetic energy is contained in a closed or periodic domain, and there is no viscous dissipation, the distribution of energy in the wave space asymptotes to the distribution dictated by the equipartition theorem. Both kinetic energy and passive scalar spectra equilibrate to the k^2 spectrum indicating that all wavenumbers possess equal energy. This behavior is produced by the nonlinear nature of the advection terms in the Navier-Stokes equations. Such a numerical experiment was performed on a 32^3 grid where the initial energy and passive scalar spectra were the DNS spectrum.

The tail-off at the high end of the spectrum is caused by the low-pass filtering described in Section 3.4.3 applied at each time step to keep the discrete Poisson equation well-behaved in the code. The total kinetic energy and scalar variance in the domain was found to be conserved by the numerical method, with a small decay of roughly 0.028% in kinetic energy and 0.041% in scalar variance caused by the filtering. The skew-symmetric formulation of the nonlinear terms along with the central, non-dissipative spatial discretization scheme

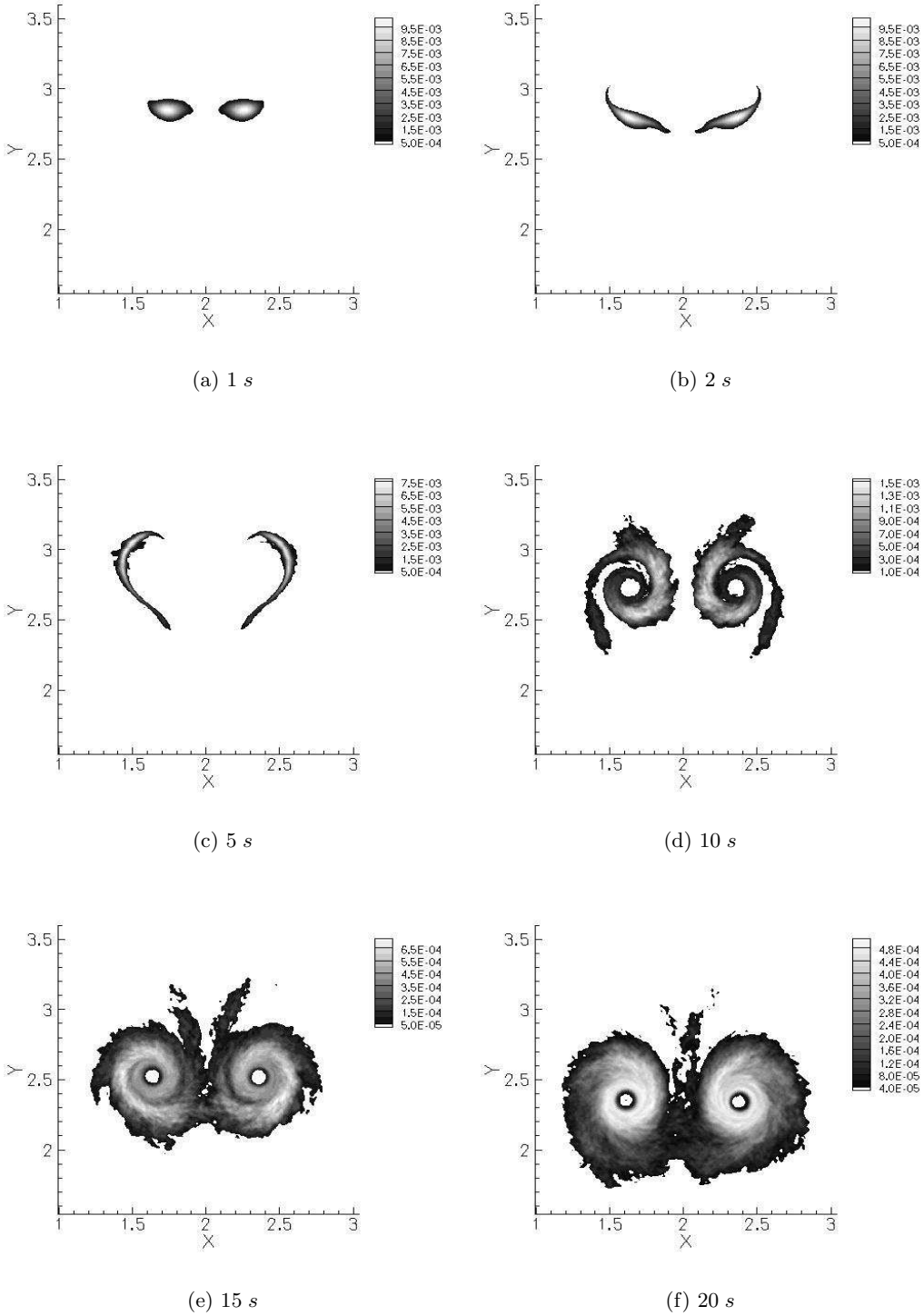

(a) 1 s (b) 2 s

(c) 5 s (d) 10 s

(e) 15 s (f) 20 s

Figure 4.6: Evolution of passive scalar for the validation case.

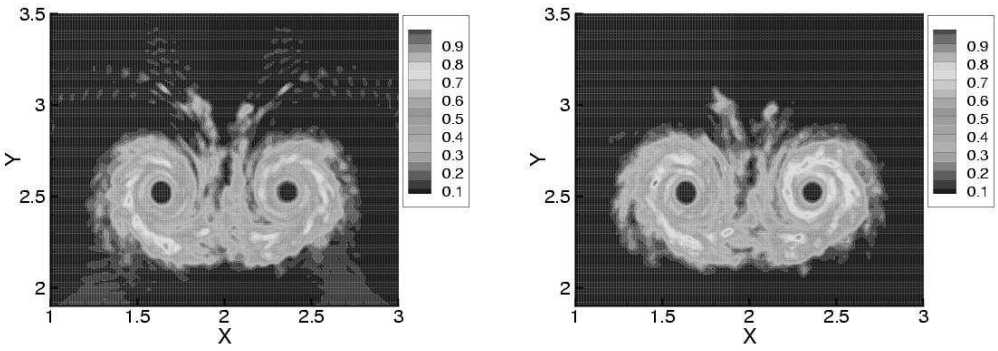

(a) Eulerian (b) Lagrangian

Figure 4.7: Normalized tracer computed in Eulerian and Lagrangian manners at 75 wing spans.

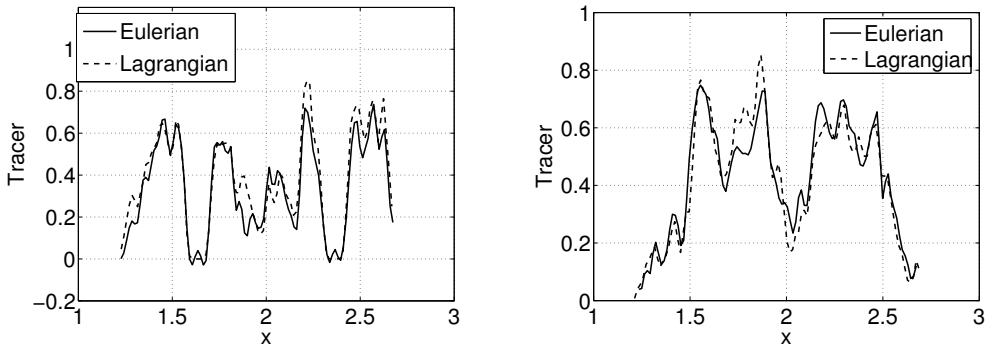

(a) $y = 2.518$ (b) $y = 2.294$

Figure 4.8: Line plots of tracer along the horizontal line passing through the vortex cores ($y = 2.518$) and away from the cores ($y = 2.294$).

ensure this conservation within the temporal errors.

4.6 Buoyancy terms: Rayleigh-Benard Instability

To test the Buoyancy terms the test problem of periodic Rayleigh-Benard instability in two dimensions ($x - y$) is considered. The description of the problem with detailed analysis

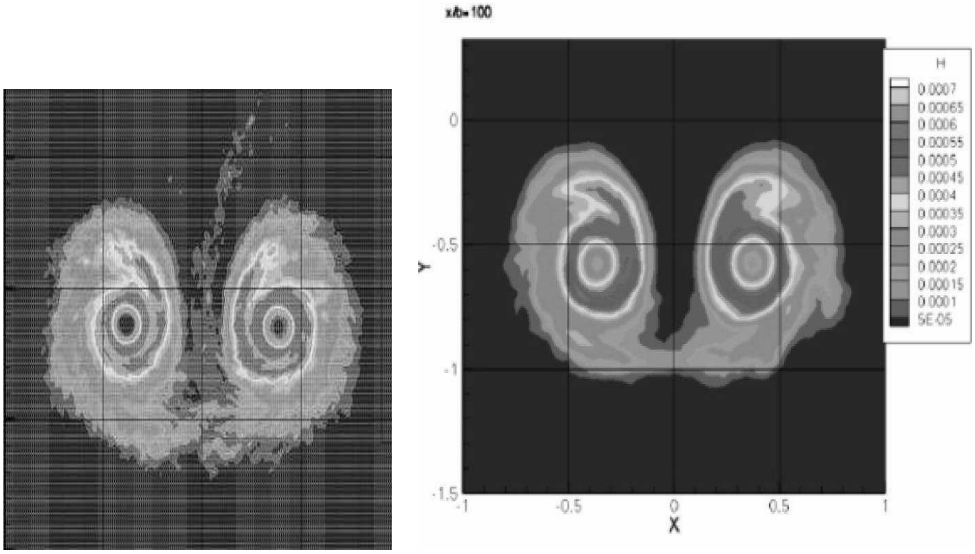

(a) This study (b) WVU LES

Figure 4.9: Passive scalar at 100 wing spans from this study and from LES by West Virginia University group (Huebsch & Lewellen, 2006).

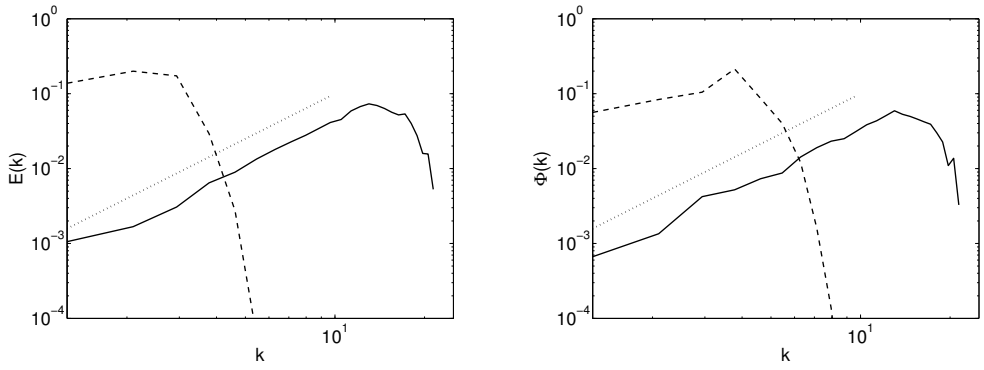

(a) Turbulent kinetic energy (b) Passive scalar

Figure 4.10: Spectra at approximately 8.27 eddy turnover times: -, initial condition: –.

can be found in Chandrasekhar (1981). A rectangular box of length $L = 1$ in both x and y directions, containing an incompressible fluid, and extending up to infinity in the

z-direction is considered. A background unstable stratification is imposed. The initial velocity and density fields are taken as isolated Fourier modes corresponding to wavelength L:

$$\begin{aligned} u &= \hat{u}\, cos(2\pi y)\, sin(2\pi x)\, e^{st} \\ v &= \hat{v}\, sin(2\pi y)\, cos(2\pi x)\, e^{st} \\ p &= \hat{p}\, cos(2\pi y)\, cos(2\pi x)\, e^{st} \\ \rho &= \hat{\rho}\, sin(2\pi y)\, cos(2\pi x)\, e^{st} \end{aligned} \tag{4.1}$$

where ρ is the perturbation (i.e. nonhydrostatic) density. The governing equations for analytical solution are the nondimensional, linearized Navier-Stokes equations with Boussinesq approximation,

$$\frac{\partial u}{\partial t} = -\frac{\partial p}{\partial x} + \frac{1}{Re}\nabla^2 u \tag{4.2}$$

$$\frac{\partial v}{\partial t} = -\frac{\partial p}{\partial y} - \frac{\rho}{Fr} + \frac{1}{Re}\nabla^2 v \tag{4.3}$$

and the incompressibility constraint imposed as the Poisson equation for pressure:

$$\nabla^2 p = -\frac{\partial \rho}{\partial y} g \tag{4.4}$$

We also have a density transport equation:

$$\frac{\partial \rho}{\partial t} = -\frac{Ra\ Fr}{Re^2\ Pr}\ v + \frac{1}{Re\ Pr}\nabla^2 \rho \tag{4.5}$$

where the Rayleigh, Froude, Reynolds and Prandtl numbers are taken as $Ra = 20,000$, $Fr = U^2/Lg = 0.10194$, $Re = 200$, $Pr = 0.71$ respectively. Using Chandrasekhar's 1981 analysis it can be shown that this set of values gives an unstable system ($s > 0$). Note that this set is arbitrarily chosen and it constitutes just one of the infinitely many combinations of the above nondimensional parameter values that give an unstable system. The velocity scale U is arbitrarily chosen as 1. Incompressibility requires $\hat{u} = -\hat{v}$. The current problem setup has periodic boundary conditions with period $L = 1$ in x and y directions. The solution does not vary in the z direction. The above governing equations can be analytically solved

to obtain (see Chandrasekhar (1981) for solution details) $s = 0.12345$. The full nonlinear equations were numerically solved for small amplitudes on a 32×32 grid and the numerical solution for amplitude growth is compared with the analytical solution in Figure 4.11.

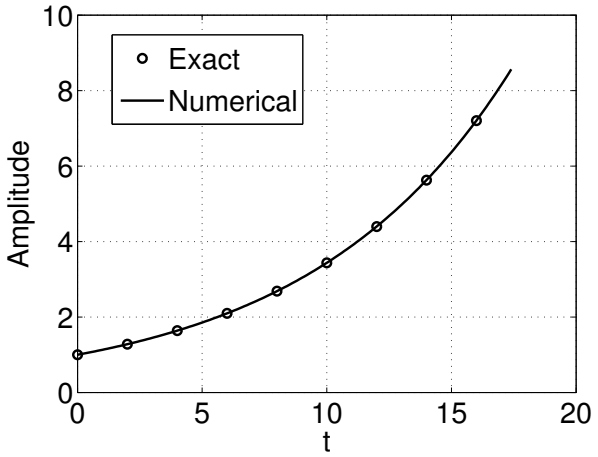

Figure 4.11: Growth rate for the Rayleigh-Benard instability.

4.7 Effect of boundary conditions

We use periodic boundary conditions in this study for their simplicity of implementation and also because they allow the use of fast FFT-based Poisson solver. This means that there are other periodic counter-rotating vortex pairs adjacent to the actual domain. A velocity correction was added to the vertical component of velocity to make the average vertical velocity equal to $-\pi I_o/6L_x^2$ (Spalart, 1996) where $I_o = \Gamma b$ is the initial impulse of the vortex pair and L_x is the periodicity length in x. This correction produces the correct descent rate of an isolated vortex pair.

We performed three different simulations of a vortex pair descending in a non-stratified atmosphere with $L_x = 3b$, $4b$ and $5b$ and tracked the descent rate in each case for one convective time scale. For the case of a B767 type aircraft one timescale is approximately 25 s. The error in the descent was observed to drop below 0.2% for $L_x = 4b$ (Figure 4.12) hence this domain length was chosen for the subsequent simulations. Note that although the error seems to accumulate in time, in the long run the contrail is dominated by stratification and this accumulation is expected to be non-monotonic due to the Brunt-Väisälä oscillations,

and hence small.

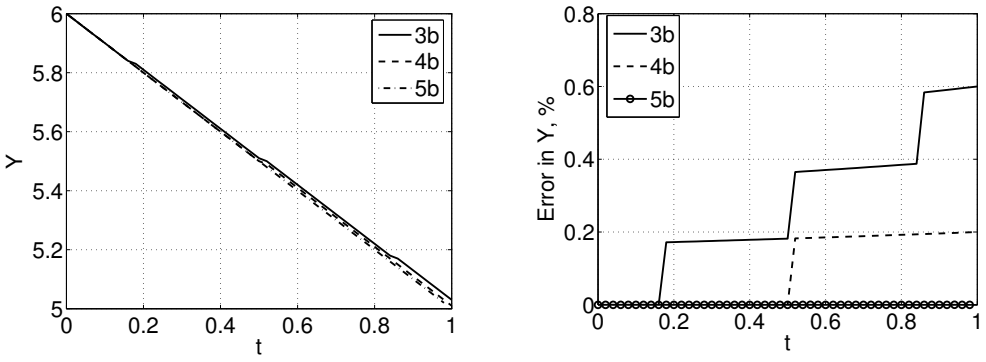

(a) Descent (b) Error

Figure 4.12: Evaluation of domain length on wake descent. The step-structure is an artifact of the vortex detection algorithm.

4.8 Jet stage

Selected simulations in this study will use synthetically generated turbulent initial conditions instead of the initial fields generated using the initial data provided by Boeing from their RANS simulations. It is instructive to understand the effect of these two different ways of generating the initial conditions on contrail properties. For generating the synthetic initial conditions, we produce a well-developed, turbulent pair of jets without ice particles. This stage of obtaining the developed turbulent jets is hereafter referred to as the jet stage. The procedure used to generate the initial turbulent jet was as follows. A homogeneous turbulent velocity field was generated and then localized in the jet region and superimposed on the jet axial velocity which was modeled by a Gaussian. The fluctuation velocity was scaled so that it was 1% of the local mean axial velocity of the jet. The resultant velocity field was projected on to a divergence-free discrete function space. Then the jet was allowed to evolve until the turbulence was well-developed.

The testing of the jet stage of the simulation was carried out on a smaller domain to keep cost reasonable. Here we report quantitative results of the temporal jet LES to assess the development of turbulence and ice particle statistics. Ice particles are also included here,

since including them will give us valuable information about the convergence of particle statistics under jet turbulence.

4.8.1 Turbulence development

First, a jet LES with no ice particles was allowed to develop. The spectra of turbulent kinetic energy (TKE) and scalar are shown in Figure 4.14. The vorticity and scalar fields are shown in Figure 4.14.

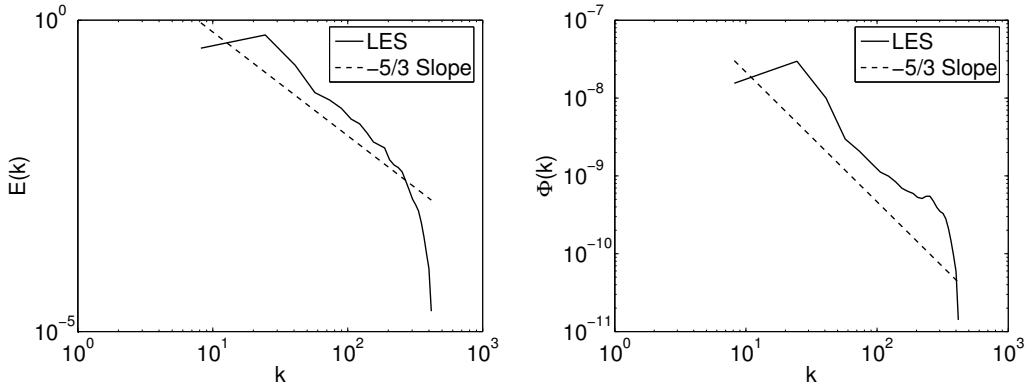

(a) Turbulent kinetic energy

(b) Scalar

Figure 4.13: Spectra at $t = 0.9$ for the temporal jet LES.

Figure 4.15 shows the centerline decay of axial velocity and scalar, and the spreading of the velocity half-width $r_{1/2}$. Figure 4.16 shows the scaled velocity and scalar profiles at different times of jet development where the velocity and scalar are scaled by the centerline values and the radial distance by $r_{1/2}$.

4.8.2 Evaluation of ice particle statistics

Another jet LES was performed with approximately 0.5 million computational ice particles injected into the jet. The atmosphere was unstratified, and ambient relative humidity was set to 110%. The jet carried no additional water vapor, i.e. a constant vapor mass fraction was specified over the entire domain including the jet region. This choice is made in order to represent the stage after the first few seconds of jet dilution, where the atmospheric water vapor is the dominant source of vapor. The radial distribution of particles within the jet

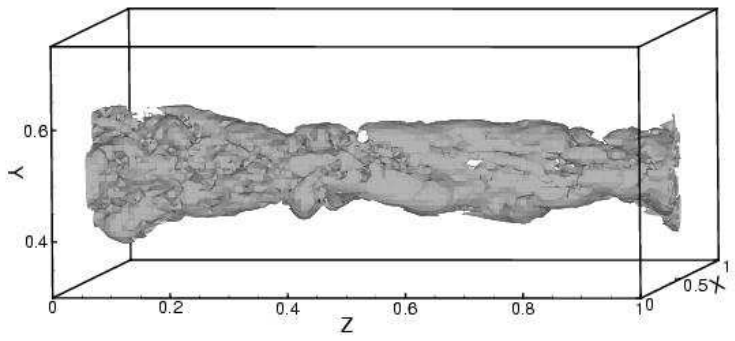

(a) Isosurface of vorticity magnitude 160.

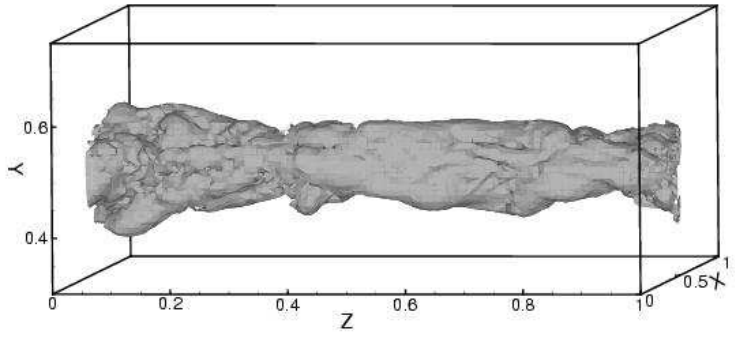

(b) Isosurface of scalar 0.0005.

Figure 4.14: Turbulent jet at $t = 0.9$ from the temporal LES.

was proportional to the local jet axial mean velocity. As before, the simulation was run up to $t = 0.9$. Figure 4.17 shows the velocity and ice particle configuration at $t = 0.9$. The conservation of total water (vapor plus ice) is maintained by the numerical method within a small error, as seen from Figure 4.18. The percentage relative error in conservation, ϵ is

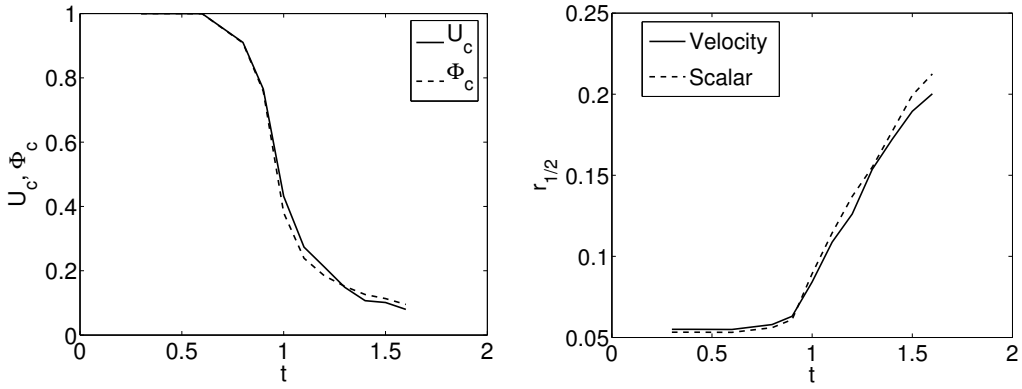

(a) Centerline values

(b) Half widths

Figure 4.15: Jet spreading characteristics from the temporal LES.

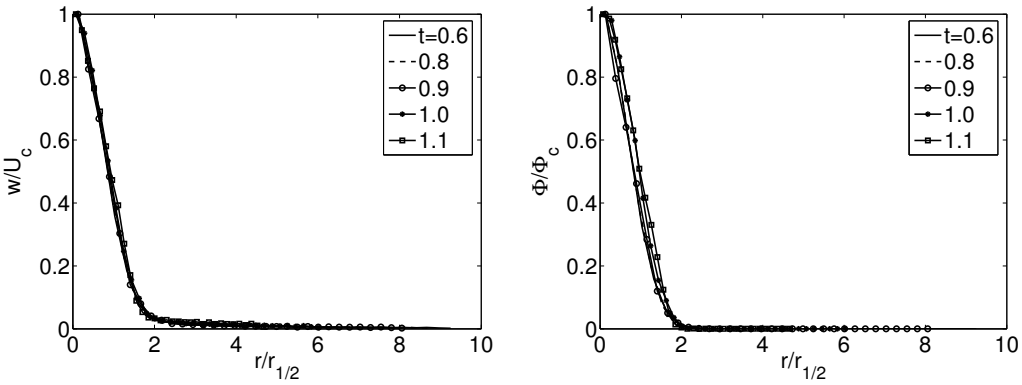

(a) Axial velocity

(b) Scalar

Figure 4.16: Radial profiles at various times. Velocity and scalar are scaled by their centerline values, and radial distance by the jet half-width.

defined as

$$\epsilon = \frac{|M_w(t) - M_w(t=0)|}{M_w(t=0)} \times 100 \quad \% \tag{4.6}$$

where M_w is the domain-integrated water mass.

To test the sensitivity of statistics to the particle sample size we chose four probe locations in the domain. They were located on the horizontal line $y = 0.5$ at $x = 0$, 0.5 $r_{1/2}$,

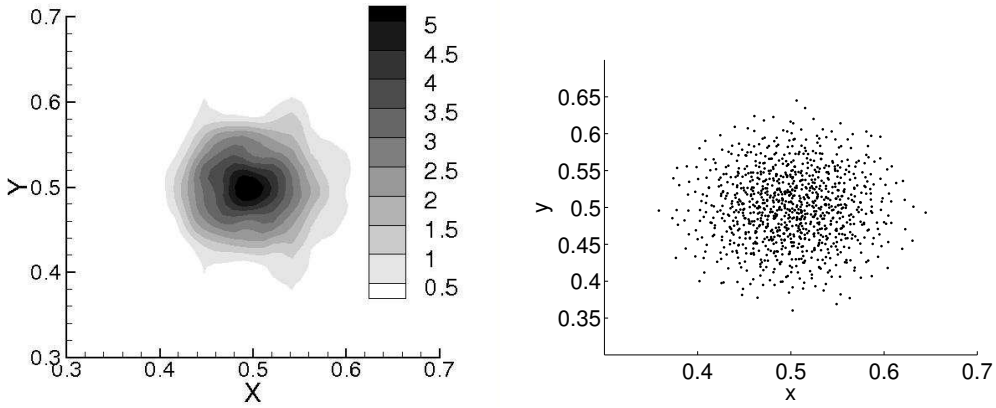

(a) Axial velocity

(b) Computational particles representing ice particles

Figure 4.17: Axially averaged view of the jet at $t = 0.9$. Only a homogeneously chosen subset of the total 0.5 million particles is shown to maintain clarity.

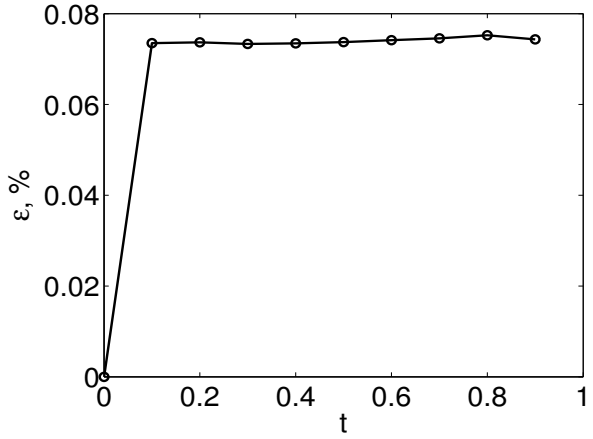

Figure 4.18: Error in the conservation of total (vapor plus ice) water in the jet LES.

$r_{1/2}$, and 2 $r_{1/2}$ in order to sample different physical conditions from the center of the jet to its boundary. Here $r_{1/2}$ is the jet half-width i.e. the radial distance at which the jet mean (ensemble averaged) velocity reduces to half its centerline value. Note that the jet centerline is at $(x, y) = (0.5, 0.5)$ and in our notation r indicates the radial distance from the centerline. Ensemble averages were calculated by averaging in a cylindrical shell with the

required radius with the shell thickness equal to $2\Delta x$. This choice of thickness is made so that we evaluate the particle statistics at a resolution consistent with that of the flow. The probe location with respect to the jet velocity profile and particle number density profile is shown in Figure 4.19.

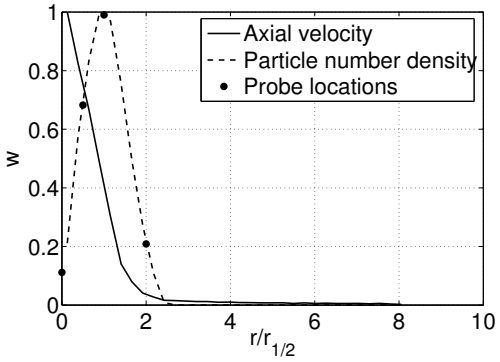

Figure 4.19: Radial profiles of jet axial velocity and particle number density at $t = 0.9$. Symbols: Probe locations.

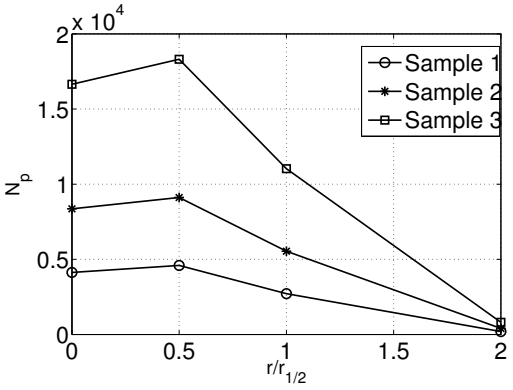

Figure 4.20: Plot showing the number of particles N_{p1}, N_{p2}, N_{p3} in the three different particle samples used at each probe for the convergence study. The x-locations of symbols indicate probe locations. The three samples correspond to taking every 4th, every 2nd, and every particle in the tube.

For the early-stage contrails ($20s$) the long-range Crow instability is not prominent hence the axial variations of the mean flow are small. Thus the flight direction can be considered a homogeneous direction along which averaging can be done. Our goal in the following is to ascertain that the Lagrangian statistics computed at a similar resolution as the flow in the contrail cross-plane are converged. Since the smallest flow features are of the scale of the grid scale (with wavelength $2\Delta x$), for each probe, we choose to average ice particle statistics inside a square tube of thickness Δx and Δy in the x and y directions with the tube extending over the whole domain in the z direction. We evaluate the accuracy at each probe using three different particle sample sizes, N_{p1}, N_{p2}, and N_{p3} corresponding to samples formed by taking every 4th, every 2nd, and every particle in the tube.

In addition to the size distribution function (which is represented in this chapter by the normalized histogram) of particles as a function of particle size, we will place special

emphasis on the first three moments of the distribution, defined as

$$M_1 = \frac{\sum r_p}{N} \tag{4.7}$$

$$M_2 = \frac{\sum r_p^2}{N} \tag{4.8}$$

$$M_3 = \frac{\sum r_p^3}{N} \tag{4.9}$$

where the 0th moment, M_0 is N, the total number of particles. The choice of the first three moments is motivated by the fact that they are proportional to, respectively, the ice particle size, surface area and mass, which are the quantities of interest in the contrail simulations. Specifically, the ice surface area is related to the optical depth of the contrail which is a measure of the impact of the contrail on the radiative energy incident on it.

From the above jet LES, with the largest particle sample size N_{p3}, the histograms at the probes are shown in Figure 4.21. The effect of varying particle sampling rate is shown in

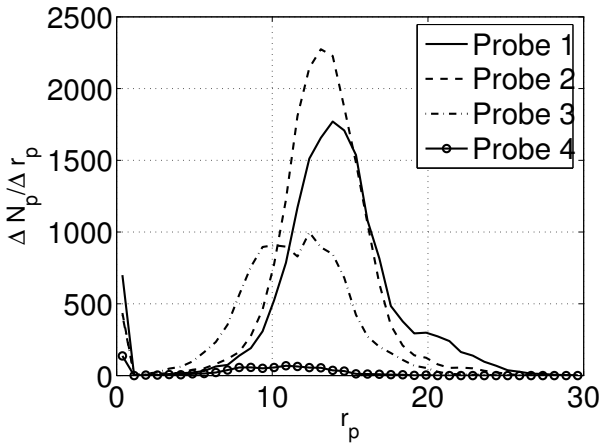

Figure 4.21: Histogram of ice particles at various probe locations as defined in Figure 4.19.

terms of the first three moments in Figure 4.22 and "errors" in the moments in Figure 4.23, where the error is defined as the relative difference between the moment at any sample size and that at the largest sample size N_{p3}. It should be noted that due to their statistical nature the errors are not monotonically decreasing with the sample size. Our goal is only to verify that the errors are small. The convergence of size distribution with sample size is shown in Figure 4.24.

4.9 Grid sensitivity of contrail simulations

4.9.1 Sensitivity to Eulerian grid size

Figure 4.25 depicts the tracer field at 100 wing spans using the nominal grid, $(N_x, N_y, N_z) = (256, 320, 64)$, and a finer grid, $(N_x, N_y, N_z) = (384, 480, 96)$. The domain size in both cases was $(L_x, L_y, L_z) = (4b, 5b, 1b)$ where b is the wing span. Figure 4.26 shows the quantitative comparison between the two grids by plotting various flow variables along a horizontal line passing through the trailing vortex centers. It is seen that although there is some difference between the two solutions (such as rounding off the vorticity peak), the solutions are quantitatively close to each other for all physical variables of interest. Hence the nominal grid size is chosen for subsequent LES.

Next, we also did a convergence study on the contrail baseline case $A1$ which has been described earlier in Chapter 3. The water vapor density and ice density fields at 100 wing spans are shown in Figures 4.27 and 4.28 respectively, for the nominal and finer grids, and quantitative comparison between the two meshes for various flow variables is done in Figure 4.29.

Since the flow is inhomogeneous in the $x - y$ plane, it is instructive to look at the PDFs at the final time, $t = 20\ s$ at various (x, y) locations in the contrail after averaging only in the homogeneous direction. For this we choose four representative probe locations, $(x, y) = (2.25, 2.40)$, $(2.70, 2.40)$, $(2.40, 2.10)$, and $(2.10, 2.00)$ and averaging in rectangular tubes around each probe. The local ice particle number densities at these probes are 3862, 1707, 3245 and 86 $\#/cc$ respectively. These locations were chosen to represent different locations in the flow dynamics, as shown in Figure 4.30. Each tube is centered at the probe location and has a cross-sectional area $4\Delta x \times 4\Delta y$, and extends in the z direction across the domain. The resultant PDFs at the probe locations are shown in Figure 4.31.

Next, the ice growth is examined. In Figure 4.32 we compare the evolution of the first three moments of the distribution, namely the mean, mean square and mean cube of ice particle radius for the two meshes. The errors are small, and especially the ice surface area (mean square of radius) which is the most important quantity for radiative properties of contrails shows very good convergence. Although the size distributions of particle in the two cases do not agree well in a very narrow range of particle size near the peak of the distribution, they show reasonable agreement over most of the radius-space (Figure 4.32(d)). The discrepancy results from higher-order particle statistics not being resolved accurately.

However for the contrail problem the physically important statistics, namely the zeroth and the first three moments, are well represented.

4.9.2 Temporal convergence

Figure 4.32 shows a very fast growth in particle size in the initial 1 second or so. This leads to a natural question about the temporal accuracy in this time duration. So we carried out short simulations with the nominal time step size of $dt = 0.06s$, and smaller time steps $0.03s$ and $0.006s$. The corresponding ice growth is compared in Figure 4.33.

4.9.3 Convergence with number of Lagrangian particles

The Lagrangian approach involves tracking N_{comp} "parcels" of ice particles (called computational particles) each representing n_p identical physical ice particles, such that the total ice particle number, $N_p = N_{comp} \times n_p$ corresponds to an aircraft engine exhaust. This leads to the choice of the two parameters, N_{comp} and n_p. Our current simulations use approximately $N_{comp} = 10^6$ (to within 1% due to integer round-off during the ensemble generation). This choice is based on the competing factors of accuracy and efficiency. This number results in the particle module taking roughly 6% of the total CPU time during a typical contrail simulation, hence the efficiency is satisfactory. In this section, we evaluate this choice for accuracy. A systematic examination of this choice is presented in Chapter 7.

We performed two separate simulations of the baseline case $A1$ – using 1000,000 and 250,000 computational particles. The time histories of the first three moments of the domain-integrated particle size distribution are shown in Figure 4.34. The size distribution of ice particles is compared in Figure 4.34(d). The peak of the distribution approximately matches with the observed value of $0.75\mu m$ (Baumgardner & Cooper, 1994) $1.5km$ behind a Lear jet 35 aircraft. The size distributions for the two simulations at the probe locations defined in Figure 4.30 are compared in Figure 4.35.

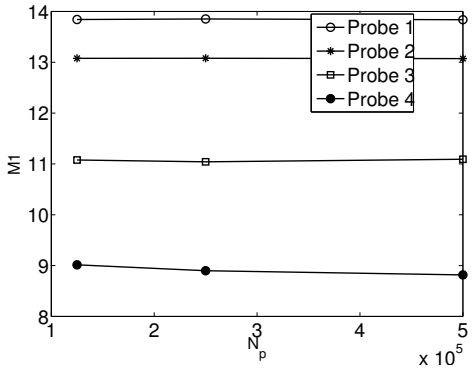

(a) M1

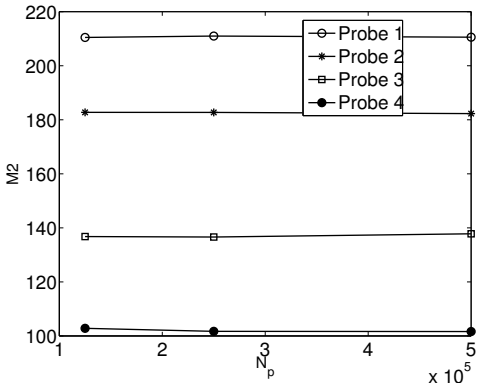

(b) M2

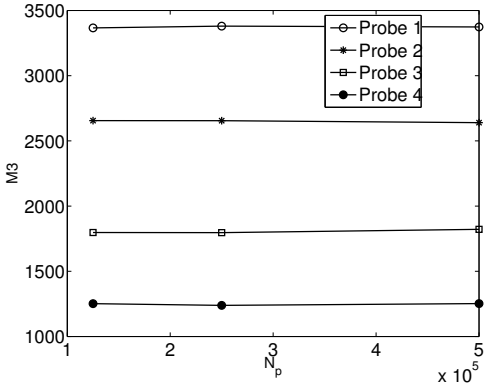

(c) M3

Figure 4.22: Variation of moments of particle distribution with sampling rate.

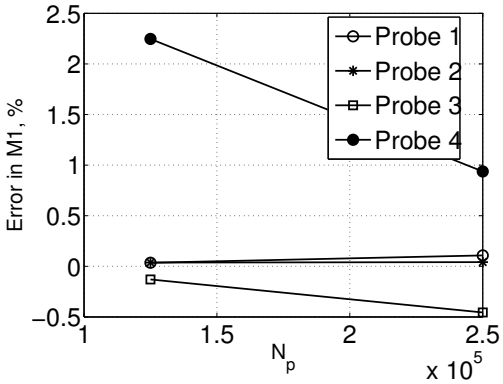

(a) Error in M1

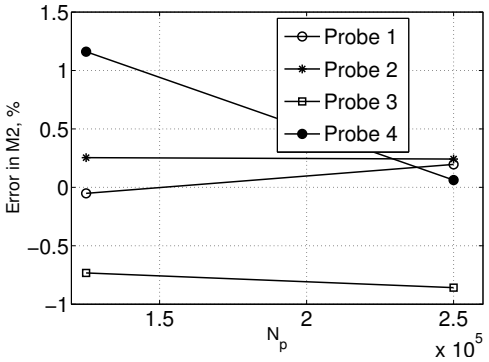

(b) Error in M2

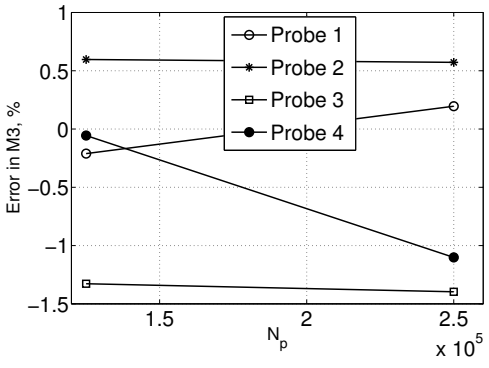

(c) Error in M3

Figure 4.23: Error in moments with sampling rate.

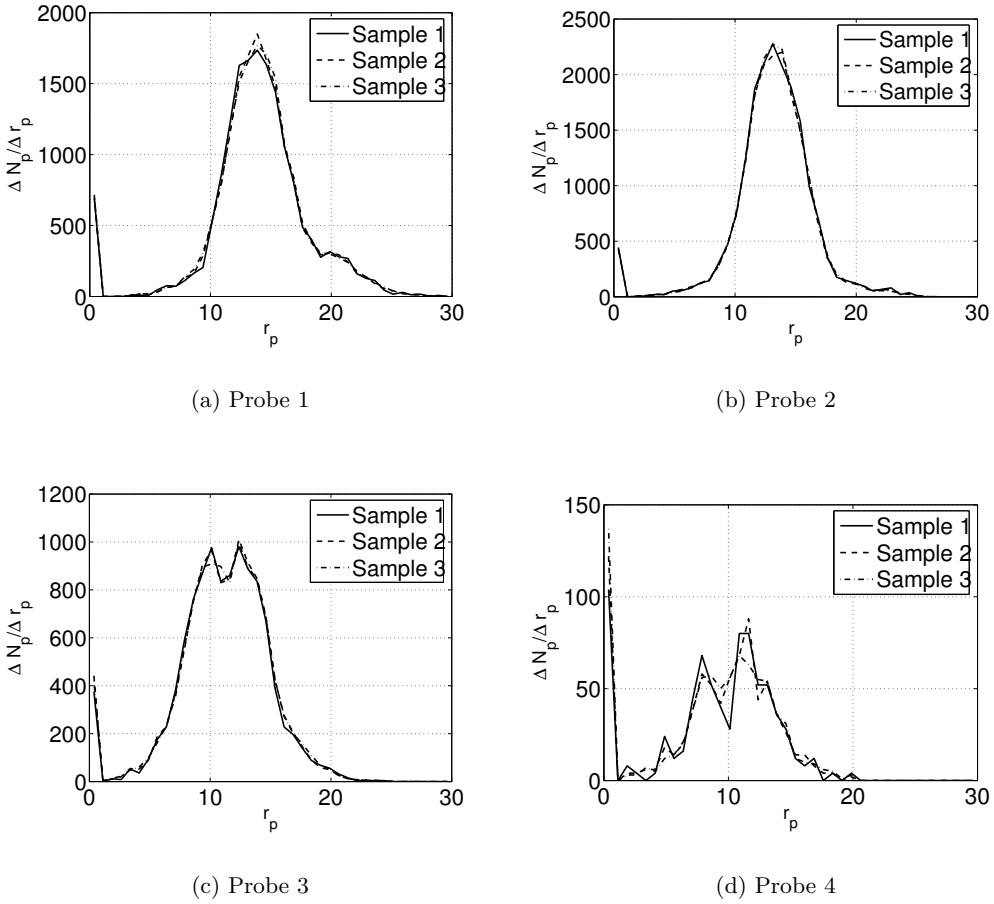

(a) Probe 1

(b) Probe 2

(c) Probe 3

(d) Probe 4

Figure 4.24: Convergence of histograms with sample size. ΔN_p has been normalized by the total sample size.

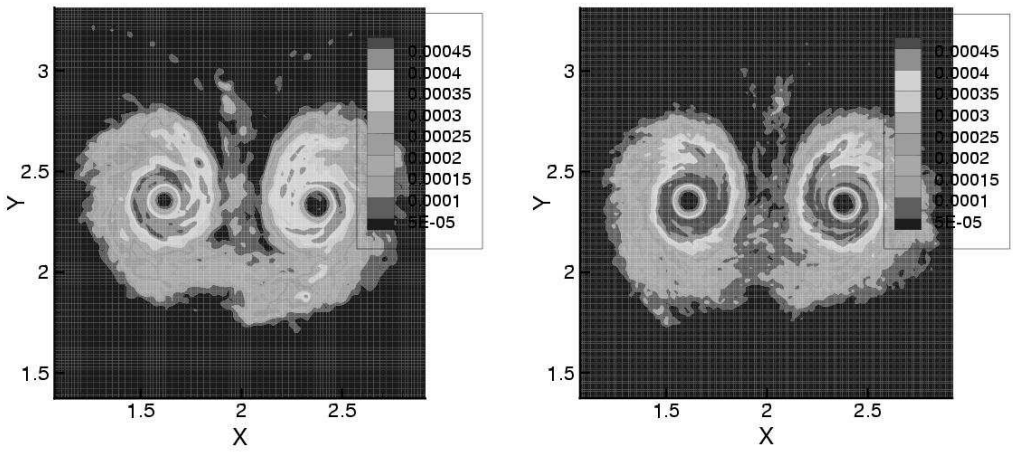

(a) Nominal grid

(b) Fine grid

Figure 4.25: Passive scalar contours with nominal and finer grids at 100 wing spans.

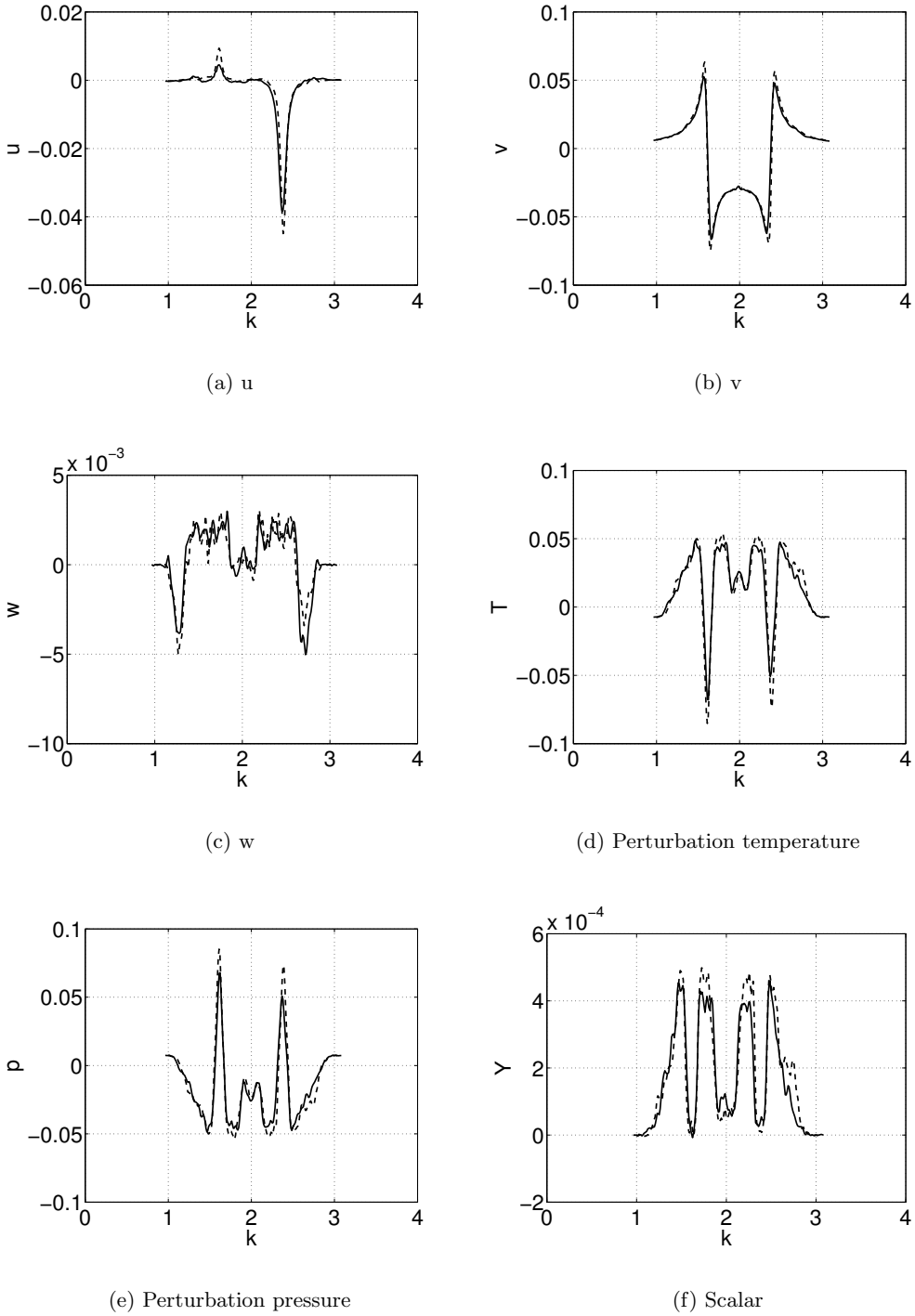

(a) u

(b) v

(c) w

(d) Perturbation temperature

(e) Perturbation pressure

(f) Scalar

Figure 4.26: Z-averaged nondimensional flow quantities from tracer LES at 100 wing spans along the horizontal line passing through the vortex centers. Solid line: nominal grid, dashed line: finer grid.

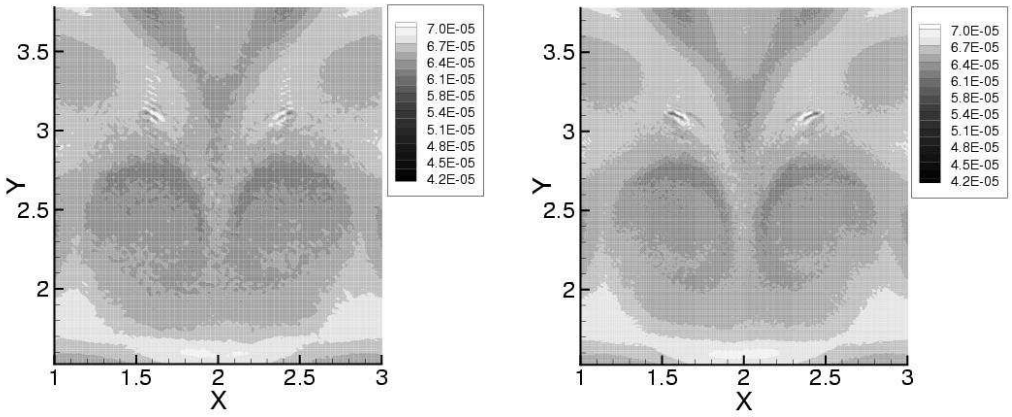

(a) Nominal grid (b) Fine grid

Figure 4.27: Z-averaged water vapor density contours (in kg/m^3) with nominal and finer grids at 100 wing spans.

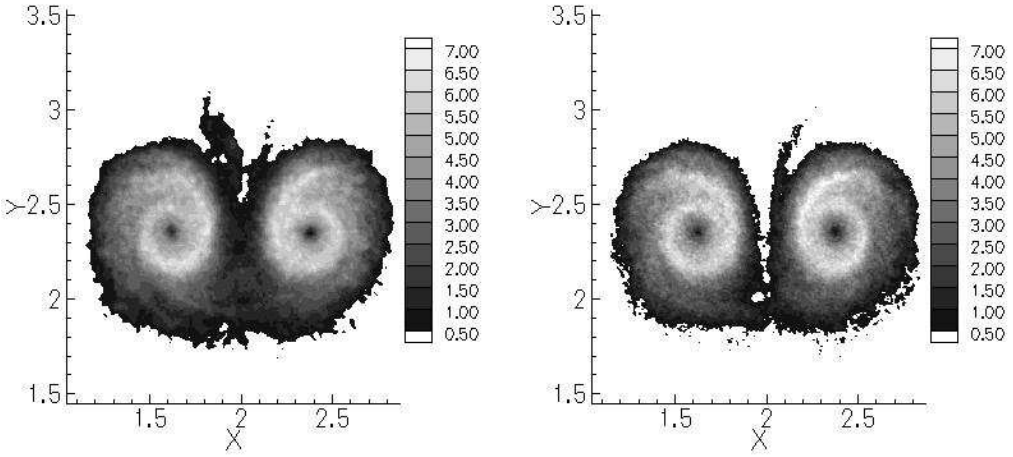

(a) Nominal grid (b) Fine grid

Figure 4.28: Z-averaged ice density contours (in mg/m^3) with nominal and finer grids at 100 wing spans.

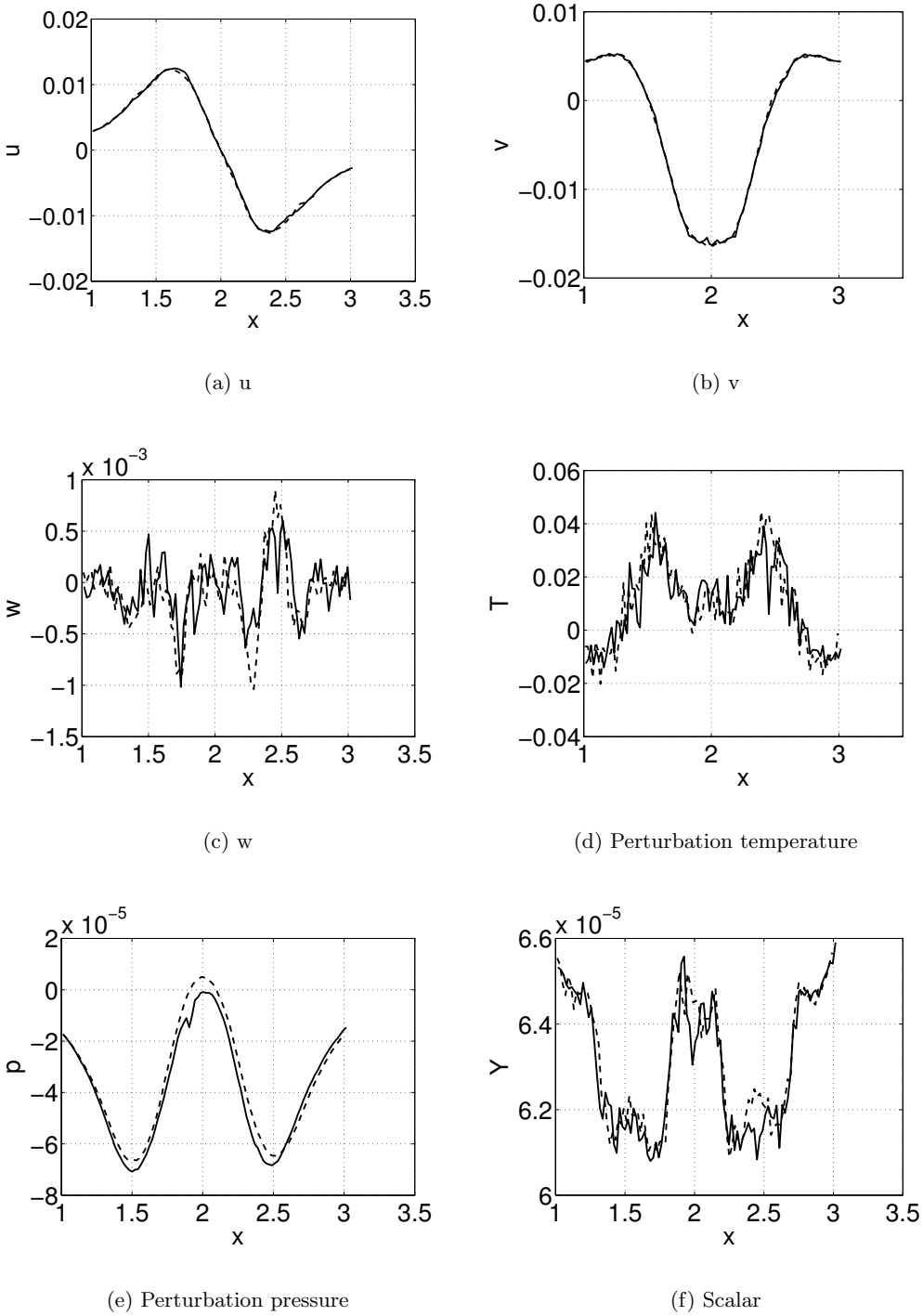

(a) u

(b) v

(c) w

(d) Perturbation temperature

(e) Perturbation pressure

(f) Scalar

Figure 4.29: Z-averaged nondimensional flow quantities from case A1 at 100 wing spans along the horizontal line $y = 2.71$. Solid line: nominal grid, dashed line: finer grid.

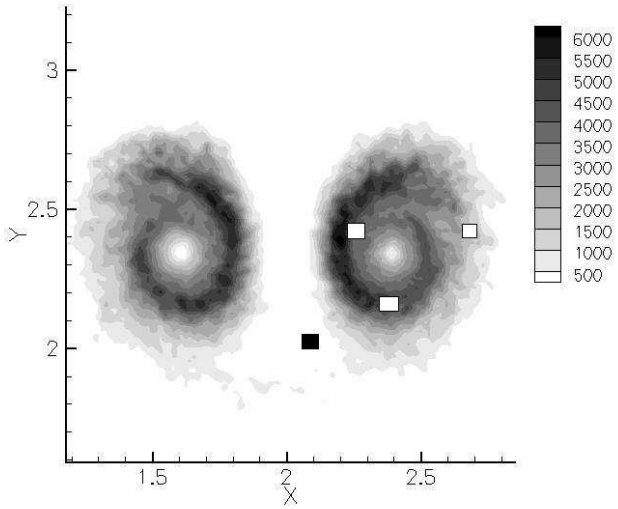

Figure 4.30: Contours of particle number density in $\#/cc$ showing probe locations at $(x, y) = (2.25, 2.40)$, $(2.70, 2.40)$, $(2.40, 2.10)$, and $(2.10, 2.00)$.

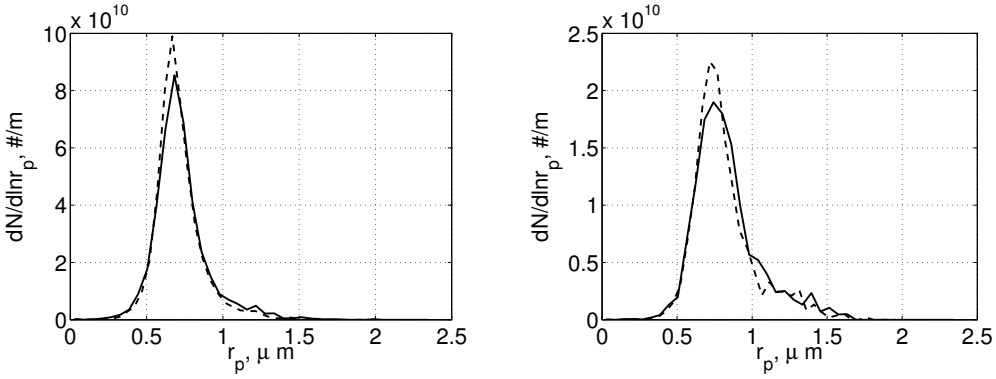

(a) Probe at $(2.25, 2.40)$

(b) Probe at $(2.70, 2.40)$

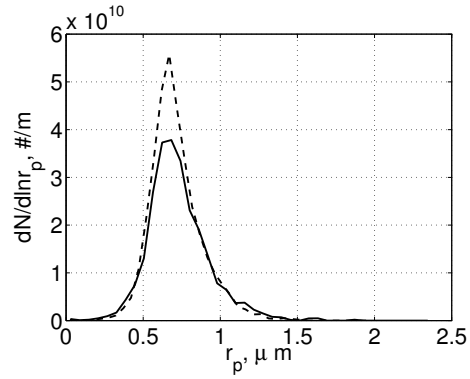

(c) Probe at $(2.40, 2.10)$

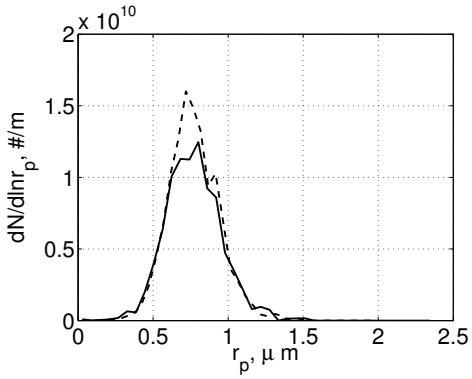

(d) Probe at $(2.10, 2.00)$

Figure 4.31: Ice particle size distribution integrated in a rectangular tube of area $4\Delta x \times 4\Delta y$ with center at the respective probe location, with nominal, —; and finer, – – grid.

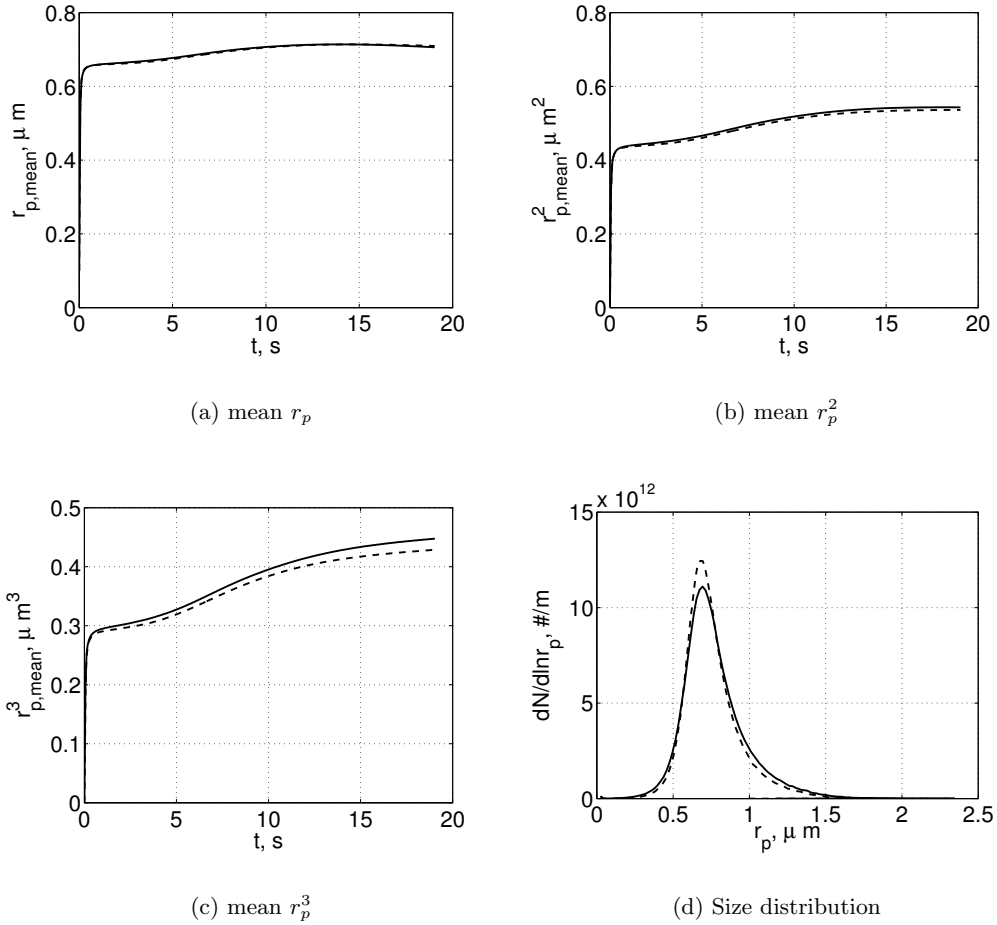

(a) mean r_p

(b) mean r_p^2

(c) mean r_p^3

(d) Size distribution

Figure 4.32: Domain integrated ice properties from case A1. Solid line: nominal grid, dashed line: finer grid.

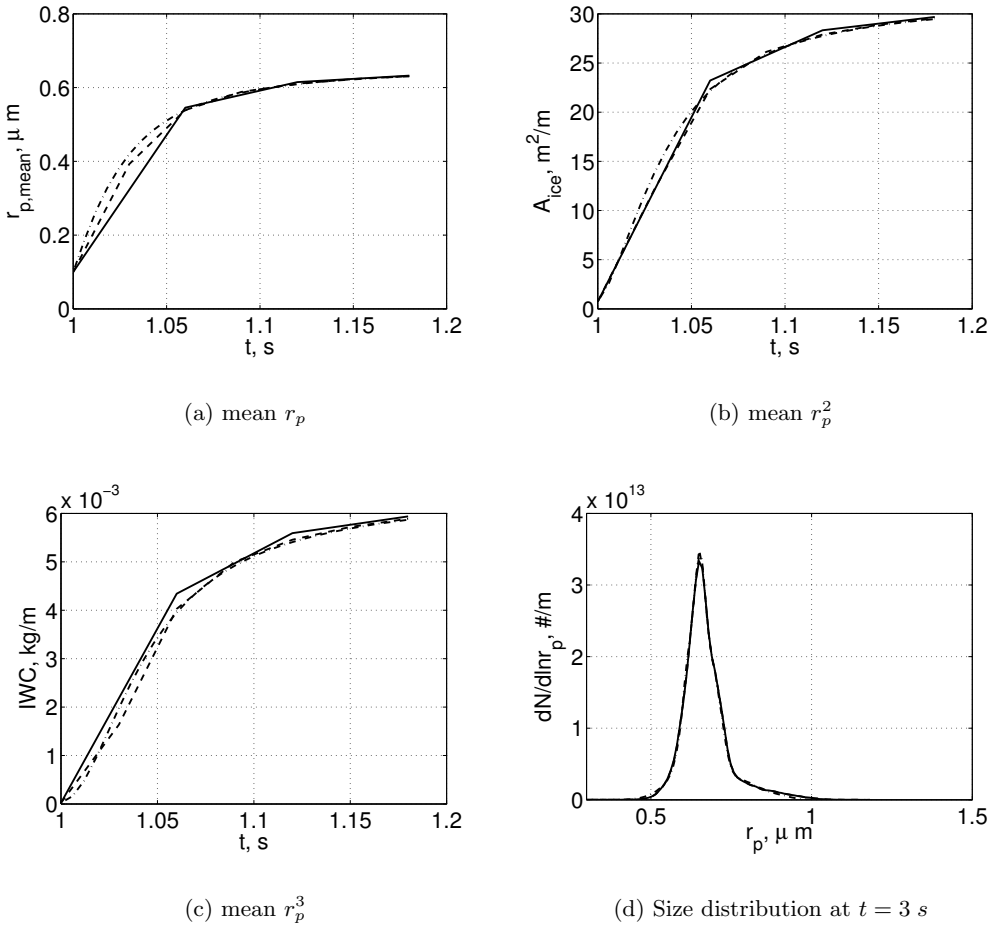

(a) mean r_p

(b) mean r_p^2

(c) mean r_p^3

(d) Size distribution at $t = 3\ s$

Figure 4.33: Temporal convergence of initial evolution of ice properties from case A1. Time step $dt = 0.06s$, —; $dt/2$, – –; $dt/10$, –·–.

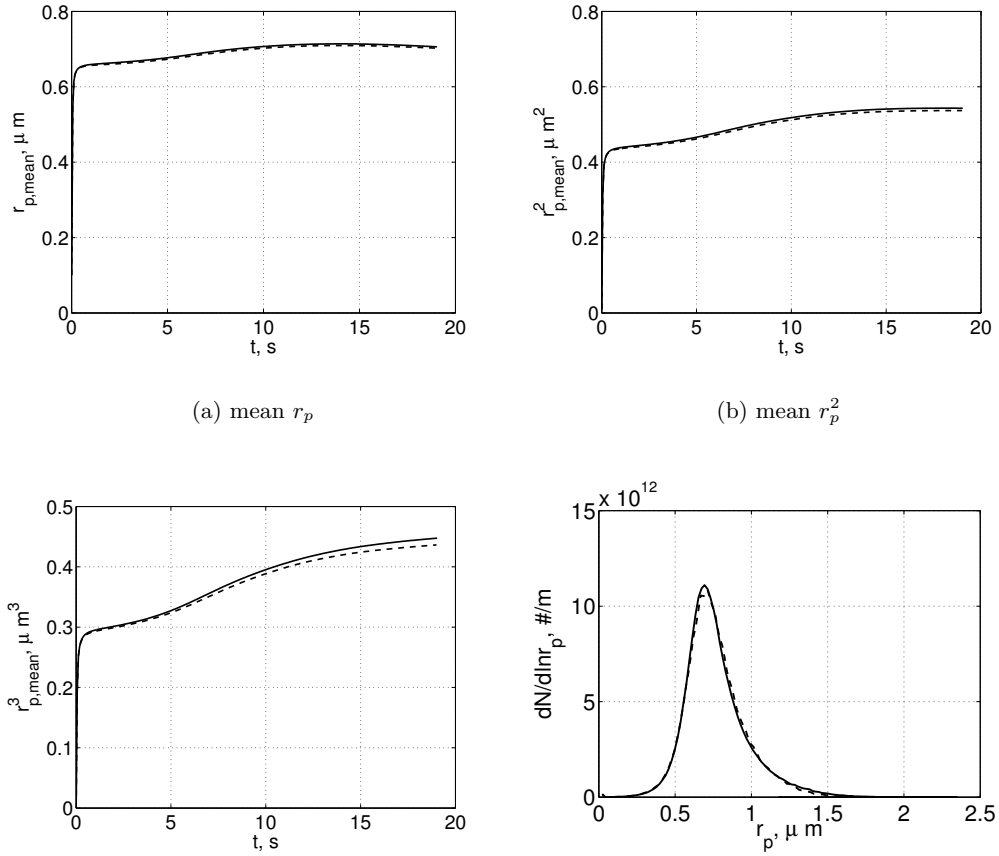

(a) mean r_p

(b) mean r_p^2

(c) mean r_p^3

(d) Size distribution at $t = 20\ s$

Figure 4.34: Domain integrated ice properties from case A1. Solid line: $N_{comp} = 1000,000$, dashed line: $N_{comp} = 250,000$.

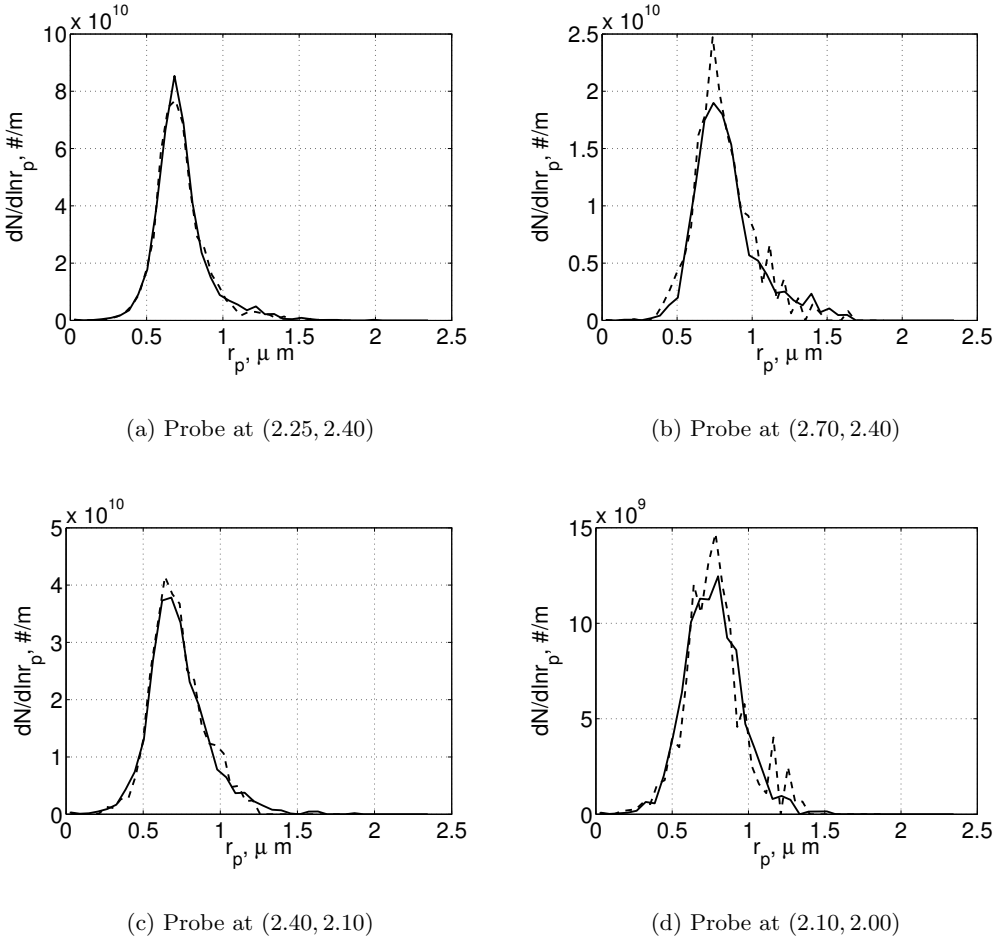

(a) Probe at $(2.25, 2.40)$

(b) Probe at $(2.70, 2.40)$

(c) Probe at $(2.40, 2.10)$

(d) Probe at $(2.10, 2.00)$

Figure 4.35: Ice particle size distribution integrated in a rectangular tube of area $4\Delta x \times 4\Delta y$ with center at the respective probe location, with $N_{comp} = 1000,000$, —; and $N_{comp} = 250,000$, – –.

Chapter 5

Two-dimensional Behavior of Buoyant Wake-Jets

5.1 Introduction

The behavior of trailing vortices of aircraft is an important problem in aviation due to its direct impact on air traffic via the vortex wake hazard. The decay of trailing vortices has been extensively studied under the effects of stratification and shear (Robins & Delisi, 1990), turbulence (Moet *et al.*, 2001; Han *et al.*, 1999), three-dimensional instabilities (Nomura *et al.*, 2006) and ground effects (Türk *et al.*, 1999). The presence of exhaust jets is often not considered while determining the overall wake behavior. Wang & Zaman (2002) performed experiments to characterize the effect of wake vortices on the development of the exhaust jets. They found that the interaction of vortices and jets gives rise to additional vortical structures and the jet distortion and decay is predominantly governed by the trailing vortices. But the other-way effect, i.e., the effect of jets on the motion of the wake vortices has not received much attention, in spite of the jet buoyancy being comparable to stratification-induced buoyancy at least in the early age (1-2 minutes for a typical large passenger aircraft).

The role of buoyancy on vortex wake dynamics has been the subject of study for many years as this aspect is relevant to air traffic control near airports (Spalart, 1998). The focus of such studies is understandably on longer term wake vortex behavior where stratification or ground effects dominate. "Longer term" here is interpreted compared to the time scale over which the exhaust jets weaken due to turbulent mixing with ambient air. Scorer

& Davenport (1970) have given scaling arguments for stratification-induced buoyancy in trailing vortices explaining how the vortical and buoyant forces influence the wake dynamics. Their analysis found that the entrainment and detrainment of ambient fluid into and away from the vortex wake also contribute to stability and breakup of the trailing vortices. In particular, they argue that entrainment leads to the eventual bursting of the vortex core. Spalart (1996) has provided analysis along with two-dimensional numerical simulation data to comprehensively look at the behavior of aircraft wakes under stratification, and has proposed reduced order models representing the buoyancy effects due to stratification.

Mechanisms similar to those identified by these authors are also expected to be triggered by the buoyancy of the exhaust jets of an aircraft. Stratification produces an effect after a few vortex turn-over time scales. At these times the baroclinic vorticity generated on the edges of the descending Kelvin oval produces noticeable effects (Spalart, 1996; Scorer & Davenport, 1970). The jets, on the other hand, are expected to act much faster, starting in the very early stages of wake descent, because their buoyancy is the strongest near the exhaust plane. This puts the exhaust jets into a different regime compared to stratification as far as the vorticity dynamics in the wake are concerned. Whether the overall effect of jets in wake descent and spacing is also restricted to the very early stage, or it persists to longer times and co-exists with stratification effects is not yet understood and is the aim of the current study.

Gerz and Hölzapfel Gerz & Hölzapfel (1999) studied the trailing vortex-exhaust jet system in an environment containing turbulence and long-wave three-dimensional vortex instability, the effects that should be modeled to get a realistic description of the wakes for a duration of more than two minutes or so (for a typical large subsonic transport aircraft). Their jets disperse quickly due to turbulence and they study the combined effect of turbulence and stratification on vortex decay as well as exhaust species distribution. The effect of jet-associated buoyant fluctuations are difficult to characterize in isolation in such complex situations involving turbulence and three-dimensional instabilities. Although the stratified wakes by themselves present interesting dynamics of relevance to realistic aircraft vortex wakes, with the buoyant exhaust jets this picture is likely to be modified and as we show here, additional vorticity generated by the jet buoyancy interacting with the gravity force plays a crucial role in determining the vortex wake behavior at least in the two dimensional setting considered here. Quackenbush *et al.* (1996) have observed this aspect in their two dimensional simulations. We explore this issue to a more fundamental level and

use parametric variation to highlight the effect of jets on wake dynamics.

5.2 Model problem

The model problem consists of a two-dimensional counter-rotating vortex pair representing the aircraft trailing vortices at cruise conditions, and two engine exhaust jets. The vorticity vector and the jet axial velocity are along the z axis, and gravity points in the negative y direction. The vortices were modeled as Lamb-Oseen vortices with core diameter $r_c^* = 0.25\ b_o^*$, where b_o^* is the initial vortex separation. (This matches with Spalart's (Spalart, 1996) value of the parameter $\sigma = r_c^*/b_o^* = 0.25$.) The dimensional variables are denoted by the superscript "*". The vorticity distribution for the Lamb-Oseen vortex with circulation Γ is

$$\omega_z(r) = \frac{\Gamma}{\pi r_c^2} e^{-r^2/r_c^2} \tag{5.1}$$

Then the location of peak azimuthal velocity is $r = 1.12\ r_c$. The physical parameters above were matched with those used for simulations by Spalart 1996 and towing tank experiments by Sarpkaya 1983. The circulation-based Reynolds number was taken as $Re_\Gamma = \Gamma/\nu = 6.366 \times 10^3$, the initial vortex separation b_o^* was taken as 47.24 m, the vortex pair descent speed $U^* = \Gamma^*/2\pi b_o^* = 1.32\ m/s$, and the Brunt-Väisälä frequency $N^* = 0.0279\ rad/s$. This resulted in the nondimensional parameters $N = N^* b_o^*/U^* = 1$ and Froude number $Fr = U^{*2}/b_o^* g^* = 3.74 \times 10^{-3}$, which is in the same range as in (Sarpkaya, 1983). The Prandtl number for the ambient fluid (air) and Schmidt number for a passive scalar which is solved for were 0.71 and 0.65 respectively. In this paper, time is nondimensionalized by b_o^*/U^*, velocity by U^*, and distance by b_o^*. Perturbation density and perturbation temperature are nondimensionalized by the characteristic jet centerline excess values (the "excess" here is in comparison to the hydrostatic value), βT_{ref}^* and $\beta \rho_{ref}^*$ where the subscript "ref" indicates atmospheric reference values at cruise altitude, and β is defined below.

The initial vortex centers were located at $(x, y) = (1.5, 7)$ and $(2.5, 7)$. The exhaust jets were modeled as Gaussian mean temperature profiles representing the thermal signature of the exhaust jets:

$$\frac{\Delta T}{T_{ref}} = \beta\ exp\left[-\left(\frac{2r}{r_j}\right)^2\right] \tag{5.2}$$

where $\Delta T(r)$ is the jet centerline temperature perturbation (with respect to the hydrostatic temperature) associated with the jet, and $\beta = \Delta T_{max}/T_{ref}$ is a parameter related to the

jet buoyancy. For the baseline case we choose $\beta = 0.05$ which will be varied later to study the effect of jet buoyancy. This baseline value of β corresponds to jet peak temperature fluctuation of roughly $10K$ at cruise altitudes of $10.5km$ where the ambient temperature is around $220K$. This in turn matches with jet temperature fluctuation estimates at approximately 5 wing spans downstream of the aircraft (which is equivalent to 1 second or so behind the aircraft at cruise speed) (Gerz & Hölzapfel, 1999; Shirgaonkar & Lele, 2006*a*). The jet radius r_j is taken as 0.15 to approximate an aircraft exhaust jet after spreading and decay experienced by it up to 5 wingspans behind the tail plane. The passive scalar, ϕ, is used to mark the jet fluid. It is initialized in the same way as the jet temperature:

$$\phi = exp\left[-\left(\frac{2r}{r_j}\right)^2\right] \tag{5.3}$$

where the scalar is normalized to have a peak value equal to unity. In the current two-dimensional setting the jet axial momentum equation becomes decoupled from the other two directions and the axial velocity behaves like a passive scalar with $Sc = 1$, hence is not explicitly tracked[1]. The two jets are placed initially at $(x, y) = (1.75, 6.9)$ and $(2.25, 6.9)$, approximately representing the configuration of the wake-jet at 5 wing spans behind a typical subsonic transport aircraft. Note that the vortex cores are taken to be larger than that for a Boeing 767 (hereafter called B767) type aircraft. Based on the analysis of Spreiter & Sacks (1951), Rennich (1997) estimates the parameter σ as 0.098, much smaller than the presently used value of 0.25. Although this value suggests early diffusion of vortices into each other, this choice is useful to compare the results with those obtained by Spalart (1996). Moreover, in a real scenario the turbulent diffusion is likely to provide a similar qualitative behavior. Since there is much uncertainty in the estimates of actual core sizes of different aircraft and of their wake turbulence levels, the value of σ is assumed to be of minor importance to the conclusions drawn in this study.

We believe this choice affects the overall wake descent in a way to compensate for the because the vortices become diffuse only in the late stage. The initial configuration is shown in Figure 5.1. The governing equations are the incompressible Navier-Stokes equations with the extended Boussinesq approximation (Shirgaonkar & Lele, 2006*b*):

[1] In reality the jets would be turbulent and spread faster by entraining ambient air. This effect is not captured in this 2D model problem.

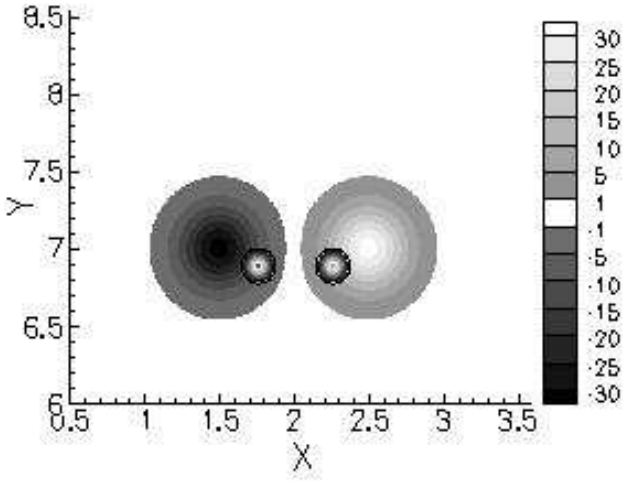

Figure 5.1: Initial configuration of vortices and jets. Filled contours: axial vorticity; lined contours (centered at $(x, y) = (1.75, 6.9)$ and $(2.25, 6.9)$): temperature with contour levels from 0.1 to 0.9 with increments of 0.1.

$$\nabla \cdot \mathbf{u} = 0 \tag{5.4}$$

$$\frac{D\mathbf{u}}{Dt} = -\nabla p' - \frac{\beta}{Fr}\rho'\hat{\mathbf{e}}_\mathbf{y} - (\rho_h(y) + \beta\rho')\frac{D\mathbf{u}}{Dt} + \frac{1}{Re}\nabla^2\mathbf{u} \tag{5.5}$$

$$\frac{DT'}{Dt} = -\frac{\epsilon}{\beta}v + \frac{1}{RePr}\nabla^2 T' \tag{5.6}$$

$$\rho' = -T' \tag{5.7}$$

and the passive scalar transport equation,

$$\frac{D\phi}{Dt} = \frac{1}{ReSc}\nabla^2\phi \tag{5.8}$$

where the subscript "h" indicates hydrostatic state and primed variables denote the perturbations about the hydrostatic state. $\epsilon = ds_h/dy = \frac{b_o^*}{C_p^*}\frac{ds_h^*}{dy^*}$ is the nondimensional vertical gradient of entropy for the hydrostatic state, and is proportional to the square of the Brunt Väisälä frequency. Ideal gas equation for air has been assumed. The detailed derivation of the above equation set can be found in Shirgaonkar and Lele 2006*b*. These equations are solved using a sixth order compact finite difference scheme (Lele, 1992; Lui & Lele, 2001). Time advancement is done with a low storage, low dissipation and dispersion Runge-Kutta

(RK) scheme of fourth order (LDDRK4) (Stanescu & Habashi, 1998). In Eq. 5.5 the term $\frac{D\mathbf{u}}{Dt}$ appears on the right hand side. To treat this term explicitly at each time step, the time-derivative part of it, $\frac{\partial \mathbf{u}}{\partial t}$, is approximated by the time derivative at the previous time step (Shirgaonkar & Lele, 2006*b*). The skew-symmetric form of the convective terms is used to achieve discrete conservation of kinetic energy and scalar variance in the inviscid non-buoyant limit. The Poisson equation for pressure is solved using a fast Fourier spectral solver. The computational domain size is $(L_x, L_y) = (4, 10)$ and the grid size is $(N_x, N_y) = (384, 960)$, close to that used by Spalart 1996 to resolve the density boundary layers which have an estimated length scale of $0.016b$ at the stagnation point (Spalart, 1996), developing on the edge of the descending Kelvin oval. The domain size was kept to be sufficiently large to keep the spurious effects of periodic boundary conditions small as described in Section 4.7.

5.3 Role of jet buoyancy

The vertical position of and spacing between the vortex centers (defined as the local extrema of vorticity) for the baseline case described in Section 5.2 are shown in Figure 5.2. The time history of the positive and negative components of the total circulation in the left symmetric half of the domain is shown in Figure 5.3 along with that of the total circulation in the left half, showing a net generation of baroclinic circulation due to stratification and jet buoyancy. We will investigate the circulation histories in more depth later in the chapter.

The vortex pair exhibits an initial descent followed by arrest, rise-up, and subsequent descent as observed in other studies (Spalart, 1996; Robins & Delisi, 1990), only more enriched by the buoyant jet. The evolution of vorticity (Figure 5.4) shows the appearance of fine structures at large times. This prompts us to ensure that the grid resolution is sufficient. Hence we did a grid convergence study with two additional grids – coarse, $(N_x, N_y) = (256, 640)$ and fine, $(512, 1280)$ – in addition to our nominal grid size of $(384, 960)$. The results from these grids (Figures 5.5,5.6) suggest that the nominal grid has sufficient resolution to predict the wake descent and the important vorticity dynamics.

The mechanism behind the observed wake descent and vortex separation can be explained by looking at the vorticity dynamics (Figure 5.4) as follows. By $t = 0.5$ strong baroclinic vorticity is generated by the interaction of density gradients and pressure forces.

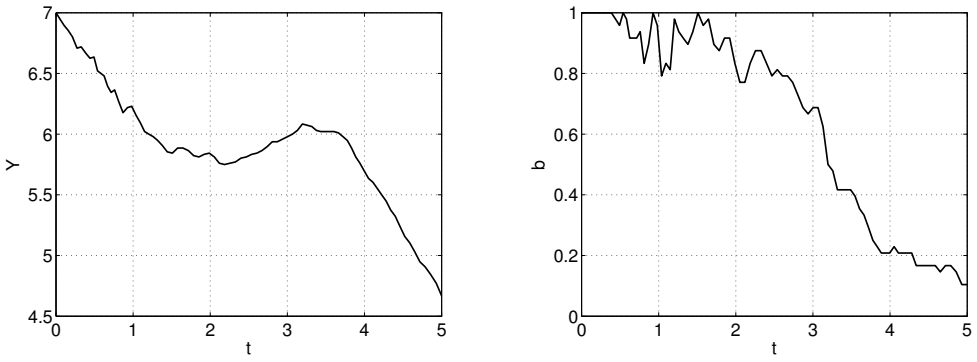

(a) Vertical position

(b) Vortex spacing

Figure 5.2: Movement of vortex centers for the baseline case. The vertical arrest of the descent due to stable stratification is visible around $t = 2$. The initial fluctuations in vortex spacing are due to the wobbling motion of vortex cores caused by the elliptic shape of the finite vortex cores.

The generation is fast and starts at very early times after $t = 0$. This vorticity has components with positive and negative signs, generated by the misalignment of density gradient with the pressure forces. This misalignment results from the fact that the strained and elongated jet has a local minimum of density and the density increases away from that minimum, resulting in gradients of density in both directions. As is well known from the literature on two-dimensional turbulence, vortices of same sign merge together resulting in larger vortices (inverse energy cascade), and those with opposite sign stay separated (Bracco *et al.*, 2000). Hence the baroclinic vorticity generated over the jet region rolls up into organized structures. Also, the component of baroclinic vorticity with the same sign as the primary vortex merges with the primary vortex. Focusing on the left vortex (clockwise, or negative vorticity in the present frame), we can see that such merger has taken place by $t = 2.0$ and the primary vortex has grown in size as a result (Figure 5.4(g)). The movement of the jet fluid indicated by passive scalar, and jet temperature are depicted in Figures 5.7 and 5.8 respectively.

Meanwhile, the combined effect of stable stratification and positive jet buoyancy has caused an arrest of vortex descent at around $t = 2.0$ (Figure 5.2(a)). The arrest location and time instance depends on the Brunt-Väisälä frequency (Spalart, 1996; Robins & Delisi, 1990), and as we show later, is also affected by the jet. The positive component of the

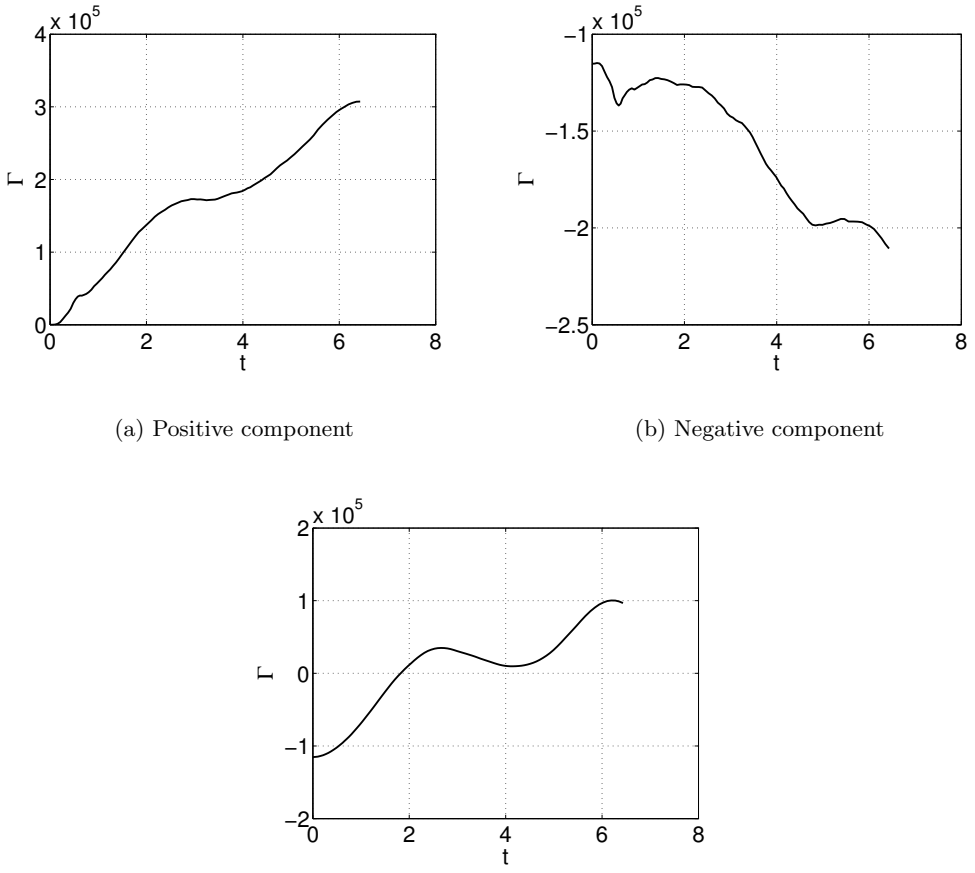

(a) Positive component

(b) Negative component

(c) Total

Figure 5.3: Positive, negative components and total circulation in the left half ($x < 2$) for the baseline case.

baroclinic vorticity now produces an induced velocity on the primary vortex which pushes the two primary vortices toward each other (Figure 5.2(b)), tending to accelerate the descent. This mechanism is schematically depicted in Figure 5.9. The competition of upward buoyancy and downward induced velocity continues and near $t = 3.5$ the effect of stronger primary vortices and induced velocity due to secondary vortices overpowers the buoyancy forces and rapid acceleration is observed in the downward direction.

5.3.1 Effect of jet temperature

As the flow dynamics are strongly affected by buoyancy, it is desirable to assess the role of jet buoyancy in the overall flow development. Along with the baseline case with the jet peak temperature given by $\beta = 0.05$ (see Equation 5.2), we performed numerical experiments for a weak jet ($\beta = 0.02$) and no jet ($\beta = 0$). It should be noted that "no jet" here means no temperature perturbation corresponding to the jet exhaust fluid (which is marked by the passive scalar). "Weak jet" means small jet peak temperature compared to the baseline case. The jet axial (z) velocity in all cases is irrelevant because the axial momentum equation is decoupled from the dynamics in the $x-y$ plane in the current 2D setting. The vortex motion (Figure 5.10) indicates that the presence of the jet supports descent and reduction in vortex separation and this trend becomes stronger for stronger jets (higher jet temperatures).

This behavior is readily explained by examining the vorticity dynamics (Figure 5.11) and appealing to the mechanism depicted in Figure 5.9. The stronger the jet is, the more baroclinic vorticity (of both signs) it generates. Part of this vorticity that has the same sign as the primary vorticity gets entrained into the primary vortex core. In addition, the warmer jet gets entrained faster because it experiences more centripetal buoyancy forces compared to the less warm jet. This entrainment of jet fluid is evident from Figure 5.12. It is seen that for stronger jet temperatures, more jet fluid is entrained into the vortex core. In fact, for $\beta = 0.05$ the jet fluid has penetrated into the core by $t = 4$. The combination of these effects provides a positive feedback for vortex descent according to the mechanism shown by Figure 5.9.

5.4 Isolated effect of jet buoyancy

In order to separate the jet effect from stratification effects and assess the impact of the jet independently, we also simulated wakes in an unstratified atmosphere with and without the jet. The vortex positions from these simulations are shown in Figure 5.13. Without the jet, the vortex wake descends with a small departure from the linear descent $Y = 7 - t$ due to the finite core sizes and resultant ellipticity of the vortex shapes. Also the vortex pair remains equidistant. With the jet, as expected, the descent is facilitated. The extent of the jet's impact is seen clearly from these results as we have isolated the jet buoyancy by choosing an unstratified atmosphere. The only source of baroclinic vorticity is the jet buoyancy (Figures 5.14(a),5.14(b)).

This is more evident from the plots of positive and negative components of the total circulation in the left half of the plane, and also the total circulation in the left half (Figure 5.15). With the jet there is positive baroclinic vorticity generation in the early stage (before $t = 1$ in this case) and in the late stages the total circulation starts dropping in magnitude due to viscous diffusion with the other symmetric half with opposite-signed vorticity. It should also be noted that the mechanism explained before regarding the role of jet buoyancy involves both positive and negative baroclinic vorticity generation from the jet. Figure 5.15 shows that the positive and negative components of baroclinic circulation balance each other to keep the total circulation nearly unchanged until additional effects of viscous diffusion come into play at around $t = 2.5$. This in conjunction with Figure 5.14(b) supports the hypothesis that the same-signed (as the primary vortex) secondary vorticity gets entrained into the primary vortex increasing its circulation, and the opposite signed component is detrained into the atmosphere.

Part of the passive scalar marking the jet fluid is predominantly entrained into the vortex core and another part escapes (detrains) into the atmosphere due to its positive buoyancy. Figures 5.14(b), 5.14(d) show that the entrained portion precisely corresponds to the baroclinic vorticity of the same sign as the primary vortex, and the detrained portion corresponds to the fluid elements carrying the opposite-signed part of the baroclinic vorticity.

5.5 Traditional vs. extended Boussinesq model

The extended Boussinesq approximation developed in Chapter 2 has a particularly relevant advantage for this study due to the presence of the buoyant jets. The vorticity created by the inertial forces acting on the density gradients associated with the jets is not captured by the traditional approximation, but the extended Boussinesq approximation captures it. The peak Froude number (based on the vortex peak azimuthal velocity and core radius) is roughly around 0.24 for the baseline case. Hence, as shown by the analysis in Chapter 2, the extended model terms become important compared to the stratification-related buoyancy term.

This effect is clarified in Figure 5.16 where we observe the transport of the baroclinic vorticity into the primary vortices. At early time $t = 1$ the effect of the extended terms has not produced much cumulative change, but at $t = 2$ it can be observed that the centripetal

forces in the extended Boussinesq approximation have pulled the negative baroclinic vorticity into the primary vorticity to a greater extent than the traditional approximation, resulting in a more concentrated vorticity distribution in the core. The cumulative effect of these differences is evident at $t = 4$ where the vertical and horizontal locations of the primary vorticity are different between the two models, and also the surrounding distribution of secondary vorticity. Qualitative difference in the wake descent and vortex separation is shown in Figure 5.17. The effect of passive scalar transport is shown in Figure 5.18. The passive scalar can be thought of as a representation of the jet fluid. In the late stages, both Figure 5.16 and Figure 5.18 exhibit rich structures of vorticity and scalar distribution. This is not the "chaotic" advection in the traditional sense because the difference between the results from the two models is not due to a difference in the initial conditions, but is due to the difference in the governing equations for the two models. Away from the primary vortices the dynamics are buoyancy-dominated, i.e., the buoyancy effects are the leading order effects in these regions (as explained by the scaling analysis in Chapter 2). Hence the difference in the modeling of buoyancy terms causes a large difference in the baroclinic vorticity structures in these regions.

5.6 Conclusion

The presence of the exhaust jets in two dimensional aircraft wakes adds additional transport mechanisms on top of those already existing for pure vortical wakes. We studied the effect of buoyant exhaust jets on laminar vortex pair descent and spacing, and identified the mechanism underlying the wake behavior. It was found that the same-signed (as the primary vorticity) portion of the jet-generated baroclinic vorticity is entrained into the trailing vortices, and the opposite-signed portion detrains into the atmosphere. This was found to strengthen the primary vorticity, reduce the spacing between the two primary vortices, and accelerate the wake descent. The parametric study indicated that the jet in general causes faster descent and reduced spacing of the vortex pair. Baroclinic vorticity resulting from stratification also favors descent in the long-term (although it may produce an intermediate arrest of the descent) (Spalart, 1996; Robins & Delisi, 1990). It should however be noted that in three dimensions, additional flow dynamics such as turbulence and three-dimensional long-wave instability (Crow, 1970) will cause the wake dynamics to become much more complex. Specifically, the turbulent mixing of the jet fluid with the

ambient fluid is likely to affect the behavior of the wakes.

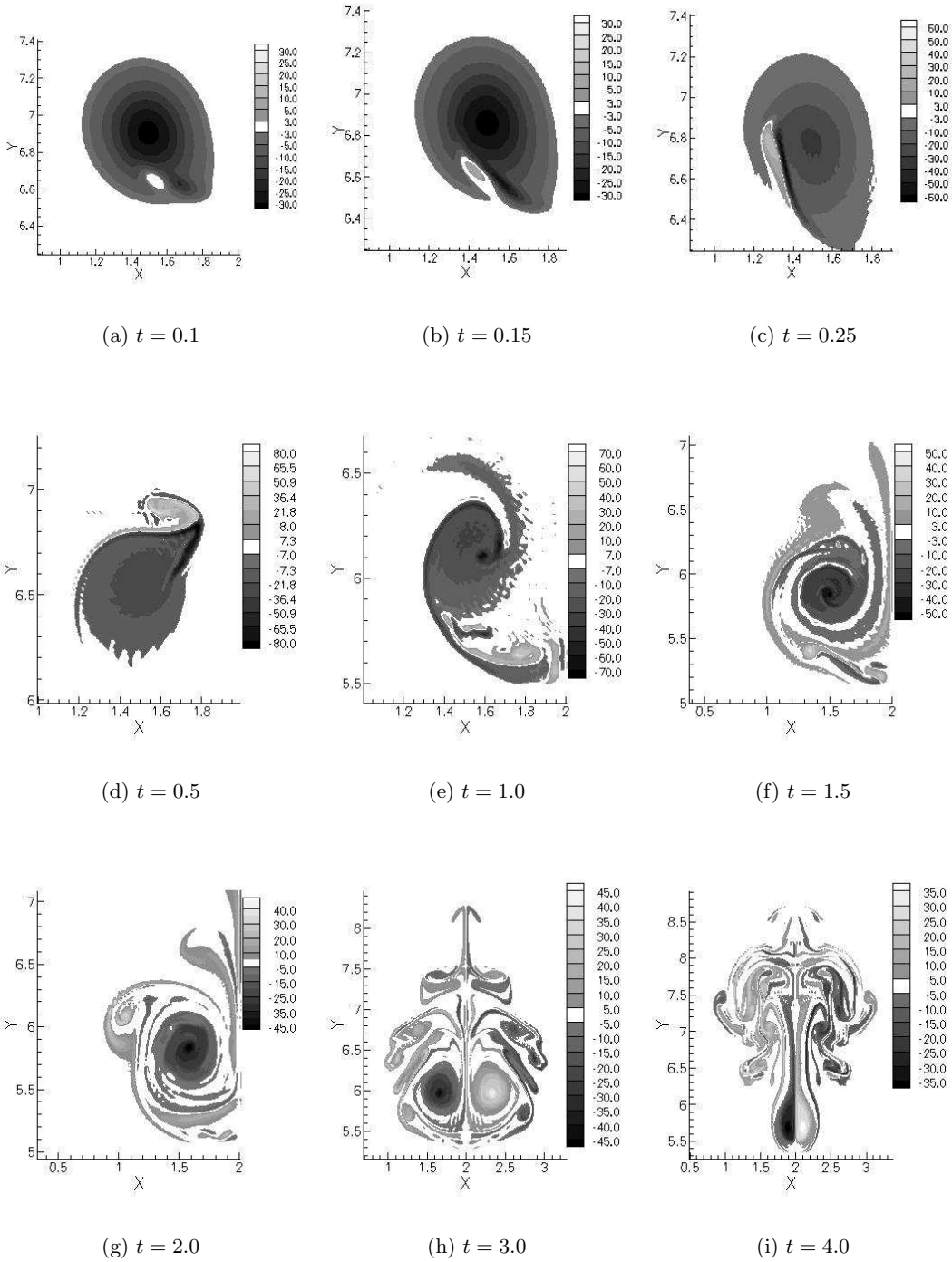

(a) $t = 0.1$ (b) $t = 0.15$ (c) $t = 0.25$

(d) $t = 0.5$ (e) $t = 1.0$ (f) $t = 1.5$

(g) $t = 2.0$ (h) $t = 3.0$ (i) $t = 4.0$

Figure 5.4: Vorticity evolution in the jet-wake flow, baseline case. Note that in (a) to (d) only the left vortex is shown for clarity. The right side is symmetric about $x = 2$.

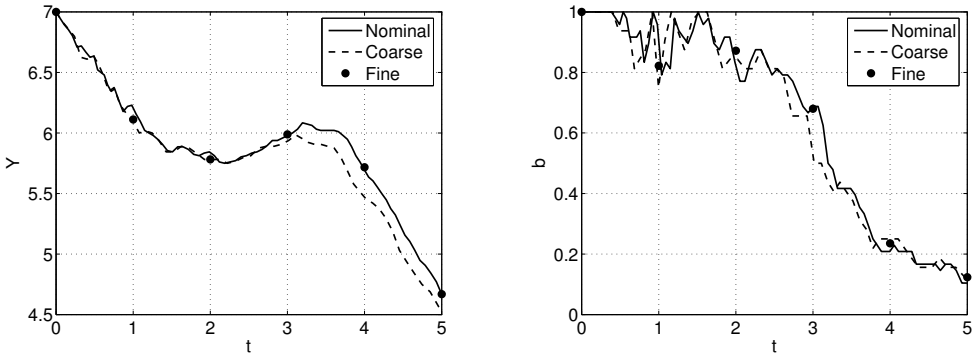

(a) Vertical position (b) Vortex spacing

Figure 5.5: Movement of vortex centers for the baseline case with three grid sizes – coarse, $(N_x, N_y) = (256, 640)$; nominal, $(384, 960)$; fine, $(512, 1280)$.

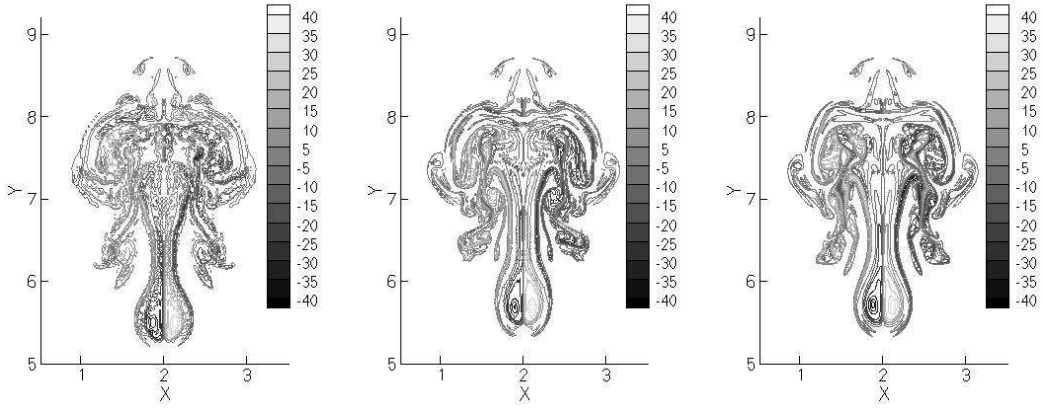

(a) Coarse (b) Nominal (c) Fine

Figure 5.6: Vorticity contours with three grid sizes – coarse, $(N_x, N_y) = (256, 640)$; nominal, $(384, 960)$; fine, $(512, 1280)$.

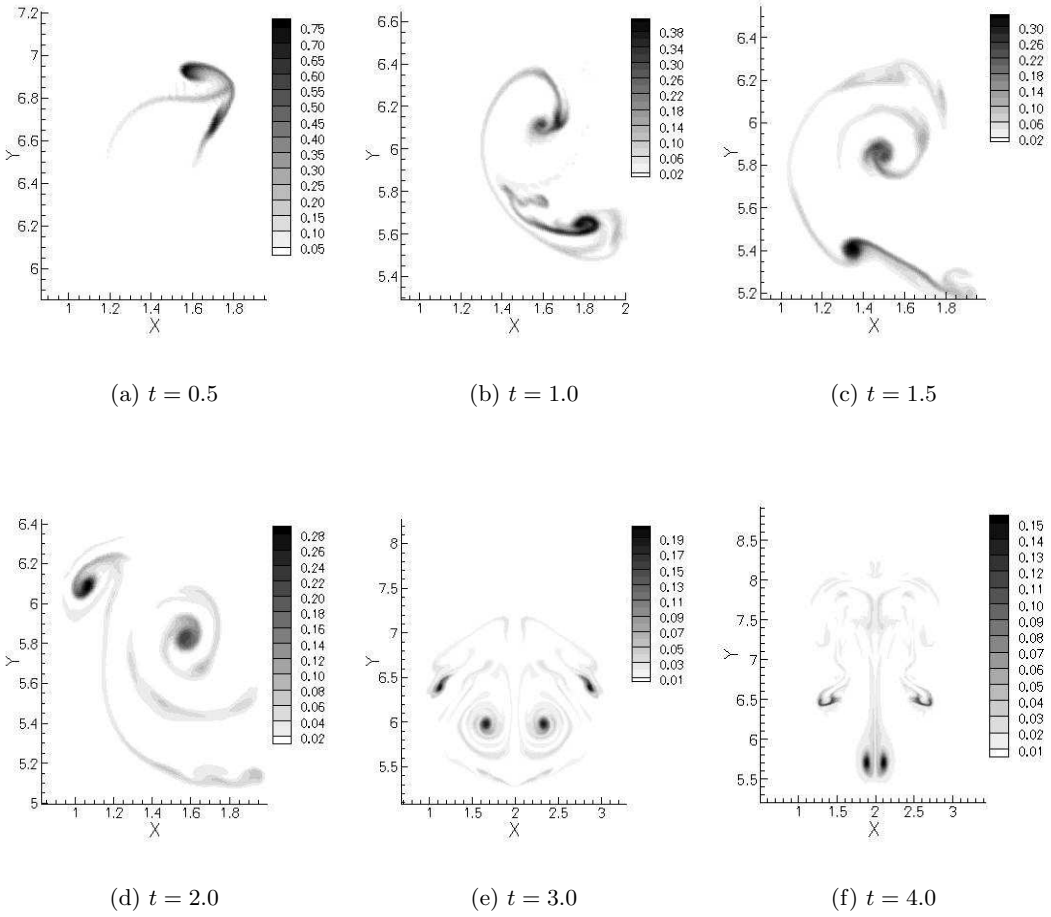

(a) $t = 0.5$ (b) $t = 1.0$ (c) $t = 1.5$

(d) $t = 2.0$ (e) $t = 3.0$ (f) $t = 4.0$

Figure 5.7: Jet fluid transport represented by passive scalar in the jet-wake flow, baseline case. Note that in (a) to (d) only the left half of the domain is shown for clarity. The right side is symmetric about $x = 2$.

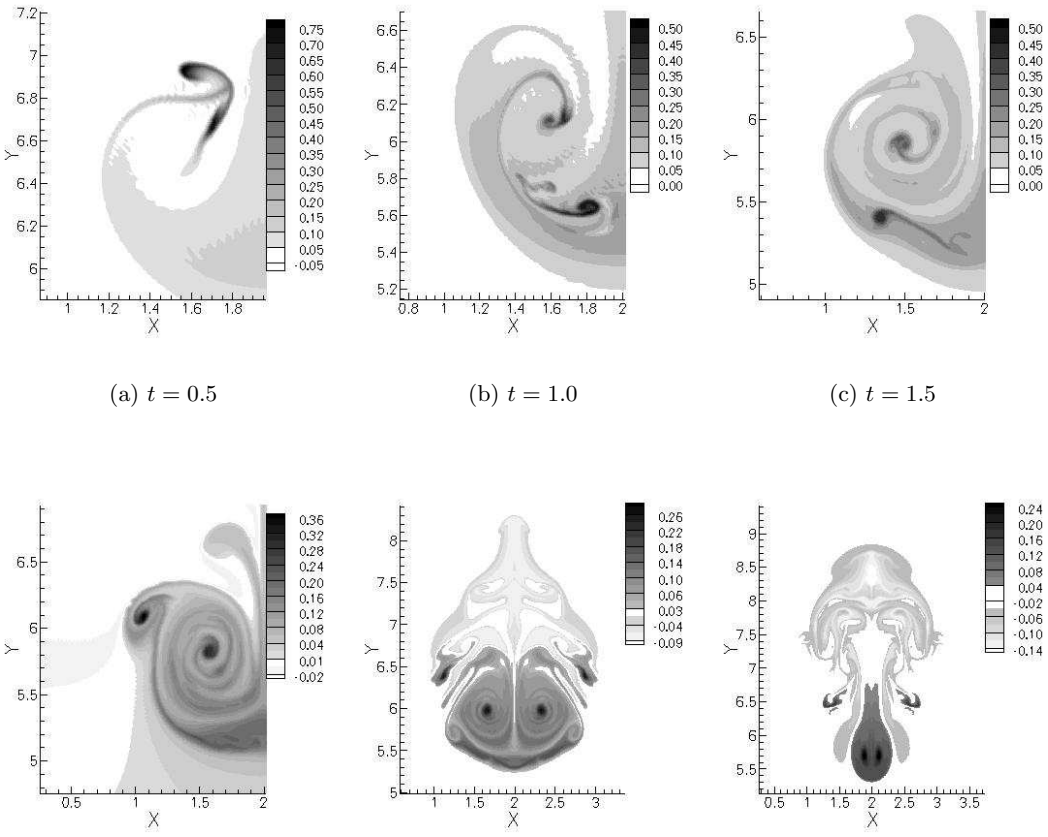

(a) $t = 0.5$ (b) $t = 1.0$ (c) $t = 1.5$

(d) $t = 2.0$ (e) $t = 3.0$ (f) $t = 4.0$

Figure 5.8: Jet perturbation temperature evolution in the jet-wake flow, baseline case. Note that in (a) to (d) only the left half of the domain is shown for clarity. The right side is symmetric about $x = 2$.

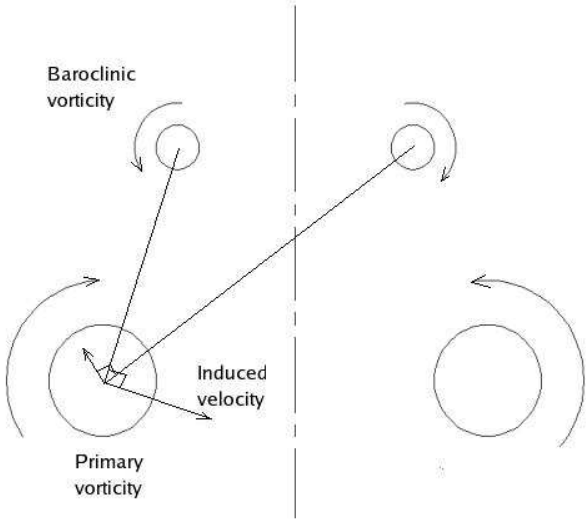

Figure 5.9: Schematic showing the motion induced by the baroclinic vorticity on the primary vorticity.

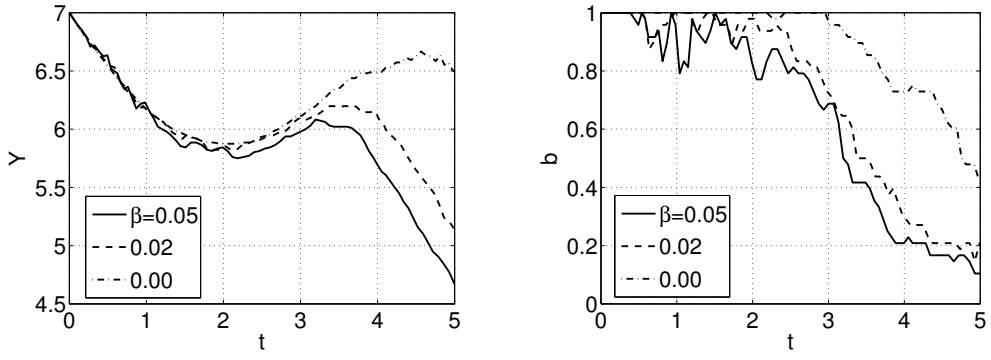

(a) Vertical position

(b) Vortex spacing

Figure 5.10: Vortex descent and separation for no jet, $\beta = 0$; weak jet, $\beta = 0.02$; strong jet, $\beta = 0.05$.

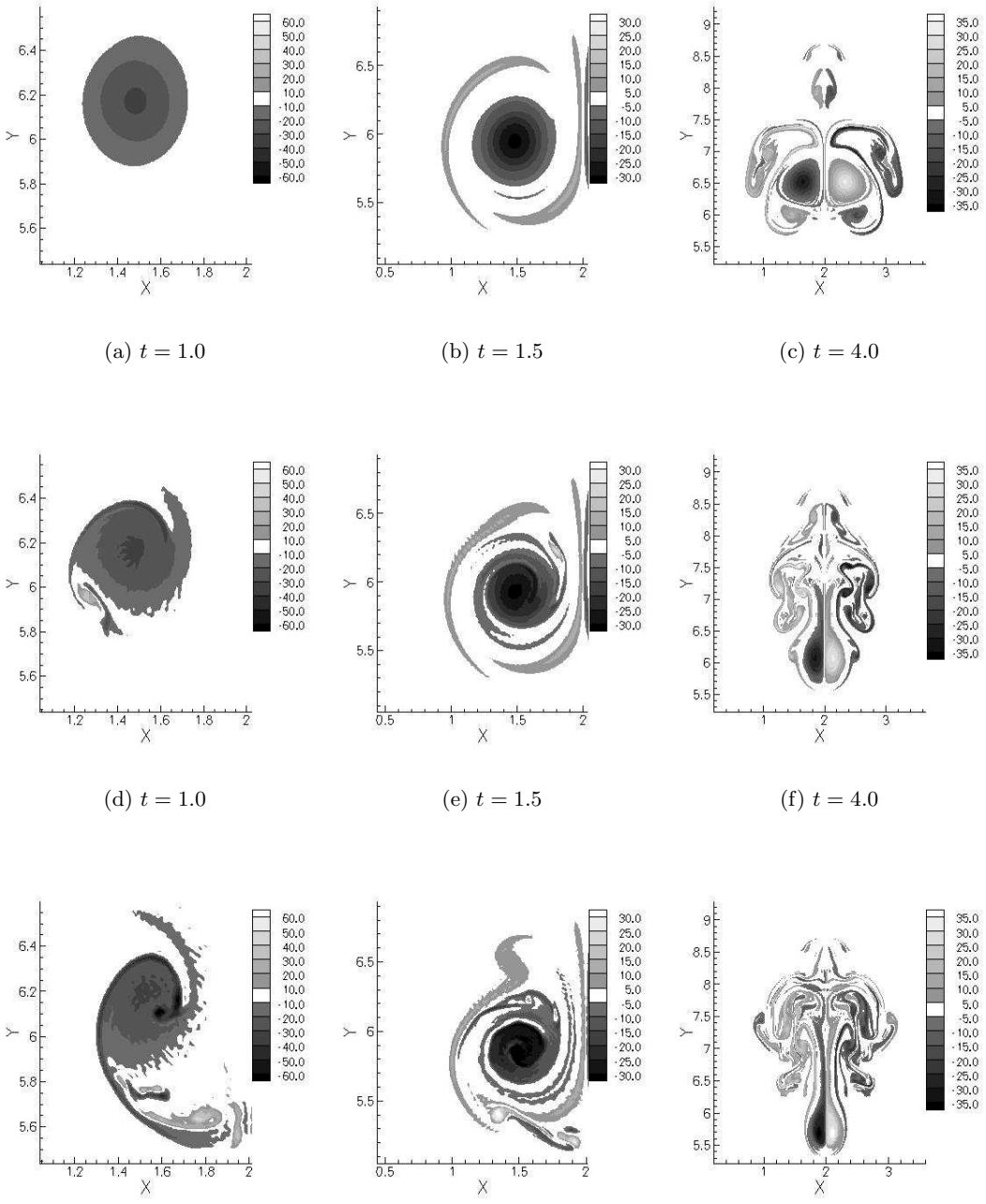

(a) $t = 1.0$ (b) $t = 1.5$ (c) $t = 4.0$

(d) $t = 1.0$ (e) $t = 1.5$ (f) $t = 4.0$

(g) $t = 1.0$ (h) $t = 1.5$ (i) $t = 4.0$

Figure 5.11: Vorticity evolution for no jet, $\beta = 0$ (top); weak jet, $\beta = 0.02$ (middle); strong jet, $\beta = 0.05$ (bottom). For $t < 4$ only the left half of the domain is shown for clarity.

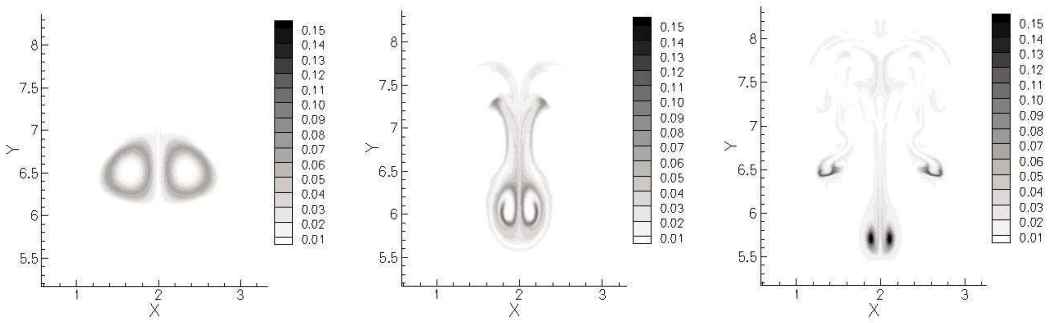

(a) No jet (b) Weak jet (c) Strong jet

Figure 5.12: Passive scalar transport at $t = 4$ for no jet, $\beta = 0$; weak jet, $\beta = 0.02$; strong jet, $\beta = 0.05$.

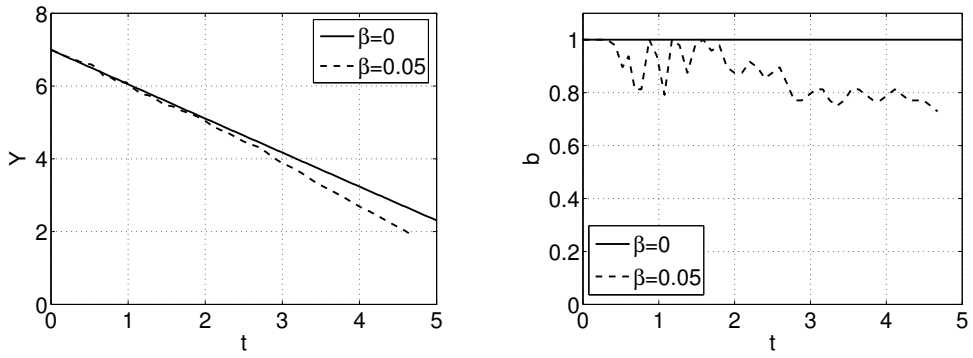

(a) Vertical position (b) Vortex spacing

Figure 5.13: Vortex descent and separation in an unstratified atmosphere without the jet, $\beta = 0$; and with jet, $\beta = 0.05$.

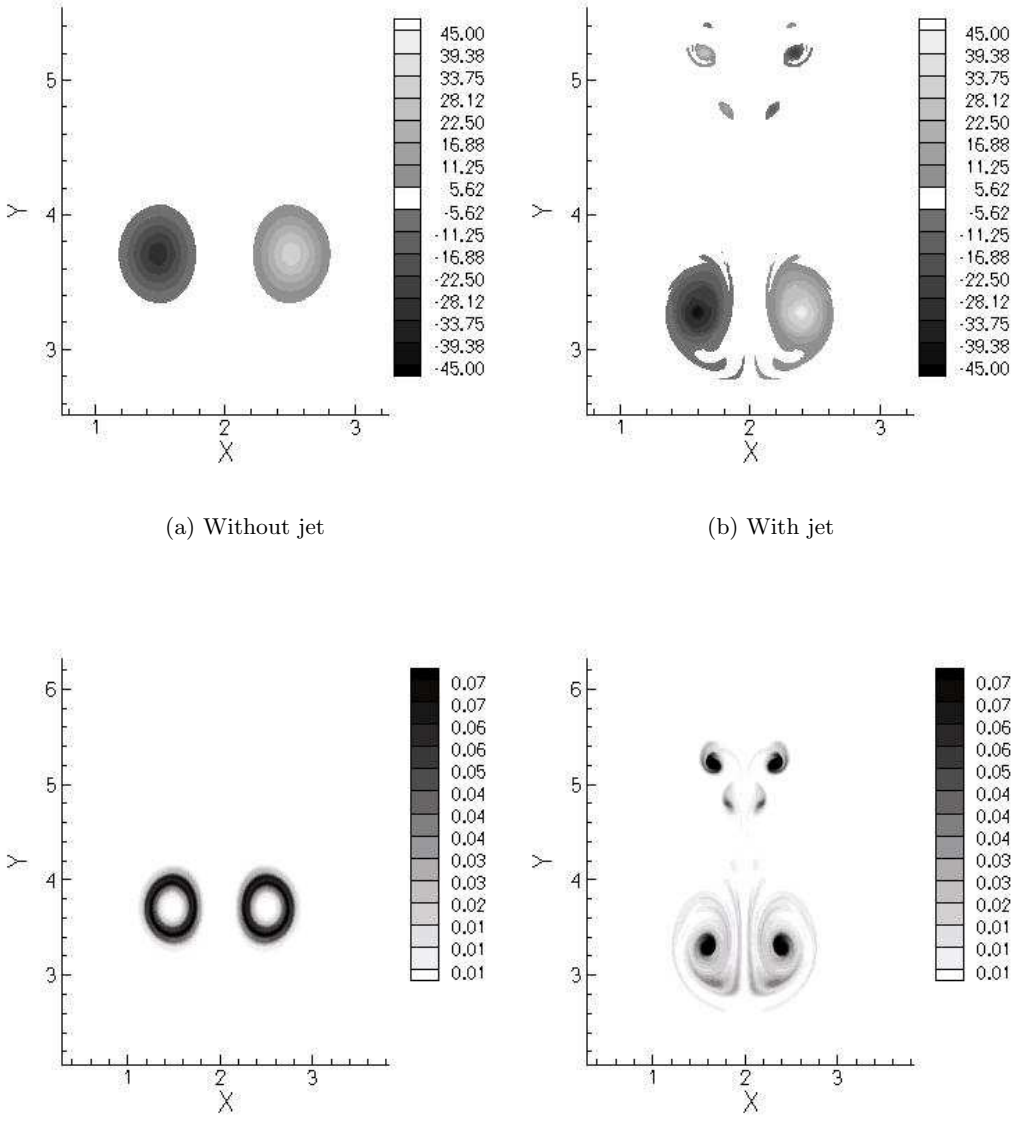

(a) Without jet

(b) With jet

(c) Without jet

(d) With jet

Figure 5.14: Vorticity (top) and passive scalar (bottom) transport at $t = 3.5$ in an unstratified atmosphere without the jet, $\beta = 0$; and with jet, $\beta = 0.05$.

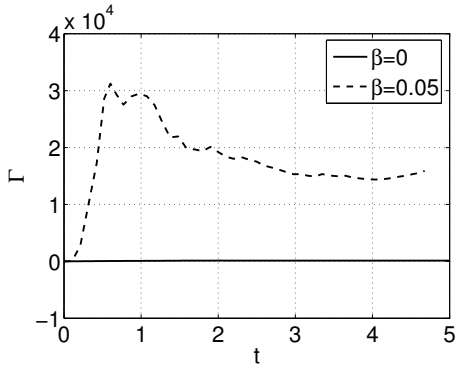

(a) Positive component

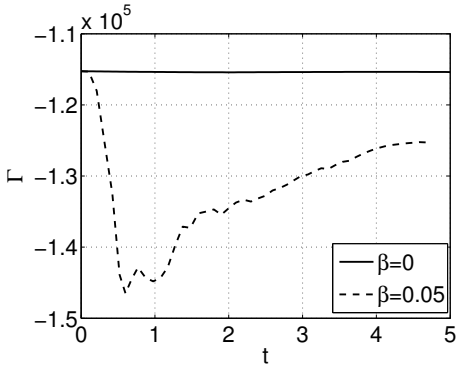

(b) Negative component

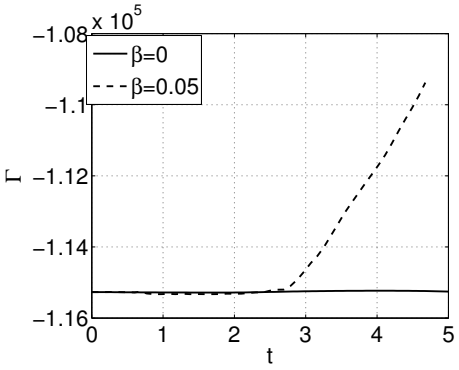

(c) Total

Figure 5.15: Positive, negative components and total circulation in the left half ($x < 2$) in an unstratified atmosphere without the jet, $\beta = 0$; and with jet, $\beta = 0.05$.

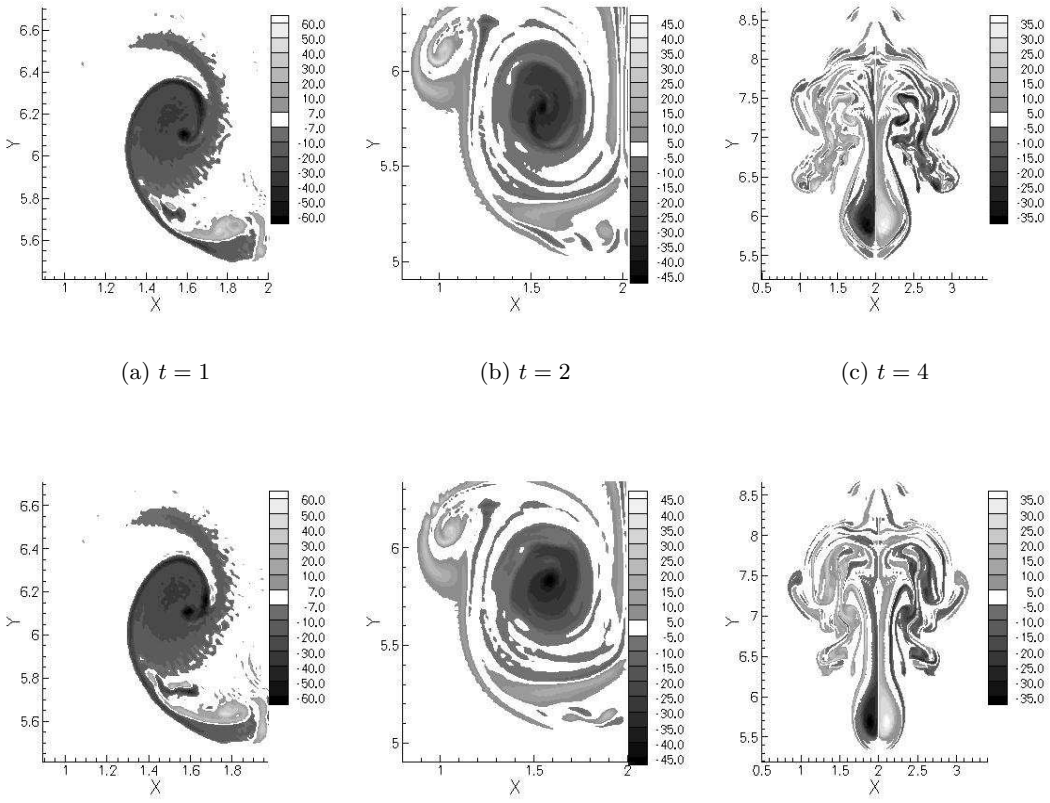

(a) $t = 1$ (b) $t = 2$ (c) $t = 4$

(d) $t = 1$ (e) $t = 2$ (f) $t = 4$

Figure 5.16: Vorticity evolution for the baseline case using traditional (upper) and extended (lower) Boussinesq approximations. Note that up to $t = 2$ only the left vortex is shown for clarity. The right side is symmetric about $x = 2$.

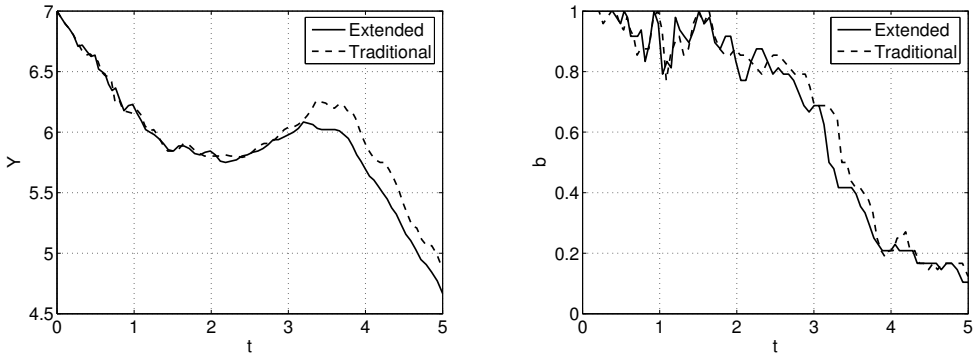

(a) Vertical position

(b) Vortex spacing

Figure 5.17: Movement of vortex centers for the baseline case with traditional and extended Boussinesq approximation.

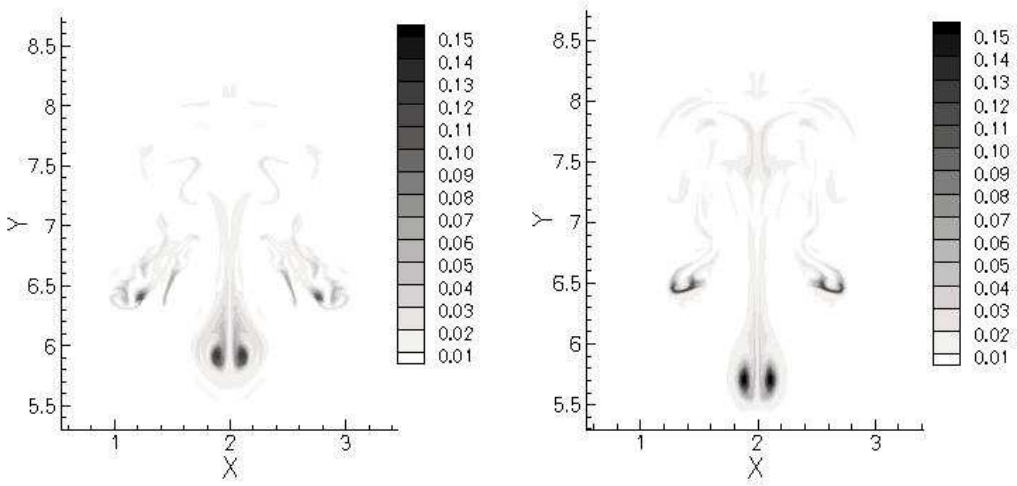

(a) Traditional

(b) Extended

Figure 5.18: Passive scalar distribution at $t = 4$ with traditional and extended Boussinesq approximation.

Chapter 6

Sensitivity Study of Early Stage Contrails

Having developed and validated the required numerical methodology, we now explore the parametric sensitivities of contrail growth on atmospheric conditions and selected aircraft exhaust parameters in the early stage. The early stage here refers to the first 20 seconds. We do not consider the effects of atmospheric turbulence. In the late stages (few minutes) as the vortices break down due to three-dimensional instabilities, atmospheric turbulence can play a dominant role (along with wind shear) in the dispersion and spreading of contrails (Jensen *et al.*, 1998; Lewellen & Lewellen, 2001; Gerz & Hölzapfel, 1999). Radiative heating plays a substantial role for long-term contrails beyond 15 minutes (Jensen *et al.*, 1998). Also, the long-wave sinusoidal instability (Crow, 1970) has a time scale of approximately $50 - 100$ seconds for the representative aircraft considered here, over which the Crow perturbation is estimated to grow by an order of magnitude (Rennich, 1997). As suggested by the RANS simulations in Chapter 3 with the help of the nondimensional parameter R, the jet-vortex wake interaction is strong in the current regime. Considering all these factors, the early stage up to 20 seconds provides us a distinct regime for obtaining valuable information about the sensitivity of the jet- and wake-scale processes to various parameters.

The jet-scale thermodynamics associated with the mixing of the jet exhaust with ambient air are strongly influenced by atmospheric conditions. The atmospheric parameters varied here are the ambient temperature and relative humidity, and the aircraft parameters varied are the number of ice nuclei in the jet exhaust and the initial ice particle radius. Since the ice nuclei are carbonaceous particulates formed by nucleation of combustion exhaust species,

the number of ice nuclei increases with the fuel burn rate. All of these parameters involve uncertainties and the prediction of themselves presents challenging modeling questions that have received attention in other studies. Therefore, a study of the sensitivity of contrails to these parameters is warranted to assess their impact on contrails.

The description of parameters for the baseline case used for comparison was presented in Chapter 3. For the parametric study we vary the ambient relative humidity with respect to ice (RHi), ambient temperature (T_{amb}), the initial number of ice nuclei (N_p), and the initial ice particle size (r_{po}). RHi is defined as X/X_{sat} where X and X_{sat} are respectively the mole fractions of water vapor in the atmosphere corresponding to the cruise altitude and the saturation water vapor mole fraction. The simulations studied here are summarized in Table 6.1. In all cases, except Case $T2$, fluid turbulence is seeded in the initial fields so as to get turbulence development in the jet (see Section 6.1 for details). Using the Case $T2$ we evaluate the extent to which the jet turbulence affects the contrail growth (Section 6.7). All simulations begin at 1 second behind the tail plane of the aircraft which is equivalent to 5 wingspans downstream of the tail-plane. The simulations were carried out for a duration of $19s$ of physical time, i.e., $20s$ after the tail plane of the aircraft. The initialization of the flowfields and ice particles is explained in Section 6.1. We will study the baseline case (A1) in detail and then the parametric variation.

All contour plots in this chapter show nondimensional variables unless units are specified. Distance is nondimensionalized by the wing span, velocities by the cruise speed, perturbation temperature by the initial peak jet temperature fluctuation, 4.376 K (this value is from the Boeing data), and water vapor density by the ambient air density. The simulations are temporal simulations, meaning that in the computational domain, the streamwise (i.e. in the flight direction) variation of ensemble-averaged flow features is neglected compared to their temporal evolution. This assumption is justified in this case because the cruise speed is very high compared to the convective flow scales of interest (i.e. vortex descent speed). It should be noted that the streamwise flow features are *not neglected*, but only the streamwise variations of their ensemble-averages are neglected. A consequence of this assumption is that the flow is considered periodic in the flight direction. The flight direction z is a slowly varying (see Chapter 3), homogeneous direction. Hence the flow visualizations are presented in the z-averaged form.

Table 6.1: Simulation cases

Case	Ambient Temperature T_{amb}, K	Relative Humidity $RHi, \%$	Number of Ice Nuclei $N_p, \#/m$	Initial ice particle radius $r_{po}, \mu m$	Turbulence seeded
$A1$	220	110	5.787×10^{12}	0.1	Yes
$A2$	220	130	5.787×10^{12}	0.1	Yes
$A3$	220	90	5.787×10^{12}	0.1	Yes
$B2$	200	110	5.787×10^{12}	0.1	Yes
$B3$	240	110	5.787×10^{12}	0.1	Yes
$C2$	220	110	2.894×10^{12}	0.1	Yes
$C3$	220	110	1.447×10^{12}	0.1	Yes
$E2$	220	110	5.787×10^{12}	0.05	Yes
$E3$	220	110	5.787×10^{12}	0.2	Yes
$T2$	220	110	5.787×10^{12}	0.1	No

The initial conditions for all cases have constant **ambient** water vapor density over the entire domain which are different for different RHi. The initial vapor density is obtained by imposing the stipulated RHi value at the initial vertical location of the vortex wake, $y = 3$, hence the RHi fields vary with y. Over this ambient vapor density field, the additional water vapor coming from the exhaust jet is added. (See Figure 6.19.)

6.1 Generation of initial conditions

The initial conditions (IC) model both the flow data and ice particles at 5 wingspans downstream of a 767 type aircraft. The process of generating the IC is described below.

6.1.1 Flow data

The initial mean fields at 5 wing spans downstream of the aircraft were provided by Boeing. They were obtained by Boeing using RANS simulations in region immediately downstream of the aircraft. The Boeing data was interpolated onto the uniform grid used in this work, and turbulence was seeded into the field. For this we first generate a homogeneous isotropic turbulence field with the von-Karman spectrum, given by

$$E(k) = C\frac{(k/k_o)^4}{(1+(k/k_o)^{17/6}}exp[-\alpha(k/k_o)^2] \tag{6.1}$$

The constant k_o and α were chosen such that the peak of the spectrum occurs at a location $k_o = 2\pi/L$, where L is the average longitudinal integral length scale in the jet-axial and azimuthal directions,

$$L = \frac{L_{11}+L_{22}}{2} \tag{6.2}$$

Empirical observations suggest that $L_{11} \approx 0.7\ r_{1/2}$ and $L_{22} \approx 0.3\ r_{1/2}$, where $r_{1/2}$ is the radial distance at which the jet axial mean velocity falls to 50% of its peak value (Pope (2001)). Hence $L \approx 0.5\ r_{1/2}$. We estimated $r_{1/2}$ from the jet mean axial velocity contours by taking the average of $r_{1/2}$ in x and y directions. This gave $r_{1/2} \approx 2.81m$. Hence $L \approx 1.4m$.

The same spectrum mentioned above is also used to seed the humidity and temperature fields by randomly-phased fluctuations. The resultant turbulent field is localized in the physical domain to regions of the jet. This is done by scaling the turbulent fields to be proportional to the local axial velocity, and superimposing them onto the mean fields. This process causes a small velocity divergence to appear. Its maximum value is approximately 0.15% of the peak vorticity in the vortex cores, and was monitored during the simulation and was found to remain at that level throughout the simulation duration. The jet peak mean humidity was matched with that being used by Boeing ($1.14 \times 10^{-4} kg/m^3$). Atmospheric humidity is added on top of the jet humidity. For the baseline case ($RHi = 110\%$ at $T_{amb} = 220K$, $P_{amb} = 238.5hPa$) the ambient water vapor density was $2.4817 \times 10^{-5}\ kgH_2O/m^3$. The initial conditions for the flow are shown in Figure 6.1. The choice of RHi for simulations

is somewhat arbitrary, but it is taken as 110% or more in most cases so as to allow for the physical problem to contain heterogeneous nucleation of ice particles (Schumann, 2005), even though the nucleation stage is not a part of the simulations and hence not modeled here.

6.1.2 Particle data

As discussed before, the choice of the number of computational Lagrangian particles $N_{comp} \approx 10^6$ was done after careful validation. An ensemble of these many particles was generated with their number density in any grid cell proportional to the local jet water vapor content. The initial ice particle size distribution is taken to be unimodal with radius $0.1\mu m$ except for cases $E2$ and $E3$. The ice properties at the initial time $t = 1\ s$ are depicted in Figure 6.2.

6.2 Baseline case

The baseline case $A1$ was simulated for the duration $t = 1\ s$ to $t = 20\ s$ and here we describe some general features before looking at parametric variation in the subsequent sections. The three dimensional isosurface of vorticity magnitude (Figure 6.3) shows the vorticity being wrapped around the trailing vortices and the elongated vorticity structures produced due to the high strain at the lower end of the descending Kelvin oval typically encountered in vortex wake descent (Spalart, 1996; Moet *et al.*, 2001). Similar structures have also been observed in LES by Paoli *et al* (2003) and Moet et al. (2001).

The evolution of water vapor density is shown in Figure 6.4. It can be seen that the main transport of humidity is dominated by the wake vorticity. The initial data from Boeing was on the domain $x \in (2, 4)$, $y \in (1.2, 4.8)$ which was mirrored about the plane $x = 0$ and interpolated onto our domain which is $x \in (0, 4)$, $y \in (0, 5)$ in such a way that in our domain the plane of symmetry is $x = 2$ and the vertical position of the wake is around $y = 3$ to allow sufficient domain height for the wake descent in 20 s. The nonuniformities in the initial data along with the small errors caused by interpolation give rise to some noise. However, these noisy features were observed to be away from the jet and the ice particles, so are not expected to affect the overall ice properties. Inside the jet-dispersion region there are a lot of small-scale variations which result from the strong coupling of the humidity field with the ice particles that have positions that were random in each grid cell. Also contributing to this small-scale "turbulence" is the phenomenon of stochastic condensation (Shaw, 2003)

which means that the spatial inhomogeneities in particle distribution will generate gradients of supersaturation in turn affecting the particle size evolution.

The initial rapid straining of the jet and the subsequent entrainment into the vortices is visible in Figure 6.4. The regions of water vapor depletion prominently appear where large amounts of ice is formed. This can be seen by comparing the spatial structures of humidity in (Figure 6.4) and of ice (Figure 6.7). The depletion effect is caused by the fact that if high particle number density exists in a cetrain fluid element, the rate at which water vapor is used up through deposition is also high resulting in a low vapor density. Similar effect is observed in the perturbation temperature (Figure 6.5) where high temperature is collocated with high ice formation. One reason for this is the initial spatial correspondence between the high-humidity and high-temperature regions in the jet. But another mechanism is the freezing of water vapor on particles which deposits latent heat into the vapor phase. Estimates based on the peak ice particle number density of $85,000\ \#/cc$ (Figure 6.6) and assuming all particles have grown to $0.6\mu m$ (Figure 6.9) give a temperature change of $0.52\ K$ locally. This is approximately 16% of the jet peak perturbation temperature at $5\ s$ and 80% of it at $10\ s$. This suggests that the latent heat transfer constitutes a significant component of the total temperature perturbation. Contours of ice water content at various times during contrail growth are depicted in Figure 6.7. To obtain the Eulerian fields corresponding to the Lagrangian particles, the quantity of interest (e.g. ice water content) in a given Eulerian grid cell is computed by integrating that quantity over all the particles inside that grid cell.

The total water budget (Figure 6.8) shows fast initial ice growth due to the high supersaturation in the jet, and corresponding water vapor depletion in the air. The total amount of water vapor plus ice is satisfactorily conserved by the numerical method at least over the duration of simulations, indicated by the fact that the error remains within 0.04% of the total water content (vapor plus ice) in the simulation duration. Part of this error can be attributed to the numerical errors in conservation of the passive scalar (Figure 4.5). It should be noted that only vapor and ice phases of water are present as by $t = 1s$ where the LES begins, the jet has diluted sufficiently so that the peak jet temperature is only $10\ K$ in excess of the ambient temperature (Figure 3.3). Hence any liquid water is assumed to have already frozen.

Figure 6.9 shows the global ice properties for the baseline case. Although the ambient RHi is supersaturated, the warm jet can cause locally subsaturated regions, hence the number of ice particles reduces due to evaporation. The turbulent transport in the jet

would affect this trend, which is not captured by simple integral models. Simulations by Lewellen and Lewellen (2001) show similar qualitative trends but the magnitudes differ possibly due to the different aircraft parameters and other model uncertainties. Probably the most important contrail property is the surface area of particles because it relates to the radiative characteristics of the contrail. The area is observed to increase under these supersaturated conditions. An interesting characteristic of ice growth that can be inferred from Figure 6.9 is the qualitatively distinct regimes of growth. The initial rapid growth in the first couple of seconds results from the large supersaturation presented by the exhaust moisture content. The ice particle radius matches well with Baumgardner and Cooper (1994) who found the mean ice particle radius at 1.5 km downstream into the wake of a Lear jet 35 aircraft to be $0.75\mu m$. Next, roughly between 3 and 10 seconds the growth characteristics are different. We discuss this phase later in Section 6.7 where we find that jet-scale turbulence affects the ice properties in this regime. Finally, a slowly-varying growth regime is reached beyond 10 s or so when the jet humidity has dissipated due to turbulence and consumed by ice formation (as seen from magnitudes of humidity in Figure 6.5), and is no longer significant. This regime is principally controlled by the atmospheric RHi as we shall see later in Section 6.3.

The size distribution of ice particles in Figure 6.10 shows that there is a rapid initial (before $t = 1.16$) evolution of the PDF of ice particle size. After that, although the peak of the PDF does not shift much, the tails of the distribution function on both sides get shifted to the right. But after 5 s the distribution starts to become broader and the peak reduces, indicating that the effect of the initial unimodal distribution has gradually faded away and the flow and thermodynamic inhomogeneities are governing the ice particle characteristics. This appearance of larger particles is important because it will change the radiative properties of the contrail, and in the long-term may facilitate inter-particle collisions, coagulation and sedimentation.

6.3 Effect of relative humidity

Ambient relative humidity is evidently one of the most important factors deciding if a contrail will be persistent or evanescent. It has been observed through Lidar measurements (Sussman & Gierens, 1999) that a supersaturated atmosphere is highly conducive to the persistence of contrail, and hence to the appearance of anthropogenic cirrus clouds. These

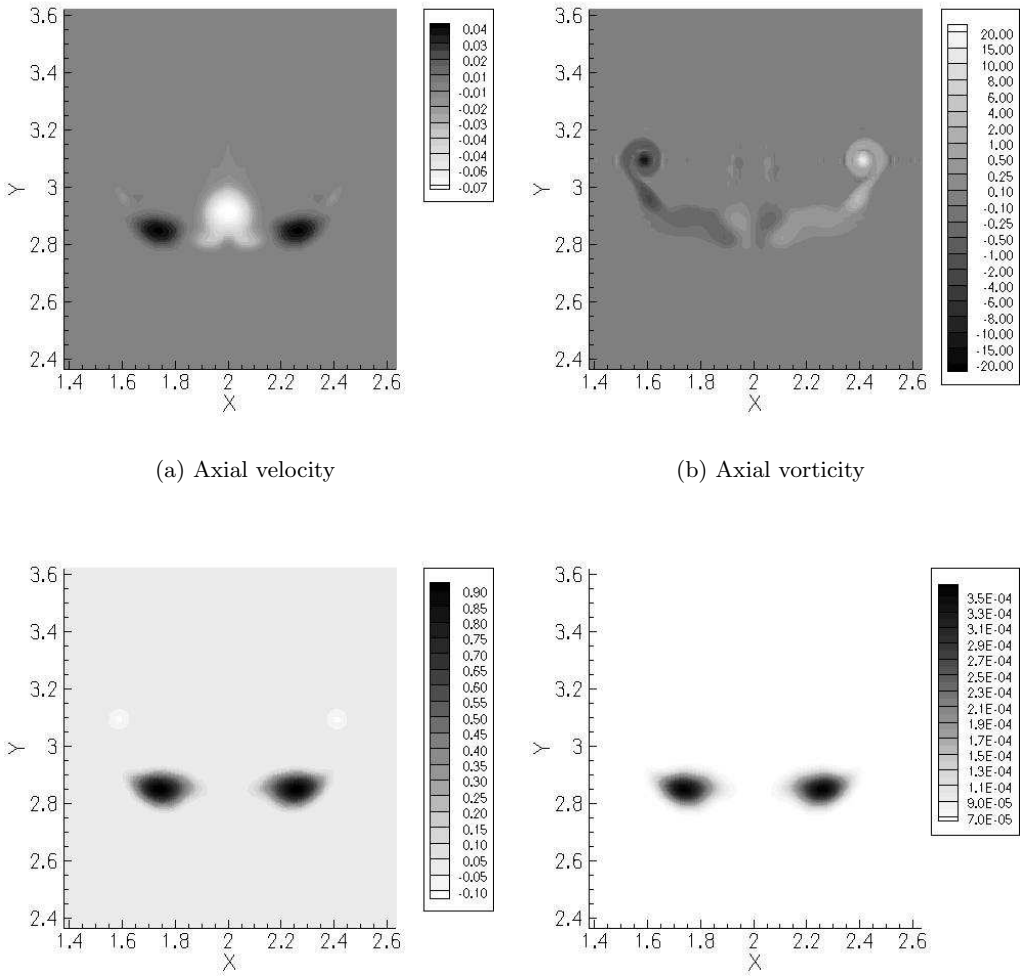

(a) Axial velocity

(b) Axial vorticity

(c) Perturbation temperature

(d) Water vapor density

Figure 6.1: Initial flowfield at 5 wingspans. It is obtained by interpolation of and turbulence addition to the data provided by Boeing which was obtained by RANS simulations performed by Boeing. All variables are normalized.

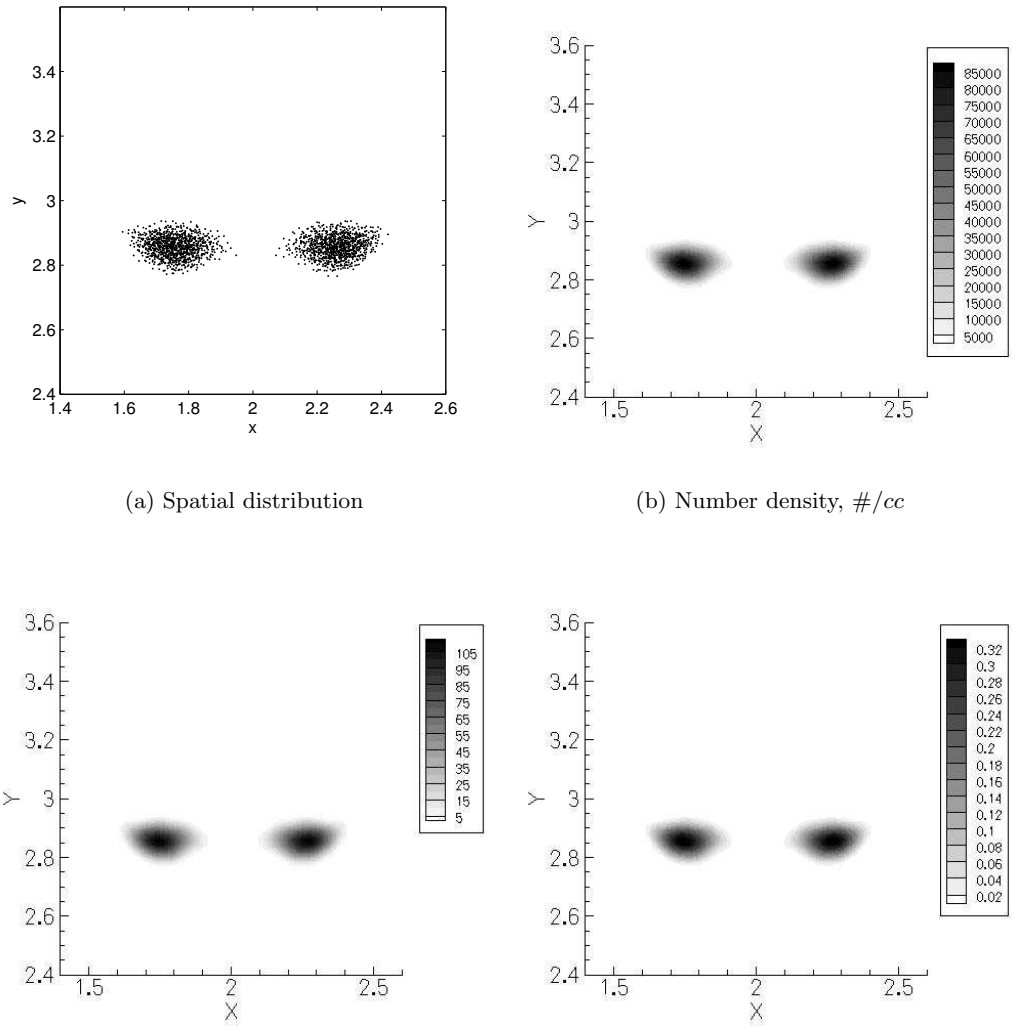

(a) Spatial distribution

(b) Number density, $\#/cc$

(c) Surface area, cm^2/m^3

(d) Ice water content, mg/m^3

Figure 6.2: Initial ice properties at 5 wingspans. Number density of particles is made proportional to the water vapor density at each grid point. Particle size distribution is unimodal with $r_p = 0.1\mu m$.

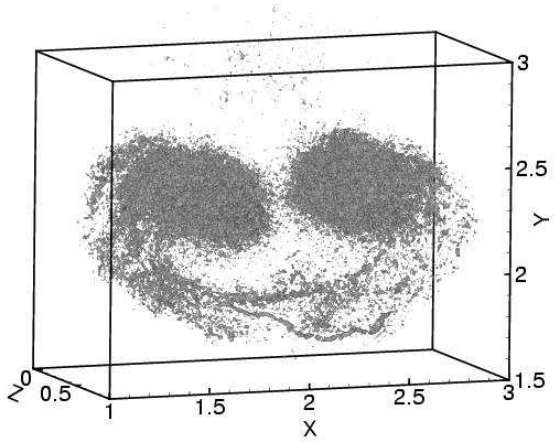

Figure 6.3: Isosurface of vorticity magnitude 1.5 at $t = 20$ s for the baseline case. Elongated vorticity structures are visible.

observations suggest that for $RHi < 100\%$, all contrails disappear at the end of the vortex regime, for $RHi \approx 100\%$ the contrails persist until the vortex breakdown but disappear in the dispersion regime, and for $RHi > 100\%$, the contrails become persistent. In addition to growth, optical depth and contrail width also strongly depend on the RHi (Jensen *et al.*, 1998). Jensen *et al.* also compare the results from their models with those from the SUCCESS (Subsonic Aircraft: Contrail and Cloud Effects Special Study) experiment which gave similar trends, but discrepancies between the model and experiments were observed below $RHi < 125\%$. This and other LES studies (e.g. Chlond, 1998) have investigated the dispersion regime (30 minutes and more), and the initial conditions are susceptible to uncertainties especially since jet-scale resolution is not computationally feasible for these long-term calculations. In the current study we vary the ambient RHi and characterize the ice properties and statistics for the early evolution.

The distribution of water vapor, perturbation temperature, ice particle number density and ice mass density are shown in Figures 6.11-6.18 for cases A2 and A3. Comparing with Figures 6.4-6.7 we see that the qualitative behavior of various variables is not so sensitive to the RHi value, but as observed from the contour levels, the magnitudes of variables are quite different for different RHi. The time histories of global ice properties are shown in Figure 6.20 for RHi values of 110%, 130% and 90%. The most interesting trend is seen in Figure 6.20(a) where it is seen that higher RHi does not necessarily slow down the loss of ice particles. The particle number decay is slower for $RHi = 110\%$ than that for

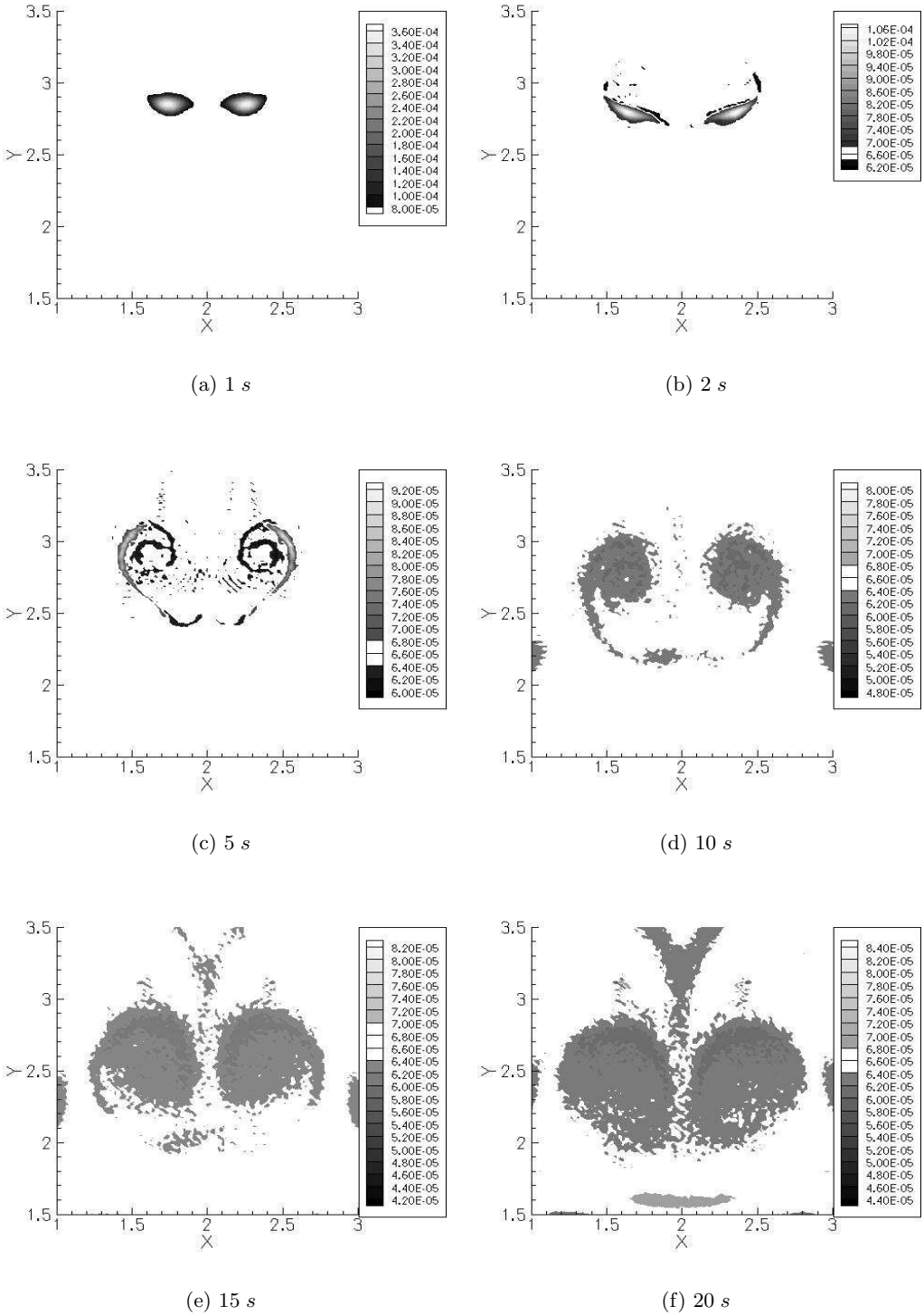

(a) 1 s (b) 2 s

(c) 5 s (d) 10 s

(e) 15 s (f) 20 s

Figure 6.4: Evolution of water vapor density for case A1.

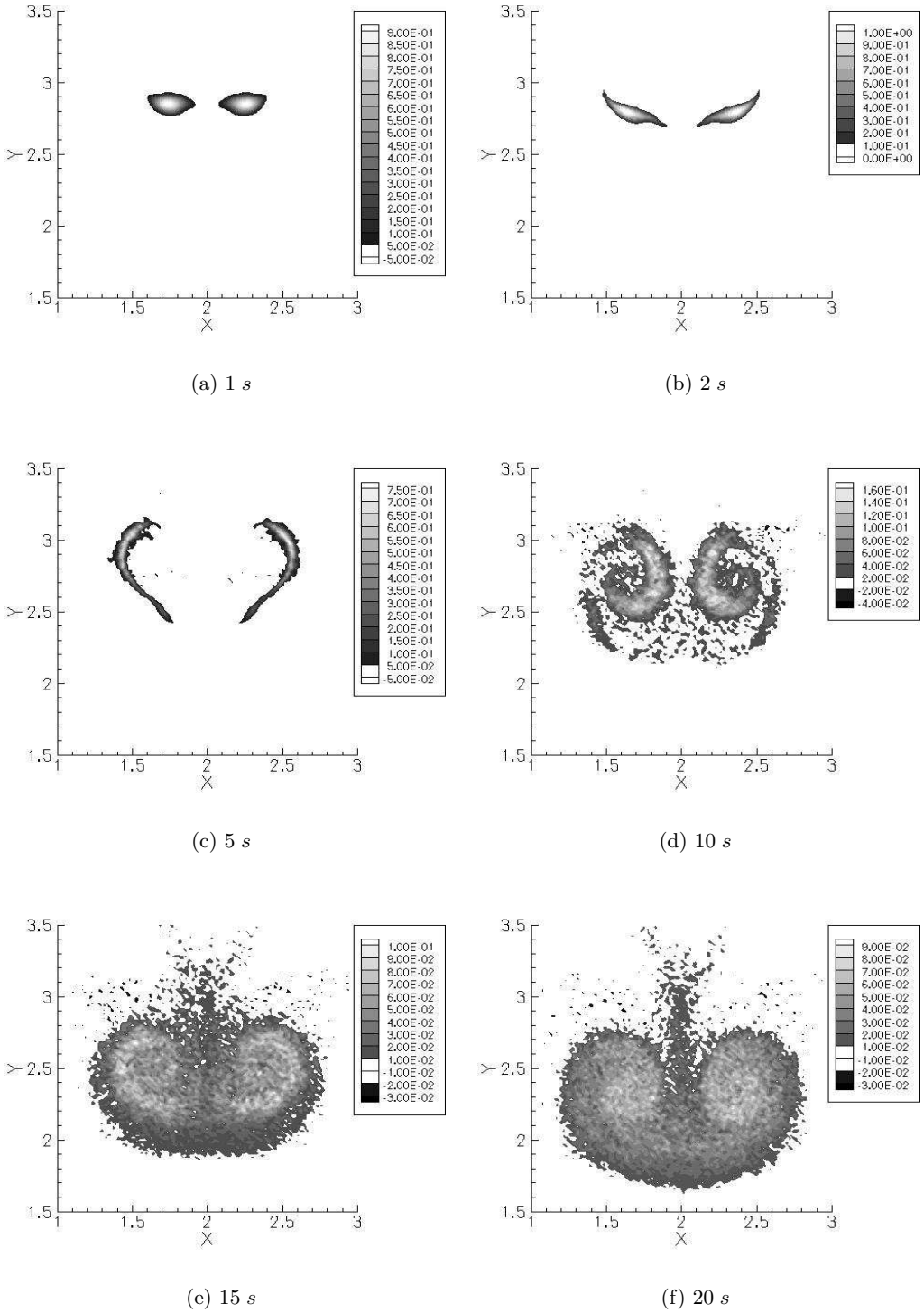

(a) 1 s (b) 2 s

(c) 5 s (d) 10 s

(e) 15 s (f) 20 s

Figure 6.5: Evolution of perturbation temperature for case A1.

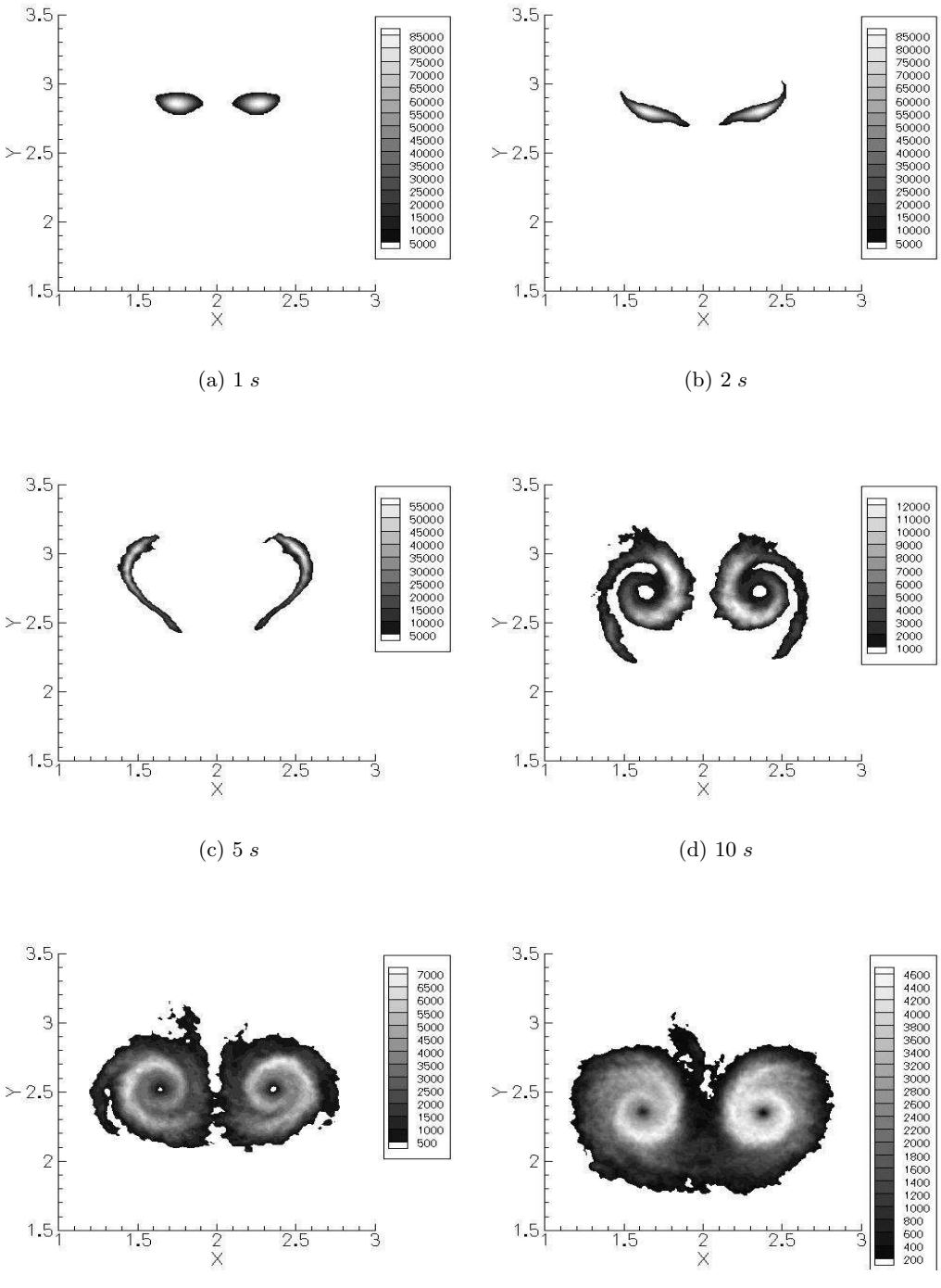

(a) 1 s (b) 2 s

(c) 5 s (d) 10 s

(e) 15 s (f) 20 s

Figure 6.6: Evolution of ice particle number density (in $\#/cc$) for case A1.

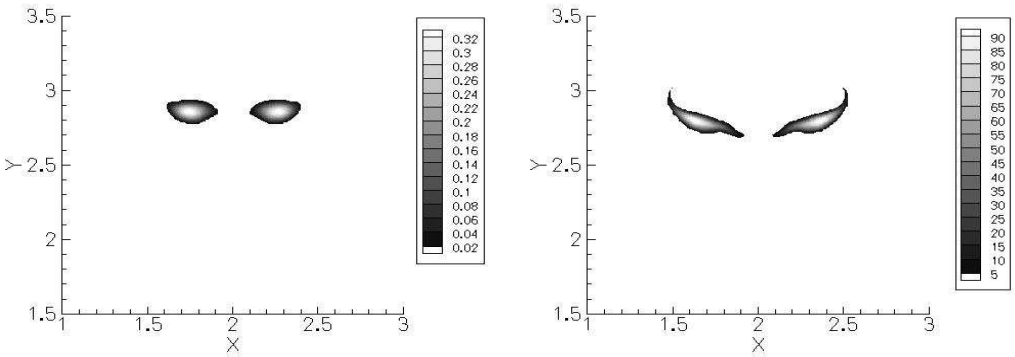

(a) 1 s

(b) 2 s

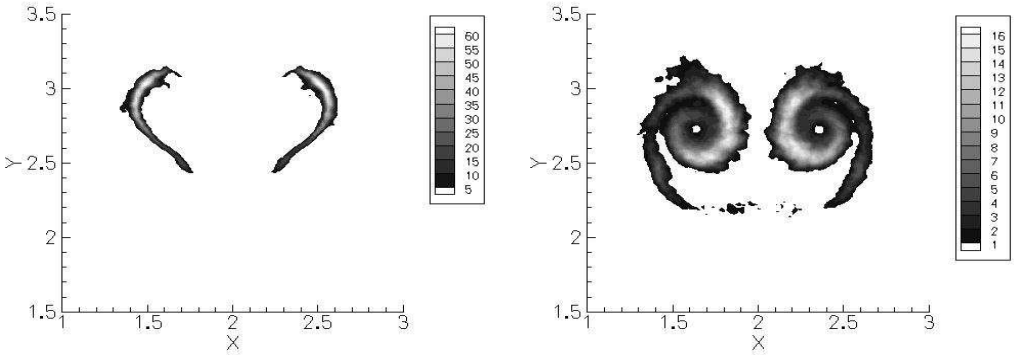

(c) 5 s

(d) 10 s

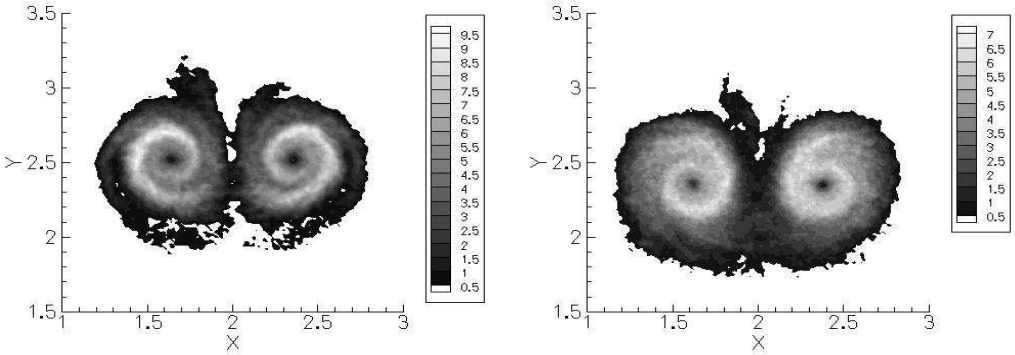

(e) 15 s

(f) 20 s

Figure 6.7: Evolution of ice water content (in mg/m^3) for case A1.

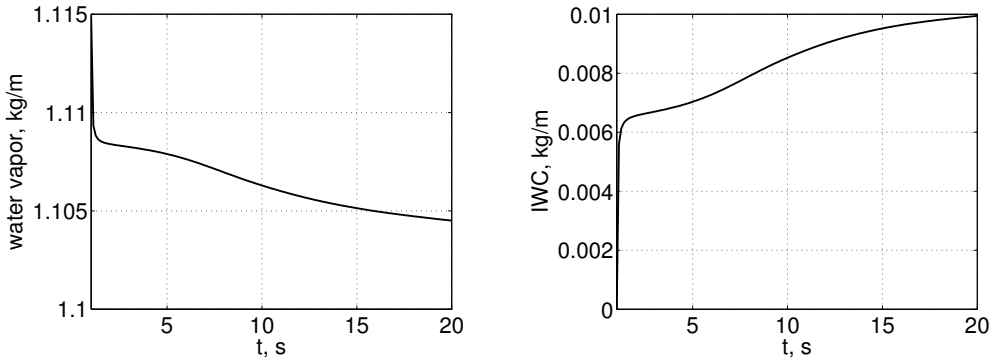

(a) Water vapor

(b) Ice

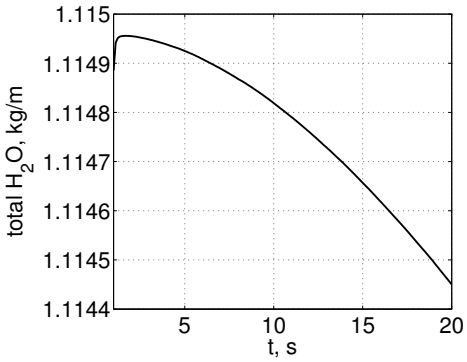

(c) Total water

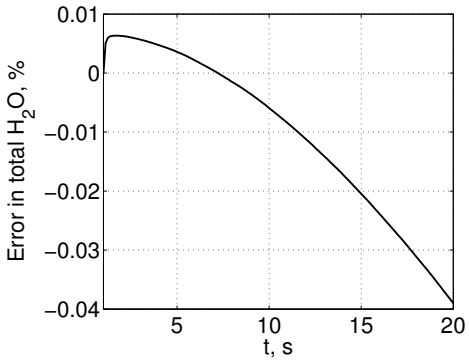

(d) Error in total water conservation

Figure 6.8: Total water budget

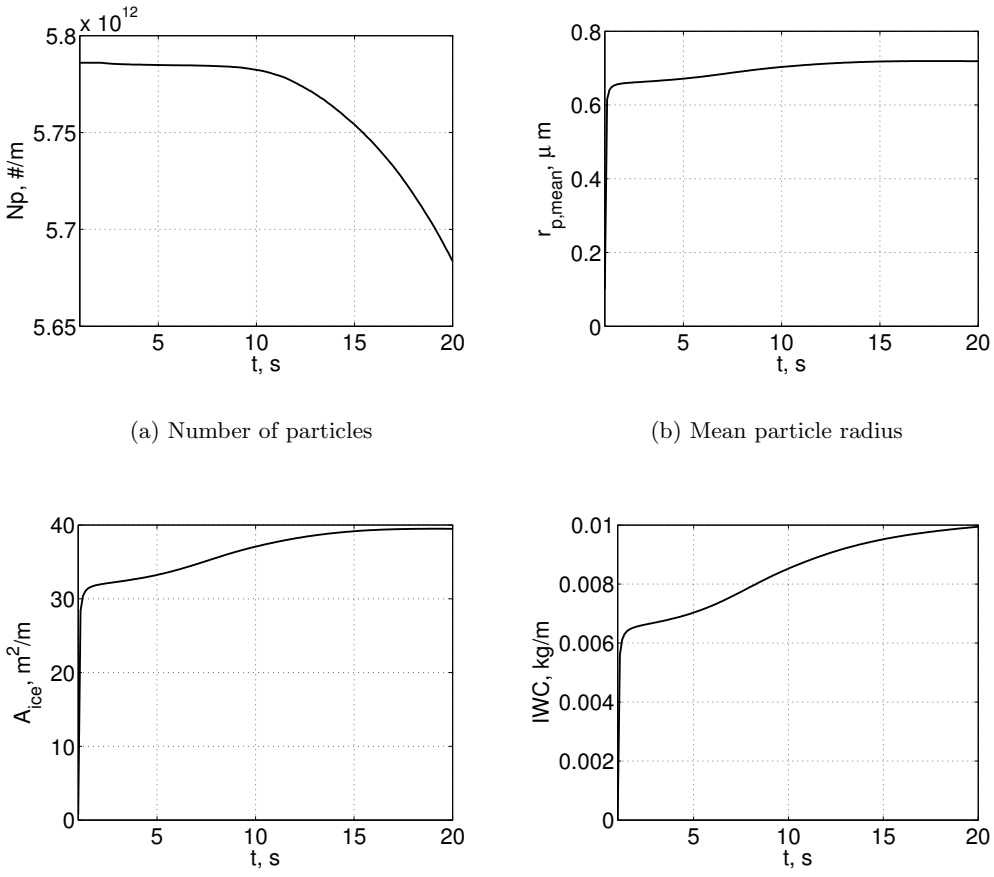

(a) Number of particles

(b) Mean particle radius

(c) Ice surface area

(d) Ice water content

Figure 6.9: Domain-integrated ice particle properties for case A1.

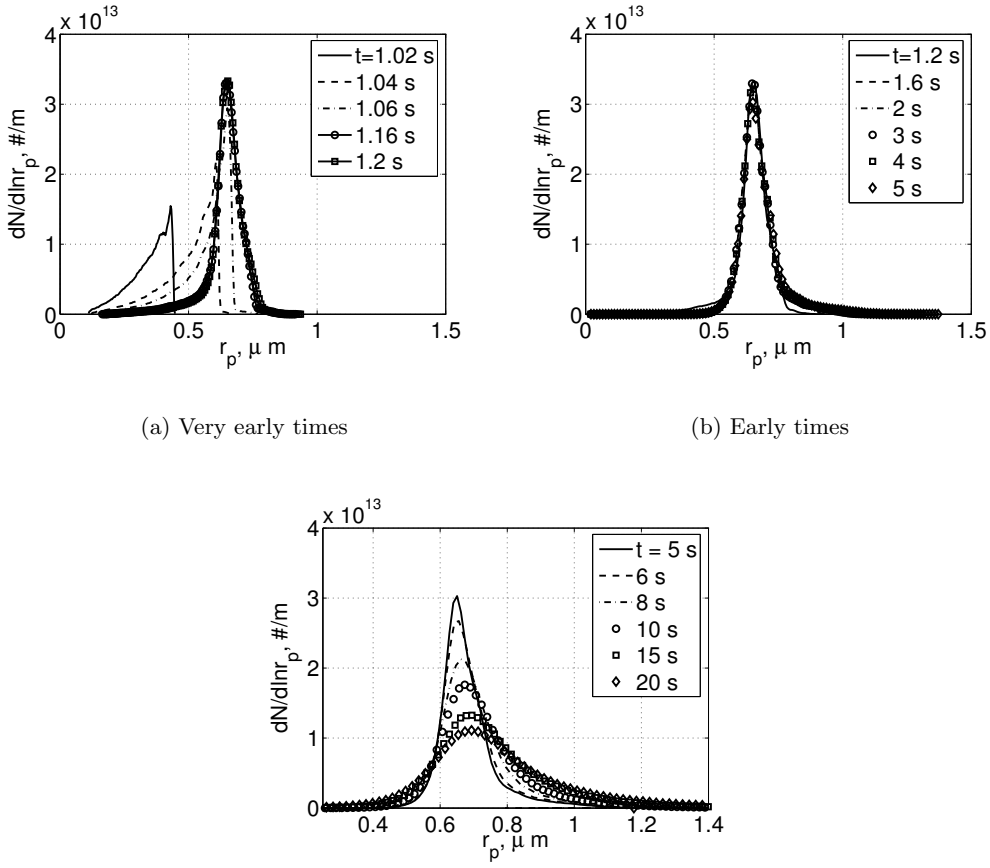

(a) Very early times

(b) Early times

(c) Intermediate times

Figure 6.10: Ice particle size distribution at various times for Case $A1$. At $t = 1s$ the distribution is unimodal with radius $0.1\mu m$. Broadening of the PDF is visible in the intermerdiate stage.

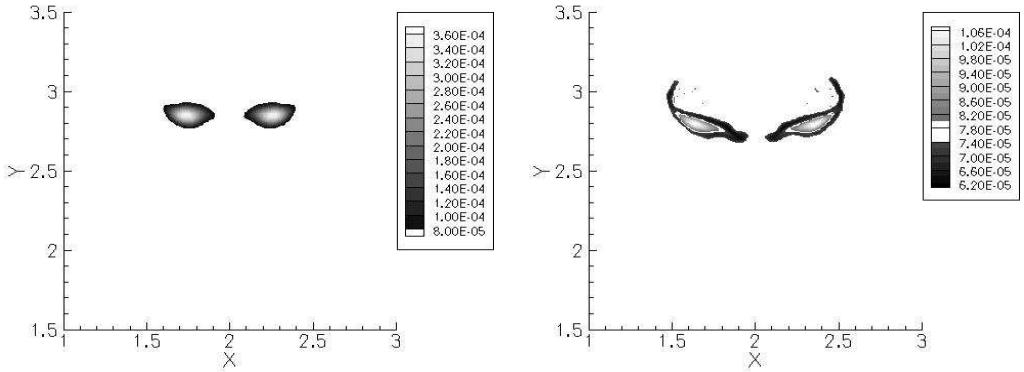

(a) 1 s (b) 2 s

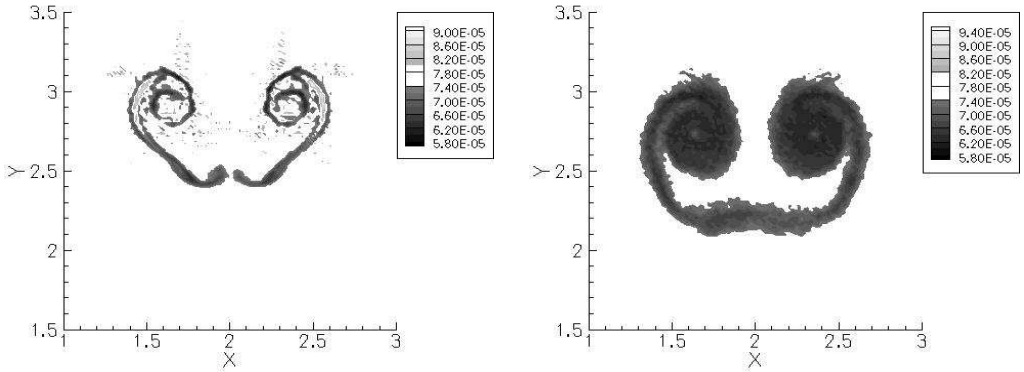

(c) 5 s (d) 10 s

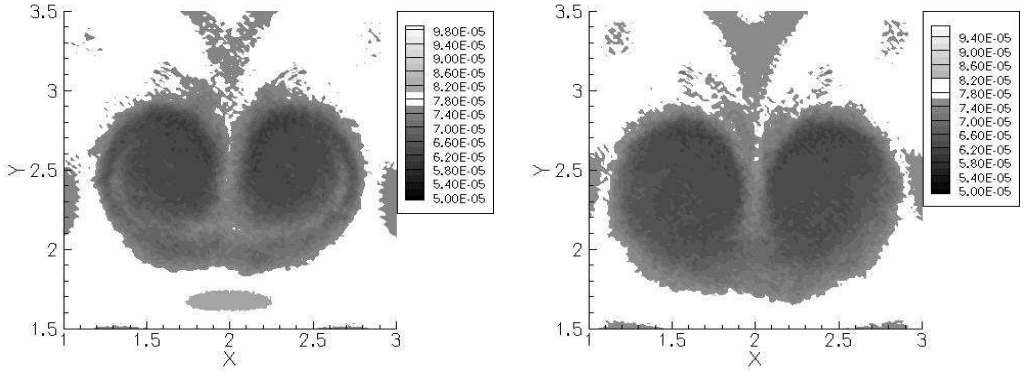

(e) 15 s (f) 20 s

Figure 6.11: Evolution of water vapor density for case A2.

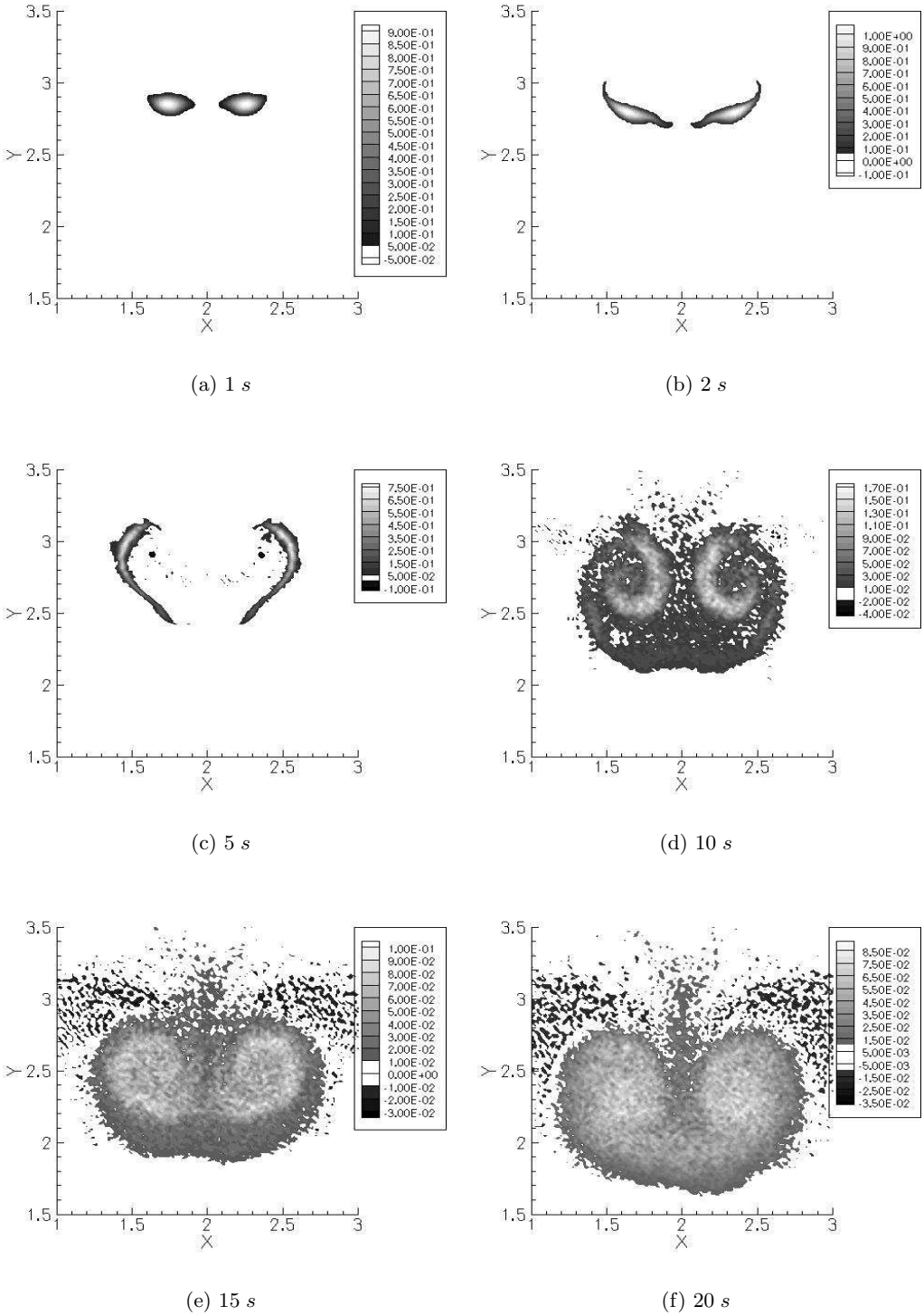

(a) 1 s (b) 2 s

(c) 5 s (d) 10 s

(e) 15 s (f) 20 s

Figure 6.12: Evolution of perturbation temperature for case A2.

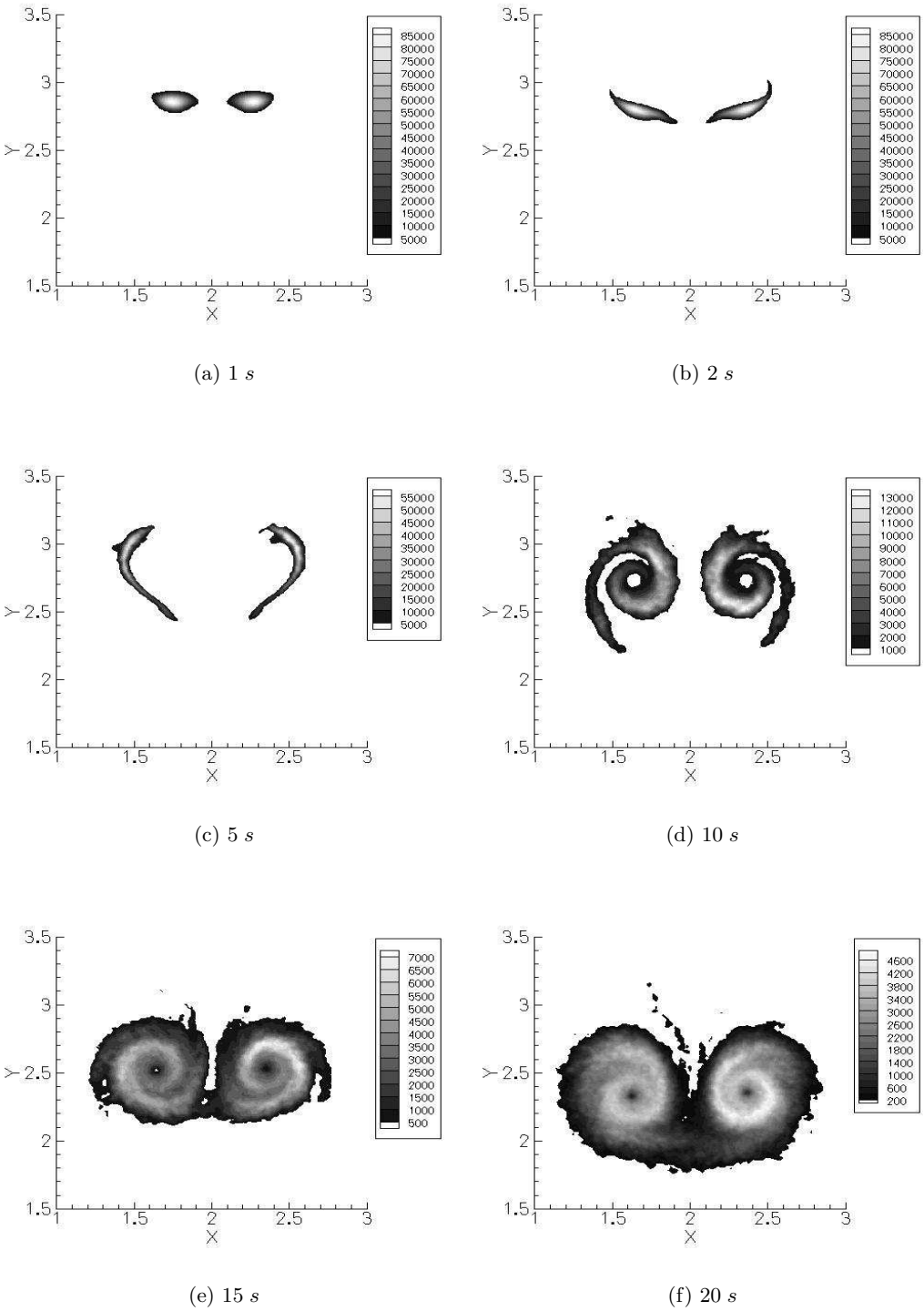

(a) 1 s (b) 2 s

(c) 5 s (d) 10 s

(e) 15 s (f) 20 s

Figure 6.13: Evolution of ice particle number density (in $\#/cc$) for case A2.

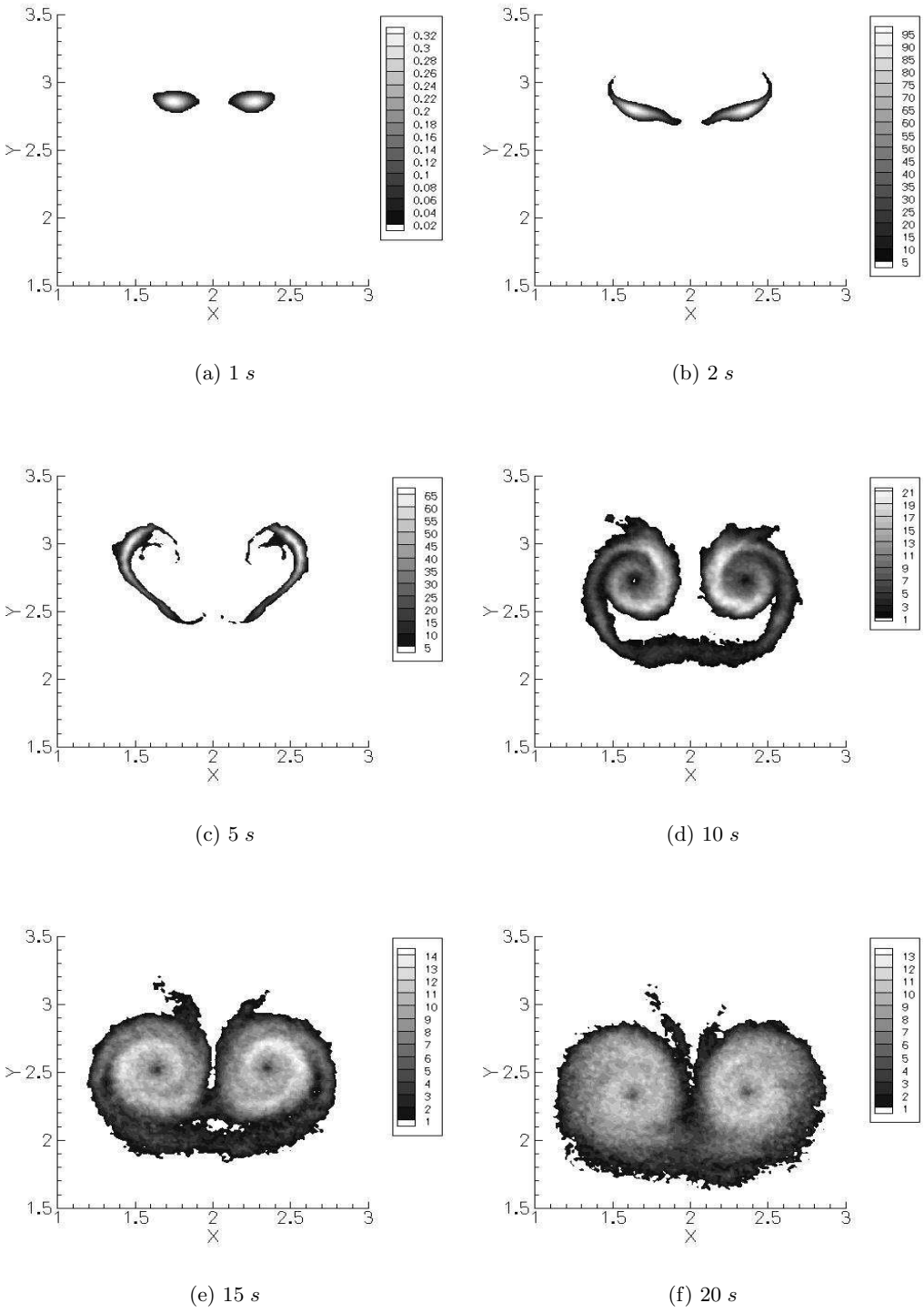

(a) 1 s (b) 2 s

(c) 5 s (d) 10 s

(e) 15 s (f) 20 s

Figure 6.14: Evolution of ice water content (in mg/m^3) for case A2.

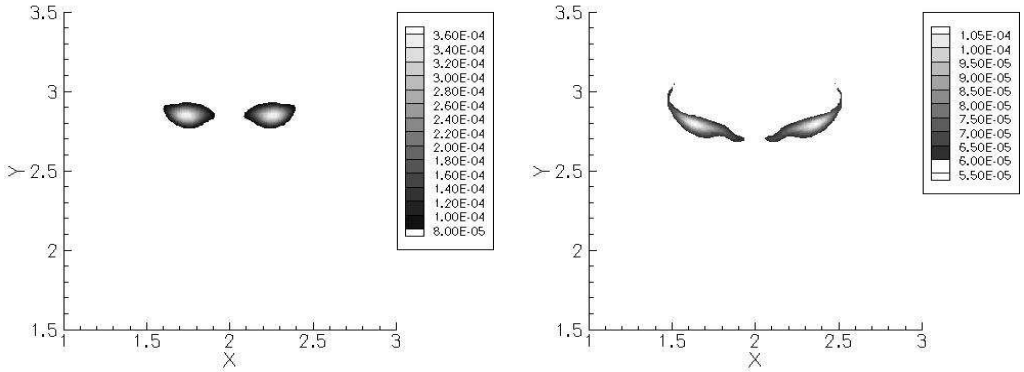

(a) 1 s

(b) 2 s

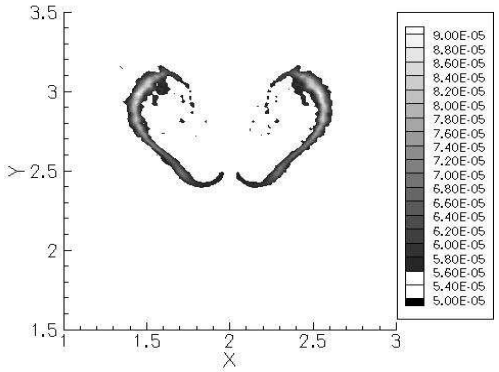

(c) 5 s

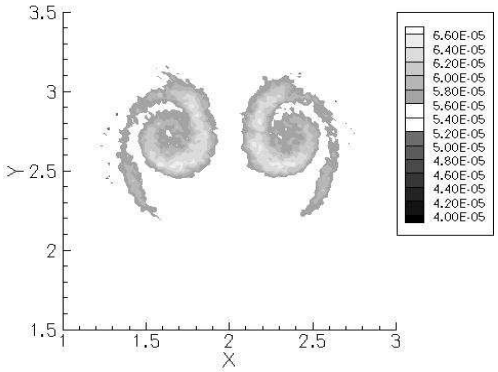

(d) 10 s

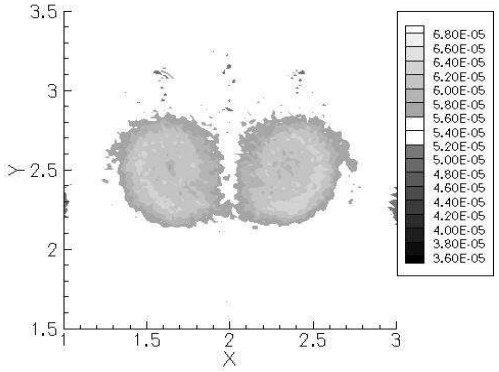

(e) 15 s

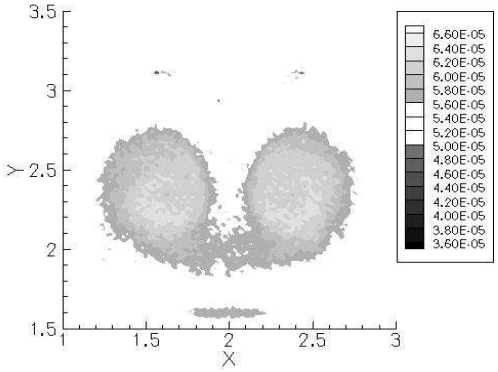

(f) 20 s

Figure 6.15: Evolution of water vapor density for case A3.

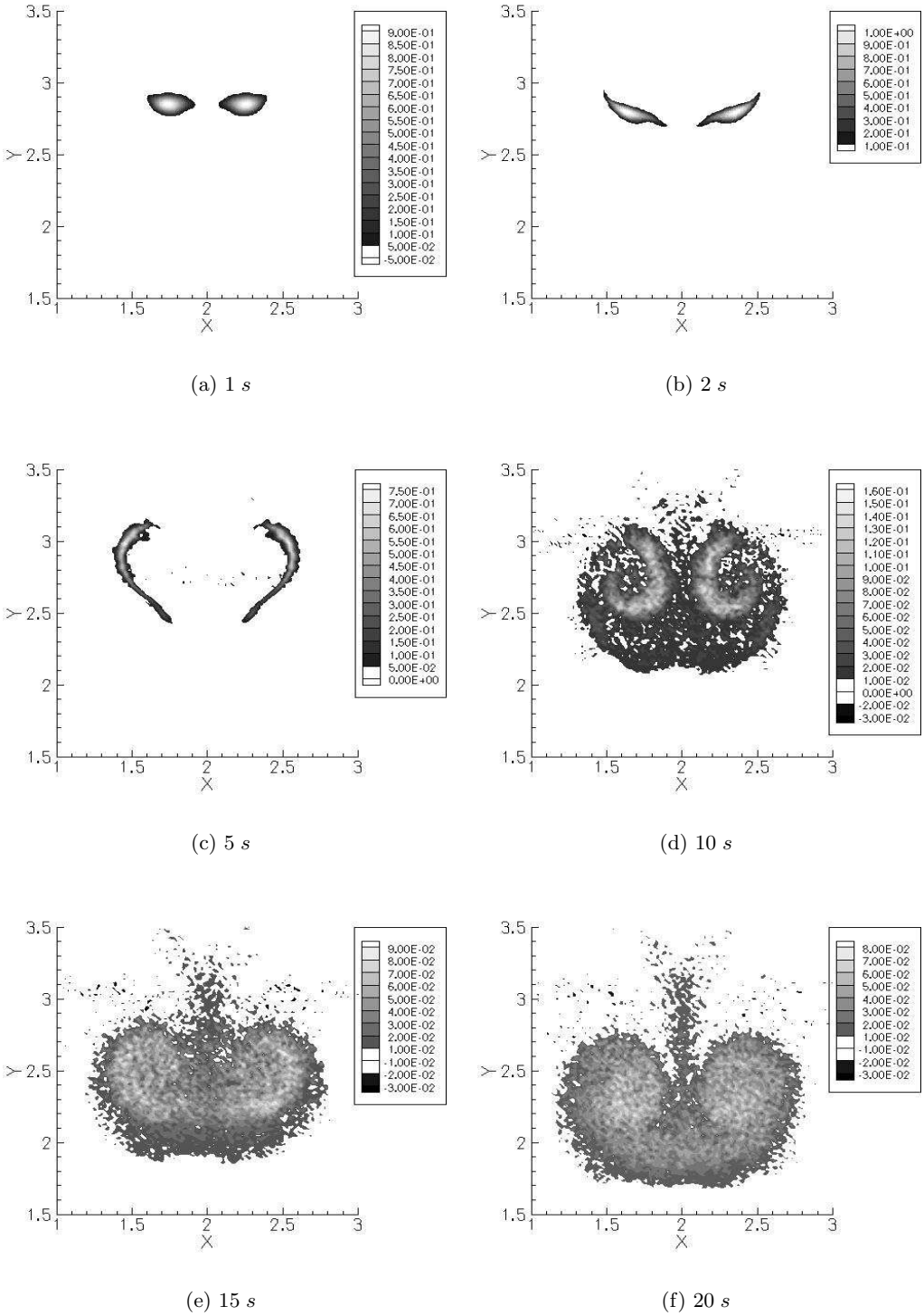

(a) 1 s (b) 2 s

(c) 5 s (d) 10 s

(e) 15 s (f) 20 s

Figure 6.16: Evolution of perturbation temperature for case A3.

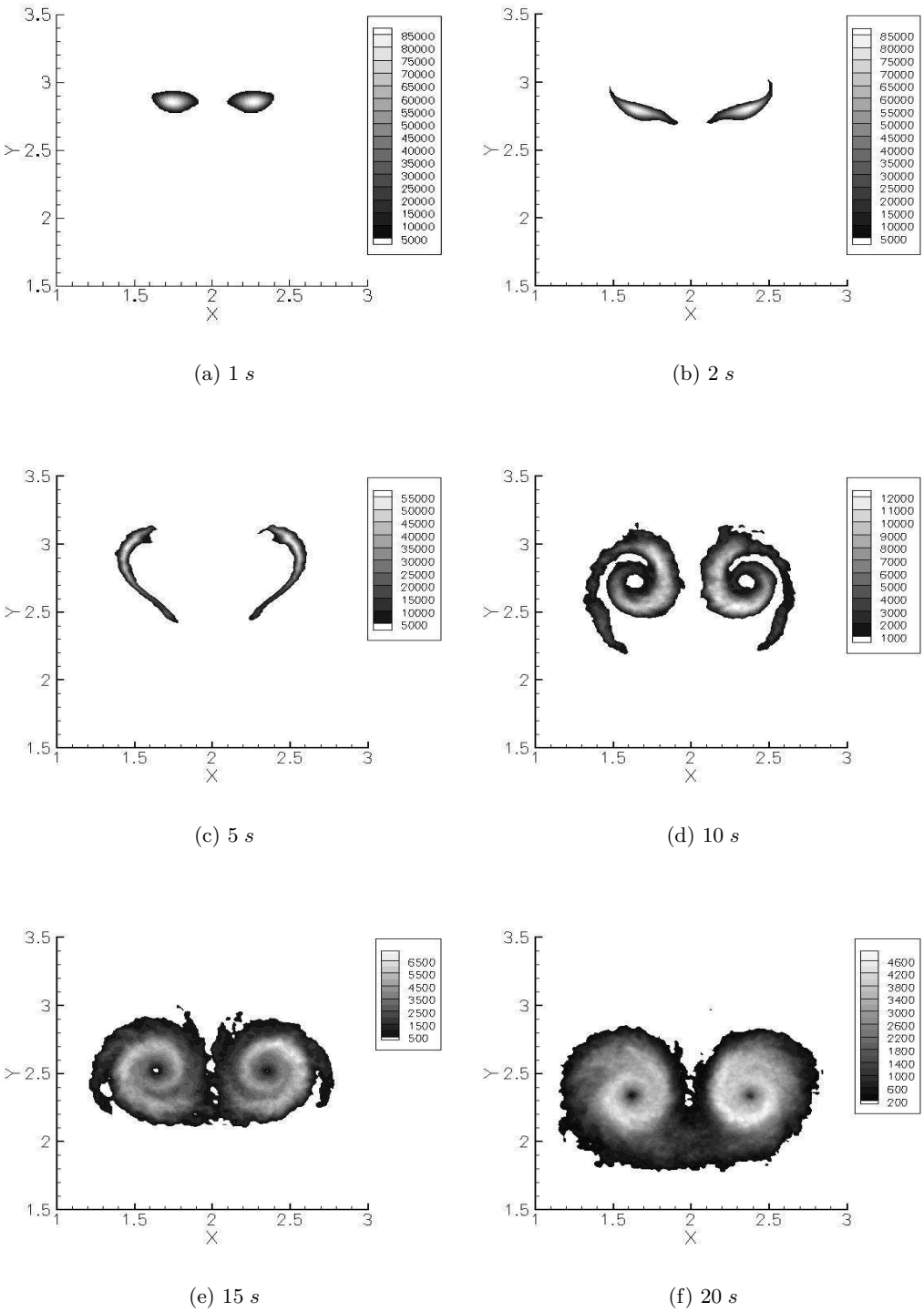

(a) 1 s (b) 2 s

(c) 5 s (d) 10 s

(e) 15 s (f) 20 s

Figure 6.17: Evolution of ice particle number density (in $\#/cc$) for case A3.

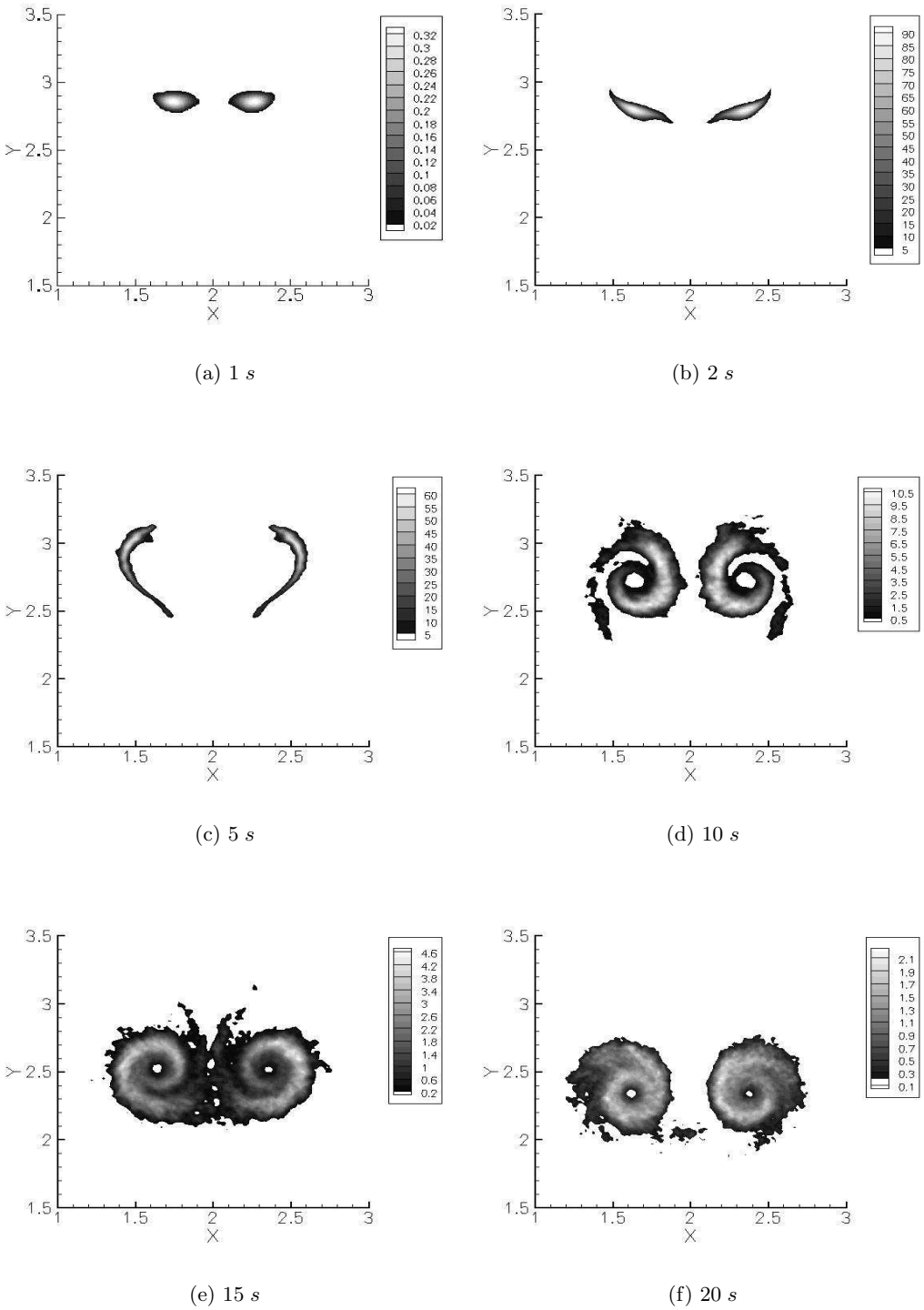

(a) 1 s (b) 2 s

(c) 5 s (d) 10 s

(e) 15 s (f) 20 s

Figure 6.18: Evolution of ice water content (in mg/m^3) for case A3.

$RHi = 130\%$. This is seemingly counterintuitive and opposite to the trends of Lewellen and Lewellen (2001). But a probable reason for this behavior is that for $RHi = 130\%$, along with the initial faster growth, the latent heat transfer between the two phases is also greater compared to that for $RHi = 110\%$. This causes increased temperatures and pushes the effective RHi to lower values. Along with the greater depletion for the higher RHi, this can cause a larger fraction of the particles to evaporate completely.

Note that our simulations use initial fields in which constant ambient water vapor density has been imposed, as opposed to constant RHi used by Lewellen and Lewellen (2001). Balloon measurements show that both water vapor mixing ratio and RHi vary with altitude (Vömel *et al.*, 2002) and over the scale of aircraft wake descent reported here, constant water vapor can be a reasonable approximation. Our results tell us that the sensitivity to the choice of constant vapor fraction or constant RHi reflects qualitatively in the number of surviving ice crystals (for the typical cruise atmosphere considered here). With constant water vapor density, the RHi decreases vertically downward (Figure 6.19). Hence as the wake descends down, it encounters lower RHi in its surroundings.

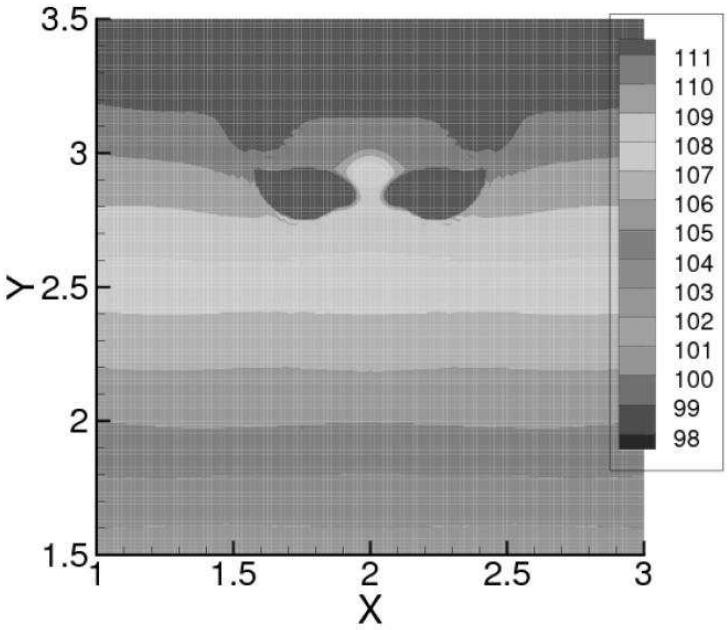

Figure 6.19: RHi field in the initial conditions with constant ambient water vapor.

The trend in the ice water content (IWC), on the other hand, is consistent with Lewellen

and Lewellen (2001) (Figure 6.20(d)). Especially in the late times where the effect of the jet has diminished, the IWC should be greater for higher RHi, a trend consistently predicted by our simulations and also those by Lewellen and Lewellen (2001) and Huebsch & Lewellen (2006). We have subsequently performed additional simulations with constant ambient RHi (instead of constant water vapor), and found that the number of surviving ice crystals is higher for higher ambient RHi. Contrail evolution results under both types of ambient humidity distributions will be reported in a journal manuscript currently in preparation.

Also it can be seen from Figure 6.20 that our earlier expectation matches with the observation that it is the intermediate stage ($t > 7$ or so) which is the most controlled by the ambient RHi as the jet humidity has been depleted in the early growth of the contrail. The size distributions for these different cases (Figure 6.21) show that the broadening of the PDF is more prominent for extreme values of humidity (whether subsaturated or supersaturated) that cause large rates of growth or decay. For higher humidity the PDF is skewed to higher particle radii, and the reverse is true for lower humidity. The PDF at very early stage ($t = 1.2\ s$) is not very sensitive to RHi, confirming that jet humidity (and not ambient humidity), is the controlling factor in this very early stage.

6.4 Effect of ambient temperature

We carried out two simulations with $T_{amb} = 220\ K$ and $240\ K$ in addition to the baseline case which has $T_{amb} = 218.8\ K$. All other parameters are the same, including the RHi. This means that the ambient water vapor density is different in the three cases depending on the temperature.

Note that the high ambient temperature case ($T_{amb} = 240\ K$) should be interpreted with care. According to the Appleman Criterion (Appleman, 1953), such warm ambient will not allow the formation of supersaturated liquid water, hence is not conducive to contrail formation. In the current code the Appleman criterion is not directly imposed, but is meant to guide the interpretation of computational results for a particular set of atmospheric conditions. Thus, although the results for this warm ambient case indicate contrail formation, this case is used only to display the sensitivity and should not be used at the stipulated ambient temperature because the Appleman criterion disqualifies this temperature for contrail formation.

Some observations can be made from the comparison of ice properties (Figure 6.22).

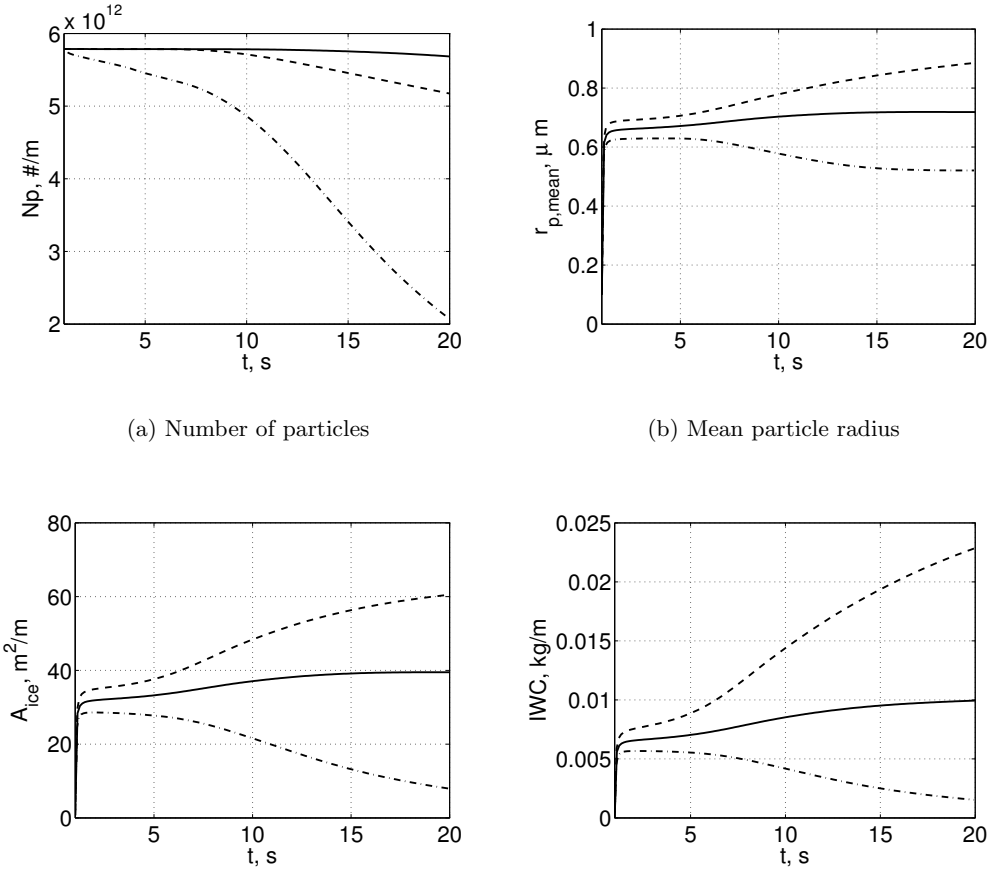

(a) Number of particles

(b) Mean particle radius

(c) Ice surface area

(d) Ice water content

Figure 6.20: Domain-integrated ice particle properties for —, $RHi = 110\%$; – –, 130%; –·–, 90%.

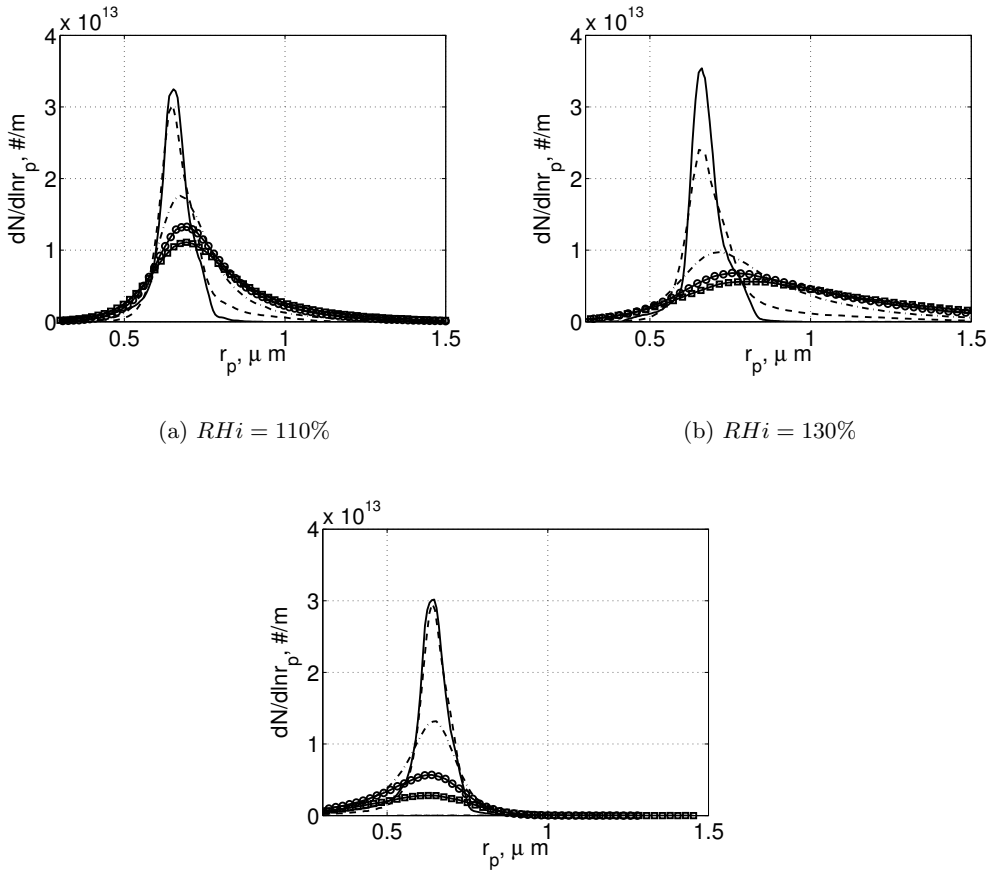

(a) $RHi = 110\%$

(b) $RHi = 130\%$

(c) $RHi = 90\%$

Figure 6.21: Dependence of particle size distribution on RHi at $t = 1.2\ s$, —; $5\ s$, – –; $10\ s$, – · –; $15\ s$, –○–; $20\ s$, –□– .

First, the existence of the jet-regime identified in Section 6.2 is accentuated here by the very different initial ice growths in the early duration (up to 5 s or so). Especially the number of surviving ice particles shows a drastically different behavior for the high temperature case (Figure 6.22(a)). This trend can be anticipated based on the fact that the jet water vapor density is kept constant and not the jet RHi. Appealing to the saturation vapor pressure curve for ice (Figure 6.23) one sees that the effective jet RHi for a higher ambient temperature is lower, slowing down the ice growth in the jet stage. This in turn has a profound impact on the way the intermediate, RHi-controlled stage behaves. For example, the mean particle radius (Figure 6.22(b)) grows a lot faster for the higher temperature primarily because the same water vapor content is available now for a smaller number of surviving droplets, as compared to the cases with lower ambient temperature. These observations suggest that the early ice processes can significantly affect the intermediate-regime contrail behavior in a way that is difficult to predict accurately by using simplified integral models, and justify the use of high-fidelity simulations for the early stage.

Another fact which becomes clear from Figure 6.22 is that the early contrail is very sensitive to the atmospheric temperature at high values of T_{amb}, as those high values fall in the region of the saturation curve (Figure 6.23) where the curve is very steep and small changes in local temperature produce amplified changes in the local effective RHi.

The size distributions in Figure 6.24 tell us that for the lower T_{amb} the PDFs have attained a shape which stays more or less constant in the intermediate stage. That means all the changes in the PDF take place in the jet regime, and the ambient RHi does not influence the asymptotic stage significantly. The reason for the jet-stage completely controlling the evolution is that for the same *absolute humidity* of the jet, lower ambient temperature results in a higher relative humidity.

6.5 Sensitivity to the number of ice nuclei

The dependence of ice growth on the total number of ice nuclei seems to be mainly quantitative, at least in the current early-stage regime where we exclude the effects of coagulation, particle collision and sedimentation. Higher ice nuclei density causes greater depletion effect, hence faster particle number decay (Figure 6.25(a)) and smaller-sized particles (Figure 6.25(b)). Interestingly, the balance of the number of surviving particles and their sizes in this case turns out to be such that the total ice water content is relatively insensitive to

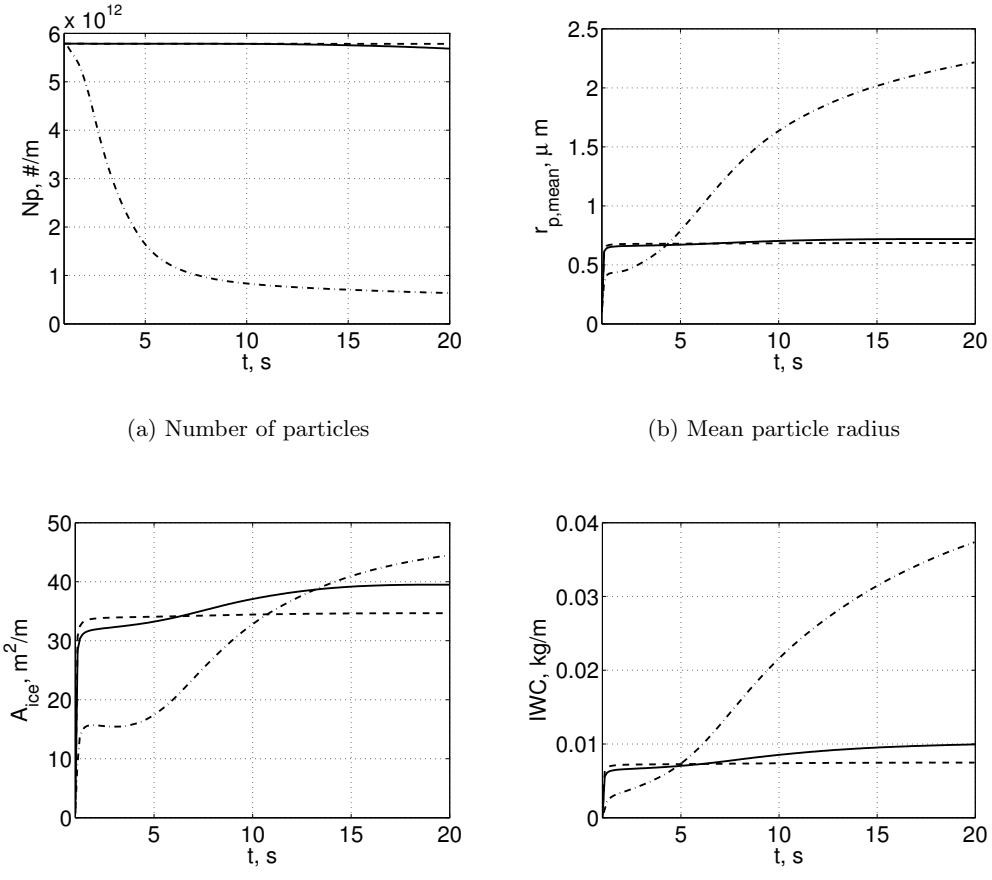

(a) Number of particles

(b) Mean particle radius

(c) Ice surface area

(d) Ice water content

Figure 6.22: Domain-integrated ice particle properties for —, $T_{amb} = 218.8\ K$; – –, 200 K; –·–, 240 K. RHi is kept constant at 110% for all three cases.

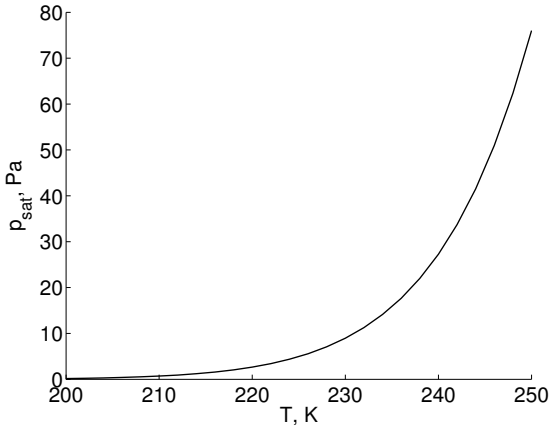

Figure 6.23: Saturation pressure of water vapor over ice, taken from Murphy and Koop (2005).

the ice nuclei density. This is consistent with the prediction of Kärcher *et al.* (1996*b*). The size distribution (Figure 6.26) seems to become somewhat broader with decreasing number of ice nuclei. Since the total ice surface area is affected by the ice nuclei number density, extinction of the incident radiation will be sensitive to the number of ice nuclei.

6.6 Sensitivity to initial ice particle size

Overall, in the current size range ($0.1\mu m$ radius) of the initial ice particles, both ice growth and the particle size distribution are fairly insensitive to the initial particle size (Figures 6.27,6.28). This can be explained by the fact that the initial jet-dominated ice growth is very rapid and it quickly overcomes the effects of initial particle size so long as the latter is small. It appears from Figure 6.27(a) that below $r_{po} = 0.1\mu m$ the effect of the initial size is very small. Since there is a noticeable change in the number of surviving ice particles while going from $r_{po} = 0.1\mu m$ to $0.2\mu m$, one has to be careful not to generalize this relative insensitivity to larger particle sizes. It is difficult to obtain precise measurements of ice particles at the downstream distance of 5 wing spans, so one may expect that it is possible to have a significant departure from the current $0.1\mu m$ initial size range, in which case the sensitivity should be re-examined for that particular size range.

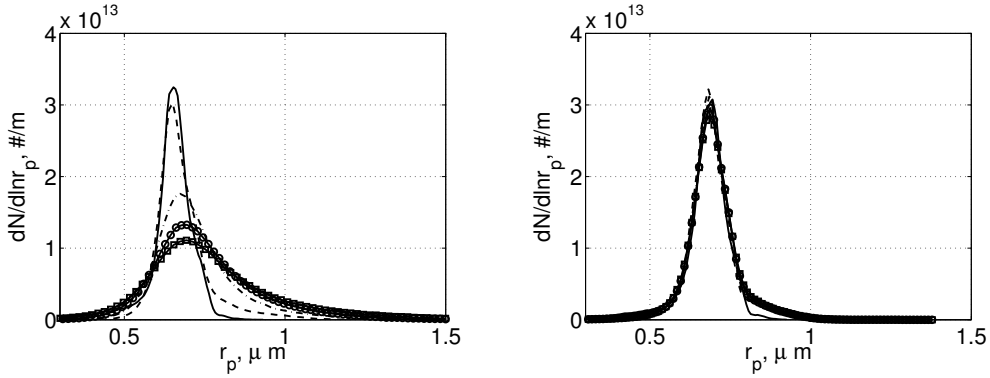

(a) $T_{amb} = 218.8\ K$

(b) $T_{amb} = 200\ K$

(c) $T_{amb} = 240\ K$

Figure 6.24: Dependence of particle size distribution on ambient temperature at $t = 1.2\ s$, —; $5\ s$, – –; $10\ s$, – · –; $15\ s$, –○–; $20\ s$, –□– .

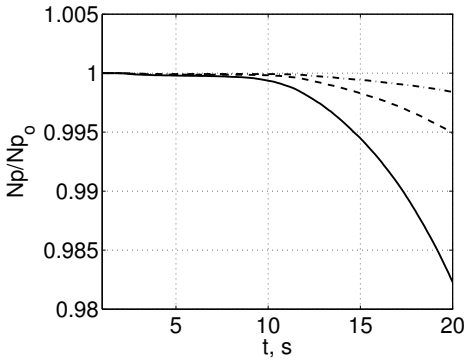

(a) Number of particles (normalized by the initial value)

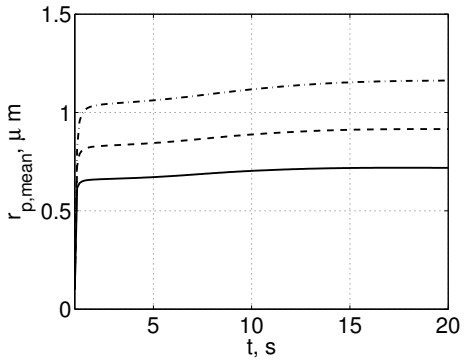

(b) Mean particle radius

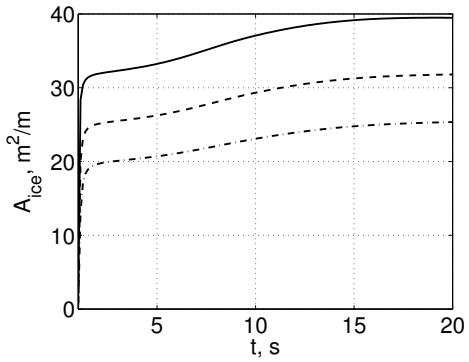

(c) Ice surface area

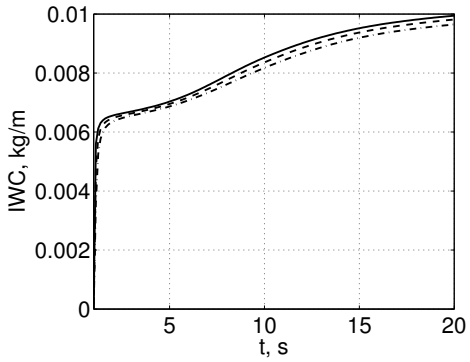

(d) Ice water content

Figure 6.25: Domain-integrated ice particle properties for —, $Np = 5.787 \times 10^{12}\#/m$; – –, $2.894 \times 10^{12}\#/m$; –·–, $1.447 \times 10^{12}\#/m$.

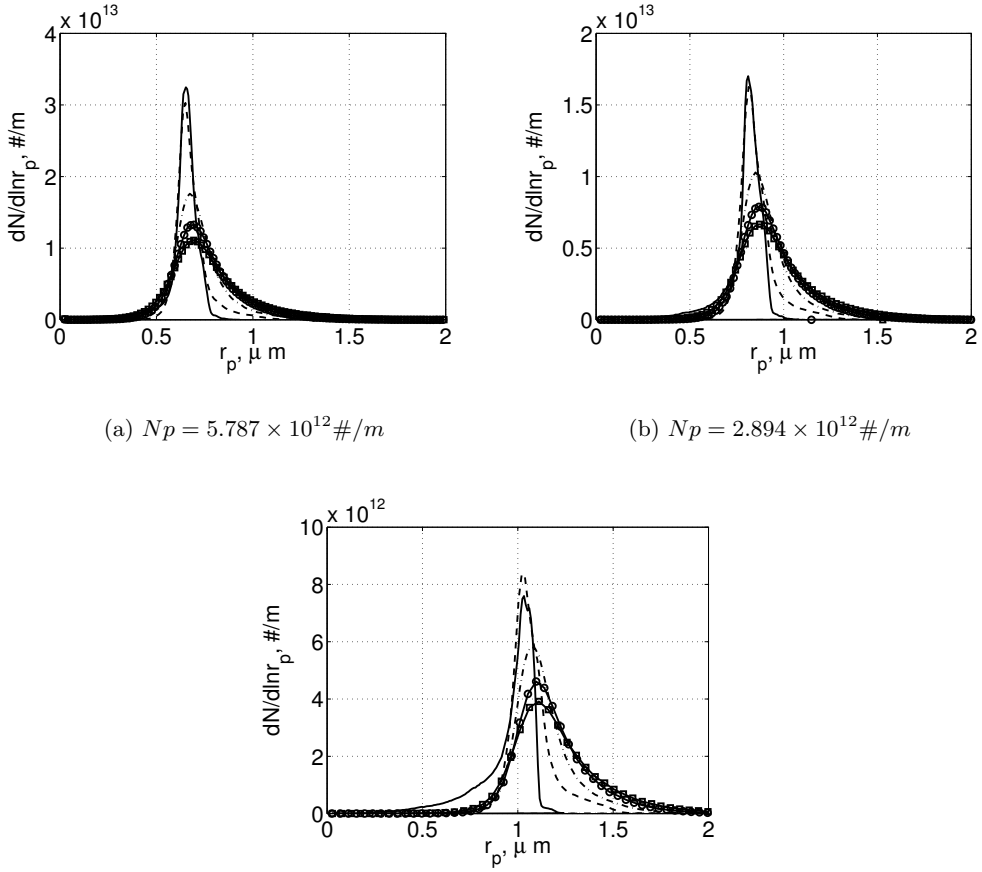

(a) $Np = 5.787 \times 10^{12} \#/m$

(b) $Np = 2.894 \times 10^{12} \#/m$

(c) $Np = 1.447 \times 10^{12} \#/m$

Figure 6.26: Sensitivity of particle size distribution to initial ice nuclei number at $t = 1.2\ s$, —; $5\ s$, – –; $10\ s$, – · –; $15\ s$, –○–; $20\ s$, –□– .

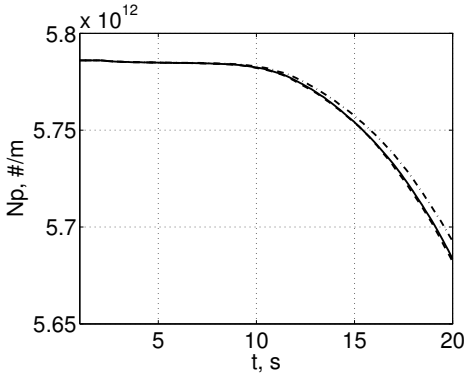

(a) Number of particles (normalized by initial value)

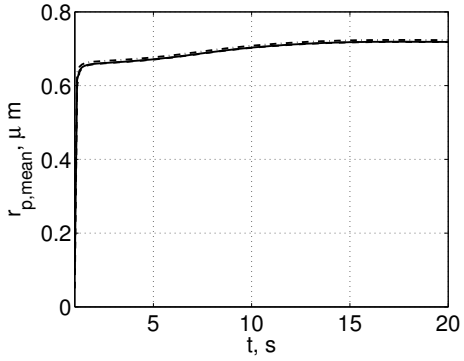

(b) Mean particle radius

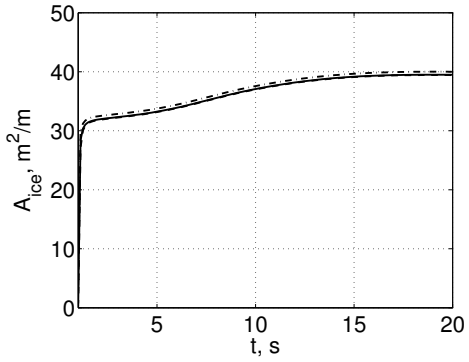

(c) Ice surface area

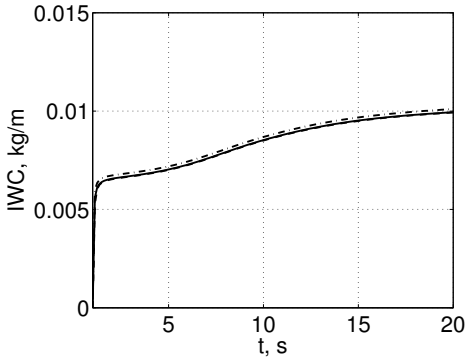

(d) Ice water content

Figure 6.27: Domain-integrated ice particle properties for —, $r_{po} = 0.1\mu m$; – –, $0.05\mu m$; –·–, $0.2\mu m$.

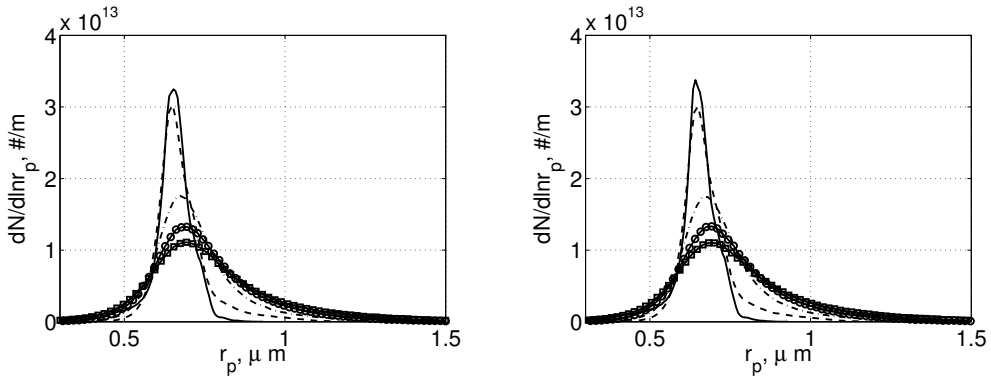

(a) $r_{po} = 0.1\mu m$

(b) $r_{po} = 0.05\mu m$

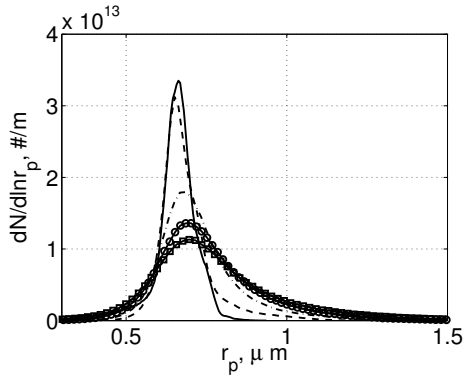

(c) $r_{po} = 0.2\mu m$

Figure 6.28: Sensitivity of particle size distribution to initial ice particle size at $t = 1.2$ s, —; 5 s, – –; 10 s, – · –; 15 s, –○–; 20 s, –□– .

6.7 Role of initial fluid turbulence seed

As discussed in Section 6.1, we seed the initial fields with turbulent fluctuations synthesized according to the procedure explained in that section. The jet axial velocity in our initial conditions is around 10 m/s which is comparable to the maximum vertical velocity in the vortex wake (around 20 m/s). But the turbulent velocity fluctuations are of the order of 1 m/s. The integral length scale estimated in Section 6.1 was 1.4 m, hence the large-scale eddy turnover time scale is $\sim$ 1.4 s which is short compared to the total duration of the simulation. So we can expect the jet turbulence to develop and dissipate quickly and play a role mainly in the early stages of contrail growth.

Figure 6.29 shows that the turbulence does not affect the very early rapid contrail growth. Since the time scale of turbulence is $\sim$ 1.4 s, the turbulence takes some time to develop and around $t = 5$ s the turbulence development seems to affect the contrail growth, although to a small extent due to the small magnitudes of turbulent fluctuations. Specifically, the surviving number of ice particles and total ice quantities computed with and without the turbulent seed differ from each other at this stage. We call this the "jet-turbulence regime" which was alluded to in Section 6.2 and occurs in between the jet-regime and the RHi-controlled regime. In Chapter 7 we distinguish this initially seeded fluid turbulence from the particle-generated stochastic fluctuations to find the numerical requirements to capture the overall effects of these fluctuations.

6.8 Sensitivity to initial conditions: Idealized initial conditions

The turbulence we injected into the initial field was artificially produced using estimates from literature (Section 6.1). Furthermore, the initial fields themselves may change according to the type of aircraft considered, and the distance behind the aircraft where we start the simulation. In this section we use a different set of initial conditions generated as follows.

A homogeneous turbulent velocity field with a von Karman spectrum with the functional form given by Equation 6.1 and peak of the spectrum at low wavenumbers was generated and then localized in the jet region by making it proportional to the local jet axial velocity at every grid point. Then it was superimposed onto the jet axial velocity which was modeled by

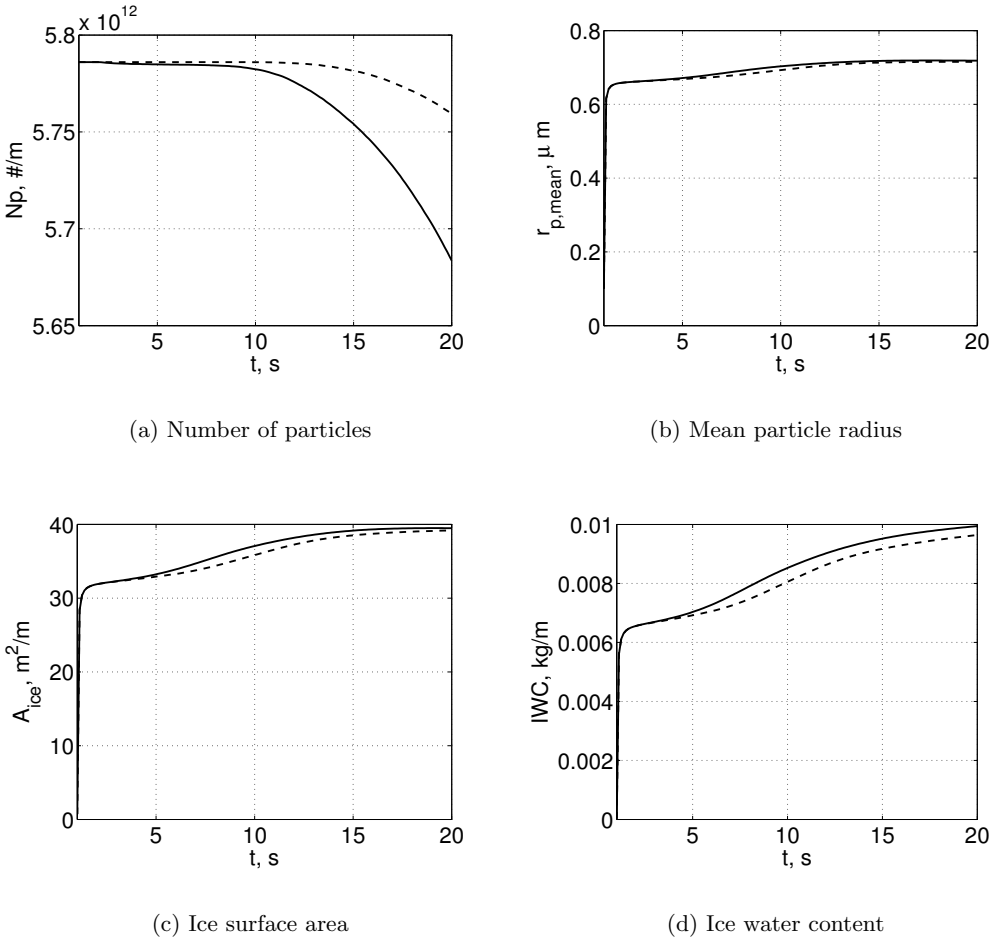

(a) Number of particles

(b) Mean particle radius

(c) Ice surface area

(d) Ice water content

Figure 6.29: Domain-integrated ice particle properties for —, with initial turbulent seed and – – without the seed.

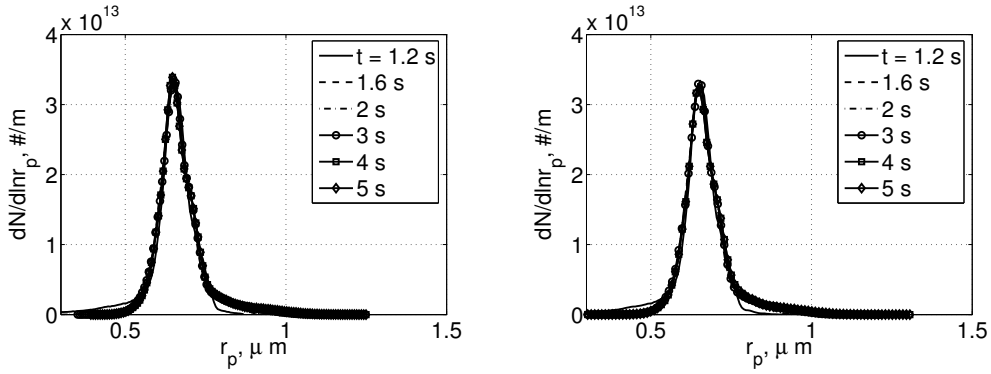

(a) Early times, without seed

(b) Early times, with seed

(c) Intermediate times, without seed

(d) Intermediate times, with seed

Figure 6.30: Dependence of particle size distribution on the presence of the initial turbulence seeding. Quantitative change is observed but qualitative trend is similar.

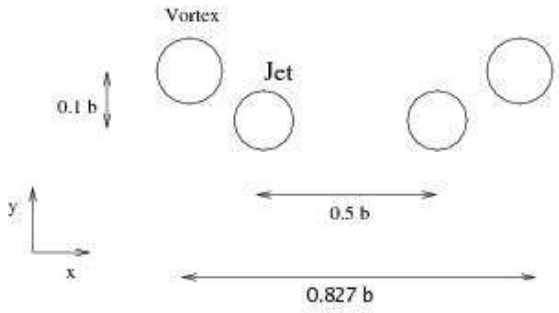

Figure 6.31: Initial vortex-jet configuration. Jet and vortex radii not drawn to scale.

a Gaussian with core radius 0.1 b where b is the wingspan. The precise location of the energy spectrum peak is not important as the jet will be allowed to evolve and select its frequencies according to its nonlinear dynamics. The fluctuation velocity was scaled so that it was 1% of the local mean axial velocity of the jet. The resultant velocity field was projected on to a divergence-free discrete function space. Then the pair of jets was allowed to evolve until it develops both large and small scale fluctuations. The development characteristics of this temporal jet evolution stage are described earlier in Section 4.8 in terms of mean fields and spectra. Once satisfactory turbulent fields are obtained, a counter-rotating Lamb-Oseen vortex pair with vorticity distribution

$$\omega_z(r) = \frac{\Gamma}{4\pi\nu t} e^{-r^2/4\nu t} \tag{6.3}$$

where r denotes the radial distance from the core, was superimposed on the jets. The initial vortex core radius, defined as the location of the maximum azimuthal velocity and given by $r_0 = 2.2418\sqrt{\nu t}$, was taken to be 0.075 b, close to that of the final rolled-up vortices in Case $A1$. All earlier simulations had flattened initial jet shapes because of strain experienced by them in the cross-plane until 1 s second. The current case (hereafter called Case $A1S$) uses the idealized circular jet, but with the realistic developed turbulence. The initial configuration of the jets and the vortices is depicted in Figure 6.31. The initial fields (Figure 6.32) show similarity with the initial fields used for Case $A1$. The initial vortex spacing, total circulation, total water vapor content, the jet peak velocity and peak temperature fluctuation were matched with the initial conditions for case $A1$. All other parameters such as stratification and RHi were the same as case $A1$.

Comparison of case $A1S$ with case $A1$ shows differences (Figure 6.33). The initial decay

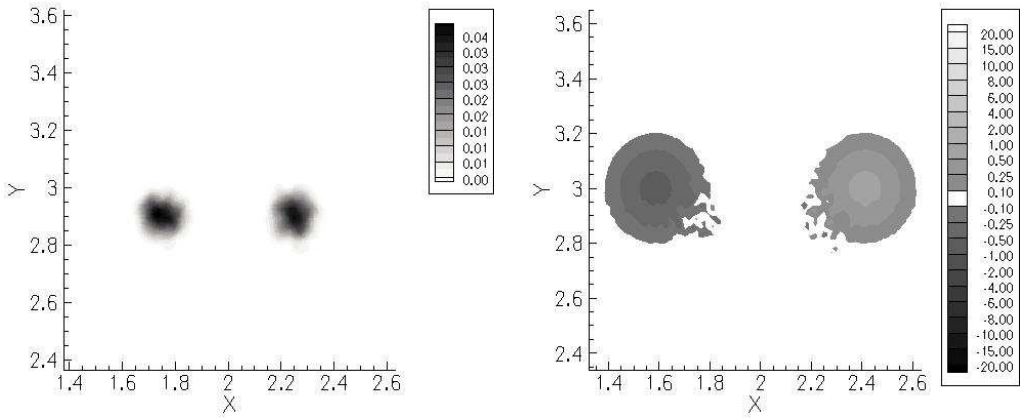

(a) Axial velocity

(b) Axial vorticity

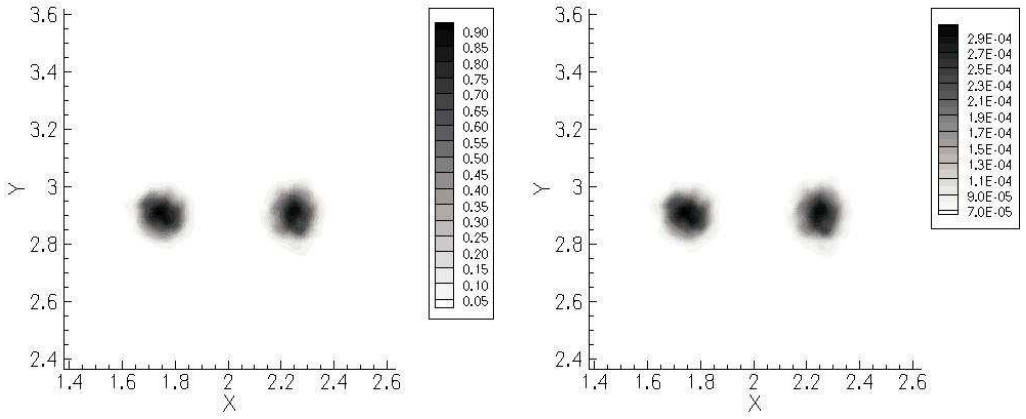

(c) Perturbation temperature

(d) Water vapor density

Figure 6.32: Idealized initial flowfield at 5 wingspans with realistic turbulent jets. All variables are normalized. The distortions visible in all fields correspond to the jet turbulence.

of the number of ice particles is much faster in case $A1S$. The decay is caused by both diffusion and depletion (see Section 6.2 for explanation). In case $A1S$ the turbulence is already developed and causes more mixing of water vapor in the early jet-regime. On the other hand, in case $A1$ turbulence is expected to first develop before it can substantially impact the ice growth. The particle size distribution is observed to be broader in case $A1S$ (Figure 6.34). This is similar to the phenomenon of stochastic condensation in clouds (Shaw, 2003) where turbulence tends to broaden the particle size spectrum. Other factors which can possibly cause the difference in ice growth are the different spatial distribution of initial vorticity, mismatch of pointwise values of water vapor content, mismatch of total heat content, and difference in the total jet momentum between the two cases.

6.9 Conclusion

Early stage ice growth in aircraft contrails is known to affect the late-stage contrails and hence needs to be studied carefully. We used large eddy simulations to study various physical aspects and trends in early behavior of contrails. Specifically, we studied the dependency of contrail growth on atmospheric relative humidity and temperature, initial ice nuclei number density, and initial ice particle size. It was found that the relative humidity is the most crucial variable affecting contrail growth. In general, higher ambient humidity causes larger ice particles and more ice surface area, but the number of particles does not follow this simple trend. The dependence of ice particle size on ambient temperature was the strongest at higher ambient temperatures. The ambient temperature severely affects the very early stage ice growth. The ice nuclei number density was found to affect the ice properties in a straightforward way which is amenable to simple scaling arguments (Kärcher *et al.*, 1996*b*). The contrail growth was insensitive to the initial ice particle size in the range of size considered. We also found the existence of jet-controlled, turbulence-controlled, and ambient RHi-controlled regimes in the early contrail growth.

The LES database thus sheds light on the contrail physics and identifies trends in contrail sensitivity. The database can be used in future to compare newly developed models against it.

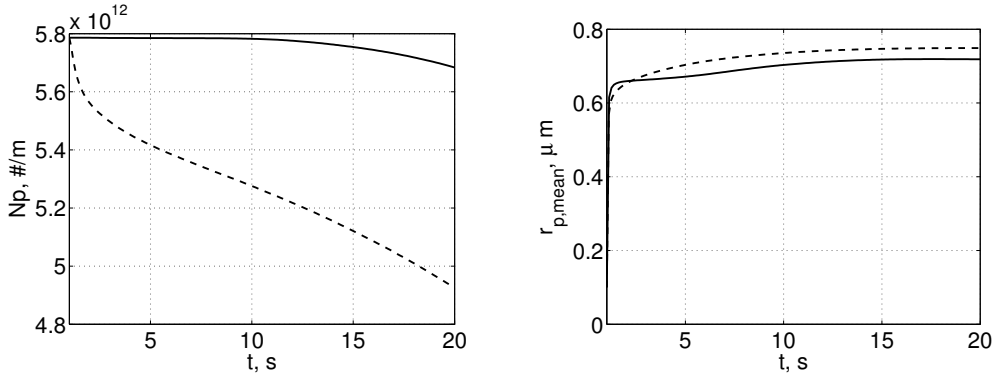

(a) Number of particles

(b) Mean particle radius

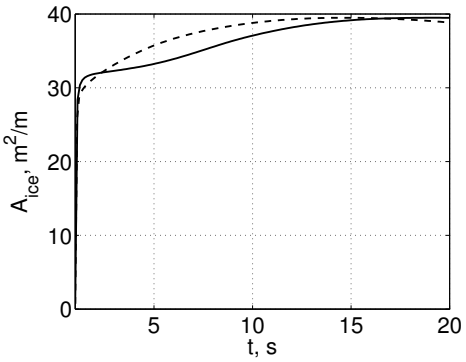

(c) Ice surface area

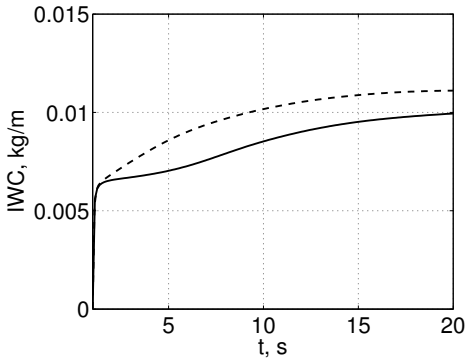

(d) Ice water content

Figure 6.33: Domain-integrated ice particle properties for —, case $A1$; – –, case $A1S$.

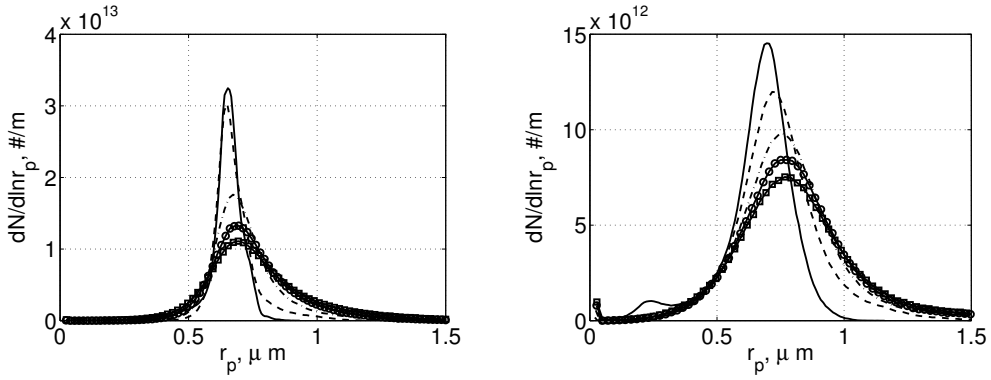

(a) Case $A1$ (b) Case $A1S$

Figure 6.34: Sensitivity of particle size distribution to initial conditions at $t = 1.2$ s, —; 5 s, – –; 10 s, – ·–; 15 s, –○–; 20 s, –□– . Note that the vertical scales are different.

Chapter 7

Convergence of Lagrangian Statistics

7.1 Background

An outstanding challenge in multiphysics problems is the great scale disparity among different physical processes such as fluid dynamics, phase changes, and chemical reactions. Accurate representation of small (spatial) and fast (temporal) scales presents serious modeling challenges. For instance, in cloud physics, these fast and small scales correspond to the evaporation/condensation of droplets, and the slow/large scales are those related to the large-scale fluid motion including mean shear, stratification, and atmospheric turbulent eddies. The ratio of energetic scales to Kolmogorov scales in clouds is typically $\mathcal{O}(10^5)$ (Shaw, 2003). The Eulerian flow field is handled by grid sizes of the order of meters (Paoli & Shariff, 2003), while the microphysics occurs at the droplet size which is of the order of a micrometer. Furthermore, the time-step for the aerodynamic calculation can be greater than $1s$, and droplet condensation time scale can be $\mathcal{O}(1ms)$. Similar scale separation is encountered in fuel sprays in combustion engines where the fuel drops evaporate much faster than the turbulent flow dynamics inside the combustor. The consequence of this scale separation is that the numerical solution becomes stiff, causing inefficiency in computations.

Resolving the flow around the particles is not computationally feasible for realistic problems such as turbulent combustion or clouds; only a limited number of studies have used this approach to study the flow physics (Burton & Eaton, 2005; Esmaeeli & Tryggvason,

2005) at low Reynolds numbers. Also, solving the particle equations for all particles can be prohibitively expensive especially in LES where the particle separation is much smaller than the grid cutoff. Examples of some of the modeling approaches used to alleviate this problem in two-phase flows are the Eulerian binned microphysics approach (Jensen *et al.*, 1994), the Lagrangian Monte-Carlo approach (Pope, 1985), the mixed Eulerian-Lagrangian approach (Paoli *et al.*, 2004; Shirgaonkar & Lele, 2006*a*), and PDF-based moment-tracking (Apte & Ghosal, 2004).

Considering the contrail problem, we found in Section 6.7 that the jet turbulence does not plays only a minor quantitative role in the development of ice properties. The fluctuations in temperature and humidity induced by the back-coupling of particle thermodynamics on the flow is however important. We will call this turbulence the "particle turbulence," as opposed to the "flow turbulence" that results directly from the initial turbulent seed and the nonlinearities in the Navier-Stokes equations. The origin of the particle turbulence is the inhomogeneous spatial and size distribution of the particles. Even when focusing only on the particle turbulence, distinct stages of droplet condensation/evaporation (or freezing/sublimation) may exist. If the initial conditions are far from the asymptotic solution manifold, there exists an early transient (the jet-regime identified in Section 6.2) when the lower moments rapidly try to approach a slowly varying, strongly attracting manifold. Such behavior has been used to devise efficient equation-free approach for computation of large-scale molecular dynamical systems (Kevrekidis *et al.*, 2004). During this transient, the condensational growth is governed by the interfacial mass transfer, which is diffusion-dominated at the *particle-size scale*. This causes inhomogeneities in the humidity field due to the random distribution of particles in a grid cell, because each particle depletes its local surroundings to a different extent. Consequently, gradients of the vapor field are created in the early regime. In the late stage (i.e. at durations much longer compared to time scale of diffusional growth of individual particles), the growth (or decay) is governed by the viscous/turbulent diffusion of these gradients. Hence the late stage is diffusion-dominated at the *interparticle separation scale*. This leads to broadening of the particle size spectrum which is referred to as stochastic condensation (Shaw, 2003). Due to these inherently different mechanisms in these two regimes, their time scales for statistical evolution are different.

Here we focus on the current mixed Eulerian-Lagrangian approach described in Chapter 3 which was shown by Paoli et al. (2002) to be a special case of the moment-tracking

approach (Apte & Ghosal, 2004) when only the zeroth moment is explicitly tracked. In such simulations it is necessary to attain the convergence of the Lagrangian statistics of interest. Since many such flows, e.g. fuel droplets in internal combustion engines, clouds, aircraft condensation trails (Paoli *et al.*, 2002; Apte & Ghosal, 2004), and atmospheric particulate transport are often simulated by LES, the particle-separation distance is smaller than the grid size, i.e. the particle-scale transport consists of sub-grid processes. Within this setting, it is important to evaluate the effect of both Eulerian and Lagrangian grids (the latter means the Lagrangian sample size used for averaging) on particle microphysics. We will evaluate this question in the specific context of early-stage contrails. In our verification and validation studies (Chapter 4) we observed that the current number of representative Lagrangian particles (10^6) is sufficient on the nominal grid used for the simulations. Also, for the same number of particles, the nominal grid size is sufficient as suggested by the grid convergence study. Here, we probe this issue further to find what minimal Eulerian grid resolution is required to obtain converged statistics for the given particle sample size.

7.2 Convergence with respect to Eulerian grid: Homogeneous direction

The type of flows considered here are dilute two-phase flows, dilute meaning small mass and volume fraction of the dispersed phase. Under this assumption the thermodynamics are predominantly one-way coupled, although the model is two-way coupled. That is, the effect of dispersed phase on the dispersion phase (fluid) is of higher order in the dispersed phase mass fraction, but the other way effect is of leading order. Then the particle dynamics and thermodynamics are controlled by the fluid motion and properties. This makes resolving the flow scales a prerequisite to obtaining accurate particle properties (Vaillancourt *et al.*, 2001). In order to study the effect of particle turbulence in isolation we do not seed any fluid turbulence in the initial conditions. The Eulerian grid resolution is governed by the smallest flow features in the descending wake and jets. In the case of contrails the mean flow inhomogeneities are restricted to the $x-y$ plane, and the flight direction (z) is homogeneous at least for the 20 second duration. Thus the grid size in z is a free parameter which we will attempt to optimize by studying the trade-off between cost and statistical convergence.

The baseline case A1 is chosen for numerical experimentation. Based on the convergence study reported in Chapter 4, the nominal grid size $(N_x, N_y) = (256, 320)$ in the $x - y$ plane

is sufficient to resolve the flow features. The grid size in flight direction N_z is varied here to see its effect on statistics. Note that the initial Eulerian flow field is two-dimensional, i.e. there is no variation along the z-axis. The three-dimensionality that develops with time is exclusively forced by the spatial distribution of particles, which is nonuniform in the z direction. A series of LES simulations with number of grid points in z, $N_z = 2$, 6, 16, 32, 64 were conducted. The limiting case $N_z = 2$ is a purely 2D flow (only one grid cell in z resolving the one-wingspan thick domain) with no subgrid scale model. The particle initial locations, however, are distributed in three dimensions, and are identical in all the cases. The idea behind this setup is to evaluate how many grid points are needed in the **homogeneous direction** to get good accuracy in Lagrangian statistics.

The results for the first four moments (Figure 7.1) indicate that the total number of ice particles, average particle radius, total surface area and amount of ice converge well for $N_z = 32$. The "turbulence regime" described in Section 6.2 which extends approximately from 2 to 10 seconds is captured quantitatively very well with 32 points and only qualitatively with $N_z = 16$, but the lower resolution grids completely fail to capture it. The domain-integrated particle size distribution is compared in Figure 7.2 which also supports the convergence at $N_z = 32$.

These results indicate that for the contrail simulations of this study, the grid size in the direction of averaging (z in this case) can be chosen in a way that further refinement in that direction will not gain significant convergence improvement. In terms of particle transport it means that the microphysics-induced flow features of importance are captured sufficiently well with this grid size. It is very important to note that we have assumed the existence of at least one homogeneous direction over which averaging can be done which provides us sufficient sample size to obtain statistics. Also, subgrid-scale microphysical modeling has been neglected here but it can become important.

Since the flow is inhomogeneous in the $x - y$ plane, it is instructive to look at the PDFs at various (x, y) locations in the contrail after averaging only in the homogeneous direction. For this we choose four representative probe locations, $(x, y) = (2.25, 2.40)$, $(2.70, 2.40)$, $(2.40, 2.10)$, and $(2.10, 2.00)$ and averaging in rectangular tubes around each probe. The local ice particle number densities at these probes are 3862, 1707, 3245 and 86 $\#/cc$ respectively. These locations were chosen to represent different locations in the flow dynamics, as shown in Figure 7.3. Each tube is centered at the probe location and has a cross-sectional area $4\Delta x \times 4\Delta y$, and extends in the z direction across the domain. The

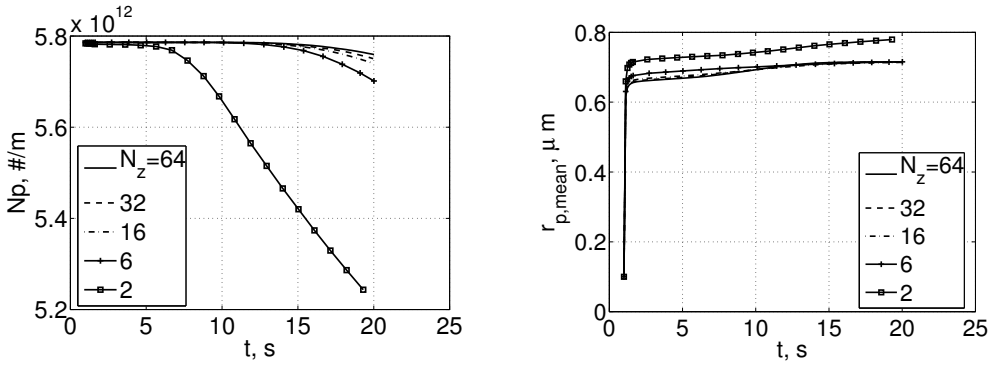

(a) Number of particles

(b) Mean particle radius

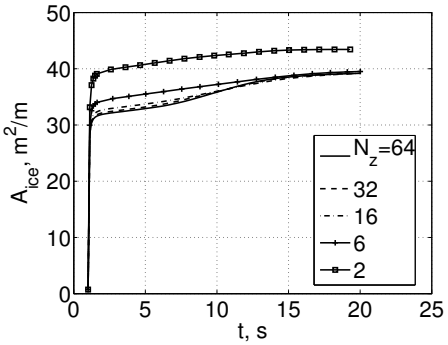

(c) Ice surface area

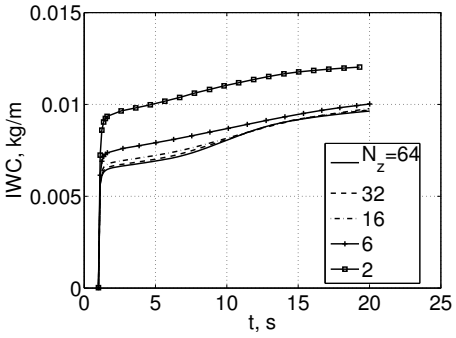

(d) Ice water content

Figure 7.1: Domain-integrated ice particle properties for the baseline case with different grid sizes in the flight direction.

resultant PDFs at the probe locations are shown in Figure 7.4.

7.3 Criteria for choosing the number of Lagrangian particles in homogeneous directions

We now try to derive a criterion for choosing the number of Lagrangian particles in a simplified model when there is no mean flow hence only particle evaporation/freezing is considered. The purpose here is to focus on the particle-induced changes in isolation. In

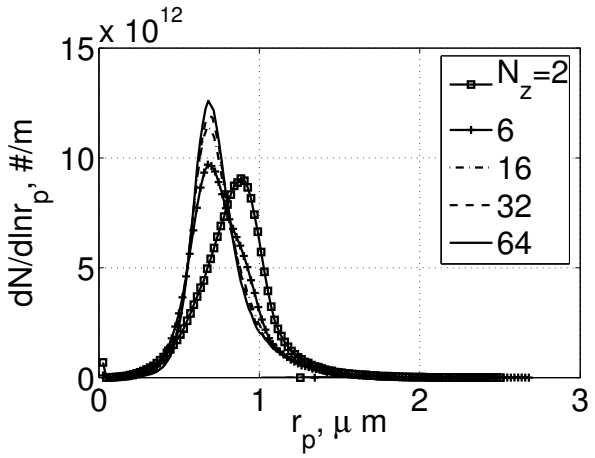

Figure 7.2: Domain-integrated ice particle size distribution for the baseline case with different grid sizes in the flight direction.

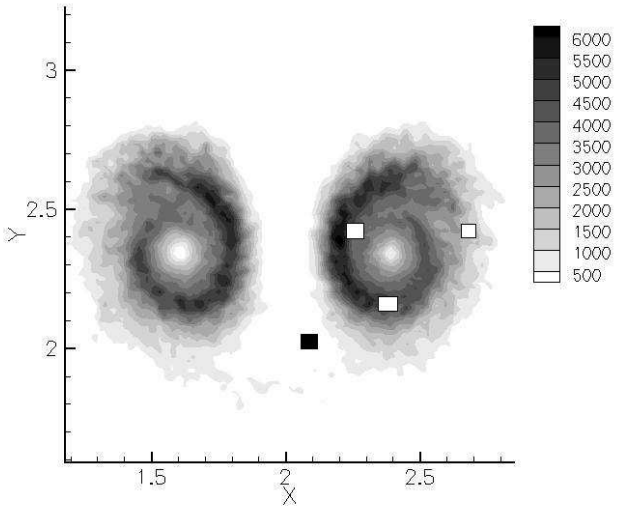

Figure 7.3: Contours of particle number density in $\#/cc$ showing probe locations at $(x, y) = (2.25, 2.40)$, $(2.70, 2.40)$, $(2.40, 2.10)$, and $(2.10, 2.00)$.

mixed Eulerian-Lagrangian formulations when the physical particle number density is so high that tracking all physical particles is prohibitively expensive, we use the computational

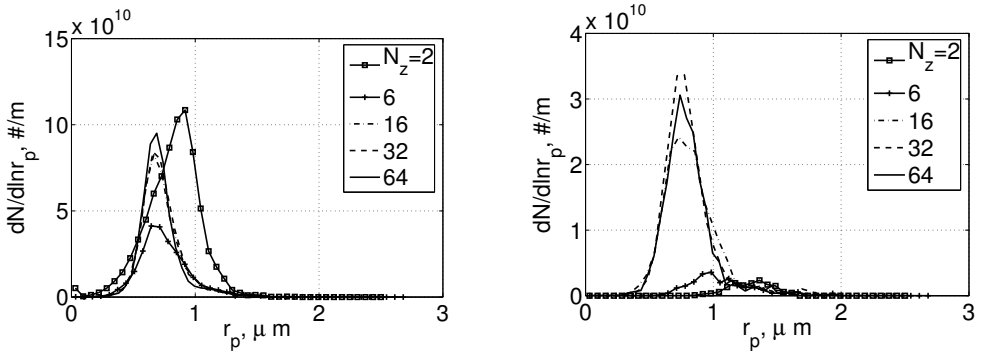

(a) Probe at $(2.25, 2.40)$

(b) Probe at $(2.70, 2.40)$

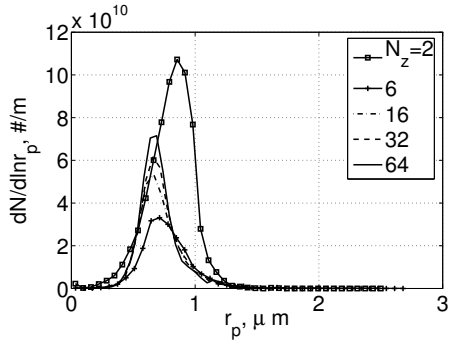

(c) Probe at $(2.40, 2.10)$

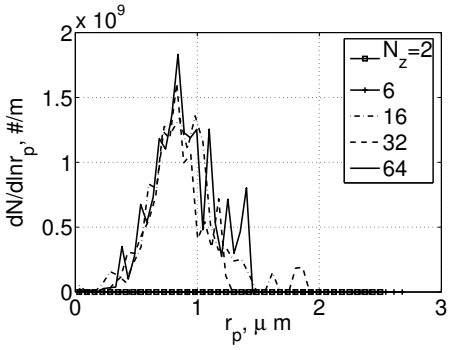

(d) Probe at $(2.10, 2.00)$

Figure 7.4: Ice particle size distribution integrated in a rectangular tube of area $4\Delta x \times 4\Delta y$ with center at the respective probe location, with different grid sizes in the flight direction.

parcels to represent a collection of identical physical particles. For N_p total physical particles, we make a choice to use N_{comp} computational particles, each representing n_p physical particles where these three numbers are constrained by $N_p = N_{comp} \times n_p$. In this section we propose criteria for choosing N_{comp}.

Firstly, as expected, choosing an Eulerian grid size sufficient to resolve the flow scales of interest is required. In this analysis we use a uniform flow and hence bypass any flow-scale requirement on the Eulerian grid. We assume that in a practical flow this requirement has been independently satisfied, and we focus on resolving particle statistics on a given Eulerian

grid. The box model used in Section 4.3 is used here. It uses an 8^3 grid to represent a $1m^3$ box. It should be noted that in this idealized box model, all three directions are considered homogeneous directions because there is no mean flow. The purpose of providing 8^3 grid cells is only for averaging over the grid cells to obtain better statistical convergence. The most important assumption here is that *if there was a mean flow*, it must be adequately resolved by the current 8^3 grid. If this is not true, we have to increase the Eulerian grid resolution. In summary, this means that we are considering the scenario in which the smallest flow scales which we want to resolve are considerably larger than the interparticle distance for the *physical* particles.

For the baseline case we choose approximately one computational particle in each grid cell ($N_{comp} = 512$, varied for other cases), and $n_p = 7.8125 \times 10^3$ so that the physical particle number density is $N = 4\#/cc$. Atmospheric water vapor content was taken to be supersaturated with respect to ice at 100.5% of the saturation value, and ambient temperature was taken as 220 K. We vary N_{comp} and n_p such that $N_p = N_{comp} \times n_p$ remains constant. The initial positions of the particles were randomly distributed in the box, and initial size distribution is unimodal with all particles having radius $0.5\mu m$. Statistics are computed by volume averaging in the box.

As described before, the microphysical evolution of particle size takes place in two stages. If the initial distribution is far from the asymptotic solution manifold, there in general is a rapid transient as observed in our contrail simulations. This stage is governed by diffusive processes (mass and energy transfer) at the particle-size scales. However, here the supersaturation is small (0.5%) hence the transient is not prominent. Next, due to the locally inhomogeneous depletion of water vapor, the size distribution further evolves. For the purpose of proposing a criterion for numerical choices, we focus on this second stage. Later in this chapter we also present results for a higher supersaturation of 10%. It will be seen that the conclusions from the low supersaturation case are also valid for this higher supersaturation case.

Figure 7.5 shows the ice properties (first three moments of the distribution) and the atmospheric relative humidity for different number of Lagrangian computational particles. With increasing N_{comp}, it is seen that until we have approximately one particle per grid cell ($N_{comp} \approx 512$), the statistics are not converged. The relative error (defined by regarding the $N_{comp} = 4096$ value as the exact solution) in the mean particle radius at $t = 300s$ shows linear decay, and at $N_{comp} \approx 512$ it falls below 1% in this case. After this threshold,

the results are fairly converged and further addition of particles does not provide much accuracy gain. The distribution, however, keeps changing in shape even after this threshold (Figure 7.7). Below the threshold, the pdf changes significantly because a sufficient sample size is not available for averaging, and also because a large fraction of the grid cells are empty. In the limit $N_{comp} \rightarrow \infty$ the PDF will reach a delta function at the converged value of the mean. Figure 7.8 indicates that the standard deviation of the distribution is tending to the limit $\sigma \sim 1/\sqrt{N_{comp}}$ as expected from the mean value theorem. In that case the high particle number density would require the modeling of interparticle processes within a grid cell using subgrid-scale models (Paoli *et al.*, 2006), so that the converged distribution would be aimed to represent a physical distribution, instead of a nonphysical one. In addition to the convergence of the moments, the behavior of the standard deviation (σ) of the distribution also shows similar trend where after the threshold value of N_{comp}, roughly quadrupling the number of particles in each cell (i.e., from $N_{comp} = 512$ to 2048) reduces σ by around $0.037\mu m$ for these test cases, which is $\sim 2\%$ of the mean value of $r_p \approx 1.6\mu m$ at $300s$.

Same trends are also observed for a higher ambient relative humidity of 110%. The effect of N_{comp} on ice properties for this case is shown in Figure 7.10, and error in the mean particle radius at $t = 300\ s$ is plotted in Figure 7.11. It is seen that the threshold on N_{comp} identified above for the $RHi = 100.5\%$ case also works for this higher supersaturation case with $RHi = 110\%$.

7.4 Conclusion

The choice of Lagrangian particles in mixed Eulerian-Lagrangian simulations can be made by considering the trade-off between statistical accuracy and computational cost. The rough criterion suggested above identifies the threshold of approximately one Lagrangian computational particle per grid cell to obtain convergence of the first three moments of the particle size distribution to within the error reported for the test problems in this chapter. Beyond this number the increase in the number of particles is not expected to provide significant physical information because one does not have information about the flow-scales below the grid size. In other words, by using many particles in a given grid cell we are not treating the Eulerian flow variables and Lagrangian particle variables to a consistent resolution unless subgrid scale models are used for particle-flow correlations.

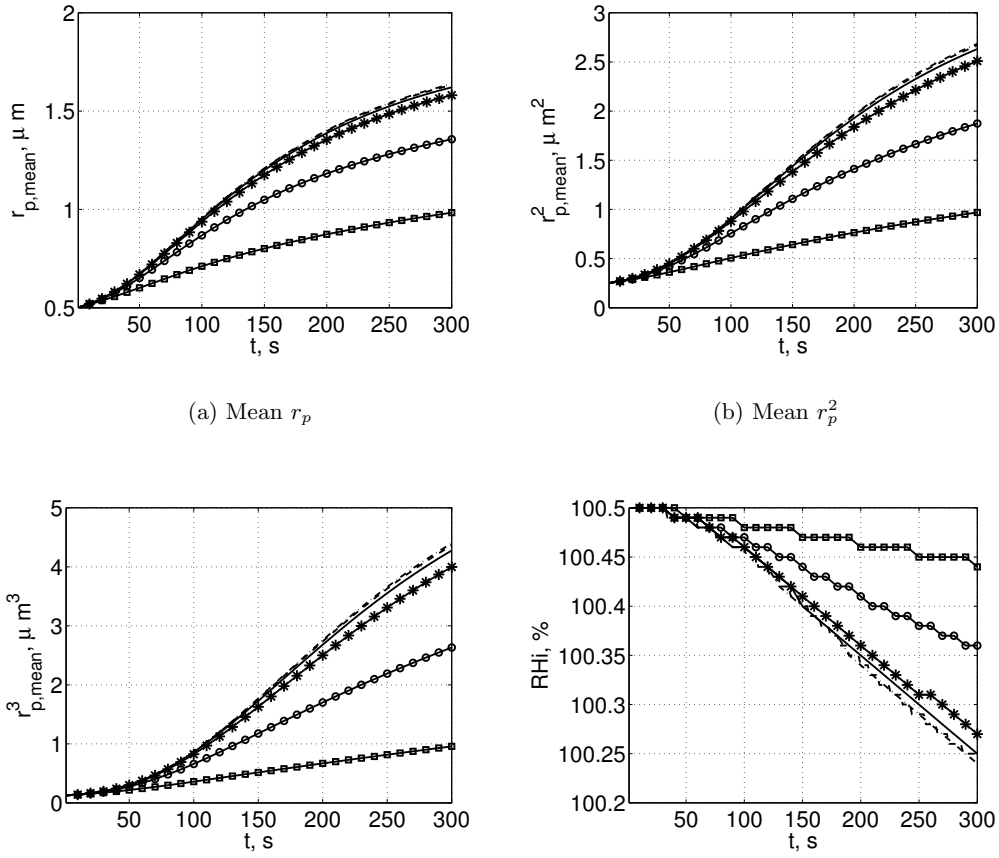

(a) Mean r_p

(b) Mean r_p^2

(c) Mean r_p^3

(d) Mean RHi

Figure 7.5: Volume-averaged particle statistics for the box model test with $RHi = 100.5\%$ for $N_{comp} = 8$, –□–; 32, –○–; 128, –∗–; 512, —; 2048, – – ; 4096, – · –

Some conditions and caveats in applying this criterion are listed below.

- The grid size should be sufficient to resolve the flow features of interest including flow turbulence.

- Sufficient number of grid cells should be available for averaging the statistics over those cells. This requirement means there should be at least one homogeneous direction along which averaging can be done. Typically the ratio of the largest to the smallest *flow scales* in high Reynolds number flows of interest here are such that resolving the

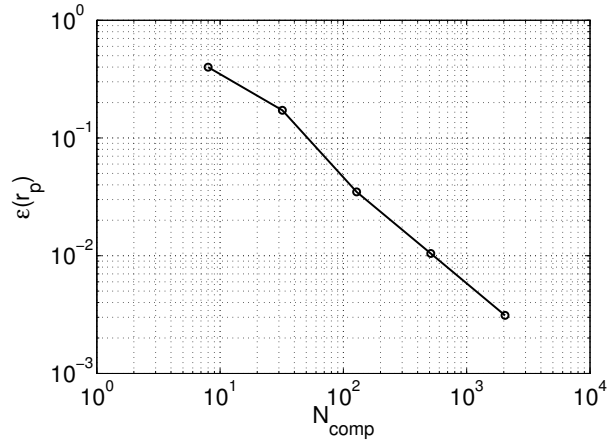

Figure 7.6: Relative error $\epsilon(r_p)$ in mean particle radius at $t = 300s$ with the box model calculations with $RHi = 100.5\%$. The solution with $N_{comp} = 4096$ has been regarded as the exact solution in defining ϵ.

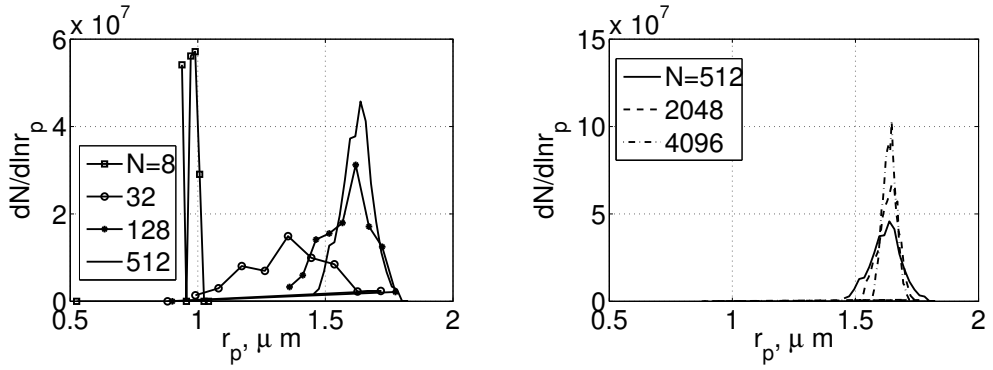

(a) < 1 #/cell (b) > 1 #/cell

Figure 7.7: Particle size distribution in the full domain for various N_{comp} for the box model calculations.

flow already requires a sufficiently fine grid in the homogeneous direction, justifying the above assumption.

- This criterion is meant for mixed Eulerian-Lagrangian formulations where the actual *physical* particle number densities are so high that the mean interparticle separation distance is smaller than the grid size. If it is comparable or larger than the grid size,

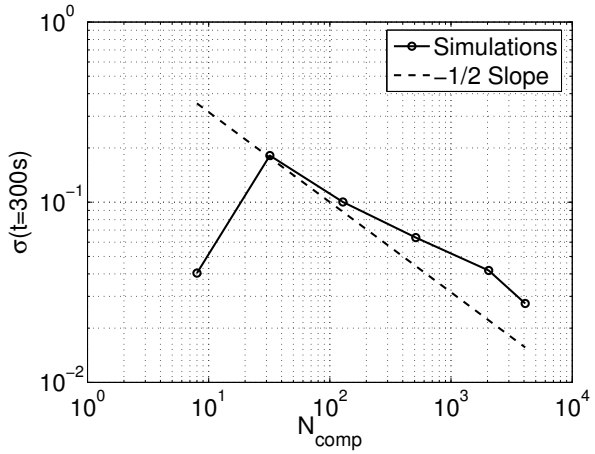

Figure 7.8: Standard deviation of particle radius distribution at $t = 300s$ vs number of Lagrangian particles.

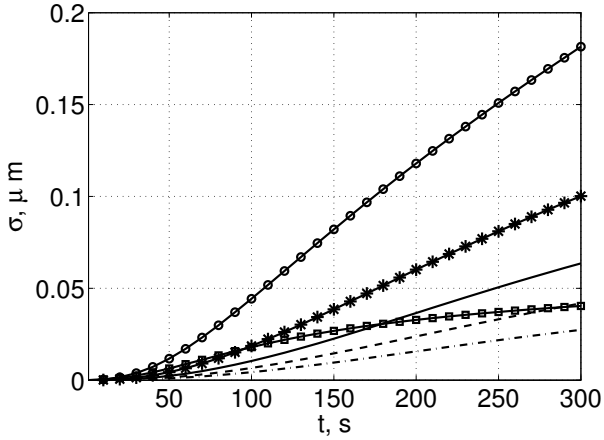

Figure 7.9: Standard deviation of the particle size distribution for the box model calculations for $N_{comp} = 8$, –□–; 32, –○–; 128, –∗–; 512, —; 2048, – – ; 4096, – · –. Note that the mean particle radius at $300s$ is $1.6\mu m$.

the computational particles can be regarded as physical particles and the choice of N_{comp} becomes trivial, equal to one. An example of such flows are clouds where the Kolmogorov scale of turbulence is of the same order as the separation between the cloud droplets (Vaillancourt & Yau, 2000; Vaillancourt *et al.*, 2001). In LES, however, since the smallest scales are not resolved, the particle separation distances are often

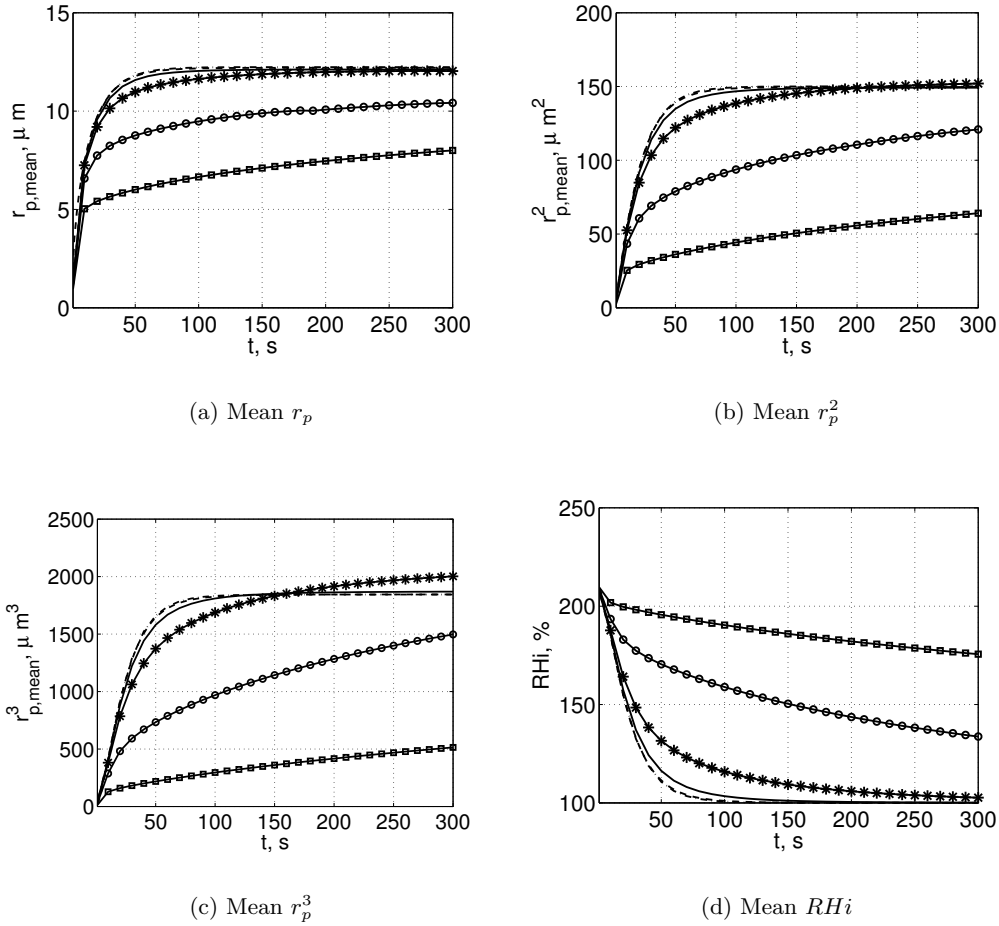

(a) Mean r_p

(b) Mean r_p^2

(c) Mean r_p^3

(d) Mean RHi

Figure 7.10: Volume-averaged particle statistics for the box model test with $RHi = 110\%$ for $N_{comp} = 8$, –□–; 32, –○–; 128, –∗–; 512, —; 2048, – – ; 4096, – · –

sub-grid.

- We have made no assumptions about the accuracy of the converged size distribution. The *real world* distribution function is influenced by sub-grid correlations between the particles and the Eulerian flow quantities such as humidity. These correlations should be taken into account using subgrid scale models (e.g. Paoli *et al.*, 2006).

- The criterion is very *flow-dependent* and sensitive to the quantities that one is finally interested in. For example, when the lower-order statistics (which are physically

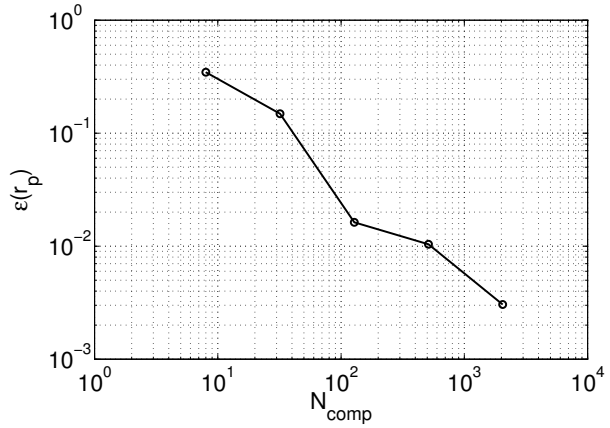

Figure 7.11: Relative error $\epsilon(r_p)$ in mean particle radius at $t = 300\ s$ with the box model calculations with $RHi = 110\%$. The solution with $N_{comp} = 4096$ has been regarded as the exact solution in defining ϵ.

most relevant) averaged in the homogeneous direction are of interest, one can choose N_{comp} according to the above criterion. If pointwise number densities or higher-order statistics are required to be predicted accurately, the choice will need to be re-evaluated. In the case of the box model, this point is clear from Figure 7.3 where although the first three moments have converged sufficiently, the size distribution is still changing with the number of Lagrangian particles.

In summary, the results presented here accentuate the need for the development of subgrid-scale models for Lagrangian models of dilute multiphase flows.

Chapter 8

Conclusions

High-resolution Large Eddy Simulations have recently been considered an attractive approach to studying the early development of aircraft condensation trails. We have used LES to extract detailed physics in contrails which gives us insight into many aspects of contrail growth. Several modeling challenges are encountered in contrail simulations due to their multiscale nature, both in terms of spatial and temporal scales. The objective of this research was to develop models for fluid dynamics and microphysics, couple them in an efficient numerical methodology, and leverage the present-day high performance computers to study contrails. Although it would require an extensive long-term research program to span a complete range of parameters in contrail modeling, this study has gained understanding in some of the fundamental aspects of contrail evolution in early stages. The major findings are stated below.

Modeling

Before coupling the flow and microphysics models it was regarded as crucial to develop accurate models for both separately. The outcomes are:

- The extended Boussinesq approximation (Shirgaonkar & Lele, 2006*b*) was developed for the class of shallow, stratified, low Mach number flows with small external entropy fluctuations. The most important advantage of it is the inclusion of additional physics of buoyancy-inertia interaction which is absent in the traditional Boussinesq approximation. In addition, a unified theory was developed for the above class of flows which treats a general fluid (compressible or incompressible). The equations are applicable

in the regime that lies between the regimes suitable for deep-water anelastic equations and shallow-water Boussinesq approximation. The extended Boussinesq approximation models the buoyancy-inertia coupling like the anelastic equations, while retaining the efficiency in numerical solutions like the traditional Boussinesq approximation.

- A microphysics model was developed using the mixed Eulerian-Lagrangian computational approach where we solve for the fluid flow in an Eulerian manner and ice microphysics is tracked by following Lagrangian ice particles moving in this Eulerian grid. This model was shown to be efficient for the present problem. The Lagrangian model takes under 6% of the total CPU time for the typical simulations reported here. The model was tested for specific test cases against other very different models used in industry. The model treats freezing/sublimation of ice and latent heat and mass transfer between the ice and vapor phases. Coagulation, particle collision, sedimentation, preferential concentration, and radiation were not modeled as they are considered to play a significant role mainly outside the regime considered.

Numerical methodology

- In Chapter 1 we emphasized the need for high-accuracy numerical simulations for contrail studies. Consequently, higher-order numerical methods are used in our code. They contain high spectral resolution finite difference schemes for spatial differencing, low dissipation-dispersion time marching scheme, and nondiffusive Lagrangian particle tracking method. The code is implemented on parallel computers and gives quick turnaround times compared to compressible flow codes.

- The numerical methodology developed above was extensively validated. We used test cases to validate the stratified flow model, the dynamic subgrid scale model, and passive scalar transport. We quantified grid sensitivity with respect to Eulerian grid size. In Lagrangian simulations it is crucial to ensure the accuracy of particle statistics. We tested the sensitivity of statistics to the number of Lagrangian particles both globally and also at selected locations in the vortex wake plane (x-y plane).

- A criterion was suggested to choose the number of Lagrangian computational particles for the present simulations (Chapter 7). It states that slightly more than one particle per grid cell was sufficient to obtain good accuracy in particle statistics, provided the Eulerian grid resolution is sufficient to resolve the flow scales of interest, and a

sufficient number of grid cells are available for sampling in the homogeneous direction. The criterion *does not* guarantee the accuracy of the size distribution obtained. In general sub-grid effects for Lagrangian particles should be accounted for by using models, irrespective of whether we use the above criterion or not.

Exploration of contrail physics using LES

- Two-dimensional behavior of aircraft wakes containing buoyant exhaust jets was studied to gain understanding of how the jet buoyancy influences the wake dynamics. We identified a mechanism in which the same-signed (as the primary vorticity) portion of the jet-generated baroclinic vorticity gets entrained into the trailing vortices, and the opposite-signed portion detrains into the atmosphere. This was found to strengthen the primary vorticity, reduce the spacing between the two primary vortices, and accelerate the wake descent.

- LES of contrails were carried out for the first 20 s duration of contrail life, starting from modeled initial conditions at 1 s downstream of the aircraft. The resulting contrail database was analyzed to quantify sensitivity of contrails to atmospheric temperature and relative humidity, initial ice nuclei number density, and the initial ice particle size.

  It was found that three distinct regimes exist in the early contrail growth – the early jet-controlled regime showing rapid ice growth, an intermediate regime where particle-induced turbulence effects are felt, and the subsequent regime mainly controlled by atmospheric relative humidity with respect to ice (RHi). RHi was found to be very critical in determining ice growth. Ambient temperature was found to have a significant effect on ice quantity only when the temperature is sufficiently high. The loss of ice particles due to sublimation did not follow a monotonic trend with RHi because in addition to the RHi-related supersaturation, the depletion effect is also present. The total ice area, ice particle size, and number density were all found to be sensitive to the initial ice nuclei number density, but the total ice mass remained insensitive to it at least in the regime considered. Ice growth was fairly insensitive to the initial particle size for the current range of initial particle size of around 0.1 μm.

8.1 Recommendations for future work

High-fidelity simulations of contrails that resolve scales as small as the jet-scales are not widespread due to their cost. But their utility is arguably very high in advancing our understanding of contrails. In the long term, they can help test new reduced-order contrail models to be used in global calculations.

To drive the current simulations closer to real world situations, it will be desirable to include additional physical processes in the model. The most important among these are perhaps coagulation, sedimentation, preferential concentration of particles, and radiation. Modeling them will enhance the physical details represented by the simulations. Atmospheric turbulence and wind shear should be included because they are known to cause contrail dispersion and spreading at durations longer than 1-2 minutes.

Finally, in order to effectively leverage the latest supercomputing technology, better algorithms can be implemented into the code. The use of a non-uniform mesh will greatly enhance the efficiency of these simulations. Multigrid or embedded mesh techniques will be needed for this purpose. Also, load-balancing in the Lagrangian module can be improved.

It is clear that in order to achieve definitive characterization of contrail behavior from LES to the extent that lower-order models can be reliably tested against these simulations, much wider range of parameters will have to be spanned. The above recommended developments can take these simulations nearer to that goal.

Bibliography

Aigner, A. & Grimshaw, R. 2001 Numerical simulations of the flow of a continuously stratified fluid incorporating inertial effects. *Fluid Dyn. Res.* **28**, 323–347.

Anderson, B. E., Winstead, E., Hudgins, C., Plant, J., Branhan, H.-S., Thornhill, L., Boudries, H., Canagaratna, M., Miake-Lye, R., Workhoudt, J., Worsnop, D., Miller, T., Ballenthin, J., Hunton, D., Viggiano, A., Pui, D., Han, H.-S., Blake, D. & McEchern, M. 2003 Overview of results from the nasa experiment to characterize aircraft volatile aerosol and trace species emissions (EXCAVATE). Proceedings of the AAC-Conference, June 30 to July 3, Friedrichshafen, Germany.

Appleman, H. 1953 The formation of exhaust condensation trails by jet aircraft. *Bull. American Meteorol. Soc.* **34**, 1420.

Apte, S. & Ghosal, S. 2004 A presumed pdf model for droplet evaporation/condensation in complex flows. *Center for Turbulence Research Annual Briefs* pp. 209–221.

Arakawa, A. & Lamb, V. R. 1981 A potential enstrophy and energy conserving scheme for the shallow water equations. *Monthly Weather Review* **109**, 18–36.

Batchelor, G. K. 2000 *An introduction to fluid dynamics*, 2nd edn. Cambridge Univ. Press, Cambridge, U.K.

Baumgardner, D. & Cooper, W. A. 1994 Airborne measurements in jet contrails: Characterization of the microphysical properties of aircraft wakes and exhaust. DLR-Mitt. 94-06, Dtsch. Zentrum für Luft- and Raumfahrt, Köln, Germany.

Blaisdell, G., Spyropoulos, E. & Qin, J. 1996 The effect of the formulation of nonlinear terms on aliasing errors in spectral methods. *Applied Numerical Math.* **21**, 207–219.

Bracco, A., McWilliams, J. C., Murante, G., Provenzale, A. & Weiss, J. B. 2000 Revisiting freely decaying two-dimensional turbulence at millennial resolution. *Phys. Fluids* **12** (11), 2931–2941.

Brenguier, J.-L. & Chaumat, L. 2001 Droplet spectra broadening in cumulus clouds. Part I: Broadening in adiabatic cores. *J. Atmospheric Sci.* **58** (6), 628641.

Brown, R. C., Miake-Lye, R. C., Anderson, M. R. & Kolb, C. E. 1996 Aerosol dynamics in near-field aircraft plumes. *J. Geophysical Res.* **101** (D17), 22,939–22–953.

Burton, T. M. & Eaton, J. K. 2005 Fully resolved simulations of particle-turbulence interaction. *J. Fluid Mech.* **545**, 67–111.

Chandrasekhar, S. 1981 *Hydrodynamic and hydromagnetic stability*. Dover Publications, New York.

Chlond, A. 1998 Large eddy simulation of contrails. *J. Atmospheric Sci.* **55** (5), 796819.

Choi, M. & Lele, S. 2001 Prediction of shock-cell structure using parabolized stability equations. AIAA Paper 2001-0744.

Christensen, U. R. & Yuen, D. A. 1985 Layered convection induced by phase transitions. *J. Geophys. Res.* **90**, 10291–10300.

Chu, B. T. & Kovásznay, L. S. G. 1958 Nonlinear interactions in a viscous heat conducting compressible gas. *J. Fluid Mech.* **3**, 494–514.

Comte-Bellot, G. & Corrsin, S. 1971 Simple Eulerian time correlation of full- and narrow-band velocity signals in grid-generated, 'isotropic' turbulence. *J. Fluid Mech.* **48**, 273 – 337.

Crow, S. C. 1970 Stability theory for a pair of trailing vortices. *AIAA J.* **8** (12), 2172–2179.

Doswell, C. A. & Markowski, P. M. 2004 Is buoyancy a relative quantity? *Monthly Weather Review* **132** (4), 853863.

Dubrulle, B., Laval, J.-P. & Sullivan, P. P. 2002 A new dynamical subgrid model for the planetary surface layer. Part I: The model and a priori tests. *J. Atmospheric Sci.* **59** (4), 861876.

DÜrbeck, T. & Gerz, T. 1995 Large-eddy simulation of aircraft exhaust plumes in the free atmosphere: effective diffusivities and cross-sections. *Geophys. Res. Lett.* **22** (23), 3203–3206.

Dutton, J. A. & Fichtl, G. H. 1969 Approximate equations of motion for gases and liquids. *J. Atm. Sci.* **26**, 241–254.

Eckart, C. 1960 *Hydrodynamics of oceans and atmospheres*. Pergamon Press, New York.

Emanuel, K. A. 1994 *Atmospheric convection*. Oxford Univ. Press, New York.

Esmaeeli, A. & Tryggvason, G. 2005 A direct numerical simulation study of the buoyant rise of bubbles at O(100) Reynolds number. *Phys. Fluids* **17**, 093303.

Fahey, D. W. 1995 In situ observations in aircraft exhaust plumes in the lower stratosphere at midlatitudes. *J. Geophys. Res.* **100** (D2), 30653074.

Gerz, T. & Hölzapfel, F. 1999 Wing-tip vortices, turbulence and the distribution of emissions. *AIAA Journal* **37** (10), 1270.

Gierens, K. M. 1996 Numerical simulations of persistent contrails. *J. Atmospheric Sci.* **53** (22), 33333348.

Gill, A. E. 1982 *Atmosphere-ocean dynamics*, *International Geophysics Series*, vol. 30. Academic Press, New York.

Gough, D. O. 1969 The anelastic approximation for thermal convection. *J. Atm. Sci.* **26**, 448–456.

Han, J., Lin, Y.-L., Arya, S. P. & Proctor, F. 1999 Large eddy simulation of aircraft wake vortices in a homogeneous atmospheric turbulence: Vortex decay and descent. AIAA Paper 99-0756.

Hill, F. M. 1975 A numerical study of the descent of a vortex pair in a stably stratified atmosphere. *J. Fluid Mech.* **71**, 1–13.

Holt, S. E., Koseff, J. R. & Ferziger, J. 1992 A numerical study of the evolution and structure of homogeneous stably stratified sheared turbulence. *J. Fluid Mech.* **237**, 499–539.

Horiuti, K. 1987 Comparison of conservative and rotational forms in large eddy simulation of turbulent channel flow. *J. Comput. Phys.* **71**, 343.

Huebsch, W. W. & Lewellen, D. C. 2006 Sensitivity study on contrail evolution. AIAA Paper 2006-3749.

Jacobitz, F. G., Sarkar, S. & Van Atta, C. W. 1997 Direct numerical simulations of the turbulence evolution in a uniformly sheared and stably stratified flow. *J. Fluid Mech.* **342**, 231–261.

Jacobson, M. Z., Kittelson, D. B. & Watts, W. F. 2005 Enhanced coagulation due to evaporation and its effect on nanoparticle evolution. *Environ. Sci. Technol.* **39**, 9486–9492.

Jacobson, M. Z. & Seinfeld, J. H. 2004 Evolution of nanoparticle size and mixing state near the point of emission. *Atmos. Environ.* **38**, 1839–1850.

Jacquin, L. & Garnier, F. 1996 On the dynamics of engine jets behind a transport aircraft. In *AGARD, CP-584*, p. 37. NATO.

Jarvis, G. T. & McKenzie, D. P. 1980 Convection in a compressible fluid with infinite Prandtl number. *J. Fluid Mech.* **96**, 515–583.

Jensen, E. J., Ackerman, A. S., Stevens, D. E., Toon, O. B. & Minnis, P. 1998 Spreading and growth of contrails in a sheared environment. *J. Geophysical Research* **103** (D24), 31,557–31,567.

Jensen, E. J., Toon, O. B., Westphal, D. L., Kinne, S. & Heymsfield, A. J. 1994 Microphysical modeling of cirrus 1. Comparison with 1986 FIRE IFO measurements. *J. Geophysical Research* **99** (D5), 10,42110,442.

Kärcher, B. 1994 Transport of exhaust products in the near trail of a jet engine under atmospheric conditions. *J. Geophys. Res.* **99** (D7), 14,509–14,517.

Kärcher, B., Busen, R., Petzold, A., Schröder, F. P., Schumann, U. & Jensen, E. J. 1998 Physicochemistry of aircraft-generated liquid aerosols, soot, and ice particles, 1. Models description. *J. Geophysical Res.* **103** (D14), 17,129–17,148.

Kärcher, B., Hirschberg, M. M. & Fabian, P. 1996*a* Small-scale chemical evolution of aircraft exhaust species at cruising altitudes. *J. Geophys. Res.* **101** (D10), 15169–15190.

Kärcher, B., Peter, T., Biermann, U. M. & Schumann, U. 1996*b* The initial composition of jet condensation trails. *J. Atmospheric Sci.* **53** (21), 3066–3083.

Kevrekidis, I., Gear, C. & Hummer, G. 2004 Equation-free: The computer-aided analysis of complex multiscale systems. *AIChE J.* **507**, 1346.

Klima, K. & Waitz, I. 2006 Assessment of a global contrail modeling method. Proceedings of the TAC-Conference, June 26-29, Oxford, U.K.

Kovásznay, L. S. G. 1953 Turbulence in supersonic flow. *J. Aero. Sci.* **20**, 657–682.

Kraabøl, A. G., Flatøy, F. & Stordl, F. 2000 Impact of no_x emissions from subsonic aircraft: Inclusion of plume processes in a three-dimensional model covering Europe, North America, and the North Atlantic. *J. Geophys. Res.* **105**, 3573,3581.

Kundu, P. K. & Cohen, I. M. 2004 *Fluid mechanics*, 3rd edn. Elsevier, Boston.

Lee, D., Clare, P., Haywood, J., Kärcher, B., Lunnon, R., Pilling, I., Slingo, A. & Tilston, J. 2000 Identifying the uncertainties in radiative forcing of climate from aviation contrails and aviation-related cirrus. DERA/AS/PTD/CR000103. UK Ministry of Defense.

Lele, S. K. 1992 Compact finite difference schemes with spectral-like resolution. *J. Comput. Phys.* **103**, 16–42.

Lele, S. K. 1998 Direct numerical simulations of compressible turbulent flows: Fundamentals and applications. In *Transition, turbulence and combustion modelling* (ed. A. Hanifi, P. H. Alfredsson, A. V. Johansson & D. S. Henningson), *ERCOFTAC*, vol. 6, pp. 421–488. Kluwer Academic Publishers, Boston.

Lewellen, D. C. & Lewellen, W. S. 1996 Large-eddy simulations of the vortex-pair breakup in aircraft wakes. *AIAA J.* **34**, 2337–2345.

Lewellen, D. C. & Lewellen, W. S. 2001 The effects of aircraft wake dynamics on contrail development. *J. Atmospheric Sci.* **58**, 390–406.

Lilly, D. K. 1992 A proposed modification of the germano subgrid-scale closure method. *Phys. Fluids A* **4** (3), 633–635.

Lui, C. & Lele, S. K. 2001 Direct numerical simulation of spatially developing, compressible, turbulent mixing layers. AIAA Paper 2001-0291.

Lukachko, S. P. & Waitz, I. A. 2005 Engine design and operational impacts on particulate matter precursor emissions. ASME Turbo Expo 2005, Reno-Tahoe, Nevada GT2005-69112.

Mahrt, L. 1986 On the shallow motion approximation. *J. Atm. Sci.* **43**, 1036–1044.

Marquart, S. & Mayer, B. 2002 Towards a reliable GCM estimation of contrail radiative forcing. *Geophys. Res. Lett.* **29** (8), 1179.

McDougall, T. J., Greatbatch, R. J. & Lu, Y. 2002 On conservation equations in oceanography: How accurate are Boussinesq ocean models? *J. Physical Oceanography* **32**, 1574–1584.

Meilinger, S. K., Kärcher, B. & Peter, T. 2005 Microphysics and heterogeneous chemistry in aircraft plumes - high sensitivity on local meteorology and atmospheric conditions. *Atmospheric Chemistry and Physics* **5**, 533–545.

Miake-Lye, R. C., Martinez-Sanchez, M., Brown, R. C. & Kolb, C. E. 1993 Plume and wake dynamics, mixing, and chemistry behind a high-speed civil transport aircraft. *J. Aircraft* **30** (4), 467.

Minnis, P., Ayers, J. K., Palikonda, R. & Phan, D. 2004 Contrails, cirrus trends, and climate. *J. Climate* **17** (8), 16711685.

Moet, H., Darracq, D. & Corjon, A. 2001 Development of a decay model for vortices interacting with turbulence. AIAA Paper 2001-0545.

Moin, P., Squires, K., Cabot, W. & Lee, S. 1991 A dynamic subgrid-scale model for compressible turbulence and scalar transport. *Phys. Fluids A* **3** (11), 2746–2757.

Müller, B. 1999 *Low Mach number asymptotics of the Navier-Stokes equations and numerical implications*. von Karman Institute for Fluid Dynamics, Rhode-Saint-Genese, Belgium.

Murphy, D. M. & Koop, T. 2005 Review of the vapor pressures of ice and supercooled water for atmospheric applications. *Quart. J. Meteorol. Soc.* **131**, 1539–1565.

Nomura, K. K., Tsutsui, H., Mahoney, D. & Rottman, J. 2006 Short-wavelength instability and decay of a vortex pair in a stratified fluid. *J. Fluid Mech.* **553**, 283–322.

Oberkampf, W. L. & Trucano, T. G. 2002 Verification and validation in computational fluid dynamics. *Prog. Aerospace Sci.* **38** (3), 209–272.

Ogura, Y. & Phillips, N. A. 1962 Scale analysis of deep and shallow convection in the atmosphere. *J. Atm. Sci.* **19**, 173–179.

Panton, R. L. 1996 *Incompressible flow*, 2nd edn. Wiley, New York.

Paoli, R., Helie, J. & Poinsot, T. 2004 Contrail formation in aircraft wakes. *J. Fluid Mech.* **502**, 361–373.

Paoli, R., Helie, J., Poinsot, T. & Ghosal, S. 2002 Contrail formation in aircraft wakes using large-eddy simulations. *Center for Turbulence Research, Proc. of the Summer Program* pp. 229–241.

Paoli, R., Laporte, F., Cuenot, B. & Poinsot, T. 2003 Dynamics of mixing in jet/vortex interactions. *Phys. Fluids* **15** (7), 1843–1860.

Paoli, R. & Shariff, K. 2003 Particle size distributions in atmospheric clouds. *Center for Turbulence Research, Annual Research Briefs* pp. 39–47.

Paoli, R., Shariff, K. & Shirgaonkar, A. A. 2006 Analysis of subgrid scale microphysics models for LES of turbulent condensation. *Center for Turbulence Research, Proc. of the Summer Program* .

Pedlosky, J. 1998 *Geophysical fluid dynamics*, 2nd edn. Springer-Verlag, New York.

Peltier, W. R. & Caulfield, C. P. 2003 Mixing efficiency in stratified shear flows. *Annual Rev. Fluid Mech.* **35**, 135–167.

Penner, J., Lister, D., Griggs, D., Dokken, D. & McFerland, M., ed. 1999 *Aviation and the global atmosphere*. Intergovernmental Panel on Climate Change, Cambridge Univ. Press.

Pierce, A. D. 1989 *Acoustics: An introduction to its physical principals and applications*, 2nd edn. Acoustical Society of America, New York.

Ponater, M., Marquart, S. & Sausen, R. 2002 Contrails in a comprehensive global climate model: Parameterization and radiative forcing results. *J. Geophysical Research* **107** (D13), 4164.

Pope, S. B. 1985 PDF methods for turbulent reactive flows. *Progress in Energy and Combustion Science* **11**, 119–192.

Pope, S. B. 2001 *Turbulent flows*. Cambridge Univ. Press, Cambridge, U.K.

Pruppacher, H. R. & Klett, J. D. 1978 *Microphysics of clouds and precipitation*, 2nd edn. D. Reidel Publishing Company, dordrecht, Holland.

Quackenbush, T. R., Teske, M. E. & Bilanin, A. J. 1996 Dynamics of exhaust plume entrainment in aircraft wake vortices. AIAA Paper 96-0747.

Rennich, S. C. 1997 Accelerated distruction of aircraft wake vortices. Ph.D. Thesis. Stanford University.

Riley, J. J. & Lelong, M.-P. 2000 Fluid motions in the presence of strong stable stratification. *Annual Rev. Fluid Mech.* **32**, 613–657.

Roache, P. J. 1998 *Verification and validation in computational science and engineering*. Hermosa Publishers, New Mexico.

Robins, R. E. & Delisi, D. P. 1990 Numerical study of vertical shear and stratification effects on the evolution of a vortex pair. *AIAA J.* **28** (4), 661–669.

Sadourny, R. 1975 The dynamics of finite-difference models of the shallow-water equations. *J. Atm. Sci.* **32**, 680.

Sarpkaya, T. 1983 Trailing vortices in homogeneous and density stratified media. *J. Fluid Mech.* **136**, 85–109.

Sausen, R., Isaksen, I., Grewe, V., Hauglustaine, D., Lee, D., Myhre, G., Köhler, M., Pitari, G., Schumann, U., Stordal, F. & Zerefos, C. 2005 Aviation radiative forcing in 2000: An update on IPCC (1999). *Meteorologische Zeitschrift* **14** (4), 555–561.

Schrader, M. L. 1997 Calculations of aircraft contrail formation critical temperatures. *J. Applied Meteorol.* **36** (12), 17251729.

Schumann, U. 1996 On conditions for contrail formation from aircraft exhausts. *Meteorol. Zeitsch* **5**, 423.

Schumann, U. 2005 Formation, properties and climatic effects of contrails. *Comptes Rendus Physique* **6**, 549–565.

Schumann, U., Konopka, P., Baumann, R., Busen, R., Gerz, T., Schlager, H., Schulte, P. & Volkert, H. 1995 Estimate of diffusion parameters of aircraft exhaust plumes near the tropopause from nitric oxide and turbulence measurements. *J. Geophysical Res.* **100** (D7), 14,147–14,162.

Scorer, R. S. & Davenport, L. J. 1970 Contrails and aircraft downwash. *J. Fluid Mech.* **43** (3), 451–464.

Serre, E., Bontoux, P. & Launder, B. E. 2004 Transitional-turbulent flow with heat transfer in a closed rotor-stator cavity. *J. Turbulence* **5** (8), N8, 1–13, dOI: 10.1088/1468-5248/5/1/008.

Shaw, R. A. 2003 Particle-turbulence interactions in atmospheric clouds. *Annual Rev. Fluid Mech.* **35**, 183–227.

Shimomura, Y. 1999 Turbulent transport modeling in low Mach number flows. *Phys. Fluids* **11** (10), 3136–3149.

Shirgaonkar, A. A. & Lele, S. K. 2005 High-resolution simulations of aircraft wake-exhaust mixing with applications to contrail formation. AIAA Paper 2005-4909.

Shirgaonkar, A. A. & Lele, S. K. 2006*a* Large eddy simulation of contrails: Effect of atmospheric properties. AIAA Paper 2006-1414.

Shirgaonkar, A. A. & Lele, S. K. 2006*b* On the extension of the Boussinesq approximation for inertia dominated flows. *Phys. Fluids* **18** (6), 066601.

Soong, C. Y. & Chyuan, C. H. 1998 Similarity solutions of mixed convection heat and mass transfer in combined stagnation and rotation-induced flows. *Heat and Mass Transfer* **34**, 171–180.

Spalart, P. R. 1996 On the motion of laminar wing wakes in a stratified fluid. *J. Fluid Mech.* **327**, 139–160.

Spalart, P. R. 1998 Airplane trailing vortices. *Annual Rev. Fluid Mech.* **30**, 107–138.

Spiegel, E. A. & Veronis, G. 1960 On the Boussinesq approximation for a compressible fluid. *Astrophys. J.* **131**, 442–447.

Spreiter, J. R. & Sacks, A. H. 1951 The rolling up of the trailing vortex sheet and its effect on the downwash behind wings. *J. Aeronautical Sci.* **18** (1), 21–32.

Stanescu, D. & Habashi, W. G. 1998 $2N$-storage low dissipation and dispersion Runge-Kutta schemes for computational acoustics. *J. Comput. Phys.* **143**, 674–681.

Steinbach, V., Hansen, U. & Ebel, A. 1989 Compressible convection in the Earth's mantle: A comparison of different approaches. *Geophys. Res. Lett.* **16**, 633–635.

Sussman, R. & Gierens, K. M. 1999 Lidar and numerical studies on the different evolution of vortex pair and secondary wake in young contrails. *J. Geophysical Research* **104** (D12), 2131–2142.

Sussman, R. & Gierens, K. M. 2001 Differences in early contrail evolution of two-engine versus four-engine aircraft: Lidar measurements and numerical simulations. *J. Geophysical Research* **106** (D5), 4899–4911.

Sykes, R. I., Lewellen, W. S. & Henn, D. S. 1988 A numerical study of the development of cloud-street spacing. *J. Atmospheric Sci.* **45** (18), 25562570.

Thunis, P. & Bornstein, R. 1996 Hierarchy of mesoscale flow assumptions and equations. *J. Atm. Sci.* **53** (3), 380–397.

Toon, O. B., Turco, R. P., Jordan, J., Goodman, J. & Ferry, G. 1989 Physical processes in polar stratospheric ice clouds. *J. Geophysical Research* **94**, 11,359–11,380.

Travis, D., Carleton, A. & Lauritsen, R. 2002 Contrails reduce daily temperature range. *Nature* **418**, 601.

Türk, L., Coors, D. & Jacob, D. 1999 Behavior of wake vortices near the ground over a large range of Reynolds numbers. *Aerospace Science and Technology* **2**, 71–81.

VAILLANCOURT, P. A. & YAU, M. K. 2000 Review of particle-turbulence interactions and consequences for cloud physics. *Bull. American Meteorol. Soc.* **81** (2), 285–298.

VAILLANCOURT, P. A., YAU, M. K. & GRABOWSKI, W. W. 2001 Microscopic approach to cloud droplet growth by condensation. Part I: Model description and results without turbulence. *J. Atm. Sci.* **58**, 1945–1965.

VÖMEL, H., OLTMANS, S. J., JOHNSON, B. J., HASEBE, F., SHIOTANI, M., FUJIWARA, M., NISHI, N., AGAMA, M., CORNEJO, J., PAREDES, F. & ENRIQUEZ, H. 2002 Balloon-borne observations of water vapor and ozone in the tropical upper troposphere and lower stratosphere. *J. Geophysical Res.* **107** (D14).

WANG, F. Y. & ZAMAN, K. B. M. Q. 2002 Aerodynamics of a jet in the vortex wake of a wing. *AIAA J.* **40** (3), 401–407.

YIH, C.-S. 1980 *Stratified Flows*, 2nd edn. Academic Press, New York.

YOUNG, K. C. 1993 *Microphysical processes in clouds*, 2nd edn. Oxford Univ. Press.

ZANG, T. 1991 On the rotation and skew-symmetric forms for incompressible flow simulations. *Appl. Numer. Math.* **7**, 27.